ATMOSPHERIC STUDIES USING REMOTE SENSING TECHNIQUES AND IN-SITU MEASUREMENTS OVER THE HIMALAYAN REGION

BY

ASHISH KUMAR

(Admission No. 2016DR1014)

THESIS

SUBMITTED TO

INDIAN INSTITUTE OF TECHNOLOGY

(INDIAN SCHOOL OF MINES), DHANBAD

for the award of the degree of

DOCTOR OF PHILOSOPHY

OCTOBER, 2019

भारतीय प्रौद्योगिकी संस्थान (भारतीय खनि विद्यापीठ),धनबाद
धनबाद, झारखण्ड, भारत, पिन-826004
INDIAN INSTITUTE OF TECHNOLOGY (INDIAN SCHOOL OF MINES), DHANBAD
DHANBAD, JHARKHAND, INDIA, PIN-826004
(An Autonomous Institute under Ministry of HRD, Govt. of India)

CERTIFICATE

This is to certify that the thesis entitled "**ATMOSPHERIC STUDIES USING REMOTE SENSING TECHNIQUES AND IN-SITU MEASUREMENTS OVER THE HIMALAYAN REGION**" being submitted by **Mr. Ashish Kumar (2016DR1014)** to the Indian Institute of Technology (Indian School of Mines), Dhanbad for the award of **Doctor of Philosophy (Ph.D.)** Degree in **Environmental Science and Engineering** is a record of bonafied research work carried out by him under our supervision and guidance. In our opinion, the thesis is worthy of consideration for the award of Doctor of Philosophy (Ph.D.) Degree in Environmental Science and Engineering in accordance with the regulation of the Institute. The results presented in this thesis have not been submitted for the award of any other degree.

Dr. Anshumali
(Thesis Supervisor)
Associate Professor

Dr. Narendra Singh
(External Supervisor)
Scientist-E, ARIES

Date: 26.10.2019

Place: IIT(ISM), Dhanbad

भारतीय प्रौद्योगिकी संस्थान (भारतीय खनि विद्यापीठ),धनबाद
धनबाद, झारखण्ड, भारत, पिन-826004
INDIAN INSTITUTE OF TECHNOLOGY (INDIAN SCHOOL OF MINES), DHANBAD
DHANBAD, JHARKHAND, INDIA, PIN-826004
(An Autonomous Institute under Ministry of HRD, Govt. of India)

Certificate Regarding Classified Data

This is to certify that the thesis entitled "**ATMOSPHERIC STUDIES USING REMOTE SENSING TECHNIQUES AND IN-SITU MEASUREMENTS OVER THE HIMALAYAN REGION**" being submitted to the Indian Institute of Technology (Indian School of Mines), Dhanbad by **Mr. Ashish Kumar (2016DR1014)** for the award of **Doctor of Philosophy (Ph.D.)** Degree in **Environmental Science and Engineering** does not contain classified information. This work is original and yet not been submitted to any institution or university for the award of any degree.

Signature of the candidate
(Adm. No. 2016DR1014)

Dr. Anshumali
(Thesis Supervisor)
Associate Professor

Dr. Narendra Singh
(External Supervisor)
Scientist-E, ARIES

Date: 26.10.2019

Place: IIT(ISM), Dhanbad

COPYRIGHT AND CONSENT FORM

To ensure uniformity of treatment among all contributors, other forms may not be substituted for this form, nor may any wording of the form be changed. This form is intended for original material submitted to the IIT (ISM), Dhanbad and must accompany any such material in order to be published by the ISM. Please read the form carefully and keep a copy for your files.

TITLE OF THESIS: ATMOSPHERIC STUDIES USING REMOTE SENSING TECHNIQUES AND IN-SITU MEASUREMENTS OVER THE HIMALAYAN REGION

AUTHOR'S NAME & ADDRESS: ASHISH KUMAR, Admission No. 2016DR1014, Department of Environmental Science and Engineering (ESE), Indian Institute of Technology (Indian School of Mines), Dhanbad – 826004, Jharkhand, India.

COPYRIGHT TRANSFER

1. The undersigned hereby assigns to Indian Institute of Technology (Indian School of Mines) all rights under copyright that may exist in and to: (a) the above Work, including any revised or expanded derivative works submitted to the IIT(ISM) by the undersigned based on the work; and (b) any associated written or multimedia components or other enhancements accompanying the work.

CONSENT AND RELEASE

2. In the event the undersigned makes a presentation based upon the work at a conference hosted or sponsored in whole or in part by the IIT(ISM) Dhanbad, the undersigned, in consideration for his/her participation in the conference, hereby grants the IIT(ISM) the unlimited, worldwide, irrevocable permission to use, distribute, publish, license, exhibit, record, digitize, broadcast, reproduce and archive; in any format or medium, whether now known or hereafter developed: (a) his/her presentation and comments at the conference; (b) any written materials or multimedia files used in connection with his/her presentation; and (c) any recorded interviews of him/her (collectively, the "Presentation"). The permission granted includes the transcription and reproduction of the Presentation for inclusion in products sold or distributed by IIT(ISM) Dhanbad and live or recorded broadcast of the Presentation during or after the conference.
3. In connection with the permission granted in Section 2, the undersigned hereby grants IIT(ISM) Dhanbad the unlimited, worldwide, irrevocable right to use his/her name, picture, likeness, voice and biographical information as part of the advertisement, distribution and sale of products incorporating the Work or Presentation, and releases IIT(ISM) Dhanbad from any claim based on right of privacy or publicity.
4. The undersigned hereby warrants that the Work and Presentation (collectively, the "Materials") are original and that he/she is the author of the Materials. To the extent the Materials incorporate text passages, figures, data or other material from the works of others, the undersigned has obtained any necessary permissions. Where necessary, the undersigned has obtained all third party permissions and consents to grant the license above and has provided copies of such permissions and consents to IIT(ISM) Dhanbad.

GENERAL TERMS

* The undersigned represents that he/she has the power and authority to make and execute this assignment.
* The undersigned agrees to indemnify and hold harmless the IIT(ISM) Dhanbad from any damage or expense that may arise in the event of a breach of any of the warranties set forth above.
* In the event the above work is not accepted and published by the IIT(ISM) Dhanbad or is withdrawn by the author(s) before acceptance by the IIT(ISM) Dhanbad, the foregoing copyright transfer shall become null and void and all materials embodying the Work submitted to the IIT(ISM) Dhanbad will be destroyed.
* For jointly authored Works, all joint authors should sign, or one of the authors should sign as authorized agent for the others.

Ashish Ku

Signature of the Author

ACKNOWLEDGEMENT

At the outset, I would like to express my special appreciation and thanks to my benevolent research Supervisors, ***Dr. Anshumali*** *and* ***Dr. Narendra Singh*** *for their continuous support and dedicated involvement in every step during my Ph.D study and related research, for their patience, motivation, and immense knowledge. Their unstinted kindness, affectionate, guidance and noble generosity has created a life-long impression on me. Researching, executing, and compiling this thesis was a very challenging and rewarding experience for me, and I could not have reached up to this stage without their valuable guidance. I could not have imagined having a better guide than* ***Dr. Anshumali*** *for my study at IIT(ISM).* ***Dr. Narendra Singh****, an inspiring Scientist, has played a wonderful role of catalyst whenever I had qualms. His kind nature and affectionate soul has made me eligible to learn his scholarly treasure.*

I express my profound and sincere gratitude to the Director, the Registrar, the Deans Academic council, Librarian-in-charge, Joint Registrar, and the DSC members of IIT(ISM), for selecting me as a Research scholar in this esteemed institution, and providing me necessary infrastructure and resources to accomplish my research work. I am thankful to the Head of Department, all Faculty members, and staffs of the Environmental Science & Engineering Department at IIT(ISM) for their kind support and encouragement for the timely submission of the thesis.

I also place on record, my deepest sense of gratitude to ***Dr. Wahab Uddin****, Director, Aryabhatta Research Institute of observational sciencES (ARIES), Nainital for giving his consent and permission to pursue my doctoral studies at IIT(ISM). Thanks are due to all the ARIES authorities, colleagues and the staff members. I shall always keep on record the sincere and great support extended by Uday, Arjuna Reddy, Chandra Prakash, Mohit Joshi, Prashant, Naveen, Hemant, Arjun Singh, Vinod Sah, Mahesh Pandey, Abhishek Sharma, Jaydeep Singh, Narendra Ojha, Raman Solanki, Manu Mehta, and Debasis Nath..*

I wish to express my sincere appreciation for the timely help and support, I received from my research colleagues and friends at IIT(ISM), especially Bijendra Kumar, Madavi Venkatesh, Ashutosh Anand, Kumari Priyanka, and Satish Kumar. I am also grateful to all those whose names may have escaped attention here but have directly or indirectly, have lent their hand in this venture.

I would like to extend my thanks and appreciation to all the Principal Investigators and their staff for establishing and maintaining the different AERONET stations (http://aeronet.gsfc.nasa.gov/) whose data are used in my current research. I am thankful to the whole team members of RAWEX-GVAX for making the field campaign at ARIES, Nainital successful, and acknowledge the U.S. DOE Atmospheric Radiation Measurement (ARM) Climate Research Facility

(https://www.arm.gov/research/campaigns/aaf2011gvax) and Indian Space Research Organization (ISRO) for providing access to the data for this work. I am grateful to the ICARE Thematic Centre, University of Wyoming's Department of Atmospheric Science, and Tropospheric Emission Monitoring Internet Service (TEMIS) for granting access to the necessary data sets. I am thankful to MODIS, CALIPSO, TRMM, AIRS, MERRA-2, ERA-Interim, and GLDAS data centers for providing access to required data. NOAA Air Resources Laboratory are also thankful for providing the provision for running the HYSPLIT transport and dispersion model used in this thesis.

Encouragement and support provided by my family during the research has been a great source of enthusiasm throughout the study. I am deeply indebted to my Mother, Brother, and Bhabhi for their unceasing encouragement, support and attention. I am grateful to my wife for her co-operation, moral support and endurance through this venture. It is rather difficult to define the experience of my charming daughter Aayushi, sweet son Aayush, and beloved Abhinav and Anvi, who were stunned out of their wits while observing me burning the midnight oil during this endeavor.

The final and most deeply felt appreciation goes to my deceased Father, who always believed in my ability to be successful in the academic arena. I know he would be proud and I will forever be grateful for the knowledge and values he instilled in me.

Ashish Kumar

SYNOPSIS

Introduction

The anthropogenic activities, together with the natural sources like air-borne dusts, storms etc. are affecting the Earth's atmosphere to a great extent at both regional and global scales by altering the physical and chemical characteristics, natural connectivity and behaviours of the key Essential Climate Variables (ECVs) in the domain of atmosphere (e.g. *Kaufman et al.*, 2002; *Mahmood et al.*, 2007; *Huffman et al*., 2007; *IPCC*, 2014, *Letcher*, 2015; *Boucher*, 2015; *Hersey et al*., 2015; *Okamoto et al*., 2018). These key variables are mainly the aerosols, clouds, precipitation, air temperature, humidity, and winds. In the past few decades pioneering efforts have been made by the scientific communities in studying these climate sensitive variables on a global scale using remote sensing and in-situ measurement techniques, to answer many difficult questions on the Earth's atmosphere and to better predict the changes in the air quality, weather, and climate (e.g. *Hartmann et al*., 1992; *Albrecht*, 1989; *Quante*, 2004; *Kumari and Goswami*, 2010; *Wang*, 2013; *Hou et al*., 2014; *Boucher*, 2015). As, different terrains and geographical locations possess different challenges in understanding the time dependent behaviours of the atmosphere. Therefore, it is equally important to conduct the regional and location specific studies on the key atmospheric variables and associated meteorology using the ground and space-borne remote sensing, and in-situ measurements. Furthermore, the regional climate, particularly, over the mountains, where the multitude of physical processes, and mountain-induced atmospheric phenomena occurs, and where the slopes are greatly affected due to the deleterious anthropogenic interventions, is highly relevant.

With the noteworthy progress in remote sensing and in-situ techniques during the last few decades, a global awareness has been build up towards understanding the variations in the atmospheric parameters, and associated meteorology from the high altitude Himalayan region (*IPCC*, 2014). The atmospheric studies from this region, where dearth of reliable ground based and in-situ measurements on the major influencing atmospheric and meteorological parameters are available (*Mal et al.,* 2016), have an unequivocal relevance, as the occurrences of cloudbursts, flash floods, landslides etc. have increased over this region due to the human's overexploitation of natural resources through rapid urbanization, industrialization, deforestation, emissions from forest-fires,

transportation etc. (*Valdiya,* 2008*; Tiwari and Joshi,* 2016). As a consequence, during the past few decades, the region has witnessed huge economic and human losses due to the catastrophes like - the flash flood and cloudburst of Kedarnath in June 2013 which resulted in more than 10,000 killings (*Dobhal et al.*, 2013; *Asthana and Asthana,* 2014; *Dimri et al*., 2017), and the devastating earthquake of April 2015 which killed more than 8,000 people (*Mendoza et al.,* 2016). The regional climate change over the Himalayan region is evidenced by several researchers (e.g. *UCOST and USERC,* 2012; *Mishra,* 2014), however, there are still limited information available on the long term variations in the key atmospheric and meteorological variables over this region, and their possible impacts on the ecosystem.

With this motivation, the work in this thesis is oriented to the study on the plethora of in-situ, ground and satellite based remote sensing tools, and their utility in advancing the knowledge on the spatio-temporal variability and characteristics of the aerosols, clouds, and precipitations, together with the variations in the meteorological parameters over the Himalayan region, taking into account a variety of temporal and spatial scales.

Study Area

Overall the study is focussed on the Himalayan region, confined in the boundary of 26.5-40.5°N, 62.5-105.5°E that mainly consists of complex chain of high mountains, rivers, elevated plateaus, deep gorges and extended valleys, and the mean elevation of this region is ~1000 m. The selected boundary also includes the Indo-Gangetic plains and foothills of the Himalaya. To investigate the variations in the atmospheric and meteorological variables on a finer scale, the in-situ and ground based measurements from a regional representative high-altitude, remote, and sparsely inhabited observing station ARIES (29.36° N, 79.46°E, ~1958 m above mean sea level), Nainital are used. Furthermore, clouds and precipitation studies are performed over northern India that encompasses the group of states namely – Jammu & Kashmir, Himachal Pradesh, Punjab, Haryana and Chandigarh, Uttarakhand, Delhi & Non-Capital Region (NCR), and Uttar Pradesh.

Data and methods

The data used in this research work includes number of ground and satellite based remote sensing and in-situ tools, and their details are tabulated in **Table 1**.

Table 1: Details on the data used in the research work.

Tools	Data product	key parameters	Duration
Ground based/ In-situ observations	AERONET	aerosols	2001 – 2018
	LiDAR	aerosols	2008- 2012
	AWS	meteorological parameters	2013 –2018
	Radiosonde	meteorological parameters	2011-2012, 2017
	RaDAR	wind parameters, Doppler spectra	2017
Satellite products	MODIS	aerosols, fire counts	2006-2016
	CALIPSO	aerosols, clouds	2006- 2017
	TEMIS (Multi-sensors)	aerosol index	1980-2017
	OMI	aerosol index	2005-2017
	AIRS	surface temperature	2002-2017
	TRMM	Rainfall	1998-2016
	DARDAR	clouds and precipitation	2007 – 2016
Trajectory model	HYSPLIT model	transport of air masses	2011, 2012
Re-analysis product	ERA-Interim	meteorological parameters	2010-2011
	MERRA-2	meteorological parameters, carbon monoxide, dust column mass density, snow depth	1980-2017
	GLDAS	Surface albedo, surface temperature	2000-2017

The methodology used in the research work are summarized below:

- Common days of reliable measurements with best temporal match were selected in the studies using the ground based LiDAR and AERONET measurements.
- Using the mean MODIS AOD values within 20 km × 20 km and 30 km × 30 km grid and AERONET AOD averaged over ±30 minutes and ±15 minutes, various cases on spatio-temporal combinations were examined and the levels of agreement were established.
- Aerosol retrievals from CALIPSO over the observing site is selected based on the criteria of high Cloud Aerosol Discrimination (CAD) score (between -35 and -100), the presence of 5 or more valid vertical profiles up to 4.5 km altitudes within the horizontal distance of ~ 100 km from the site, and the availability of coincident AERONET measurements within ± 30 minutes of the closest CALIPSO ground track.
- For comparison between the AOD measurements both from MODIS and CALIPSO, the required data is selected based on the number of screening and coincidence constraints.
- The wavelength conversions from 500 nm (AERONET) to 550 nm (MODIS) or to 532 nm (CALIPSO) were performed using the formula devised by *Eck et al.*, 1999.
- Various performance metrices are used in the satellite product assessment and comparison between the data used in this study. Some of these metrices are – Pearson's correlation, Mean

Bias Error (MBE), Root Mean Square Error (RootMSE), Average Error Ratio (AER), and, Percentage Mean Relative Deviation (MRD).

- Iterative approach is used in the estimation of LiDAR Ratio (LR) of the LiDAR system.
- To estimate the Boundary Layer (BL) heights from radiosonde, vertical gradient method is used for the Potential Temperature (PT) and Specific Humidity (SH).
- To retrieve the BL height from CALIPSO, two methods, namely the threshold (*Melfi et al.*, 1985*; Jordan et al.*, 2010) and Wavelet Covariance Transform (WCT) (*Brooks*, 2003*; Compton et al.*, 2013) are used.
- In the development of Graphical User Interface (GUI) demonstrating the pulse compression technique in atmospheric RaDAR, the software tools like LabVIEW and MATLAB are used.

Research objective and significance

The major research objectives and their significance are:

1) *Study on the atmospheric aerosols – variation in its optical properties, evaluation, utilization in deriving the LiDAR ratio and Boundary Layer (BL) height, and the case studies on aerosol transport over the Himalayan region*.
   - ✓ The AErosol RObotic NETwork (AERONET) based aerosol observations from ten stations located in the Himalayan and adjacent Indo-Gangetic plains are investigated at seasonal scales. The study will help in understanding the optical, and physical/ chemical properties of aerosols to different air mass origins and local aerosol sources, and their spatio-temporal characteristics. It may also serves as the crucial input for modeling and in predicting the air quality and climate system over the mountainous region.
   - ✓ Accuracy of the latest version of remotely sensed aerosol estimations from MODerate-resolution Imaging Spectroradiometer (MODIS) and Cloud-Aerosol Lidar and Infrared Pathfinder Satellite Observations (CALIPSO) satellites were assessed against ground based measurements over a complex terrain in the southern part of central Himalayan region. This study may help in checking and correcting the artefacts or inconsistencies associated with theoretical or operational exactitudes in satellite-based measurements (*Ramachandran and Kedia*, 2013) before drawing any conclusions, or before formulating the current and future climate change over this complex mountainous region.
   - ✓ Focusing the AERONET measurements from the observing site, the LiDAR ratio (LR) for the three different LiDAR systems is estimated and discussed using collocated

measurements with the evaluated MODIS satellite retrievals. The methodologies adopted in LR estimation, can be utilized by the larger science community worldwide in reducing the uncertainty in their calculation on aerosol extinction coefficients and Aerosol Optical Depth (AOD) values.

- ✓ The BL height is an essential parameter used for understanding the vertical transfer of momentum, energy and mixing of pollutants in the lower troposphere. It is also very useful parameter for weather, climate and pollution studies (*Monks et al*., 2009). Therefore, making use of the validated satellite product, together with the in-situ observations, the BL height is determined over the complex high altitude observing site and over the geographical boundary 26-36°N and 72-86°E, where the major portion of north India is confined. Different methods were explored in estimating the BL height, and the most suitable and highly accurate methods among them were identified.
- ✓ Cases on the continental transport of smoke plumes emanating from crop-residue burning, and the long range transport of dust, together with a case where hygroscopic ultra-fine aerosol particles dominates (formation of local cloud) are discussed by making use of the remote sensing and in-situ measuremets, and trajectory modeling at local and regional scales over the Himalayan region. Further, impact study is carried out using the long-term active fire, carbon monoxide emission, dust column mass density, snow depth, albedo and snowfall data sets obtained from re-analysis models over this region. These studies may expand the horizon of knowledge on the contributions from the major pollutants pertaining to the climate change in the Himalayan context.

2) *Climatological study on the absorbing aerosols over the Himalayan region using multi-sensor remote sensing data*:
   - ✓ The transport and accumulation of the absorbing aerosols, mainly dust, negatively contribute to cloud formation, snowfall, and retreat of glaciers. Therefore, study on the seasonal climatology and trends on the absorbing aerosols with main emphasis on dust has been attempted on a global scale as well as over the Himalayan region, using 38 years (1980-2017) of data records from multi-sensors and re-analysis data.
3) *Study on the distribution of clouds and precipitation over Northern India*:
   - ✓ Clouds are the critical and multi-scale atmospheric features least understood (Alley et al., 2007), and has close associations with precipitation. Both of these climatic

variables plays a major role in regional climate change and have the potential to modulate the flow of incoming solar and outgoing thermal radiation, climate, weather, hydrological cycle, circulations and chemical reaction processes occurring in the atmosphere (e.g. Cess et al., 1989, 1990, 1996; Ramanathan et al., 1989; Hartmann et al., 1992; Stephens, 2005; Qian et al., 2012). Therefore, the present study deals with regional study on the distribution and association of these two variables.

- ✓ The study make use of a decade (2007-2016) observations from CloudSat and CALIPSO satellites, to obtain a detailed climatology and three-dimensional distribution of seven basic cloud types, together with the liquid and solid precipitation patterns over the Northern States of India (NSI).

4) *Study on the meteorological parameters using remote sensing and in-situ measurements:*

- ✓ The long term variations in the meteorological parameters at both horizontal and vertical scales over any region is essential to mitigate the meteorological hazards, or to plan for some preventive measures or remedial actions, beforehand. Therefore, the present study deals with the study on the key meteorological variables – air temperature, pressure, humidity, and winds over the local and broader scales in the Himalayan region.
- ✓ There is a shortfall in understanding the performance of ground based active remote sensing tools like RaDAR over the hilly and mountainous terrain, where the multitude of intriguing atmospheric phenomena occurs due to mountain-valley circulations that manifests the diurnal pattern of the meteorological parameters. Therefore, a portion of the study is also devoted on the preliminary investigations on the validation of three-dimensional wind information obtained from ARIES Stratosphere- Troposphere (ST) RaDAR facility.

Major Findings

The summary of key findings are:

1) The seasonal variations in the aerosol optical parameters, mainly volume-size distribution, total, fine and coarse mode AODs, and Fine Mode Fraction (FMF) from ten AERONET stations (Nainital, Pantnagar, Kanpur, New Delhi, Lahore, Gual Pahari, Gandhi College, Jaipur, Lumbini, and Pokhara) revealed the dominance of coarse mode particles (mainly from long-range

transport of dust) during pre-monsoon and monsoon seasons (≥ 0.2 $\mu m^3/\mu m^2$) for Kanpur, New Delhi, Lahore, Gual Pahari, Gandhi College, and Jaipur stations, and about two times lowest over the Himalayan foothills (Nainital, Lumbini, and Pokhara). The prevailing fine mode aerosols are observed for almost all the stations during post-monsoon and winter, which are mainly attributed to biomass burning and are of continental origine. Lower AOD values are observed at the high altitude station i.e. Nainital than densely populated, low-altitude urban and industrialized stations.

2) Analysis revealed that AOD from the latest MODIS Terra C6.0 deep blue (DB) 30 km × 30 km and CALIPSO version 4.10 (overpass within ~100 km distance) are in a very good agreement (R ≥ 0.9) with that from coincident AERONET measurements averaged over the span of ±30 minutes, as shown in **Fig. 1** and **Fig. 2**, respectively. About 77 % of the AOD retrieved using MODIS and ~ 87 % from CALIPSO were found to be within the expected error (EE) limits. The AOD comparison between MODIS Terra C6.0 DB and CALIPSO version 4.10, suggested their synergic use in aerosol characterization over the Himalayan region.

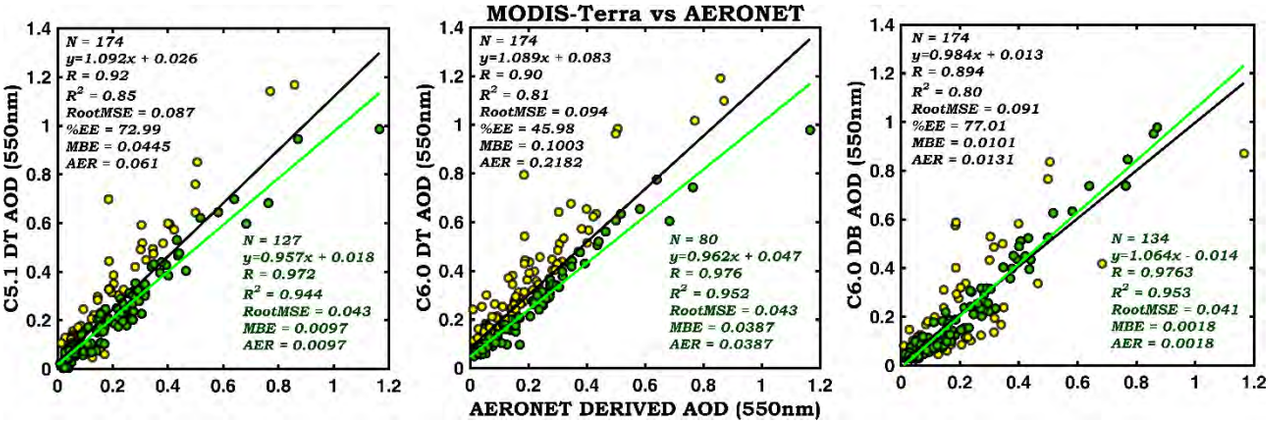

Fig.1. Scatter plot with one-one line comparison for MODIS Terra and AERONET AOD measurements; green + yellow = complete, green = for values within %EE.

3) In comparison to the earlier versions, CALIPSO version 4.10 is found to have undergone substantial changes and marked improvement in the surface elevation, vertical feature and tropospheric aerosol classification, and the long term inter-comparison between the two versions (versions 3 and 4), in the grid 28.86°-29.86° N and 78.96°-79.96° E revealed that their vertical feature and aerosol sub-types are in agreement of ~ 94.6 % and ~ 68.6 %, respectively.

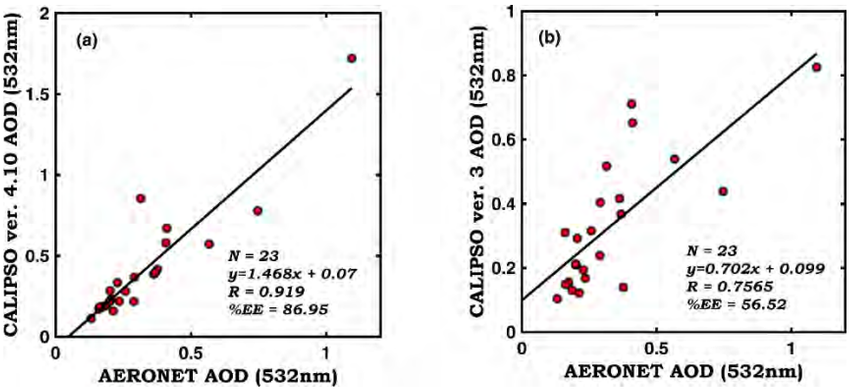

Fig. 2. Scatter plot with one-one line comparison for AERONET AOD and **(a)** CALIPSO ver. 4.10, **(b)** ver. 3 column AOD measurements.

4) Utilizing the AOD retrievals from AERONET and MODIS collections, the iteratively computed LR for three LiDAR systems operated from ARIES, Nainital was found to between 6 and 52, under various atmospheric conditions, and the LR is found to be lower (< 16) during winter and higher (> 43) during summer.
5) Study on the BL height estimations suggested that the Wavelet Covariance Transform (WCT) method for CALIPSO could be the best choice as compared to the threshold method, and complements well with the specific humidity gradient method used with the radiosonde observation.
6) The long term seasonal analysis on BL height using the satellite measurements over the geographical boundary 26-36°N and 72-86°E discovered higher BL height during March-May (MAM), as compared to December-February (DJF).
7) Case studies on the major pollutants confirmed the dominance of smoke (**Fig. 3**) and dust (**Fig. 4**) over the Himalayan region, mainly during post-monsoon and summer/spring, respectively.
8) Study revealed that the dust loading is highest during summer/spring season across the globe and over the Himalayan region, however, the contribution from dust over the Himalayan region to the total global dust volume is highest (8.5 %) during monsoon, and lowest during winter (4.7 %). Monthly analysis on dust column mass density over the period 1980-2017 showed that May and December are the maxima and minima dust depositing months over the Himalayan region.
9) The absorbing aerosol index was observed highest (~ 0.4) during June-August and March-May over the globe and Himalayan region (~0.75), respectively.

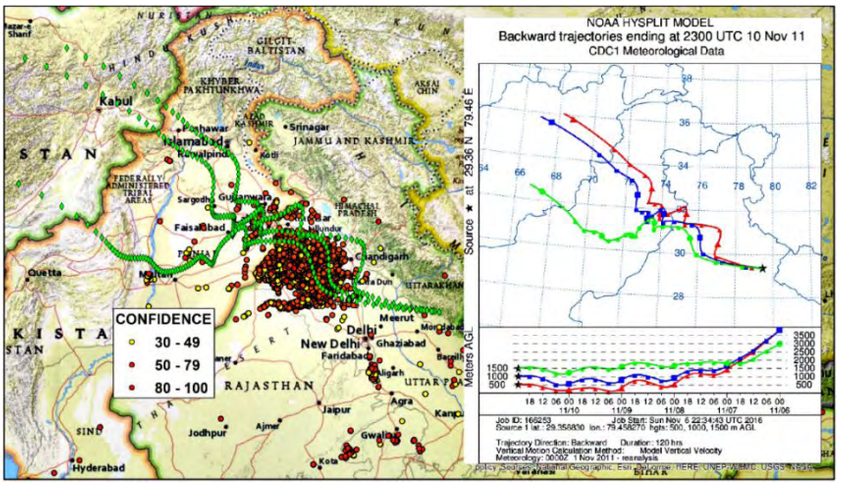

Fig. 3. Region showing fire occurrences during 1-10 November 2011, along with the 5-days HYSPLIT back-trajectories of air mass ending at the study site.

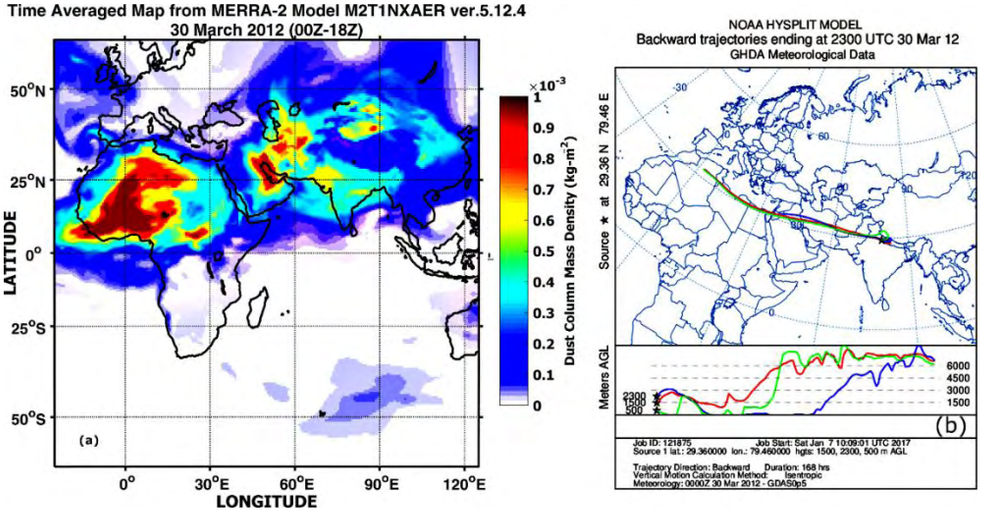

Fig. 4. (a) Time averaged plot of MERRA-2 based dust column mass density (in kg m^{-2}), and **(b)** 168 hrs HYSPLIT back-trajectories for 30 March 2012 showing the transport of air mass to the site.

10) Rising trend in the absorbing aerosols are found over the Himalayan region during the past 38 years of the study.

11) Investigation on different cloud types and precipitation over Northern Indian states demonstrates the tendency of seasonal variations. Study revealed maximum cloud appearances (>50%) and occurance of liquid precipitation during southwest monsoon seasons (June-September), while during the active period of western disturbances (December-March), ~25% of the total annual clouds appeared in addition to the dominant solid precipitation over most of the NSI region. Uttarakhand, Himachal Pradesh, and Jammu & Kashmir experienced the maximum liquid and solid precipitations during the last decade.

12) Climatological study on different cloud types found that during last decade, the Altostratus (*As*) is the most frequently occurring cloud type (~ 20%) over the region, while during the active months of southwest monsoon and western disturbances, the most dominant cloud types are deep convective (~ 25%) and nimbostratus (~ 33%), respectively. The association of deep convective (*DC*) and nimbostratus (*Ns*) with solid precipitation on an annual scale are observed as 1.6 % and 76 % of their total co-occurances, respectively. On the other hand, their association with liquid precipitation are found as 98.4 % and 23.7 %, respectively, and hence implying that *Ns* and *DC* clouds are the main contributor in solid and liquid precipitation occurences over the NSI region during the last decade.

13) The climatologies and long-term study on meteorology over the Himalayan region revealed significant departures in the meteorological variables from their usual ranges, especially the surface temperature. **Table 2** shows the least-square linear regression trend in temperature anomalies during past 38 years (1980-2017) over Nainital and the entire Himalayan region. Overall the trends in surface temperature at both regional and local scales are positive, with their slopes as +0.019 and +0.0062, respectively, and hence confirming the warming of the Himalayan region.

14) The preliminary inter-comparison on the wind parameters obtained from the ARIES ST RaDAR and radiosonde, showed reasonably good agreements. However, there is further scope of improvements in the RaDAR data processing aspect, that essentially to work out during the commissioning phase.

Table 2: The year-wise anomalies in annual mean surface temperature for the past 38 years (1980-2017) over Nainital and Himalaya using MERRA-2 re-analysis model. The trends ≥ 0.5 are shaded in 'yellow', and that ≤ -0.5 are shaded in 'green'.

Nainital										
Year	**+0**	**+1**	**+2**	**+3**	**+4**	**+5**	**+6**	**+7**	**+8**	**+9**
1980	+0.01	-0.26	-0.96	-0.80	-0.07	-0.14	-0.42	+1.11	+0.45	+0.14
1990	+0.05	+0.21	+0.16	+0.21	+0.27	+0.12	-0.23	-0.84	-0.03	+0.69
2000	-0.19	+0.16	+0.53	-0.19	-0.12	-0.37	+0.31	-0.25	-0.52	+0.45
2010	+0.54	-0.74	-0.22	-0.45	+0.02	+0.03	+0.79	+0.54		
Himalaya										
Year	**+0**	**+1**	**+2**	**+3**	**+4**	**+5**	**+6**	**+7**	**+8**	**+9**
1980	-0.44	-0.55	-0.77	-0.64	-0.41	-0.11	-0.46	+0.28	+0.36	-0.50
1990	+0.14	-0.06	-0.47	-0.09	+0.19	-0.15	-0.23	-0.34	+0.54	+0.63
2000	+0.06	+0.34	+0.40	-0.02	+0.26	-0.19	+0.58	+0.23	-0.16	+0.24
2010	+0.35	-0.16	-0.56	+0.23	-0.05	+0.25	+0.85	+0.42		

Conclusions

Making use of plethora of in-situ, ground and satellite based remote sensing tools and ancillary data sets, the key atmospheric parameters – aerosols, clouds, and precipitation, and the meteorological variables mainly the temperature, pressure, humidity, winds etc. over the Himalayan region are investigated. The study on these parameters are very critical from present climate change perspective, and may serve as an inevitable input for placing an emphasis on the necessity of more ground based and in-situ instrument systems, and network of stations with their telecommunication and co-ordination over the data sparce Himalayan region. Quantitative investigation on the absorbing aerosols, mainly dust over the Himalayan region is performed, which can be extended further to understand the driving mechanisms behind snow surface darkening, undue melting of snowpack's, increase in the extreme weather events etc. and overall radiative impacts on the high altitude Himalayan region. Cloud and precipitation (solid or liquid) dominant regions were also detected over annual and seasonal time scales.

This research work, to some extent, fills the gap exists in the atmospheric studies of highly sensitive mountain environment across the world. The outcome of this study will provide a satisfactory impetus to improve the database system and will provide a general background to the Scientists involved in atmospheric and Earth sciences, and to the policy makers for more specific studies on the key atmospheric parameters and their inter-relations. In addition, this study may serve as one of the inevitable reference while placing an emphasis on the urgent requirements of the stations with more ground based and in-situ instrument systems, and while planning for establishment of the network of such stations over the data sparse Himalayan region.

RECOMMENDATIONS

The research on aerosols, clouds, and precipitation over Himalayan region presented in this thesis is almost exclusively based on freely available datasets, therefore, it is essential that such datasets should continue to be made free of charge and easily accessible to carry out further research on the topic in future. Further, there is a great need of time to time assessment on the temporal and spatial accuracy and representativeness of the latest releases of satellite remote sensing data products. It is also very much essential to orient the emphasis of the Himalayan research more towards the information-rich approach, instead of principle-based approach, by installing more ground based remote sensing tools, and by establishing large number of in-situ observing facilities.

TABLE OF CONTENTS

Contents

LIST OF TABLES

LIST OF FIGURES

ACRONYMS AND ABBREVIATIONS

AAI	Absorbing Aerosol Index
ACF	Auto-Correlation Function
ACP	aerosols, clouds, and precipitation
AE	Angstrom Exponent
AER	Average Error Ratio
AERONET	AErosol RObotic NETwork
AGL	above ground level
AI	Aerosol Index
AIRS	Atmospheric Infrared Sounder
amsl	above mean sea level
AMSR-E	Advanced Microwave Scanning Radiometer-Earth
AMSU-B	Advanced Microwave Sounding Unit-B
AOD	Aerosol Optical Depth
APD	Avalanche Photo Diode
ARIES	Aryabhatta Research Institute of observational sciencES
ASTRAD	Aries ST RADar
ATSR	Along Track Scanning Radiometer
a.u.	arbitrary unit
AVHRR	Advanced Very High Resolution Radiometer
AWS	Automatic Weather Station
BL	Boundary Layer
CAD	Cloud Aerosol Discrimination
CALIOP	Cloud and Aerosol LiDAR with Orthogonal Polarization

CALIPSO	Cloud-Aerosol Lidar and Infrared Pathfinder Satellite Observations
CATS	Cloud–Aerosol Transport System
CCN	Cloud Condensation Nuclei
CERES	Clouds and the Earth's Radiant Energy System
CESM	Community Earth System Model
CIRA	COSPAR International Reference Atmosphere
CMORPH	CPC MORPHing Technique
CNES	Centre National d'Etudes Spatiales
COSPAR	COmmittee on SPAce Research
CPC	Climate Prediction Centre
CPR	Cloud Profiling Radar
CRE	Cloud-Radiative Effect
CRU	Climatic Research Unit
DARDAR	raDAR/liDAR
DB	Deep Blue
dB	decibel
DBS	Doppler Beam Swinging
DEM	Digital Elevation Map
DJF	December-January-February
DJFM	December-January-February-March
DMSP	Defense Meteorological Satellite Program
DOE	Department of Energy
DT	Dark Target
DUP	Data User Programme
EARLINET	European Aerosol Lidar Network
ECMWF	European Centre for Medium-Range Weather Forecasts
ECV	Essential Climate Variable
EDC	EROS Data Center
EE	Expected Error

e.g.	For example
EOS	Earth Observing System
ERA	ECMWF Re-Analysis
EROS	Earth Resources Observation and Science
ERTS	Earth Resources Technology Satellite
ESA	European Space Agency
FAO	Food and Agriculture Organization
FCF	Feature Classification Flag
FFT	Fast Fourier Transform
FIR	Finite Impulse Response
FIRMS	Fire Information for Resource Management System
FMF	Fine Mode Fraction
FOV	Field Of View
FPGA	Field Programmable Gate Arrays
FRP	Fire Radiative Power
FTP	File Transfer Protocol
GCOS	Global Climate Observing System
GCM	General Circulation Model/ Global Climate Model
GEO	Geostationary
GES DISC	Goddard Earth Sciences Data and Information Services Center
GHCN	Global Historical Climatology Network
GLAS	Geoscience Laser Altimeter System
GLDAS	Global Land Data Assimilation System
GMAO	Global Modeling and Assimilation Office
GOES	Geostationary Operational Environmental Satellite
GOME	Global Ozone Monitoring Experiment
GPCP	Global Precipitation Climatology Project

GPS	Global Positioning System
GSMaP	Global Satellite Mapping of Precipitation
GTOPO30	Global 30 Arc-Second Elevation
GUI	Graphical User Interface
GVAX	Ganges Valley Aerosol Experiment
hPa	hectopascal
HSRL	High Spectral Resolution Lidar
HYSPLIT	Hybrid Single Particle Lagrangian Integrated Trajectory
i.e.	that is
ICARE	Interactions Clouds Aerosols Radiations Etc
ICSU	International Council for Science
IGP	Indo-Gangetic Plains
IIR	Infinite-Impulse Response
IISc	Indian Institute of Science
IMD	India Meteorological Department
IPCC	Intergovernmental Panel on Climate Change
IPP	Inter-Pulse Period
IR	Infra-red
ISCCP	International Satellite Cloud Climatology Project
ISL	Integrated Side-lobe Level
ISM	Indian Summer Monsoon
ISRO	Indian Space Research Organization
ISS	International Space Station
ITU	International Telecommunication Union
IWC	ice-water content
JAXA	Japan Aerospace Exploration Agency
JJA	June-July-August
JJAS	June-July-August-September

LAMP	LiDAR for Atmospheric Measurement and Probing
LASER	Light Amplification by Stimulated Emission of Radiation
LEO	Low Earth Orbiting
LiDAR	Light Detection And Ranging
LIS	Lightning Imaging Sensor
LITE	Lidar in-Space Technology Experiment
LNA	Low Noise Amplifier
LP DAAC	Land Processes Distributed Active Archive Center
LR	LiDAR Ratio
LT	Local Time
MAM	March-April-May
MBE	Mean Bias Error
MERRA	Modern-Era Retrospective analysis for Research and Applications
MISR	Multiangle Imaging Spectro-Radiometer
MODIS	MODerate-resolution Imaging Spectroradiometer
MPLNET	Micropulse LiDAR Network
MRD	Mean Relative Deviation
MS-AAI	Multi-Sensor Absorbing Aerosol Index
MSG	Meteosat Second Generation
MSS	Multi Spectral Scanner
MST	Mesosphere-Stratosphere-Troposphere
MTI	Multispectral Thermal Imager
MTSAT	Multifunctional Transport Satellites
MW	Microwave
NASA	National Aeronautics and Space Administration
NCEP	National Centers for Environmental Prediction

NCAR	National Center for Atmospheric Research
NCR	Non-Capital Region
Nd:YAG	Neodymium-Doped Yttrium Aluminum Garnet
NMS	Network Management Software
NNR	NCEP-NCAR re-analysis
NOAA	National Oceanic and Atmospheric Administration
NSI	Northern State of India
OMI	Ozone Monitoring Instrument
PARASOL	Polarization and Anisotropy of Reflectances for Atmospheric Science coupled with Observations from a Lidar
PDF	Probability Density Function
PERSIANN	Precipitation Estimation from Remotely Sensed Information using Artificial Neural Networks
PHOTONS	PHOtométrie pour le Traitement Opérationnel de Normalisation Satellitaire
PM	Particulate Matter
PMT	Photo-Multiplier Tubes
POLDER	Polarization and Directionality of the Earth's Reflectances
PR	Precipitation RaDAR
PRL	Physical Research Laboratory
PRT	Pulse Repetition Time
PSD	Power Spectral Density
PSL	Peak Side-lobe Level
PT	Potential Temperature
PW	pulse width
RaDAR	Radio Detection And Ranging
RAWEX	Regional Aerosols Warming Experiment

RCS	Range-Corrected Signal
RF	Radio Frequency
RFI	Radio frequency Interference
RH	Relative Humidity
RMS	Root-Mean-Square
RootMSE	Root Mean Square Error
RS-232	Recommended Standard-232
RT	real time
RWP	RaDAR Wind Profiler
SAD	Spaced Antenna Drift
SCIAMACHY	SCanning Imaging Absorption spectrometer for Atmospheric CHartographY
SD	Standard Deviation
SDA	Spectral De-convolution Algorithm
SeaWiFS	Sea-viewing Wide Field-of-view Sensor
SEM	Standard Error of Mean
SEVIRI	Spinning Enhanced Visible and InfraRed Imager
SH	Specific Humidity
SNR	Signal to Noise Ratio
SON	September-October-November
SSA	Single Scattering Albedo
SSM/I	Special Sensor Microwave/Imager
SSMIS	Special Sensor Microwave Imager-Sounder
ST	Stratosphere - Troposphere
TCW	Total Column Water
TEMIS	Tropospheric Emission Monitoring Internet Service
TIROS	Television Infrared Observation Satellite
TMI	TRMM Microwave Instrument
TMPA	TRMM Multi-satellite Precipitation Analysis
TOMS	Total Ozone Mapping Spectrometer

TRM	Transmit-Receive Module
TRMM	Tropical Rainfall Measuring Mission
UHF	Ultra High Frequency
UN	United Nations
UNEP	United Nations Environment Programme
UNFCC	United Nations Framework Convention on Climate Change
UNESCO	United Nations Educational, Scientific and Cultural Organization
US	United States
USGS	United States Geological Survey
ver.	version
VFM	Vertical Feature Mask
VHF	Very High Frequency
VIRS	Visible and Infrared Scanner
VIS	Visible
WCC	World Climate Conference
WCP	World Climate Programme
WCRP	World Climate Research Program
WCT	Wavelet Covariance Transform
WD	Wind direction
WHO	World Health Organization
WMO	World Meteorological Organization
WRF	Weather Research and Forecasting
w.r.t.	with respect to
WS	Wind speed
ZDC	Zero-Doppler Clutter

Chapter 1

INTRODUCTION

CHAPTER 1
INTRODUCTION

1.1. The Earth and its surroundings

The Earth is the fifth largest planet of the solar system, located at about 150 million km away from the Sun. It revolves around the Sun once in every 365 days and rotates on its own axis in 24 hours. The Sun is an important source of energy needed for sustaining life on the Earth. The radiation from the Sun that reaches the Earth's surface (shortwave radiation) varies geographically and seasonally, depending upon the prevailing atmospheric condition and the level of absorption/scattering from the atmosphere surrounding the Earth (*Hart*, 1978; *Hartmann,* 1994). The concept of atmosphere was first brought by Aristotle in his book '*Meteorologica*' written in 347 BC. According to this book, the atmosphere is a mixture of gases, and the water vapour is present to balance the precipitation (*Seinfeld and Pandis,* 2012). By the nineteenth century, Scientists discovered the major gaseous components present in the atmosphere together with their compositions, production, and exchange processes. These gaseous components are mainly nitrogen (N_2) with a volume percentage of ~78.09 %, oxygen (O_2) with ~20.95 %, Argon (Ar) with ~0.93 % and carbon dioxide (CO_2) with ~0.03 % (*Saha,* 2008). The composition of these gaseous components, that regulates and governs the balance between incoming and outgoing radiation to the Earth and its atmosphere, are steadily changing due to human activities, and hence causing warming over the Earth's surface. The volume percentage of water vapour (H_2O), that plays a major role in the formation of clouds, are showing high spatio-temporal variability ranging from almost 0 to 5% (*Wallace and Hobbs,* 2006), and their abundance is mainly controlled by evaporation and precipitation (*Seinfeld and Pandis,* 2012). However, all these gaseous components are basically sub-agents of the full atmospheric system, and their composition and effects are well documented and understood to some extent (e.g. *Houghton et al*., 2001; *Lal*, 2007; *Butler and Lawrence*, 2009;

Parrish et al., 2011; *IPCC*, 2014; *Baklanov et al*., 2016). On the other hand, the role of some main atmospheric agents like aerosols, clouds, precipitation, temperature, winds etc. that are getting estranged from their natural connectivity and behaviors, have very low level of understanding. Therefore, it becomes necessary to perform rigorous studies on these main agents which has the potential to alter the climate system, in the view of predicting the future climate.

1.2. Changes in the Earth's Atmosphere

The atmosphere is one of the vital component for Earth system, and to ensure our continued survival we need to protect it by developing a comprehensive understanding of its structure and dynamics. The phenomena such as fossil fuel combustion and biomass burning are directly linked to the anthropogenic activities across the globe, affecting the weather and climate at various spatial and temporal scales (*Kumar et al.,* 2018). In the recent years it has been realized that these anthropogenic sources as well as the natural sources like air-borne dusts, storms etc. are affecting the atmosphere to a great extent both at regional and global scales (*Mahmood et al.*, 2007; *IPCC,* 2014, *Letcher,* 2015; *Boucher,* 2015).

Since the pre-industrial era, humans have been contributing in changing the atmospheric compositions on a large scale through anthropogenic emissions, which has led to an unprecedented rise in the atmospheric concentration of the leading greenhouse gases, as evident in **Fig. 1.1**.

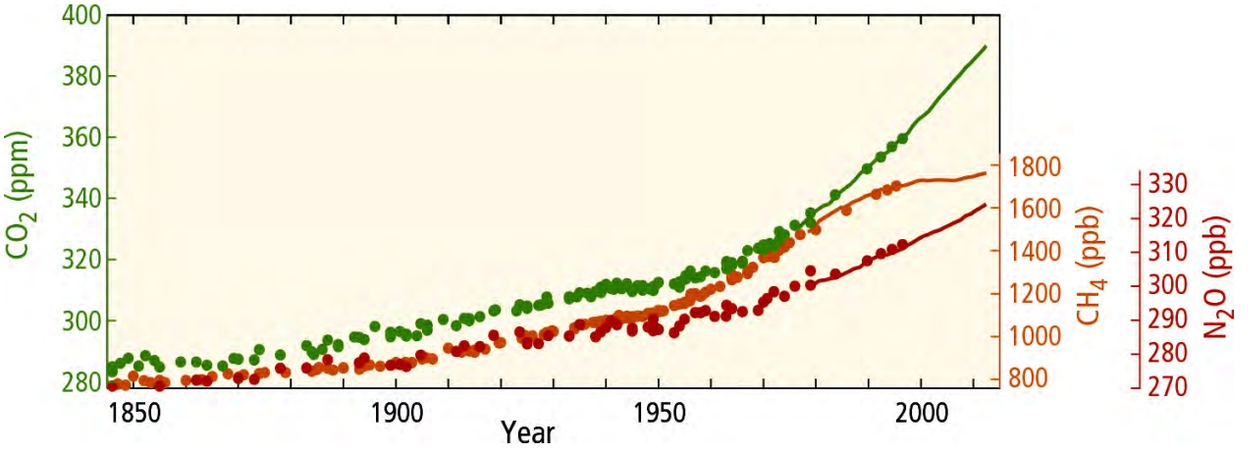

Fig. 1.1. Global averaged time series of the atmospheric concentration of carbon dioxide (CO_2), methane (CH_4) and nitrous oxide (N_2O) from 1848-2012 (*IPCC,* 2014).

According to the Fifth Assessment Report of the Intergovernmental Panel on Climate Change (IPCC), the global surface temperature (combined land and ocean) shows an increasing trend with warming of 0.85°C (0.65 - 1.06 °C) over the period from 1880 to 2012, and the contributions to this warming are very likely from the anthropogenic increase in the concentration of the greenhouse gases and other anthropogenic forcings together (*IPCC,* 2014), as evident from **Fig. 1.2**.

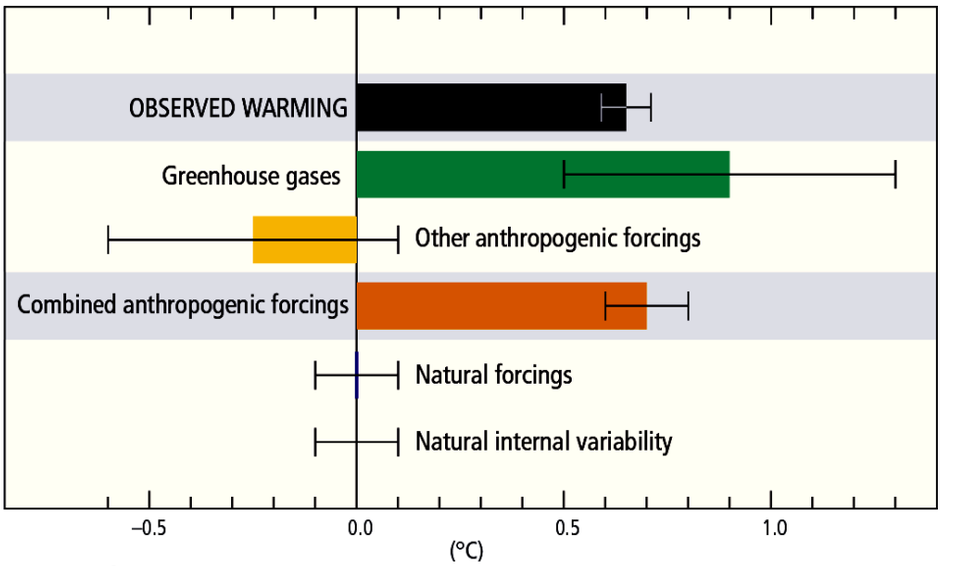

Fig. 1.2. Global surface warming trends over the period 1951 to 2010, and the corresponding contributions from the greenhouse gases, and from anthropogenic and natural forcing's (*IPCC,* 2014). The likely ranges are shown as whiskers, and the average value as bars.

The key factors driving the changes in anthropogenic greenhouse gas emissions and other anthropogenic forcing's are the population, economic growth, urbanization, changes in the energy usage and pressure on the land resources etc. These anthropogenic sources as well as the natural sources like air-borne dust, storms etc. alters the concentration, chemical composition, size distribution and shapes of the atmospheric components (*Boucher,* 2015), mainly the aerosols, clouds, and precipitation (ACP). Any such alterations can affect the climate on regional, as well as on global scales (*IPCC,* 2014*; Hansen and Sato,* 2016). The extent of such alterations in the atmosphere due to these changes can be accessed through the measurements using the remote sensing techniques and in-situ tools (*Robinson,* 1974; *Bell,* 1995; *Hoff and Christopher,* 2009; *Emeis,* 2010). At the same time, it is essential that before drawing any conclusions, or before

formulating the current and future predictions, an understanding has to be developed on the relationship between the remote sensing techniques and in-situ measurements. In addition, any artefacts or inconsistencies associated with the theoretical or operational exactitudes in their measurements are necessarily be checked and corrected (*Ramachandran and Kedia,* 2013).

1.3. Relevance of studying the key atmospheric variables – aerosols, clouds, and precipitation

There are variety of changes happening in the atmosphere, which are resulting in poor air quality, catastrophic weather events, and changes in the Earth's climate. Intense scientific studies on ACP are being conducted across the globe to answer many difficult questions about the Earth's atmosphere and to better predict the changes in the air quality, weather, and climate (e.g. *Hartmann et al*., 1992; *Albrecht*, 1989; *Quante*, 2004; *Kumari and Goswami*, 2010; *Wang*, 2013; *Hou et al*., 2014; *Boucher*, 2015). Similarly, to improve the methods for limiting pollution, and to forecast the harmful air quality conditions, information on ACP is crucial. The importance of ACP and their relevance in the present study is discussed below.

The aerosols play an important role in the Earth's atmospheric system and its chemistry (*Andreae and Crutzen*, 1997). It tends to neutralise the effect of greenhouse gases by contributing to the cooling of the atmosphere, however, there are several types of aerosol, such as black carbon and mineral dust that partially absorbs the incident sunlight and terrestrial radiations, thereby contributing to the warming of the atmosphere. The increased levels of some natural and anthropogenic aerosols like dust, fog, smoke etc. alters the air quality and are responsible for serious health hazards and other undesired changes in the weather or climate. The relative impact of natural aerosols and those from human origin has to be quantified accurately. Moreover, the understanding of aerosol properties and their variations over any region in conjunction with the prevailing meteorological conditions improves the knowledge of atmospheric processes such as the radiation balance, cloud formation, precipitation and chemical processes aloft. Rising concerns on the climate change demands better insight of physical and optical properties of the aerosols by means of ground and satellite based measurements such as AErosol RObotic NETwork (AERONET), Light Detection And Ranging (LiDAR), Cloud-Aerosol Lidar and Infrared Pathfinder Satellite Observations (CALIPSO) and MODerate-resolution Imaging Spectroradiometer (MODIS). In addition, the correlations and improved understanding on their relationships are also essential in formulating the reliable current and future predictions (*Ramachandran and Kedia,* 2013). Past

studies have emphasized that satellites are the best tool for broader understanding of aerosol parameters on a global scale, however, satellite measurements possess certain uncertainties, especially, at the regional or local scales which can be quantified through their assessment with the ground based or in-situ measurements (*Kokhanovsky et al.,* 2007; *Hersey et al.,* 2015; *Mehta et al*., 2016; *Kumar et al*., 2018). In this context, it is also important that the satellite based latest release of aerosol products are examined from time to time and corrected with the ground based observation on a regional scale at finer spatial resolutions. In addition, while dealing with the aerosol optical product retrieval algorithms, it is quite common to make some priori assumptions in the retrieval processes that sometime may lead to the erroneous results and incorrect conclusions. One such assumption is the unknown aerosol LiDAR Ratio (LR) value of any Mie LiDAR system, whose wrong selection may produce uncertainty in the calculation of aerosol extinction coefficients and Aerosol Optical Depth (AOD) values. Likewise, the aerosol retrieval algorithms based on satellite data demands few assumptions regarding aerosol optical properties like Single Scattering Albedo (SSA) and refractive index (*Kokhanovsky et al.,* 2007*; Wang et al.,* 2011). Hence, their rigorous assessments are also essential for studies on aerosol distribution.

On the other hand, clouds are the critical and multi-scale atmospheric features least understood (*Alley et al.,* 2007). They occurs over a wide spatio-temporal scales and plays a crucial role in the Earth's radiation budget by modulating the flow of incoming solar and outgoing thermal radiation, climate, weather, hydrological cycle, circulations and chemical reaction processes occurring in the atmosphere (e.g. *Cess et al.,* 1989, 1990, 1996*; Ramanathan et al.,* 1989*; Hartmann et al.,* 1992*; Stephens,* 2005*; Qian et al.,* 2012). The quantitative investigation on the vertical structures, spatial variability, distribution, and properties of clouds is a necessary step (*Wang and Sassan,* 2001*; Stephens et al.,* 2002*; Rajeevan et al.,* 2013), as it has close connection with the climate system (e.g. rainfall, water cycle etc.). Their accurate representation, especially at regional scales, is needed to understand the functioning of different atmospheric processes and their association with underlying forcing and feedback mechanisms in which they are involved. The study on regional scale may help in unravelling the subtle influences e.g. due to orography. Additionally, the study may further be supportive in forming the base-lines for the development and validation of the regional climate models and simulations for better predicting the weather and climate changes (*Cess et al.,* 1989, 1990, 1996*; Wang et al.,* 2004*; Foley,* 2010; *Singh et al*., 2016).

Precipitation is also an important observable for researchers and decision makers in the areas such as weather forecasts, landslides mapping, flood forecasting and mapping, agriculture, and industries. The spatio-temporal distribution of precipitation is variable and intermittent on regional or local scales. An accurate measurement of precipitation with high spatial and temporal resolution is possible using the ground based rain gauge networks and weather Radio Detection And Ranging's (RaDARs) (*Yilmaz et al*., 2005; *Krishnamurti et al*., 2009). However, due to the limitations posed by the Earth's topography and lack of resources to install and manage the hydro-meteorological stations, it is very difficult to have a good distribution and density of such networks, especially in the less accessible regions like Himalaya (*Rainbird*, 1967; *Rodríguez-Iturbe and Mejía*, 1974). Moreover, the high operational and maintenance cost restricts one to build the networks of ground based weather RaDAR in the developing countries like India. Further, the rain gauges in India are insufficiently dense, unevenly distributed, and mainly clustered in the lower altitude regions (plains), in the basins and rift valleys of the mountains like Himalayas, which may not represent the high spatial variability of precipitation (e.g. *Rajeevan et al*., 2006; *Mishra and Coulibaly*, 2009; *Immerzeel et al*., 2014). For producing the district-wise (which are more than 500 in numbers) rainfall climatology and forecast in India, the India Meteorological Department (IMD), a government body, is holding the responsibility for recording the synoptic meteorological variables. IMD have deployed a total of about 1350 automatic rain gauges, covering almost every district, however, that still may not be sufficient to represent the rainfall variability for a district or a state. Innovations in satellite remote sensing technology has provided an alternate platform of retrieving regional and global based precipitation data with high spatial and temporal resolutions, effectively and economically to fill the gaps in the data sparse regions, where the ground instruments are not available (*Adler et al*., 2000; *Mitra et al*., 2003; *Bajracharya et al.,* 2015; *Prakash*, 2019). Utilizing the satellite tools to investigate this chaotic atmospheric variable (*Fritsch et al.,* 1998*; Sivakumar*, 2001) and especially over the data sparse Himalayan region is a necessary step.

1.4. Himalaya and its Environment

Himalaya is made up of two words – '*hima*' and '*alaya*' meaning snow and home, respectively. This represents Himalaya as a 'home of the snows'. The Himalayan region covers ~ 17 % (3 million hectares) of the mountains running from east to west i.e. from mount Namcha

Barwa (~ 7756 m) to Nanga Parbat (~ 8126 m), continuing for about 2,500 km (*Singh et al*., 2011), and includes the world's 14 mountains higher than 8000 m (**Fig. 1.3**), in which the Mount Everest (~ 8850 m), also known as Mt. Qomolangma, is the highest mountain peak in the world.

Fig. 1.3. Himalayan mountains higher than 8000 m (courtesy: Daktylek Krakow, March 2011).

Himalaya is regarded as one of the 'steady water tower' full of glaciers and snow packs (*Messerli et al.*, 2004; *Viviroli et al.*, 2007; *Bandyopadhyay*, 2013), that supports perennial downstream rivers (e.g. Ganges, Yamuna, Indus, Brahmaputra, Yangtze, Yellow river) and caters

the hydrological demands of huge population locally and in the adjoining Asian countries (Afghanistan, Bangladesh, Bhutan, China, India, Myanmar, Nepal, and Pakistan), including their domestic, agricultural and industrial water requirements (*Archer et al.*, 2010). This spectacular and dramatic region is the third largest deposit of ice and snow in the world. The increase in natural and anthropogenic activities, greenhouse gases and human induced modifications like deforestation, overgrazing and recreational activities are making the Himalayan ecosystem more vulnerable to the climate change, leading to the great loss of endemic flora and fauna (e.g. *Xu et al*., 2009; *Chettri et al.*, 2010; *Gurung and Bajracharya*, 2012; *Pant et al.*, 2018). The undue interventions over this region are also affecting the hydrological cycle by eventually melting the 'steady water tower' of glaciers and snow packs, which in turn, leading to several glacial hazards, like catastrophic glacial lake outbursts that killed hundreds of people and livestock in the Himalaya during last 50 years (*Richardson and Reynolds*, 2000). To some extent, the increase in natural and anthropogenic activities may be accounted for an increase in extreme weather and climate events (drought, flood, cloud bursts, earthquakes etc.), leaving colossal losses and trauma. During the past few decades, the Himalayan region has encountered huge economic and human losses (mortality and morbidity) due to the catastrophes like - the flash flood and cloudburst of Kedarnath in June 2013 which resulted in more than 10,000 killings (*Dobhal et al.*, 2013; *Asthana and Asthana*, 2014; *Dimri et al*., 2017), and the devastating earthquake on 25 April 2015 in Nepal which killed more than 8,000 people (*Mendoza et al.*, 2016).

1.5. Relevance of Atmospheric studies over the Himalayan region

In the present era of ground based, airborne and satellite observations along with the modeling of Earth atmosphere system, a wealth of data is being produced and processed over land and ocean. In the past few decades pioneering efforts have been made by the scientific communities on global scale studies by means of the networks of ground based instruments and satellite missions to understand the complex atmospheric phenomenon, their forecasts and predictions worldwide (*Holben et al*., 1998; *Kaufman et al.*, 2002; *Winker et al*., 2002; *Huffman et al*., 2007; *Hersey et al*., 2015; *Okamoto et al*., 2018). Since different terrains and geographical locations possess different challenges in understanding the time dependent behaviours of the atmosphere. Therefore, it is equally important to conduct regional and location specific studies on the atmospheric phenomenon using the ground and space-borne remote sensing and in-situ measurements. Furthermore, the

regional climate, particularly over the mountains, where the multitude of physical processes and mountain-induced atmospheric phenomena occurs, and where the slopes are greatly affected due to the deleterious anthropogenic interventions, is highly relevant.

With the noteworthy progress in remote sensing and in-situ techniques during the last few decades, a global awareness has been build up towards understanding the variations in the atmospheric parameters, and associated meteorology from the high altitude Himalayan region (*IPCC,* 2014). The atmospheric studies from this region, where dearth of reliable ground based and in-situ measurements on the major influencing atmospheric and meteorological parameters are available (*Mal et al.,* 2016), have an unequivocal relevance, as the occurrences of cloudbursts, flash floods, landslides etc. have increased over this region due to the human's overexploitation of natural resources through rapid urbanization, industrialization, deforestation, emissions from forest-fires, transportation etc. (*Valdiya,* 2008*; Tiwari and Joshi,* 2016). The regional climate change over the Himalayan region is evidenced by several researchers (e.g. *UCOST and USERC,* 2012; *Mishra,* 2014), however, there are still limited information available on the long term variations in the key atmospheric and meteorological parameters, mainly the ACP, temperature, winds, relative humidity (RH) over this region, and their possible impacts on the ecosystem. This includes the preliminary assessment on climate change with impact studies on temperature and rainfall, snow cover and glaciers, biodiversity, streams and rivers, agriculture and other sectors conducted for a portion of the Himalayan region (*UCOST and USERC,* 2012; *Mishra,* 2014). Taking the reference of the past studies and considering the remote sensing and in-situ measurements as valuable data source, particularly for monitoring the key atmospheric parameters, a long term study on the variations, mainly in temperature, RH, winds, aerosols, clouds, and precipitation, over the Himalaya at local and regional scales, has been presented in this thesis. The study allows researchers to move a step forward in understanding the climate change over this 'third pole' i.e. Himalaya in a much better way.

1.6. Objectives of the study

The major research objectives are:

1) ***Study on the atmospheric aerosols – variation in its optical properties, evaluation, utilization in deriving the LiDAR ratio and Boundary Layer (BL) height, and the case studies on aerosol transport over the Himalayan region*:**

The investigation on the aerosol size distribution over ten AERONET stations located in the Himalayan region is performed. Apart from this, the performance of latest version of satellite products is evaluated against in-situ and ground based measurements, as previously done by the researchers (e.g. *Choudhry et al.,* 2012*; Solanki and Singh,* 2014) on earlier versions. The AOD retrievals from the latest level-2 data collections (C5.1 and C6.0) of MODIS onboard Aqua and Terra satellites and CALIPSO versions (4.10 and 3.xx) are subjected for quantitative analysis to assess the level of agreement with the quality assured level-2.0 ground based AERONET measurements from Aryabhatta Research Institute of observational sciencES (ARIES), Nainital, a high altitude regional representative site in the Himalayas. This would enable subsequent usage of the satellite products for understanding the aerosol characteristics and their impact over the region.

Focusing the AERONET measurements over ARIES, Nainital, the LR for three different Mie LiDAR systems is estimated and discussed using collocated measurements with the evaluated MODIS satellite retrievals. Further, making use of the latest version of CALIPSO dataset and in-situ radiosonde measurements, the BL height is estimated using different numerical methods, in order to identify the most suitable and accurate one. Further, a long term seasonal analysis on BL heights is carried out over a sub-portion of the Himalayan region using latest version of CALIPSO data sets.

Case studies on the continental transport of smoke plumes emanating from crop-residue burning, and the long range transport of dust, together with a case where hygroscopic ultra-fine aerosol particles dominates (formation of local cloud) are discussed using the collocated ground based measurements from a regional representative site, in conjunction with the satellite measurements (MODIS and CALIPSO), re-analysis data and trajectory modeling. Impact study using the long-term data on active fire, carbon monoxide (CO) emission, dust column mass density, snow depth, albedo and snowfall over the glaciated surfaces of the Himalayan region, are also included in the case studies.

2) ***Climatological study on the absorbing aerosols over the Himalayan region using multi-sensor remote sensing data***:

Himalaya, a fragile mountain system is getting affected due to aerosols mainly of absorbing in nature (e.g. dust, smoke etc.). To understand the spatial distribution and temporal variations of the absorbing aerosols, mainly dust, across the globe and over the Himalayan region, climatological study is performed on the seasonal and monthly scales using 38 years of multi-sensors and re-

analysis data sets. Additionally, trend analysis are also performed on monthly scales to understand their influence.

3) ***Study on the distribution of clouds and precipitation over Northern India***:

Clouds and precipitation are closely associated to each other and a baseline understanding of such meteorological parameters is necessary at various scales including their regional climatology. In this research work, a detailed climatology and distribution of seven basic cloud types, alongwith the investigation on the liquid and solid precipitation patterns over the Northern States of India (NSI) are performed using the combined CloudSat and CALIPSO observations. To understand the rainfall pattern over this region, latest version of the Tropical Rainfall Measuring Mission (TRMM) data is also analyzed in this study.

4) ***Study on the meteorological parameters using remote sensing and in-situ measurements***:

Last few decades have witnessed several meteorological hazards and environmental degradations in the Himalayan region. Therefore, it is important to understand the long term variations in surface meteorological parameters, and their vertical characteristics over this mountainous region. In this context, preliminary investigations are performed using the available in-situ measurements (e.g. temperature, pressure, humidity, winds, and rainfall) from Nainital, and Delhi stations. For studying the surface meteorology, the data obtained from ground-based Automatic Weather Station (AWS) measurements at ARIES, Nainital is used. In addition, to study the long-term surface temperature change at local and regional scales, the evaluated re-analysis data is used, and for understanding the vertical distribution of meteorological parameters, radiosonde observations available for Nainital and Delhi stations are also utilized in this study. Other than meteorological studies, some preliminary results on pulse compression technique, data quality, and scientific validation of wind parameters (zonal wind, meridional wind, wind speed and direction) obtained from ARIES RaDAR system using the co-located in-situ observations are also discussed.

1.7. Research Hypotheses

To fulfil the research objectives, falsifiable hypotheses have been formulated.

The **objective 1** and **2** mainly focusses on aerosols, and their main hypotheses are:

i. Over different locations in the Himalayan region, there are systematic differences in the sizes and concentrations of aerosols.

ii. Large errors in satellite remote-sensing estimates on aerosols can be reduced through their assessments using in-situ and ground based observations.
iii. Making use of the co-ordinated ground based aerosol measurements with satellite overpasses can help in estimating the unknowns like LiDAR ratio, and boundary layer heights with high degree of accuracy.
iv. The transport of pollutants over the Himalayan region are from distinct locations and have different sources of production.
v. The intrusions of pollutants have adversely affected the Himalayan ecosystem.

For **objective 3** the main hypotheses are:

i. The satellite based RaDAR and LiDAR could be used to measure the vertical structure, spatial variability, distribution, and properties of different cloud types, their macro-physical properties, and climatology over any region.
ii. Clouds have close connection with the climate system (e.g. precipitation, surface meteorology etc.).
iii. Not all the cloud type triggers precipitation or extreme weather events.
iv. The characteristics of clouds and precipitation patterns over the region shows seasonal variability.
v. The clouds and precipitation patterns over northern India have changed due to anthropogenic activities.

For **objective 4** the main hypotheses are:

i. There is significant shifts in the meteorological parameters (temperature, humidity, winds etc.) at regional and local scales over the Himalayan region.
ii. Himalayan environment are getting warmer due to changes in the key atmospheric and meteorological parameters.
iii. Continuous monitoring of surface meteorology over the mountains and complex terrains in the Himalayan region is crucial for accurate modeling and forecasting.

1.8. Outline of the Thesis

The thesis is structured over six chapters, including a brief introduction about the Earth system and the changes in the atmospheric variables in **Chapter 1**. This chapter also gives an overview of Himalaya and its environment, and the relevance of atmospheric studies over this region using remote sensing and in-situ tools. At the end, this chapter provided the objectives, hypotheses, and the brief outline of other chapters. **Chapter 2** reviews the literature relevant to the thesis and provides the global and national scenario pertaining to the topics of research. The chapter builds fundamental understanding on the key atmospheric parameters – aerosols, clouds, and precipitation, and further elaborates the role of in-situ and remote sensing tools used in their measurements. The chapter also provided literature survey on the active remote sensing tools like LiDAR and RaDAR covered in the research. This chapter is followed by the details on the study areas in **Chapter 3**. Further, **Chapter 4** describes the data sets obtained from remote sensing and in-situ measurements, used in this thesis. The focus of the chapter then progresses onto the methodologies adopted in the evaluation of the satellite retrievals with the ground truths, and their utility. This include discussions on various methods and criterion defined for data selection, their processing and analysis. The results and discussions are covered in **Chapter 5**, which discusses on the assessment of aerosol retrievals, their utility, case studies on aerosol transport, climatology of absorbing aerosols, studies on the clouds and precipitation, and long term variations in the meteorological parameters, at the end. The summary and conclusions of the thesis alongwith the recommendations are covered in **Chapter 6**. Collectively, these chapters develop an analytical picture on the use of remote sensing techniques and in-situ measurements in atmospheric studies over the Himalayan region.

Chapter 2

REVIEW OF LITERATURE

CHAPTER 2
REVIEW OF LITERATURE

2.1. Global scenario of the research

The World Meteorological Organization (WMO) is the specialized agency of United Nations (UN) that came into force on 23 March 1950 (*https://public.wmo.int/en/about-us*). It is the central framework that coordinates the activities of 185 countries and 6 territories in the generation and exchange of information related to meteorology (weather and climate) and hydrology according to the international standards. In 1974, the sixth special session of UN General Assembly invited WMO to conduct a study on the global climate change (*Zillman*, 2009), and following this, a report was prepared by a panel of experts nominated by WMO. The report brought out the necessity of having a single physical framework within which all the mechanisms or processes affecting the climate can be studied. It emphasized on continuous monitoring of the natural and anthropogenic parameters (e.g. CO_2, trace gases, aerosols, clouds, surface albedo), meteorological parameters (e.g. surface temperature, precipitation, winds), and various interactive processes (e.g. interaction between radiation, clouds and aerosols). Further, the report stresses on the development of high-end coupled atmosphere-ocean-ice models, and other simpler numerical climate models for making reliable climate change assessments and forecasts (*Gibbs et al*., 1977). Inspired by this study, WMO decided to convene the World Climate Conference (WCC) to review the world's climate on a broader perspective (*White*, 1979). The first WCC was held during 12 - 23 February 1979 at Geneva in collaboration with the United Nations Educational, Scientific and Cultural Organization (UNESCO), the Food and Agriculture Organization (FAO), the World Health Organization (WHO), the United Nations Environment Programme (UNEP), the International Council for Science (ICSU), and other scientific partners (*White*, 1979). This conference led to the formation of World Climate Programme (WCP) with an objective of promoting the climate change studies and their

implications on society and the environment (*WMO*, 1979). After this conference, the tenth World Meteorological Congress meeting was held in May 1987 that discusses the need of creating a panel that can take-up the responsibility of conducting periodic assessment of human-induced climate changes, and their impacts on a comprehensive, objective, open and transparent basis, and suggests the option for their adaptation and mitigation (*WMO*, 1987). This led to the creation of joint WMO-UNEP IPCC panel in 1988. IPCC in its very first assessment report concluded that an improved and systematic observations on the climatic variables at global scale is very essential to evaluate the human induced climate change (*Houghton et al.*, 1990). The second WCC in 1990 led to the establishment of the Global Climate Observing System (GCOS) and the United Nations Framework Convention on Climate Change (UNFCCC). The objective of UNFCCC is to regulate the concentration of greenhouse gases in the atmosphere (*Freestone*, 2016). The GCOS was set up in 1992 with an objective to provide reliable and, comprehensive data and information on the total climate system to the IPCC and UNFCCC. It includes data/information on climate system from in-situ, airborne and satellite based measurements, for conducting national, international and global studies on climate change. Furthermore, to meet the important requirements of the IPCC and UNFCCC, the GCOS has defined a list of 54 Essential Climate Variables (ECVs) based on their relevance in characterizing the Earth's climate system. This also included the technical feasibility in deriving or obtaining them, and their costs effectiveness in generation and archieval. These ECVs are essentially classified into three broad categories, namely the Atmospheric, Oceanic, and Terrestrial, as shown in **Fig. 2.1**. The study on these ECVs is required for a wide range of applications, including monitoring, mitigating, adapting to the climate changes, as well as the empirical basis required to understand the past, current, and possible future climate variability (e.g. *Hollmann et al*., 2013; *Bojinski et al*., 2014; *Bodeker et al*., 2016; *Blunden and Arndt*, 2017). The study on ECVs have gained wide popularity in respect to the present climate change, and various renowned journals have called for special issues on ECVs, like Elsevier (Remote sensing of Environment) has published ~ 19 papers in the issue on 'Earth Observation of Essential Climate Variables' in 2017 (*Buchwitz et al*., 2017). Likewise, the MDPI's Remote sensing journal has published about 8 papers on ECVs in its special issue on 'Remote sensing in climate monitoring and analysis' during 2011 (*https://www.mdpi.com/ journal/remotesensing /special_issues/*).

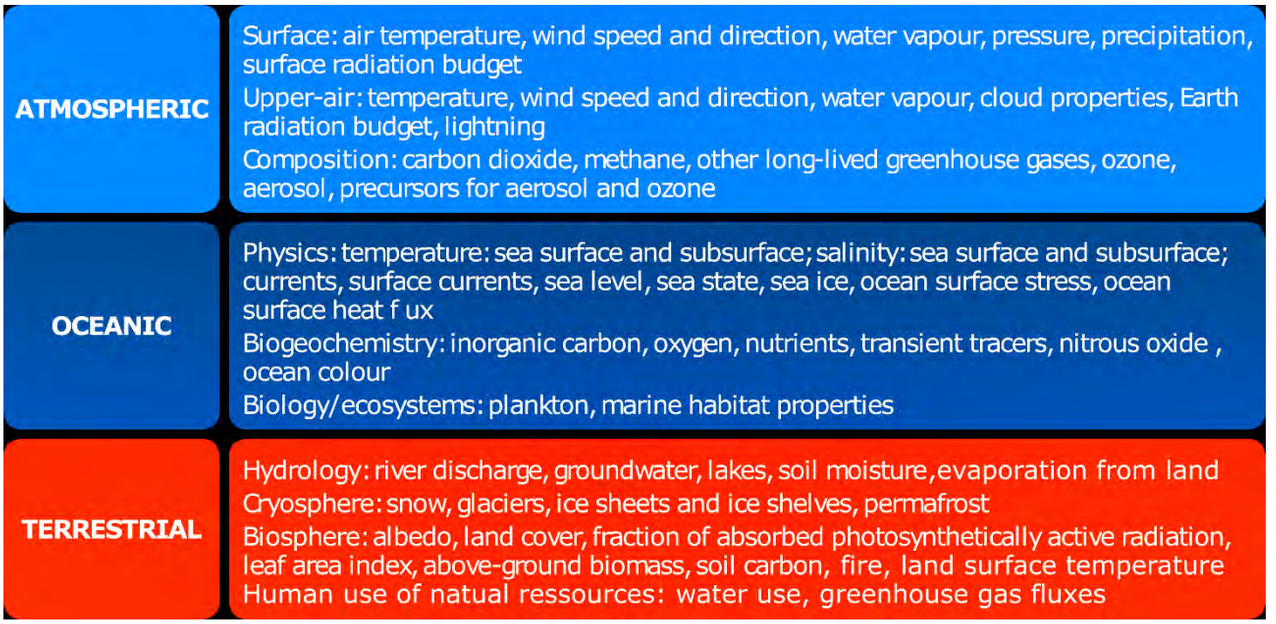

Fig. 2.1. List of 54 Essential Climate Variables defined by GCOS (source: *https://gcos.wmo.int*).

The scope of the present study is limited to the first category i.e. atmospheric variables, which is further classified into three sub-categories – Surface (that includes the measurements at standardized, but globally varying heights in close proximity to the surface), Upper-air, and the Composition. Globally, researchers have been working on many of the Atmospheric variables which are available for long term in order to study and understand the climate change and its impacts (e.g. *Bodeker et al*., 2016; *Blunden and Arndt*, 2017). These variables mainly include air temperature, winds, precipitation, clouds and aerosols, and their mutual interactions. However, among these variables, the role of ACP remains poorly understood individually, and yet represents an area of intense research, owing to their significance in Earth's radiation, surface energy balance, weather, hydrological cycle etc. (*Fan et al*., 2016; *Islam et al*., 2018). The advent of modern remote sensing and in-situ tools, have shown marked improvements in the measurement techniques and retrieval approaches of ACPs, and brought new opportunities and challenges in the exploration of different aspects of ACP research. Despite the progress made in understanding and quantifying the climatic effects of ACPs, many uncertainties still exists (*IPCC*, 2013, 2014). Part of these uncertainties arises because of incomplete knowledge on their spatio-temporal distributions, trends and their associated properties (*Mehta et al*., 2016; *Islam et al*., 2018). It is, therefore, important to improve the characterization of ACPs over different regions of the globe. Some relevant studies on

the global variations and trends on ACPs have been reported (e.g. *Stephens and Kummerow*, 2007; *Boucher et al*., 2013; *Mehta et al*., 2016; *Islam et al*., 2018).

The data on the number of ECVs in the domain of atmosphere are obtained by accumulating the regular measurements made in different temporal and spatial scales and hence introduces the inhomogeneity that limits their usefulness in studying the long-term variations in climate. To overcome this, atmospheric re-analysis products (e.g. ERA-Interim, MERRA, MERRA-2, NCEP/NCAR) have been established, that uses modern data-assimilation systems to reprocess the observations taken over the past several decades. Such re-analysis-based ECV data sets have now became an important source of information for conducting studies on climate variations (*Dee et al*., 2011, 2014) and for assessing the climate models (*Gleckler et al*., 2008; *Zhao et al*., 2013; *Bender et al*., 2018).

The change in global climate can be quantified by means of indicators defined by GCOS (**Fig. 2.2**), and among them, the most commonly used indicator is the global-mean surface air temperature taken over a long period of time because of its ability to represent the energy exchange process over the Earth's surface (*Vinnikov et al*., 1990; *Pant et al*., 2018).

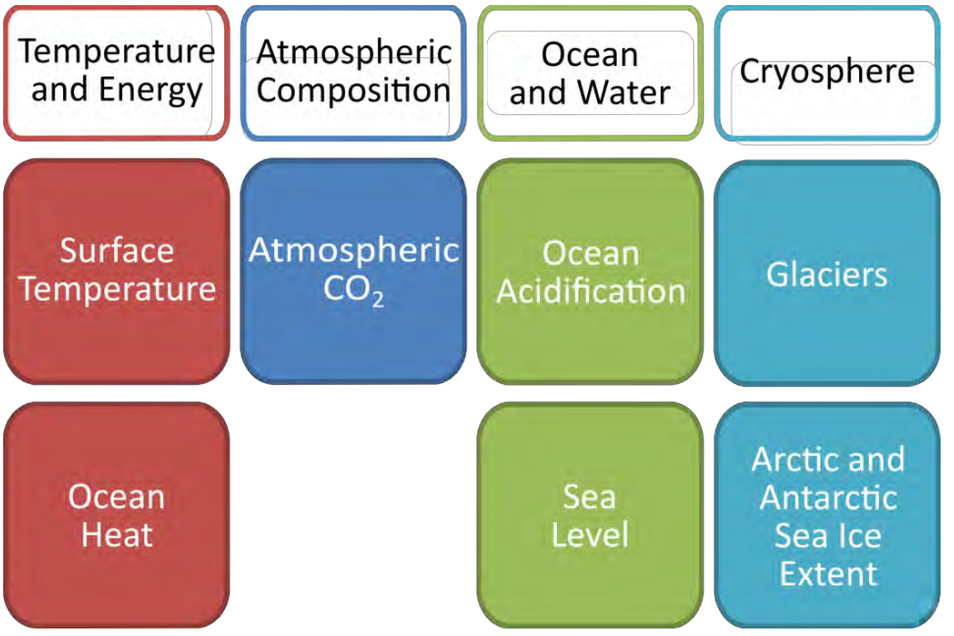

Fig. 2.2. Indicators of climate change, defined by GCOS (source: *https://gcos.wmo.int*).

The monthly global-mean surface air temperature anomalies plotted from January 1979 to January 2019, relative to the 1981-2010 period, using European Centre for Medium-Range Weather Forecasts (ECMWF) Re-Analysis (ERA)-Interim dataset is shown in **Fig. 2.3**. The figure clearly shows the consistent rising trends, possibly due to the current tendency of natural and human-influenced global activities. Recent comparison using re-analysis and several other data sets, has confirmed ERA-Interim as one of the preferable choice for studying the changes in global-mean surface temperature (*Dee et al*., 2011; *Simmons et al*., 2017).

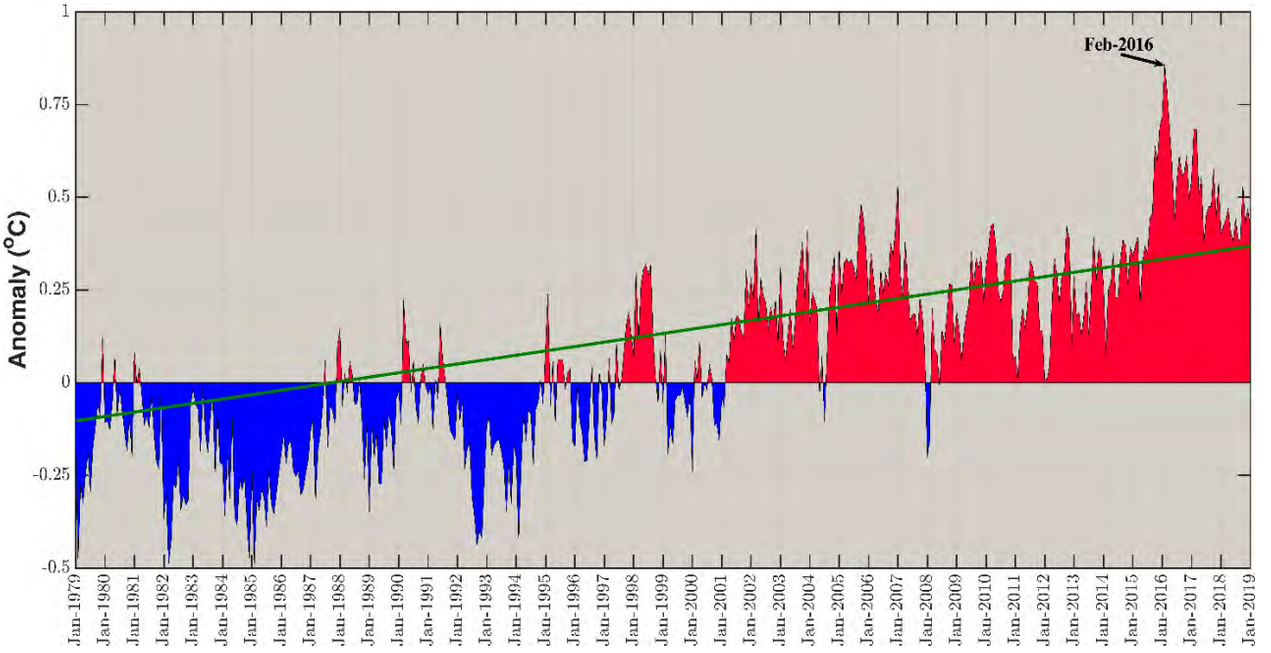

Fig. 2.3. Monthly global-mean surface air temperature anomalies relative to 1981-2010, from January 1979 to January 2019 using ERA-Interim product (*credit*: ECMWF, Copernicus Climate Change Service).

According to IPCC's assessment (*IPCC,* 2013), changes in the precipitation pattern is expected globally in the next few decades due to the sustained increase in global temperature and anthropogenic interventions. The global annual mean precipitation rate, according to the fifth IPCC report is 2.7 mm/day, with 3 mm/day over ocean and 2.1 mm/day over the land (*Boucher et al.*, 2013). The global scenario on mean precipitation trends from 1901 to 2005 for the individual regions have been compiled in the fourth IPCC assessment report (*Trenberth et al.,* 2007), as shown in **Fig. 2.4**. In this assessment, it is observed that the changes in precipitation extremes are much

less coherent than surface temperature, however, the decadal trend in total annual precipitation from very wet days (95th percentile) is on the higher side in the recent decades than earlier decades. Furthermore, the positive changes in intense precipitation is observed for more than one half of the global land area, in addition to the changes in the mean precipitation of many extratropical regions including United States (*Groisman et al*., 2005).

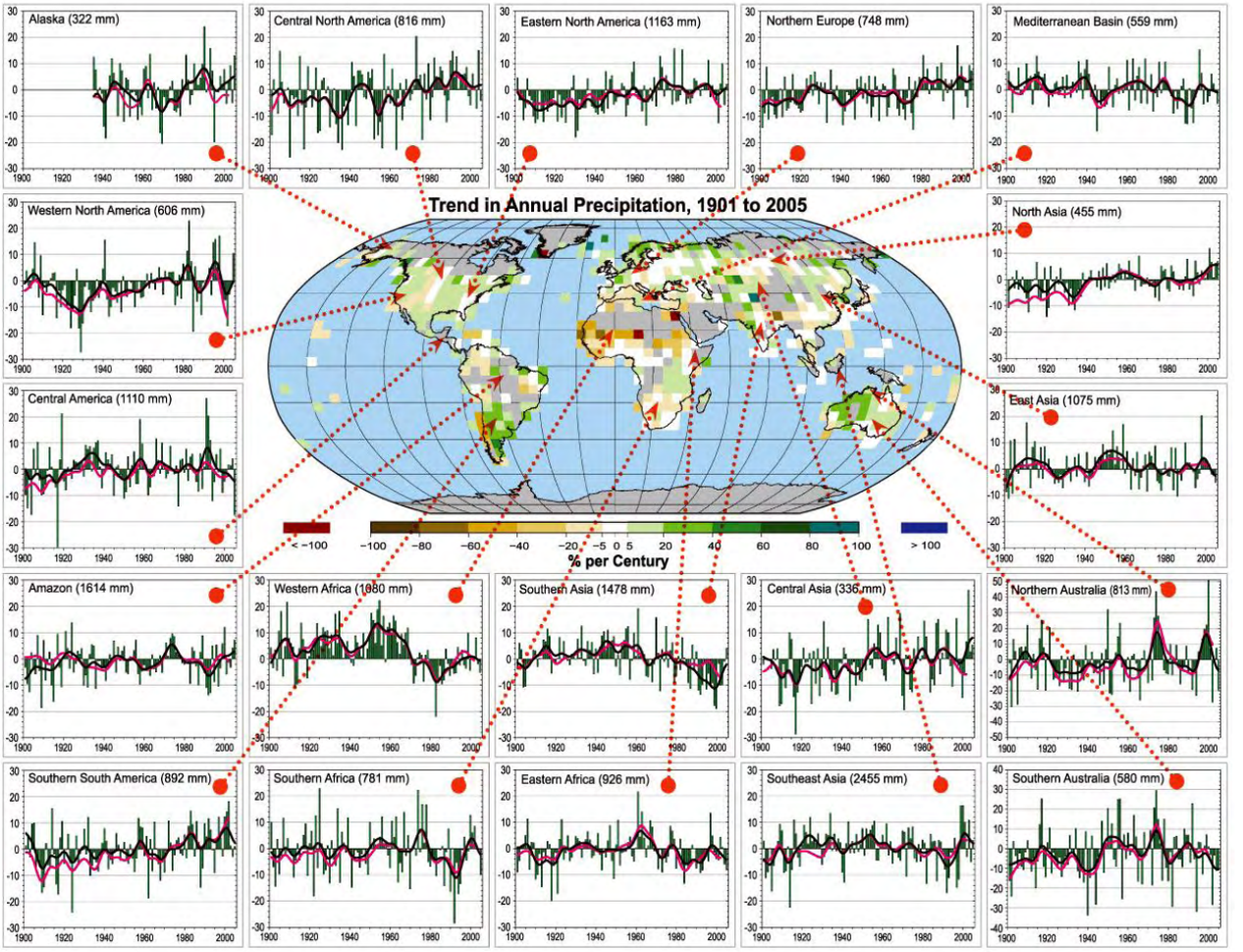

Fig. 2.4. Global scenario on mean precipitation trends from 1901 to 2005 for 19 regions whose names are mentioned at top of the surrounding plots. The central map shows the trends in % per century, while the surrounding 19 plots shows the time series of annual precipitation (in % of mean, with mean over the period 1961-1990 is given at top). The green bar in the surrounding plots are produced from Global Historical Climatology Network (GHCN) precipitation data, the black curves are for the decadal variations of it, and for comparison, the Climatic Research Unit (CRU) decadal variations are shown by magenta curves (*Trenberth et al.*, 2007).

2.2. National scenario of the research

India is geographically located north of the equator between 8°4' N - 37°6' N and 68°7' E – 97°25' E. It is the seventh largest country of the world with total area of ~3,287,590 km^2, extending from snow-capped mountain ranges of Himalaya in the north, to the coasts along the Indian Ocean in the south, and from the arid salt-pans of the west to the tropical rainforests in east. It has the land frontier of ~ 15,200 km and coastline of ~ 7,500 km (*Census*, 2011), and the country is bordered by densely populated and industrialized areas on the east and west sides, from where different pollutants are produced and transported. India experiences a large variability in its climate, ranging from continental to coastal, from hot to cold extremes, from extreme aridity and negligible rainfall, to excessive humidity and heavy rainfall. The country's climate is strongly influenced by the Himalayas and the Thar desert. The urban population in India is ~ 31.14 % of the total population, and the rate of urbanization have intensified in post-1970 period with increase in the number of million-plus population sized cities from 9 in 1971 to 53 in 2011 (*Census*, 2011; *Sudhira and Gururaja*, 2012).

With diverse and contrasting geographical features, dense population, rapid economic development, urbanization and industrialization, coupled with contrasting synoptic meteorological conditions associated with the Indian Summer Monsoon (ISM), India is quite susceptible to the adverse impacts of climate change. Therefore, it is important to monitor the spatio-temporal variability and to observe the long-term trends in ECVs, especially the atmospheric variables like temperature, winds, precipitation, aerosols and clouds over India, as they have close associations with the climate change (e.g. *Rajeevan et al*., 2013; *Ramachandran and Kedia*, 2013a). Additionally, the long-term changes in aerosols and clouds are gaining increased interest recently over Indian subcontinent due to their importance in global climate change (e.g. *Dey and Girolamo*, 2011; *Ramachandran et al*., 2012; *Sreekanth*, 2016; *Satheesh et al*., 2017).

The trend and magnitude of warming over India in the past century is broadly consistent with the global trend and magnitude (e.g. *Arora et al*., 2005; *Dash et al*., 2007; *Kothawale et al*., 2010; *Ross et al*., 2018). In conformity with the rising trend observed in the global surface temperature (0.85±0.18°C) since 1901 (*IPCC*, 2014), the annual mean surface temperature for the period 1901-2017 over India (**Fig. 2.5**) has also shown a significant increasing trend of +0.66 °C/100 years (*IMD*, 2018; *MoEFCC*, 2018). This analysis from IMD observational network, also provided the lists of nine warmest years of India, in the order as: 2016 (anomaly +0.87°C), 2009 (+0.85°C), 2010

(+0.82°C), 2015 (+0.59°C), 2006 (+0.56°C), 2002 (+0.45°C), 2007 (+0.417°C), 2014 (+0.415°C) and 1998 (+0.41°C).

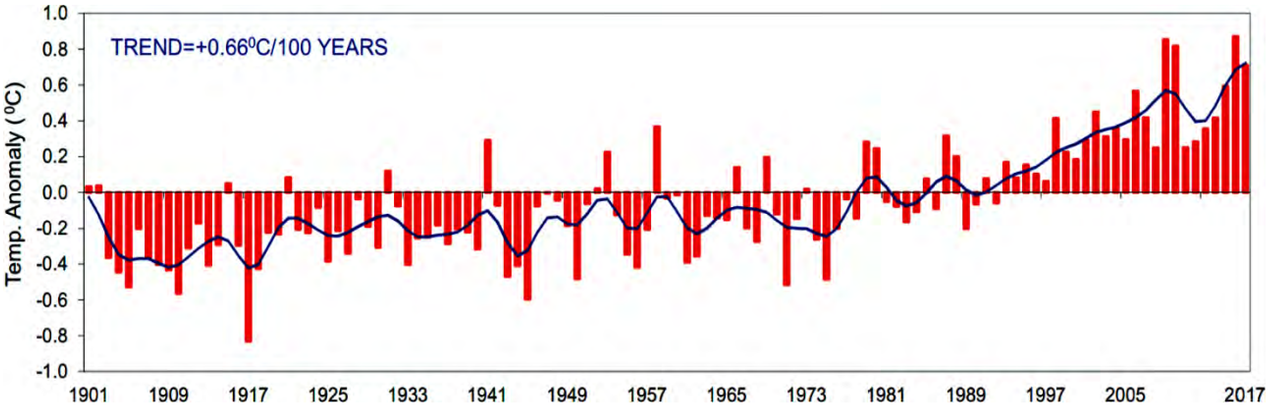

Fig. 2.5. Annual mean surface temperature anomalies for the period 1901 to 2017, relative to 1971-2000 average. The solid blue curve has sub-decadal time scale variations smoothed with a binomial filter (source: *IMD*, 2018).

Several studies observed that there is no significant trend in average rainfall over the country as a whole (e.g. *Guhathakurta and Rajeevan*, 2007; *Basistha et al.*, 2007; *Kumar et al.*, 2010), however, last few decades have witnessed significant decreasing/increasing trends in rainfall at some locations, increase in the extreme rainfall events, decrease in the number of rainy days in some regions, and so on (e.g. *Goswami et al*., 2006; *Mall et al*., 2006; *Dash et al.*, 2007; *Kumar et al*., 2010; *Kharol et al*., 2013; *Duhan and Pandey*, 2013; *Bharti et al*., 2016). Any change in the rainfall pattern influences the spatial and temporal distribution of runoff, soil moisture and groundwater reserves, which would affect the frequency of droughts and floods. The Indian climate is dominated by the ISM (June-September), which accounts for ~ 80 % of the total rainfall in the country. The rainfall during ISM season is important for the Indian economy and in the studies of global circulations. The rainfall during July is highest and contributes ~25 % of the annual rainfall, and in August the rainfall is slightly lower than that of July and contributes ~22 % of the annual rainfall. The rainfall in other two months i.e. June and September are almost the same, with their individual contributions as ~ 15 % of the annual rainfall. A recent study on inter-annual variations in the rainfall (percent departure) over India (based on 306 rain gauges) during ISM season (**Fig. 2.6**) revealed that over the period 1871-2016, there were 20 major flood years (green bars), 27

major drought years (red bars), and 99 normal years (blue bars) in India (*Kothawale and Rajeevan*, 2017). The linear trend in rainfall during ISM season, for the entire period (1871-2016) is found negative i.e. -0.18 mm per year, and hence indicating reduction in the rainfall during this season (*Kothawale and Rajeevan*, 2017).

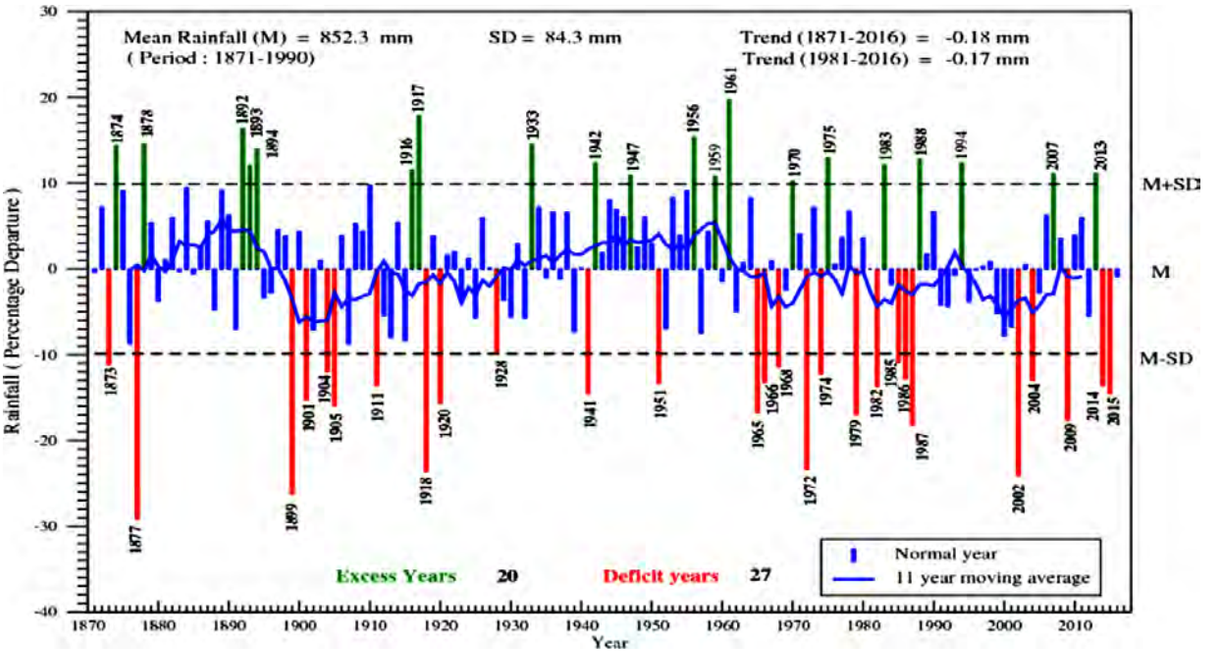

Fig. 2.6. All-India area-weighted mean rainfall anomalies (percent departures from its long-term mean) in the Indian Summer Monsoon (June-September) during 1871-2016. (source: *Kothawale and Rajeevan*, 2017).

2.3. Major Atmospheric variables

2.3.1. Aerosols

Aerosols are the suspended solid or liquid particles of varying sizes, mass, physical and chemical properties, ubiquitously present in the Earth's atmosphere. They are anthropogenic or natural, and gets emitted either at the source as particles (primary production) or as vapours, which later condenses on the existing particles or nucleates to form new particles (secondary production). The size of the aerosol particles varies from few nanometers to around hundreds of micrometers, and an example illustrating their typical size distributions is shown in **Fig. 2.7**.

The size distribution of aerosols usually exhibit one or several modes and submodes (**Fig. 2.7**) according to their formation process, and source/sink mechanisms. In number distribution of

aerosols, there are two modes – Nucleation mode and Aitken mode, while in volume distribution, in addition to these modes (Accumulation mode and Coarse mode), there are two submodes – Condensation and Droplet submodes. The Accumulation mode in volume distribution is also referred as the Fine mode, and depending on the particle diameter it is also characterized as the Ultrafine mode. Further details on the modes and submodes in the aerosols particle size distribution, including the major source of their production are provided in **Table 2.1**.

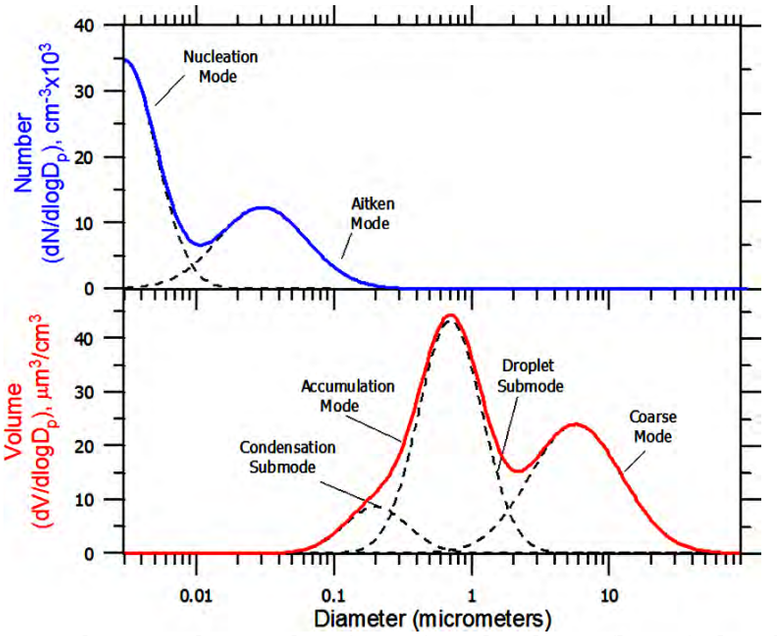

Fig. 2.7. Typical curves showing the number (upper) and volume (lower) distribution of aerosols. (Modified from *Seinfeld and Pandis*, 2012).

Table 2.1: Details of modes and submodes in aerosols number and volume distribution.

	Aerosols number distribution		**Aerosols volume or mass distribution**		
	Modes		*Modes*		
	Nucleation	**Aitken**	**Ultrafine**	**Accumulation/Fine**	**Coarse**
diameter	< 10 nm	10 – 100 nm	< 100 nm	100 nm – 2.5 μm	2.5 μm – 50 μm
life-span	transient or few minutes	minutes to hours	days to week		minutes to days
formation	nucleation (gas-to-particle conversion) of volatile gases	condensation of gases and water vapour	combustion (wood, oil, coal, gasoline and other fuels); coagulation (collision or sticking of two or more particles together) of tiny particles; condensation of sulphates, nitrates and other organics; smelters; mainly man-made		mechanical disruption such as bursting of bubbles in the ocean (sea salt), wind or erosion picking up dust, pollens, soil etc.; mainly natural
			overlapping *Submodes* of Accumulation mode		
			Condensation		**Droplet**
			coagulation and vapour condensation		created during cloud processing of some particles

The concentration of aerosols varies with location and altitude, e.g. over oceans it is about 100 ~ 300 per cm^3, and over rural areas it is about 1000 ~ 10000 per cm^3 (*Seinfeld and Pandis*, 2012). Many aerosols such as Particulate Matter (PM) with diameter < 2.5 μm i.e. PM-2.5 or with diameter < 10 μm i.e. PM-10 poses detrimental effect on human health (*Lippmann et al.*, 2000*; OECD*, 2014). Moreover, the aerosols have direct and indirect effects on climate (**Fig. 2.8**), that varies significantly between different regions of the globe (*Haywood and Boucher*, 2000*; Lohmann and Feichter*, 2005*; Boucher et al.*, 2013; *Boucher*, 2015*; Banerjee et al.*, 2018). Most of the aerosols scatter light and, hence, cools the environment, while, the absorbing class of aerosols like smoke, dust and volcanic ash, modifies the rate of atmospheric heating and modulates the properties and lifetime of neighbouring clouds and precipitation (*Hansen et al.*, 1997*; Ming et al.*, 2010*; Lau et al.*, 2010*; Wang*, 2013*; Lee and Wang*, 2015).

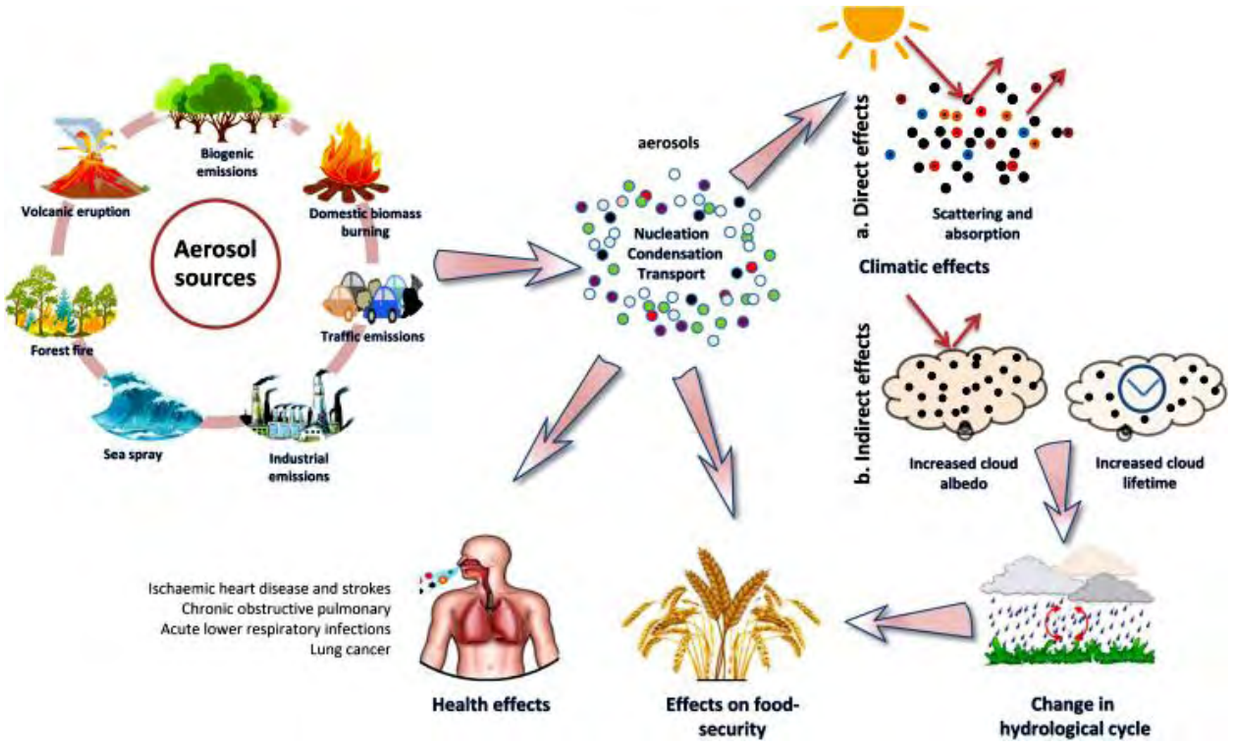

Fig. 2.8. Sources of aerosols and their impacts (*Banerjee et al.*, 2018)

Earth's atmosphere are directly affected from the emission of natural and anthropogenic aerosol sources by absorbing/scattering the incoming solar radiations (shortwave), and by absorbing/re-radiating the outgoing radiations (longwave) emitted from the Earth. These

perturbation in the solar radiation due to aerosols both of natural and anthropogenic origin, the physical drivers of climate change, influences the Earth's energy budget, and the level of this energy perturbation is quantified through aerosol radiative forcing, whose value greater than zero leads to warming, and lesser than zero signifies the cooling in the atmosphere. The estimation of aerosol radiative forcing is done on the basis of in-situ and remote sensing observations, or from the model calculations (*Kaufman et al.,* 2002*; Yu et al.,* 2006*; Schulz et al.,* 2006*; Hoff and Christopher,* 2009*; IPCC,* 2014).

IPCC in its fifth assessment (*IPCC,* 2013) reported that over 1750-2011, the direct radiative forcing from the anthropogenic sources (mineral dust, sulphate, nitrate, organic carbon, and black carbon) is −0.27 Wm^{-2} (−0.77 to +0.23 Wm^{-2}), and hence contributing to net cooling of the atmosphere. However, the aerosol radiative forcing is highly complex and has largest uncertainty with respect to the future climate change. This is because apart from some aerosols that contributes in cooling the atmosphere, there are several types of aerosol such as black carbon and mineral dust, which partially absorbs the incident sunlight and terrestrial radiations, thereby leads to warming of the atmosphere. In fact, in future, it is anticipated that the warming effect from black carbon may balance the cooling effect of other anthropogenic aerosol constituents, and especially the sulphate component, which is one of the major contributor to aerosol cooling (*Jacobson,* 2001*; Bond et al.,* 2013).

The aerosols affect the climate indirectly by acting as Cloud Condensation Nuclei (CCN) and ice nuclei, and can change the cloud microphysical properties and precipitation efficiency (*Albrecht,* 1989), and over the period 1750-2011, its contribution to the radiative forcing, as reported by IPCC in its fifth assessment (*IPCC,* 2013) is −0.55 Wm^{-2} (−1.33 to −0.06 Wm^{-2}). In contrast to the cooling effects, the total anthropogenic contributions in the year 2011 relative to the year 1750 shows the warming, with radiative forcing of +2.29 Wm^{-2} (+1.13 to +3.33 Wm^{-2}).

2.3.2. Clouds

Clouds are generally formed when the RH of air masses exceed the saturation threshold. They are basically the complex three-dimensional mass of condensed water vapour, ice particles or both, which are suspended in the atmosphere, and distributed over a wide range of spatio-temporal scales. Their properties change widely with time, location, changing weather or climate, and season. At any given time, on an average, they occupies more than 60 % of the Earth’s atmosphere, with ~ 10 %

more clouds over oceans than over land, and are closely linked to the Earth's radiation budget, atmospheric convection, precipitation etc. (*Quante,* 2004*; Stephens,* 2005).

Clouds are classified as low, middle or high levels on the basis of their height from the surface of Earth, and their visual appearances like colour, density, shapes, and the extent of their covers (*WMO,* 1956). Generally, the clouds lying within ~2 or 3 km vertical are classified as low level clouds (stratocumulus, stratus, and cumulus), between 2-7 km as middle level (altocumulus, altostratus, and nimbostratus), and above 7 km as high level clouds (cirrus that also include cirrocumulus and cirrostratus). Cumulonimbus clouds (or deep convective) extend through all the three levels. **Fig. 2.9** shows the different cloud types, corresponding to each levels.

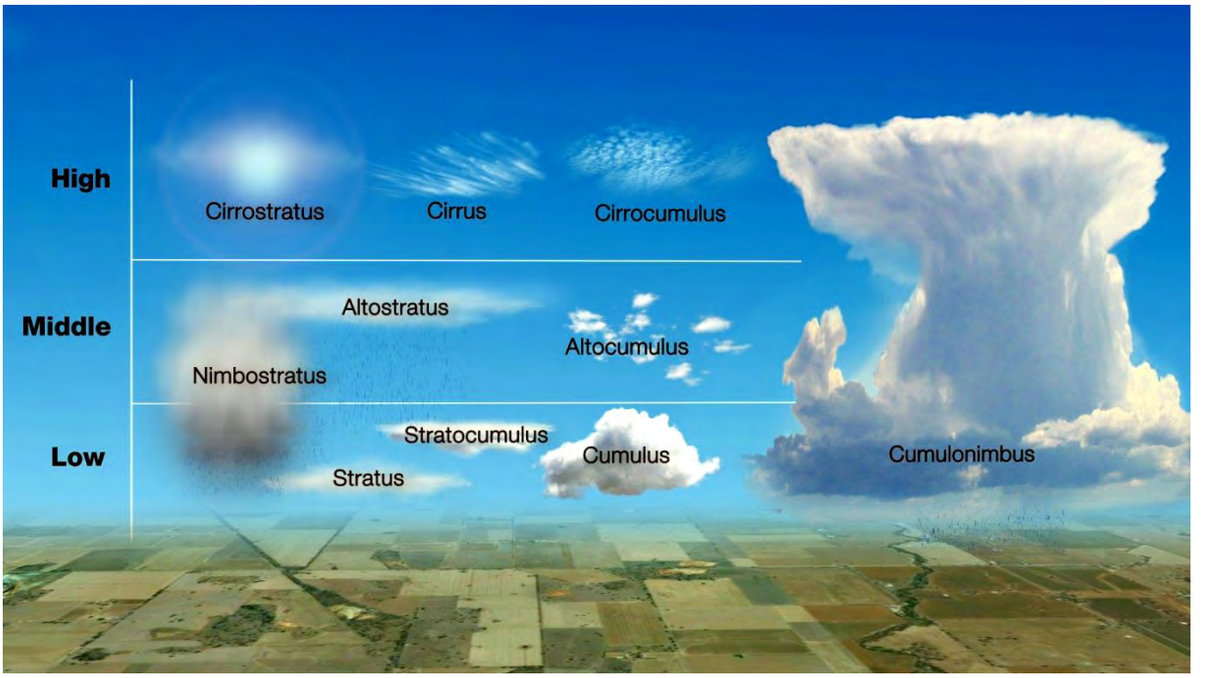

Fig. 2.9. Low, middle and high level cloud types (source: *Bureau of Meteorology, Australia*)

Clouds of sufficient thickness acts as effective reflector of the solar radiation. The effect of clouds on the Earth's radiation balance is measured in terms of Cloud-Radiative Effect (CRE), which is computed as the difference between the radiations under the all-sky and clear-sky conditions (*Ramanathan et al.*, 1989*; Quante,* 2004). The net global mean CRE of approximately –20 Wm^{-2}, implies a net cooling effect (*Boucher et al.*, 2013). There are two important radiative effects of the cloud:

(a) Cooling of the Earth through cloud albedo (ratio of reflected-to-incoming solar energy) forcing, that occurs due to reflection of incoming solar radiation (shortwave) from clouds back to space. Generally, low level clouds reflect more shortwave radiations back to space than mid or high level clouds. The global and annual mean shortwave CRE over the period 2001-2011 is reported in the fifth IPCC report as –47.3 Wm^{-2} (*Boucher et al.,* 2013).

(b) Warming of the Earth through clouds greenhouse forcing, that is caused when the longwave radiations emitted by the Earth are absorbed and re-emitted by some of the clouds like cirrus. The global and annual mean (2001- 2011) longwave CRE contribution is reported as +26.2 Wm^{-2} (*Boucher et al.,* 2013).

2.3.3. Precipitation

Precipitation is the frozen (snow) or liquid (rain) water falling from clouds (*Trenberth et al.,* 2007). It is one of the multifaceted climate variable that controls the landscape morphology and Earth's surface processes (*Bonnet and Crave,* 2003). The formation of precipitation primarily depends upon the distribution of clouds and moisture in the vertical column of the atmosphere (*Trenberth et al.,* 2007). Within the water cycle, water vapour condenses into clouds from which precipitation may fall, returning water from the atmosphere to the surface, and provides a primary source of fresh water vital to life on the Earth (*Kidd and Huffman,* 2011). The underlying processes play an important role in manipulating the atmospheric heating profiles and in maintaining the monsoon circulation (*Levermann et al*., 2009; *Wu et al*., 2012). The spatio-temporal distribution of precipitation is highly variable and intermittent, mainly at regional or local scales, than other climate variables such as temperature and pressure. Precipitation plays a crucial role in the vegetation growth, hydrology and surface mass transport on Earth, hence, its measurement and analysis are immensely needed (*Istanbulluoglu and Bras,* 2006; *Dubois et al*., 2014). The quantification of precipitation is also essential for the production of climate scenarios for climate change analysis and impact studies (e.g. *Hulme et al*., 1999; *Duan et al.,* 2006; *Kidd and Huffman,* 2011; *Guzman et al*., 2018; *Giorgi et al*., 2019), developing a good prediction and warning system, for evaluating various climate models like General Circulation Model/Global Climate Model (GCM), Community Earth System Model (CESM), and hydrological or biogeochemical system models (*Michaelides et al*., 2009; *Kucharik et al.,* 2000; *Hong and Adler,* 2007; *Tapiador et al*., 2017).

Precipitation varies across a wide range of space–time scales. At all the scales, precipitation is inherently the most important ECV than other commonly reported climate variables, such as temperature and pressure, and its measurement and analysis are more demanding than other ECVs (*New et al*., 2001). It is difficult to confirm the direct role of humans in triggering the precipitation related disasters, such as drought, floods, or extreme precipitation events, however, it contributes both in the dynamic and thermodynamic processes associated with global warming (*Easterling et al*., 2000; *Emori and Brown*, 2005; *IPCC*, 2013, 2014). A warmer atmosphere, in general, is more conducive to precipitation because it can hold more water. Regional and global studies have shown that there are more land regions where the mean and extreme precipitation events and the frequency of prolonged dry periods have increased (e.g. *Groisman et al.,* 2005*; Goswami et al*., 2006; *IPCC*, 2013, 2014). Consequently, precipitation measurements with good spatial and high temporal resolution, recorded over a long time span are essential in better understanding its impact, and predicting changes over the land masses. The increased occurrence of extreme precipitation events, and the increased frequency of prolonged dry periods, may have serious consequences for human life, property, agriculture, water resources, and ecosystems (*Easterling et al*., 2000; *IPCC*, 2013, 2014). A consequence of extreme precipitation is increasing faster than mean precipitation in response to the atmospheric warming (e.g., *Allen and Ingram*, 2002; *Lintner et al*., 2012). This may be attributed to the greater thermodynamic effect on the extremes due to increase in atmospheric water vapor and thus thunderstorm activity, particularly over the subtropics. Another process is dynamically related, that involves the changes in circulation pattern of precipitation intensity in middle and high latitudes (*IPCC*, 2013, 2014). It is also crucial to have a quantitative classification of the extreme precipitation events so that the policy makers and stakeholders can facilitate better mitigation measures.

2.4. Remote sensing and in-situ tools for atmospheric measurement

The tools used in monitoring the atmosphere are divided into two main categories – (a) in-situ, and (b) remote sensing. In-situ tools measure the atmosphere at a localized point and requires the instrumentation to be located at the same point and in contact with the atmospheric column to be measured. They are often fixed or mounted on a mobile platform such as a balloon or an aircraft. Remote sensing tools, on the other hand monitors the atmosphere at a location or at some distance away from the subject of interest. Remote sensors are either passive or active systems. Passive

sensors receive information that are naturally emitted from a region in the atmosphere, whereas active instruments generally emit an electromagnetic signal and record the characteristics of this signal after it interacts with an object or surface and returns back to the sensor. Remote sensing techniques used in atmospheric monitoring generally employ optical or microwave radiation, and acoustic sounders to probe the atmosphere (*Hewitt and Jackson*, 2008).

The satellite and ground based remote sensing, together with the in-situ measuring tools are primarily engaged for baseline monitoring and management of the Earth's atmosphere and planetary resource-bases at scales from local to global. The in-situ techniques involve the apparatus and region of interest being co-located, while the remote sensing basically involves conveying information about an object by observing the interaction between radiation and the object of interest. In-situ measuring devices are the most common method for observing the atmosphere. Kites, balloons, rockets, aircrafts etc. have been used to perform in-situ measurements of the atmosphere. Kites were first used by Alexander Wilson in 1749 to study the variation of temperature with altitude (*Shaw*, 1926). Manned balloons were first introduced in 1783, and in 1927, the use of radiosonde started for vertical profiling of atmosphere (*Rolt*, 1966; *Wallace and Hobbs*, 2006). The use of rockets and commercial aircraft for atmospheric purposes was initiated in the late 1940's (*Dickinson*, 1975). These in-situ techniques have high accuracy in individual measurements but are restricted to measure the parameters at only one location at a given instance. On the other hand, remote sensing tools have advantage of being able to make multiple measurements from a range of heights simultaneously with high temporal and spatial resolution compared to the in-situ measurements (*Tsang et al*., 1985; *Janssen*, 1993). The remote sensing is a powerful technique that integrates a broad set of human knowledge and technologies to observe, acquire, process, interpret, and monitor the marine, terrestrial and atmospheric phenomenon by means of active or passive sensors that are not in contact with the object, area, or phenomenon under investigation (*Elachi*, 1987*; Sabins*, 2007*; Lillesand et al.*, 2008). The collected data from remote sensors are of great interest to the scientific community for studying the global and regional climate changes, assessment and monitoring of environmental impacts resulting due to urbanization, land cover change, deforestation, natural calamities etc., and various other devastating changes caused due to human interventions with the natural resources. The data acquired from the remote sensing tools are also used to initialize and validate various computational models (e.g.

global climate models, regional climate models, energy balance models etc.) developed for simulating and predicting changes in the Earth's environment.

The science of remote sensing has advanced enormously since the pigeon era, and today it become possible to monitor the state of Earth-atmosphere system with substantially high degree of spatio-temporal resolutions and geographic coverage. Its application in Earth observations and monitoring was first begun in 1960's when the Television Infrared Observation Satellite (TIROS) series of meteorological satellites were launched into the orbit, e.g. TIROS-1 launched in 1960 for weather analysis and forecasting (*Natl. Res. Counc.*, 2008). Since then, numerous passive and active satellites were introduced. The passive remote sensing satellite sensors are widely being used to retrieve the properties of ACPs on a scales from a local to global with good spatio-temporal resolutions (**Table 2.2**). The passive sensors alone can only provide access to integrated information in the atmospheric column, hence to perform a comprehensive study, the measurements of the vertical distribution of atmospheric particles is also very essential, which can be achieved through active remote sensing sensors, and the most notable active sensors are listed in **Table 2.2**.

Table 2.2: Satellite based passive and active remote sensing tools.

Passive sensors	Active sensors
AVHRR (*Stowe et al.*, 1992) TOMS (*Torres et al.*, 2002a) GOME (*Carboni*, 2006) SeaWiFS (*Wang et al.*, 2000) POLDER (*Deschamps et al.*, 1994) MODIS (*King et al.*, 2003) MISR (*Diner et al.*, 1998) MTI (*Chylek et al.*, 2003) ATSR (*Veefkind et al.*, 2000) OMI (*Torres et al.*, 2002b) SCIAMACHY (*Noël et al.*, 1999) SEVIRI (*Schmid*, 2000) TRMM Microwave Imager (*Huffman et al.*, 2007)	LITE (*Winker et al.*, 1996) GLAS (*Zwally et al.*, 2002) CALIPSO (*Winker et al.*, 2002) CloudSat (*Stephens et al.*, 2002) TRMM Precipitation RaDAR (*Huffman et al.*, 2007) CATS (*McGill et al.*, 2015)

2.4.1. Aerosols measurement

The properties of aerosols, mainly the AOD, Angstrom Exponent (AE), etc. which provides the information on aerosol load and size distribution, are directly measured by analysing the in-situ samples, or retrieved from remotely sensed data acquired at ground-based stations or by instruments

carried on the satellite platforms. Time to time, the physical, chemical, and optical properties of aerosols have been examined from different regions of globe by means of field campaigns (e.g. ACE-1 and 2, AEROSOLS99, SHADE, INDOEX, ICARB, SAFARI 2000), however, due to the rare occurrences of these campaigns, the aerosol measurements from them are relatively limited in space and time. Therefore, making use of in-situ and remote sensing tools, the aerosol measurements were started through ground-based networks since the early seventies (*Bodhaine*, 1983). In 1998, National Aeronautics and Space Administration (NASA) established a global network of ground-based automatic sun photometers: the AERONET (*Holben et al.*, 1998) that performs passive measurements of column-mean aerosol microphysical and optical properties like AOD, AE, SSA, phase function, size distribution (fine and coarse), at more than 400 stations across the globe. The access to different levels and quality assured AERONET data sets for all the stations are made free (*https://aeronet.gsfc.nasa.gov/*), and the researchers are utilizing them for long term aerosol studies and product validations (*Holben et al.,* 2001; *Torres et al.,* 2002a*; Bréon et al.,* 2011*; Bibi et al.,* 2015*; Bilal et al.,* 2016).

Satellite based measurement of aerosols were started in 1972 through the Multi Spectral Scanner (MSS) sensor aboard Earth Resources Technology Satellite (ERTS) – 1 (*Griggs,* 1975). After the successful study of aerosol parameters over water surfaces by MSS, several instruments such as radiometers, spectrometers, polarimeters, LiDARs etc. were deployed in succession on polar orbiting sun-synchronous and geostationary satellites, for conducting aerosol studies from space at both global and regional scales. To facilitate the aerosol measurements through satellite remote sensing, NASA's Earth Observing System (EOS) have launched the constellation of polar orbiting satellites, equipped with passive and active sensors like MODIS on Terra and Aqua satellites, Multiangle Imaging Spectro-Radiometer (MISR) aboard Terra, Ozone Monitoring Instrument (OMI) on Aura, Polarization and Directionality of the Earth's Reflectances (POLDER) on Polarization and Anisotropy of Reflectances for Atmospheric Science coupled with Observations from a Lidar (PARASOL) platform, and Cloud-Aerosol Lidar with Orthogonal Polarization (CALIOP) on board the CALIPSO platform, that are widely being used for aerosol studies (*Kaufman et al.,* 2002*; Winker et al.,* 2002*; Chylek et al.,* 2003*; Natl. Res. Counc.,* 2008*; Hoff and Christopher,* 2009). The Cloud–Aerosol Transport System (CATS) satellites from the International Space Station (ISS) is another elastic backscatter LiDAR operating at 1064, 532 and 355 nm wavelength since February 2015, and is equipped with the High Spectral Resolution Lidar (HSRL)

at 532 nm that offers high resolution studies of aerosol distribution and transport, together with cloud motion (*McGill et al.,* 2015). With the launch of various space missions, an extensive studies on the aerosols are being done over a large scales, however, the ground based aerosol measuring instruments are still considered as most reliable source of measurements, and widely used for the evaluation and validation of the aerosol parameters retrieved using satellites.

2.4.2. Clouds measurement

The reliable estimate of clouds and their variations on spatio-temporal scale increases the level of understanding their roles in modulating the radiation budget (*Hartmann et al.,* 1992). Observing clouds with in-situ sensors (e.g., *Evans et al.,* 2006*; Brenguier et al.,* 2013), ground-based remote sensors (e.g., *Mahesh et al.,* 2001*; Wang et al.,* 2018) and satellite remote sensing systems (e.g. *Stephens et al.,* 2002*; Winker et al.,* 2002*; Stephens and Kummerow,* 2007*; Hartmann et al.,* 2013), all contribute to an understanding on the composition and distribution of clouds in the atmosphere. The most important cloud optical properties that can be estimated from these sensors are cloud optical thickness, cloud albedo, cloud top height, horizontal extent and variability, phase (liquid or ice), etc. Better use of the in-situ and remote sensing in understanding the cloudiness over any region relies on the analysis methodology, availability of data with higher spatio-temporal resolution, and the use of quality control information, and first guess.

The satellites are the observing platform that offers the characterization of clouds with much better spatial and temporal coverages compared to the ground-based or in-situ sensors (*Hartmann et al.,* 2013*).* Under many conditions, the satellite sensors proved to locate and quantify the clouds accurately (*Smith and Platt,* 1978*; Wielicki and Coakley,* 1981*; Wang and Sassen,* 2001*; Stephens and Kummerow,* 2007*; Qian et al.,* 2012*; Zhu et al.,* 2015*; Foga et al.,* 2017), and provided their macrophysical and microphysical properties (*Minnis et al.,* 1995*; King et al.,* 2003*; Wang and Sassen,* 2001*; Liu et al.,* 2013).

The first long term observations on clouds from satellite remote sensors is made in 1978 with the launch of the TIROS-N satellite (*Swanson et al.,* 1980). During the last few decades, the proliferation of satellite platforms carrying modern and advanced sensors are explored extensively to foster the wealth of cloud related information (e.g., *Rossow and Schiffer,* 1991*; Minnis et al.,* 1995*; Stephens et al.,* 2002*; Mace et al.,* 2009*; Okamoto and Sato,* 2018). Examples of some notable sensors providing the cloud information are - the Cloud Profiling Radar (CPR) aboard the

CloudSat satellite (*Stephens et al.,* 2002), the CALIOP on board the CALIPSO satellite (*Winker et al.,* 2009), the MODIS (*King et al.,* 2003) on the EOS, the MISR (*Diner et al.,* 1998) etc. The oldest records (since 1983) on the clouds and radiative flux is available with International Satellite Cloud Climatology Project (ISCCP) (*Schiffer and Rossow,* 1983) of World Climate Research Program (WCRP).

2.4.3. Precipitation measurements

The primary sources of obtaining the precipitation information are in-situ and remote sensing tools (*Prigent,* 2010*; Brenguier et al.,* 2013*; Hou et al.,* 2014). Measuring precipitation over the desired period of time using rain gauges, is the most common approach used by meteorologists and hydrologists on a local scale, however, the global distribution of these gauges are quite variable, sparse, and almost non-existent over the ocean (*Prigent,* 2010), and hence unsuitable for climate or hydrological models, which requires high resolution precipitation data as input. Remote sensing using ground based weather RaDAR is another approach for precipitation measurement from the land surfaces, that provides data with high spatial and temporal resolutions than rain gauges (*Csiszár et al.,* 1999), however, due to its high operational and maintenance costs, it is not feasible to build the networks of such RaDARs, and moreover, they still lacks in providing the measurement over oceans surfaces.

With the rapid advancements in space technology, there has been immense progress in carrying out the precipitation measurements using satellite remote sensing tools, which are primarily based on the interpretation of solar radiation that is scattered or emitted from hydrometeors, and underlying surface. Presently, the satellite based precipitation products such as TRMM, Global Precipitation Climatology Project (GPCP), Climate Prediction Centre (CPC) MORPHing Technique (CMORPH), Global Satellite Mapping of Precipitation (GSMaP), and Precipitation Estimation from Remotely Sensed Information using Artificial Neural Networks (PERSIANN), are available at high spatial (≤ 0.25°) and temporal (≤ 3 hours) resolutions over regional and global scales (*Huffman et al.,* 2007*; Hou et al.,* 2014*; Ashouri et al.,* 2015*; Sun et al.,* 2018). However, the estimation methods used in these products are relatively complex and most of them make use of the Visible (VIS) (0.4 - 0.7 µm), thermal Infra-red (IR) (10.6 – 12.6 µm), and Microwave (MW) (0.3 – 3 cm) bands of the electromagnetic spectrum. Precipitation can be estimated from Geostationary (GEO) satellites like Meteosat Second Generation (MSG) satellites,

two Geostationary Operational Environmental Satellite (GOES) and the Japanese Multifunctional Transport Satellites (MTSAT) series, which typically carries VIS and IR sensors. Low Earth Orbiting (LEO) satellites using the multi-channel VIS/IR, and MW (passive and active) sensors also provides the precipitation retrievals. The GEO satellites moves at speed of the Earth's rotation, and hence are capable of providing measurements at a fixed location on the Earth continuously, while the LEO satellites that are positioned in sun-synchronous orbits, revisits any spot on the Earth at regular intervals in a day. The low temporal resolution of LEO satellites can be compensated by integrating the data obtained from the GEO satellites to acquire precipitation data with high temporal and spatial resolution. The satellites that carries passive MW sensors are Defense Meteorological Satellite Program (DMSP) satellites series of Special Sensor Microwave/Imager (SSM/I) and Special Sensor Microwave Imager-Sounder (SSMIS), Aqua satellite includes the Advanced Microwave Scanning Radiometer-Earth (AMSR-E) observing system, National Oceanic and Atmospheric Administration (NOAA) satellite series of Advanced Microwave Sounding Unit-B (AMSU-B) system, and TRMM (*Stephens and Kummerow*, 2007; *Huffman et al.*, 2007*; Hou et al.*, 2014*; Sun et al.*, 2018). The use of active MW observations from satellites was started with the launch of the TRMM mission in 1997, which made it possible to capture the three-dimensional structure of precipitation (*Kummerow et al.*, 2000). This mission has provided wealth of precipitation data, and the researchers are using them extensively to understand the local and regional scales (e.g. *Schumacher and Houze*, 2003; *Hirose and Nakamura*, 2004; *Shrestha et al*., 2012; *Maranan et al*., 2018).

2.5. Remote sensing of the atmosphere using ground-based RaDAR and LiDAR

Remote sensing tools have advantage of being able to make multiple measurements from a range of heights simultaneously with high temporal and spatial resolution compared to the in-situ measurements (*Tsang et al.*, 1985*; Janssen*, 1993). They emerge as the best tool to study the dynamically changing environments due to their repetitive capability and synoptic coverage. The RaDAR and LiDAR are active remote sensing tools that relies on the propagation of radio waves and light waves, respectively. Over the last few decades, they have gained immense popularity in the atmospheric research, and are still serving as the backbone tools for true monitoring of vertical layers of atmospheric constituents with finer resolution (e.g. *Doviak and Zrnic*, 1984; *Melfi et al*., 1985; *Rao et al*., 1996; *He et al*., 2006; *Baars et al*., 2008; *Singh et al*., 2008; *Solanki and Singh*, 2014).

RaDAR is a state-of-art, active remote sensing aid for detecting the presence of target, determining their direction and range, and recognizing their character by means of radio waves (*Skolnik*, 2008). The RaDAR primarily used for the atmospheric probing and wind profiling are called atmospheric RaDAR, which generally operates in pulsed mode, typically in the Very High Frequency (VHF) and Ultra High Frequency (UHF) frequency bands (*Röttger and Larsen*, 1990*; Skolnik*, 2008). The turbulent fluctuations in the refractive index of atmosphere serves as targets for these RaDAR. The atmospheric RaDAR, profiling the vertical structure of the atmosphere, has a long history (*Doviak and Zrnic*, 1984*; Kumar et al.*, 2011), starting from early thirties (*Hardy and Gage*, 1990). The pioneering work of Woodman and Guillen demonstrated the potential of high power VHF RaDAR in exploring the structure and dynamics of the middle atmosphere with unprecedented height and time resolutions (*Woodman and Guillen*, 1974). The first largest atmospheric RaDAR system in the VHF band (at 49.9 MHz) was installed in Jicamarca, Peru in 1961 (*Steen*, 1992) which is still in operation for studying the equatorial ionosphere and the neutral atmosphere. It was the first major discovery in the atmospheric research after 1941, when the first meteorological RaDAR observations started (*Sauvageot*, 1992). Thereafter, number of different types of atmospheric RaDARs have been developed for middle and upper atmospheric research, and several research communities are utilizing their resources for understanding and monitoring the Earth's atmosphere (e.g. *Gage and Balsley*, 1978*; Balsley and Gage*, 1980*; Röttger and Larsen*, 1990).

The optical probing of atmosphere is primarily achieved using LiDAR, which probes the atmosphere by two means i.e. ground based as well as airborne or space-borne (*Welton et al.*, 2000*; Winker et al.*, 1996, 2002). The ground based LiDAR system plays a vital role in calibration and validation of space-borne missions such as CALIPSO (*Winker et al.*, 2002*; Solanki and Singh*, 2014), and sometimes used in synergy with them to study various characteristics of the atmosphere (*He et al.*, 2006). The atmospheric observations using ground based LiDAR was started in 1960's (*Fiocco and Smullin*, 1963), and during that time the LiDAR was popular as optical RaDAR or as Light Amplification by Stimulated Emission of Radiation (LASER) RaDAR (*Fiocco and Smullin*, 1963*; Standford*, 1967*; Kent and Wright*, 1970). In India, the first backscatter Neodymium-Doped Yttrium Aluminum Garnet (Nd:YAG) LASER RaDAR for middle atmospheric studies was started in April 1992, at Physical Research Laboratory (PRL), Ahmedabad (23° N, 72.5° E) (*Jayaraman et al.*, 1995). The global network of eye-safe ground based LiDARs, called Micropulse LiDAR

Network (MPLNET) collocated with unique AERONET stations, were started by NASA in 2000 for aerosol and cloud vertical profiling and related studies across the globe (*Welton et al.,* 2000). To provide the comprehensive climatological database for qualitative studies on spatio-temporal distribution of aerosols on a continental scale, the first ground based aerosol LiDAR network (comprising of more than 25 permanent stations) - European Aerosol Lidar Network (EARLINET) were also established in the year 2000 (*Bösenberg et al.,* 2001). With the advancements in technology, the ground based LiDAR systems are now became highly robust, and the use of small diode pumped Nd:YAG LASER, solid state photo-diodes, photon counting detectors, and cost-effective multi-channel scalar signal acquisition, have made the system much compact and portable than earlier days.

Chapter 3

STUDY AREA

CHAPTER 3
STUDY AREA

3.1. Observational site: ARIES, Nainital

Nainital (**Fig. 3.1a**) is a hill station, situated amidst the lavish green mountains of central Himalaya, in the state of Uttarakhand, India. The station occupies a unique place known for its salubrious climate, scenic natural splendour, and diversified floras and fauna. It belongs to the sub-tropical part of the globe and because of its altitudinal location, it exhibits the temperate climate, which is characterized by warm and short summer, moist and wet rainy, and pronounced and severe winter. This historical station is full of small lakes (popularly called "Tal") of which the Naini Lake, a pear shaped Tal surrounded by green mountain peaks from the three sides and a downhill slope on the south-east side, is the '*heart of the city*'. It is one of the oldest and largest lake (~ 0.7 km^2) amongst all the lakes in Nainital (**Fig. 3.1b**).

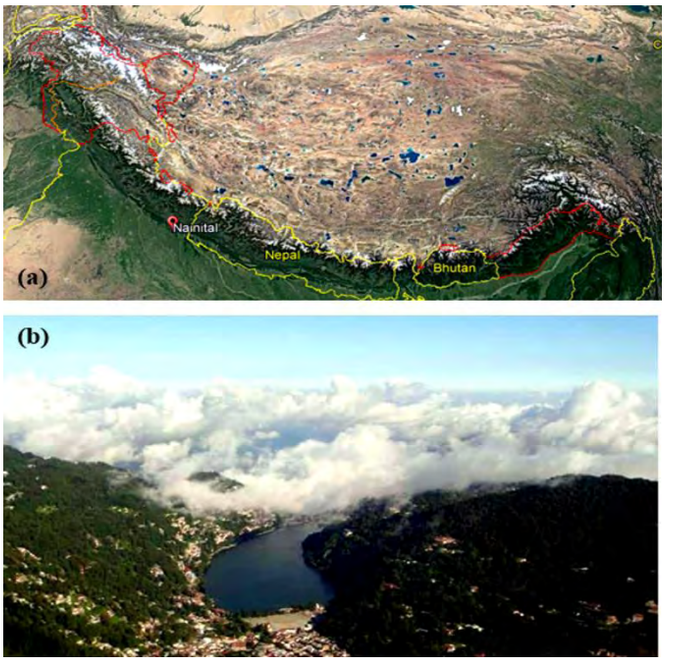

Fig. 3.1. (a) Location of Nainital on Google Earth, and **(b)** view of Naini Lake, Nainital.

ARIES (29.36° N, 79.46°E, ~1958 m above mean sea level (amsl)), a 50 years old observatory, is located amidst calm environs on the top of a majestic hill of Nainital called Manora peak, which is covered with trees (mostly Banjh oak and Chir pine trees) and shurbs on all sides (**Fig. 3.2a**). It is located at ~ 2 km (aerial) distance from the popular Naini Lake (**Fig. 3.2b**), and just ~100 km (aerial) away from the southern peaks of the central Himalayas, and witnessed as one of the best regional representative site for atmospheric studies by various researchers (*Sagar et al.,* 2004, 2015*; Hegde et al.,* 2009*; Solanki and Singh,* 2014*; Sarangi et al.,* 2014*; Ojha et al.,* 2014*; Solanki et al.,* 2016*; Kumar et al.,* 2018).

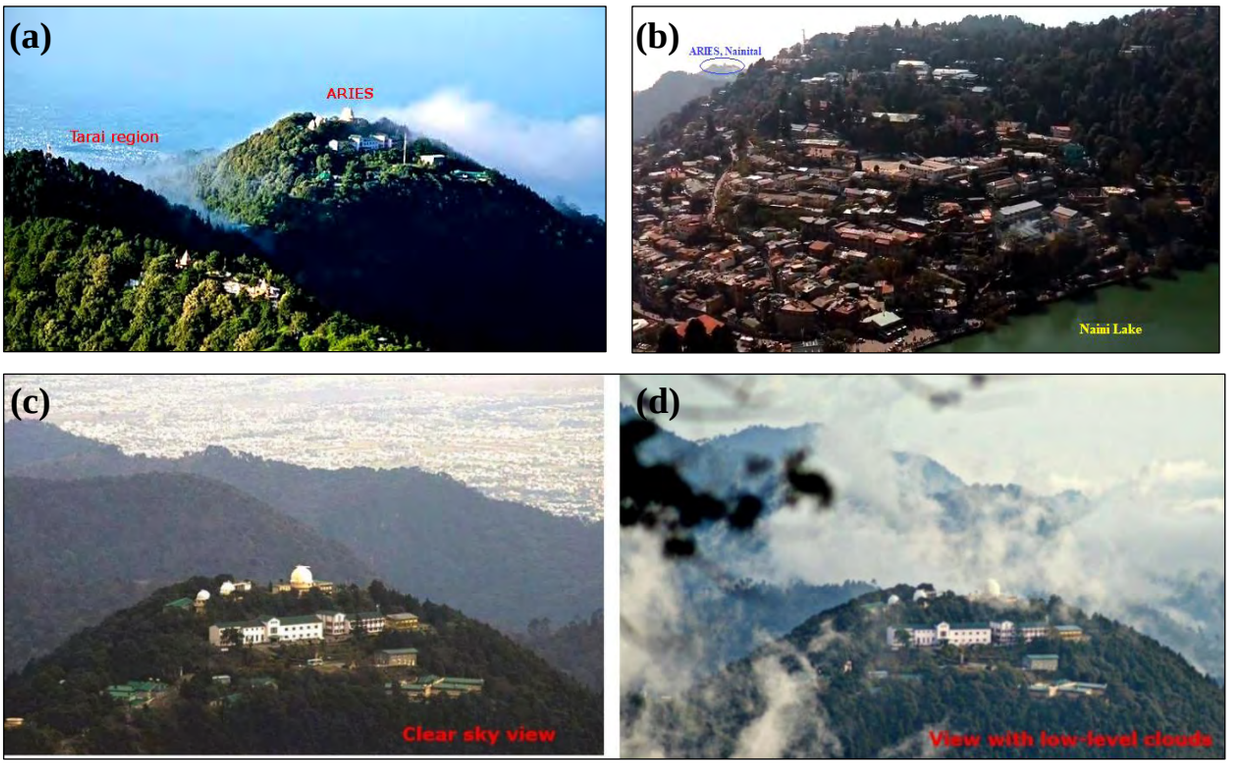

Fig. 3.2: A panoramic view of ARIES, Nainital showing **(a)** its location at Manora peak and nearby 'Tarai' regions, **(b)** its aerial separation from the Naini Lake, and its view under **(c)** no cloudy, and **(d)** cloudy conditions.

The study using ground and satellite based measurements over this high-altitude, remote, and sparsely inhabited site amidst undulating topography in the free tropospheric conditions is of great relevance (*Sagar et al.,* 2004, 2015). This pristine site is surrounded by sharply rippling mountain

ranges in north and north-east, and towards its south and south-west, there are low-elevated lands of Indo-Gangetic Plains (IGPs) (known as 'Tarai') as evident in **Fig. 3.2a** and **c**. The nearby hills and valleys surrounding the site are quite often shrouded with low level slow-moving clouds as seen in **Fig. 3.2d**. During past two decades, industrialization has grown up rapidly in these 'Tarai' portions (*Kazuo,* 2014) and the pollutants are being transported to the site quite often (*Ojha et al.*, 2012*; Sarangi et al.*, 2014). Therefore, the site has a great advantage to study the influence of continental as well as long range transport of the pollutants, and additionally it provides the background values of the aerosol parameters. Further details of the site, variations in meteorology and synoptic-wind patterns can be found elsewhere (*Ojha et al.*, 2014*; Singh et al.*, 2016).

3.2. Himalayan region (26.5-40.5°N, 62.5-105.5°E)

The aforementioned spectacular and dramatic region of Himalaya mainly consists of complex chain of high mountains, rivers, elevated plateaus, deep gorges and extended valleys, and the mean elevation of this region is ~1000 m (**Fig. 3.3**). The selected region traverses across number of Asian countries including Tajikistan in the west to Myanmar in the east with Afghanistan, Pakistan, India, Nepal, Bhutan, northern and southern portion of Bangladesh and China, respectively.

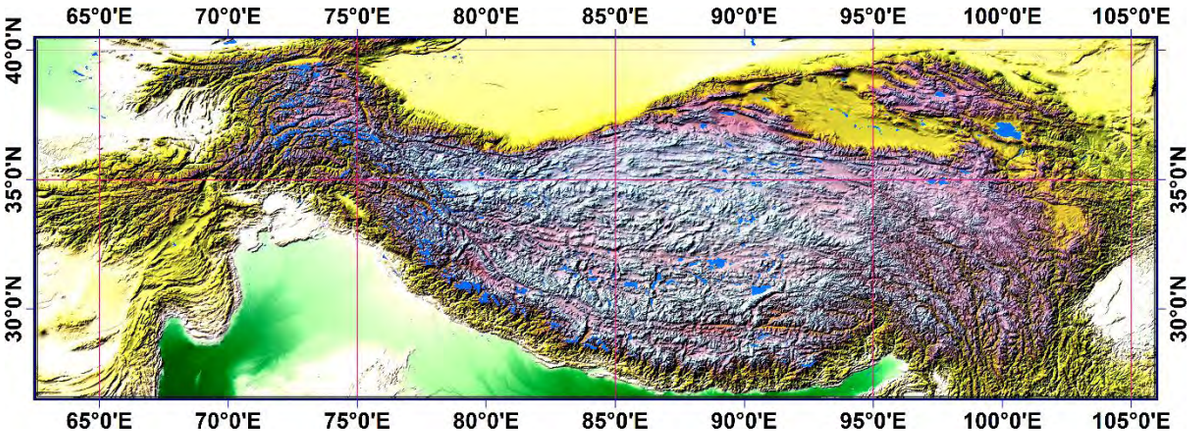

Fig. 3.3. Map showing the portion of Himalayan region lying in the geographical boundary 26.5-40.5°N, 62.5-105.5°E.

The abrupt rise of the Himalayan landmasses from less than few hundreds of meters to more than 8,000 m results in a diversity of ecosystems. Despite of the apparent remoteness and

inaccessibility, the population growth in this most productive ecosystems is rapid, and due to the increase in anthropogenic activities, the climate of the region is getting affected to a great extent. Several studies have found that the glaciers in this region have retreated considerably in the last few decades (*Bolch et al*., 2012; *King et al*., 2017), that leads to catastrophic outburst floods etc. (*Richardson and Reynolds*, 2000; *Immerzeel et al*., 2013; *Dimri et al*., 2017) due to the formation of several glacial lakes. Manifestations in climate change indicators, such as an increase in temperature and decrease in precipitation are also evident in this region (*Bhutiyani et al*., 2007, 2010; *UCOST and USERC,* 2012; *Mishra,* 2014*; Dimri et al*., 2018). One of the key areas of knowledge gap over this region is the influence of aerosols, mainly those having absorbing characteristics (e.g. smoke, dust and volcanic ash), at different time scales. These aerosols gets lifted up from the surface to high elevation quite often, to this climatically sensitive region, and alters the rate of snow melt via snow darkening effect (*Wiscombe and Warren*, 1980; *Hansen and Nazarenko*, 2004), and at the same time changes the properties and lifetime of neighbouring clouds and the stability of the atmosphere (*Hansen et al*., 1997; *Ackerman et al*., 2000; *Koren et al*., 2008; *Lee et al*., 2015). The loading of absorbing aerosols on snow surfaces over the Himalayan region reduces the snow-albedo and allows snowpack to absorb more sunlight, resulting in the accelerated snow melting. This entire process is referred as snow darkening effect (*Warren and Wiscombe*, 1980; *Hansen and Nazarenko*, 2004).

Considering these aspects, this work pursues the study on the seasonal and monthly climatology of the absorbing aerosols over the defined Himalayan region, by making use of the updated and long-term data obtained from multiple sensor measurements.

3.3. NSI region

The northern states of India is confined within the geographical boundary 23° - 38°N and 72° - 85°E, and encompasses the group of states namely – Jammu & Kashmir, Himachal Pradesh, Punjab, Haryana and Chandigarh, Uttarakhand, Delhi & Non-Capital Region (NCR), and Uttar Pradesh. The total area of the region is about 0.67 million km^2, comprising of approximately 20 % of India's total land area. These states possess diverse topography and cover the major portion of the Himalayan ranges as well as IGP. **Fig. 3.4(a, b)** shows the map with elevation details of the study NSI region.

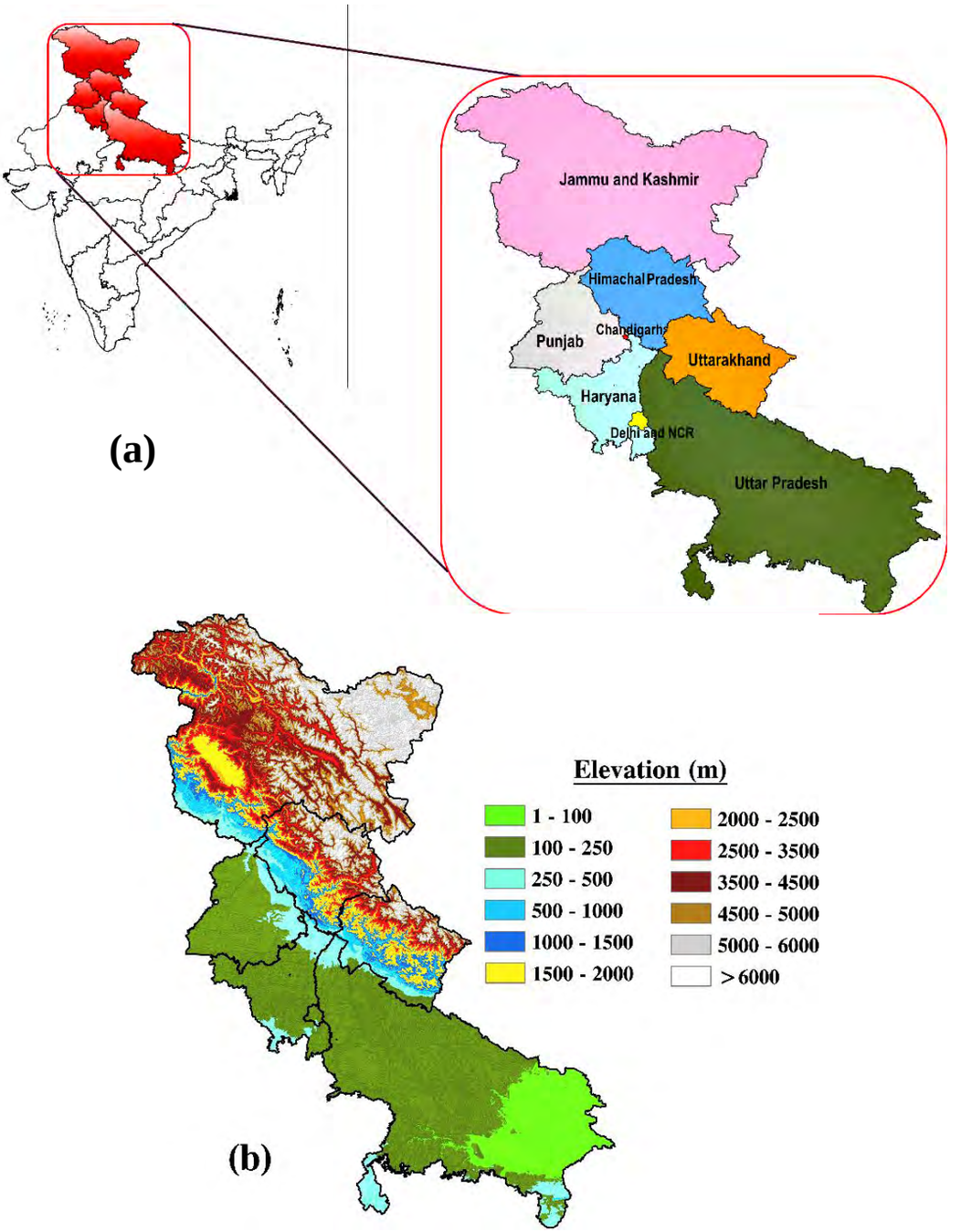

Fig. 3.4(a). Map of study region i.e. northern states of India, and **(b)** its elevation map

The understanding on cloud vertical structures, their microscopic and macroscopic properties, and spatio-temporal distribution of clouds and precipitation, describing the impact on changing climate over the NSI region is still poor. Its states like Uttarakhand and Himachal Pradesh are highly prone to extreme rainfall reception and cloudbursts, due to their physiography, especially

during June-September (e.g. 4-5 September 1995 in Kullu valley of Himachal Pradesh, 17-19 July 2001 in Mandi, 09-10 August 2001 in Shimla, 5-6 July 2004 in Chamoli, 14-15 September 2010 in Almora, 2-8 August 2012 in Uttarkashi, 14-17 June 2013 in Kedarnath). Even, Jammu & Kashmir also have the records of cloudbursts (e.g. 23-24 June 2005, 31 July-1 August 2006 and 4-6 August, 2010 in Leh, 8 June 2011 in Doda) despite of experiencing a little monsoon activity. Since there are Himalayan mountain ranges in the larger portions of Uttarakhand, Himachal Pradesh, and Jammu and Kashmir, hence, the orographic enhancement of precipitation and its interaction with the cloud microphysical processes may be thought as the driving mechanism behind the cloudbursts in addition to the thermodynamic factors, in these regions (*Thayyen et al*., 2013; *Asthana and Asthana*, 2014; *Dimri et al*., 2017). The heavy rainfall and cloudbursts activities, in the NSI region occasionally leads to the disastrous flood incidents e.g. 14-17 June 2013 in Kedarnath (Uttarakhand), and 4–6 September 2014 in many parts of Jammu and Kashmir etc. Such floods often occurs due to large scale disturbed atmospheric conditions as a consequence of the interaction between the westward-moving monsoon low and the eastward-moving deep trough in the mid-latitude westerlies. Hence, the quantitative study focussed on the clouds and precipitation over this region using the remote sensing tools may be an important step in the direction of mitigating the natural catastrophes like cloudbursts, flash floods, and landslides causing the loss of life and ecosystem, and to some extent in diagnosing and predicting the icing conditions, precipitation and other weather hazards associated with clouds. The analysis on cloud-related parameters over this region will help in reducing the uncertainties associated with regional climate models, and in quantifying the feedback by the clouds in radiation and latent heat calculations (*Cess et al.,* 1996*; Wang and Sassen,* 2001*; Kumari and Goswami*, 2010; *Rajeevan et al*., 2013).

The varied and complex topography of NSI, covering the major part of IGP as well as the Himalayan region, possesses the large variability in meteorological parameters particularly the rainfall pattern, which is mainly controlled by two major atmospheric circulations – southwest monsoon (June – September), and the western disturbances during December - March. These two contrasting periods: (i) June-July-August-September (JJAS), and (ii) December-January-February-March (DJFM) encompassing the southwest monsoon and active periods of western disturbances, respectively, are hence taken up for the seasonal investigations over the region.

Chapter 4

MATERIALS AND METHODS

CHAPTER 4
MATERIALS AND METHODS

4.1. Ground based and in-situ measurements

4.1.1. AERONET

The AERONET program is an inclusive federation of ground-based remote sensing aerosol networks established by NASA and PHOTONS and greatly expanded by networks and collaborators from national agencies, institutes, and other partners (*Holben et al.,* 1998). The program provides a long-term database of globally distributed observations of aerosol optical, microphysical and radiative properties. It uses Cimel sun/sky radiometers that measures direct sun and diffuse sky radiances within 340-1020 nm and 440-1020 nm spectral ranges, respectively (*Holben et al*., 1998). AERONET data is available at three levels: level 1.0 (unscreened), level 1.5 (cloud screened; *Smirnov et al*., 2000), and level 2.0 (cloud screened and quality assured; *Holben et al*., 1998; *Smirnov et al*., 2000). The access to these different levels AERONET data sets for the stations, which are ~ 400 in number across the globe, are made free (*https://aeronet.gsfc.nasa.gov*/), and the researchers are utilizing them for long term aerosol studies and product validations (e.g. *Holben et al., 2001*; *Torres et al., 2002a; Bréon et al., 2011; Bibi et al., 2015; Bilal et al., 2016*). AERONET performs passive measurements of column-mean aerosol microphysical and optical properties like AOD, AE, SSA, phase function, and size distribution (fine and coarse). The AERONET measurements are considered as the ground truth due to its worldwide use and acceptability in the validation and bias corrections of the satellite retrievals (*Bréon et al.,* 2011*; Bibi et al.,* 2015*; Bilal et al.,* 2016). Only level-2 data is used in this research work, that includes automatic cloud screening and utilizes the tools such as 1-min stability, diurnal stability, smoothness tests etc., and the uncertainty in the AOD values is 0.01 to 0.02 (*Eck et al*., 1999).

The AERONET data from ten stations, that are distributed within 1500 km distance (aerial), and situated in the defined Himalayan boundary, are investigated on seasonal scales, where seasons are defined namely as, pre-monsoon during March to May (MAM), monsoon during June to August (JJA), post-monsoon during September to November (SON), and winter during December to February (DJF). The selected stations are – Nainital, Pantnagar, Kanpur, New Delhi, Lahore, Gual Pahari, Gandhi College, Jaipur, Lumbini, and Pokhara (**Fig. 4.1**). The details of the chosen stations are presented in **Table 4.1**. Except, Lahore in Pakistan, and Lumbini and Pokhara in Nepal, other seven stations are located in India.

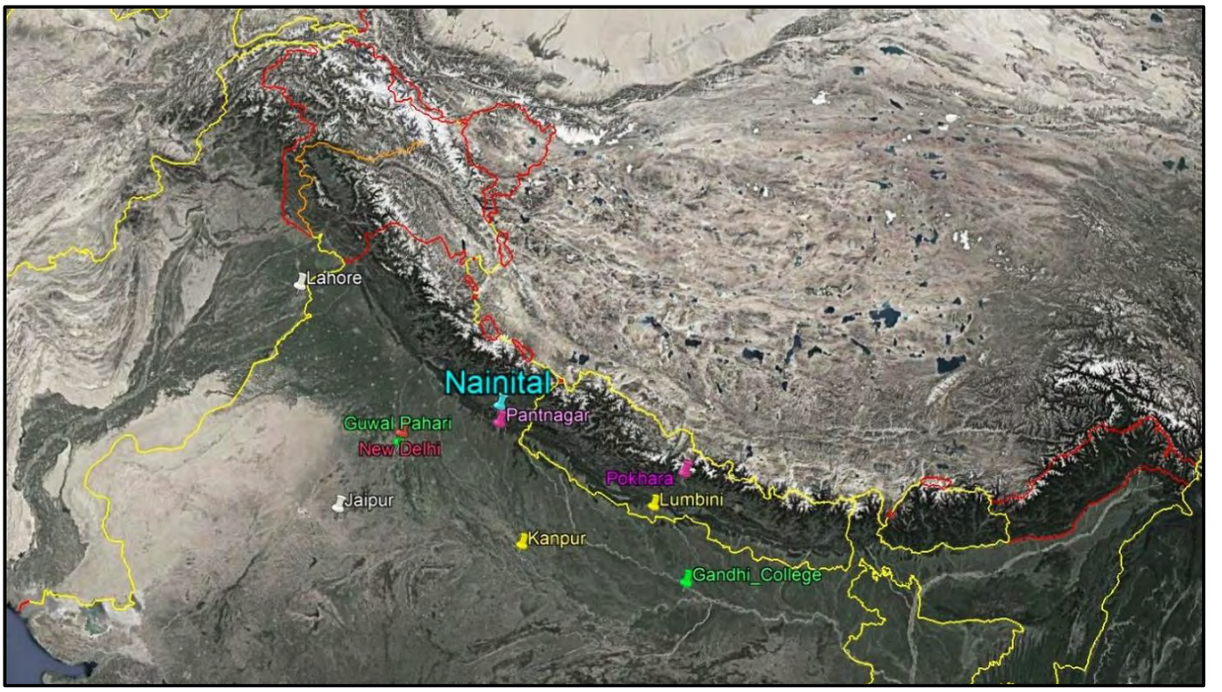

Fig. 4.1. Map showing the location of ten AERONET stations - Nainital, Pantnagar, Kanpur, New Delhi, Lahore, Gual Pahari, Gandhi College, Jaipur, Lumbini, and Pokhara.

Table 4.1: List of ten selected AERONET stations for aerosols study.

Station	Latitude (°N)	Longitude (°E)	Elevation (m)	Duration (MMM YYYY)
Nainital	29.36	79.46	1939 1943	May 2008 – Feb 2011 Oct 2011 – Mar 2012
Pantnagar	29.05	79.52	241	Apr 2008 – Oct 2009
Kanpur	26.51	80.23	123	Jan 2001 – Mar 2018
New Delhi	28.63	77.17	240	Jan 2009 – Dec 2009
Lahore	31.48	74.26	209	Jan 2007 – Apr 2015
Gual Pahari	28.43	77.15	384	Dec 2008 – Jan 2010

Gandhi College	25.87	84.13	60	Apr 2006 – June 2017
Jaipur	26.90	75.81	450	Apr 2009 – Dec 2016
Lumbini	27.49	83.28	110	Jan 2013 – Aug 2018
Pokhara	28.19	83.97	800	Jan 2010 – May 2018

Nainital is a high altitude, rural site in the central Himalayan region. The place is surrounded by high-altitude mountains of central Himalayas having dense forest with thick vegetation, and free from industries (*Sagar et al.*, 2004, 2015*; Hegde et al.*, 2009*; Dumka et al*., 2014; *Solanki and Singh*, 2014*; Sarangi et al.*, 2014*; Ojha et al.*, 2014*; Solanki et al.*, 2016*; Kumar et al.*, 2018). Pantnagar is a rural/semi urban site in the foothills of Himalayas. This site is surrounded by regions of small-scale industries (*Dumka et al*., 2014). Kanpur (located in IGP region) is one of the extremely polluted and urban site of north India with a population of ~ 5 million (*Tripathi et al*., 2005; *Ram et al*., 2016). New Delhi, a mega-city of Asia, lies east of the Thar desert and south of the Himalayas in the IGP region (*Srivastava et al*., 2012, 2014). Gual Pahari in Gurgaon is a semi-urban site located at about 25 km south of Delhi, where the anthropogenic sources are mainly city traffic, emissions and power production (*Hyvarinen et al*., 2010). Gandhi College is in the north-eastern India, towards the south of Himalayas and east of Thar desert. This station is located in the village of Mirdha which is ~ 10 km from the city of Ballia, in Uttar Pradesh. Jaipur, an urban city of eastern Rajasthan, is located in the vicinity of Thar desert. The city is more influenced by nearby dust sources, than the industrial activities (*Verma et al*., 2015, 2017). Lahore is the second largest, and densely populated (~ 10 million people) city of Pakistan. It is the hub of major industries, and transportation centres (*Alam et al*., 2012; *Ali et al*., 2014). Lumbini, a sacred birth place of Lord Buddha, is the world heritage, semi-urban Tarai portion of Nepal. The place occupies the southern portion of Nepal, and located between the highly polluted IGP to its south and the foothills of the central Himalaya to its north (*Rupakheti et al*., 2017, 2018). The last station, Pokhara is a low elevation (~ 800 m), second largely populated (> 2,50,000) sub-urban valley in Nepal. This AERONET station is surrounded by mountains of approximately 1500 m tall. Further north of Pokhara, within less than 40 km distance, there is a sharp elevation gradient (over 7000 m amsl or higher) favoring the orographic lift of humid air masses. Due to distinct topography, Pokhara is one of the largest receptor of precipitation in Nepal (*Aryal et al*., 2015).

For all the above mentioned stations, the seasonal variations in aerosol volume-size distribution, total, fine and coarse mode AODs, and Fine Mode Fraction (FMF) at 500 nm are

computed and subjected for investigation. The aerosol volume-size distribution, in 22 radius size bins ranging from 0.05 to 15 μm, is governed by the following equation (*Schuster et al*., 2006):

$$\frac{dV(r)}{d\ln r} = \sum_{i=1}^{n} \frac{C_{v,i}}{\sqrt{2\pi}\sigma_i} \exp\left[\frac{-(\ln r - \ln r_{v,i})^2}{2\sigma_i^2}\right] \quad (4.1)$$

where, $\frac{dV(r)}{d\ln r}$ (in $\mu m^3/\mu m^2$) is the aerosol volume particle size distribution, $C_{v,i}$ is the particle volume concentration of particulate matter ($\mu m^3/\mu m^2$), *n* is the number of log-normal aerosol modes, σ_i is the variance or width of each mode, *i*, and $r_{v,i}$ is the geometric volume mean or median radius (μm). The aerosol volume-size distribution deduced from AERONET are often described as two volumetric modes: an accumulation or fine mode (mean radii of the particle is < 0.6 μm), and a coarse mode with geometric mean radii > 0.6 μm (*Dubovik et al*., 2002).

The AOD is a measure of aerosols from the surface of earth to top of the atmosphere. The fine and coarse mode AODs at 500 nm are based on the Spectral De-convolution Algorithm (SDA) (*O'Neill et al*., 2003). The total AOD is the sum of fine and coarse mode AODs, and is defined as the extinction of solar radiation from both fine and coarse mode aerosols. Whether dominant aerosols in the atmosphere are coarse (e.g. dust) or fine, is determined using FMF, defined as the ratio of fine mode AOD to the total AOD. The FMF values of 0 and 1 represent the purely coarse mode particles (originating from natural sources such as wind-blown mineral dust and sea salt) and purely fine or accumulation mode particles (which are formed due to gas to particle conversion mainly from anthropogenic activities and produce sulfate, black carbon, organic carbon, nitrates etc.), respectively, and practically, the value lies in between the two, where both coarse and fine modes contributes to the total AOD in proportion.

4.1.2. LiDAR

Background

The range resolved measurement of aerosols, clouds, water vapour, temperature etc. for understanding the complex mechanism that governs the atmosphere, can be efficiently performed using the LASER based active remote sensing tool, known as LiDAR. It mainly comprises of four

elements – a pulsed LASER light source and transmitter optics, a receiver module equipped with a telescope and optical assembly used to focus and filter the received light, a detector assembly usually consisting of Photo-Multiplier Tubes (PMT), Avalanche Photo Diodes (APDs) or other high gain photoelectric modules, and high-speed data acquisition boards that samples the signal and provide the received information in terms of photon counts at pre-defined dwell times. By definition, the LiDARs are monostatic, that is, its transmitter and receiver are at the same location. They may be coaxial, with axes of the transmitted beam and receiver Field Of View (FOV) coinciding, or side by side, or may be biaxial, with the two axes parallel or near-parallel, but not identical.

The atmospheric profiling using LiDAR is done by transmitting the LASER beam vertically up in the atmosphere, from where it gets scattered or absorbed by atmospheric aerosols and molecules. Scattering in the atmosphere takes place mainly due to two processes - the Mie scattering, and the Rayleigh scattering. The Mie scattering is effective from lower heights where the size of the aerosols, cloud droplets, and other particles are larger or comparable to wavelength of the LASER beam, whereas, the Rayleigh scattering is from the atmospheric molecules and it is dominant at higher altitudes (> 20 km).

LiDAR systems at ARIES, Nainital

From ARIES, Nainital, three Mie LiDAR systems were operated for vertical profiling of the atmospheric aerosols and clouds during the period 2006 - 2014. All the three LiDAR systems primarily consists of three major subsystems - transmitter, receiver and detector & data acquisition system, and the basic block diagram of one of the system (LiDAR-II) is shown in **Fig. 4.2**. The first Mie LiDAR system (LiDAR-I) was operated during 2006-2008 (*Hegde et al.,* 2009), and the second system (LiDAR-II) between 2010 and the mid of 2011 (*Bangia et al.,* 2011). The third system (LiDAR-III) named as LiDAR for Atmospheric Measurement and Probing (LAMP) is an upgraded version of the first one which was made operational since October 2011 (*Solanki et al.,* 2013*; Solanki and Singh,* 2014). LAMP is much more compact monostatic version of the first one and is equipped with Recommended Standard-232 (RS-232) and Ethernet interfaces, built-in acousto-optic modulator for Q-switching and high quality optical assemblies. **Fig. 4.3** provides the snapshot of the above-mentioned versions of the LiDAR systems, together with their essential electronics. Further, **Table 4.2** summarizes the major differences among all these systems.

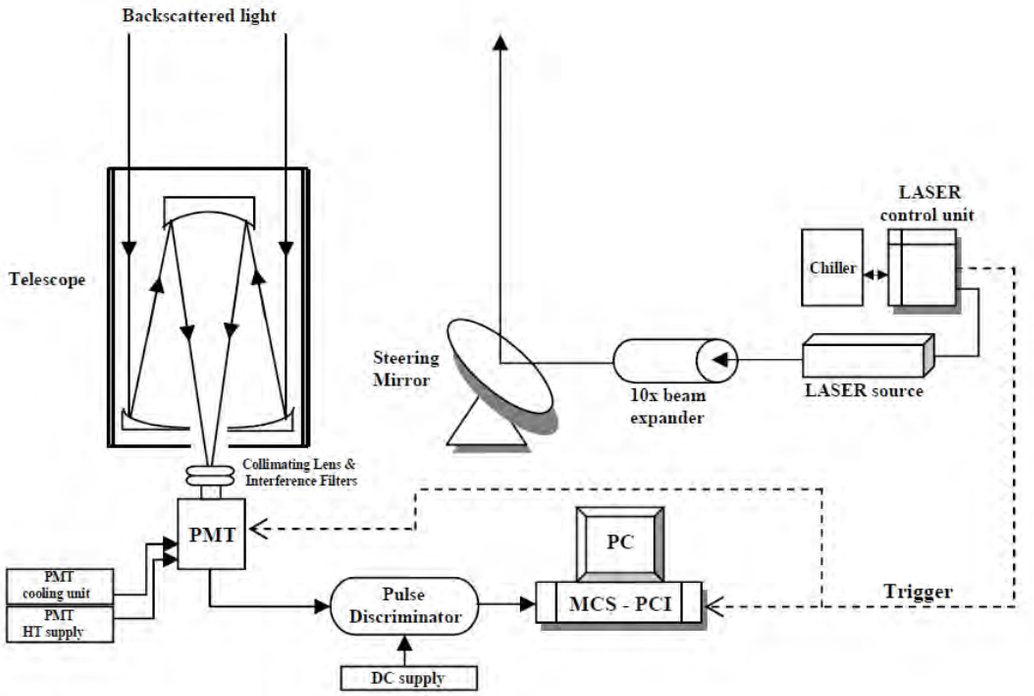

Fig. 4.2. A typical block diagram of a Mie LiDAR system (source: *Bangia et al*., 2011).

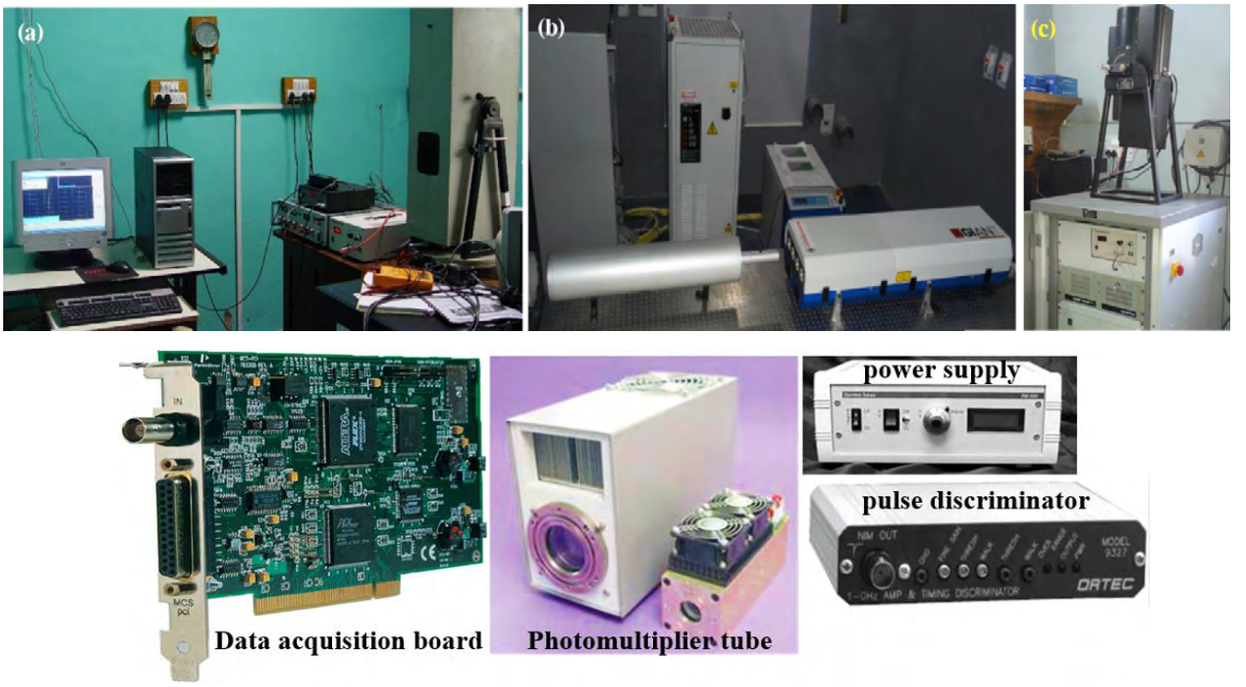

Fig. 4.3. The Mie LiDAR systems operated at ARIES **during the period 2006 - 2014 (a)** LiDAR-I, **(b)** LiDAR-II, and **(c)** LiDAR-III. The bottom figures shows some of the essential electronics of these systems.

Table 4.2: Technical specifications of the Mie LiDAR systems operated at ARIES, Nainital.

Parameters	**LiDAR-I**	**LiDAR-II**	**LiDAR-III**
Wavelength	532 nm	532 nm	532 nm
Telescope	Cassegrain, 150 mm dia, ~ 1 mrad Focal ratio – f/9	Cassegrain, 380 mm dia, ~ 6 mrad Focal ratio – f/15	Cassegrain, 150 mm dia, ~ 400 µrad Focal ratio – f/9
LASER type	Q-switched, Nd:YAG	Q-switched, Nd:YAG	Acousto-optic, Q-switched, Nd:YAG
Beam expander	8X	10X	8X
Resolution	30 m	300 m	15 m
Complete Overlap	~150 m	~300 m	~90 m

The statistics on the LiDAR observations from the site during each years, corresponding to individual months is shown in **Fig. 4.4**.

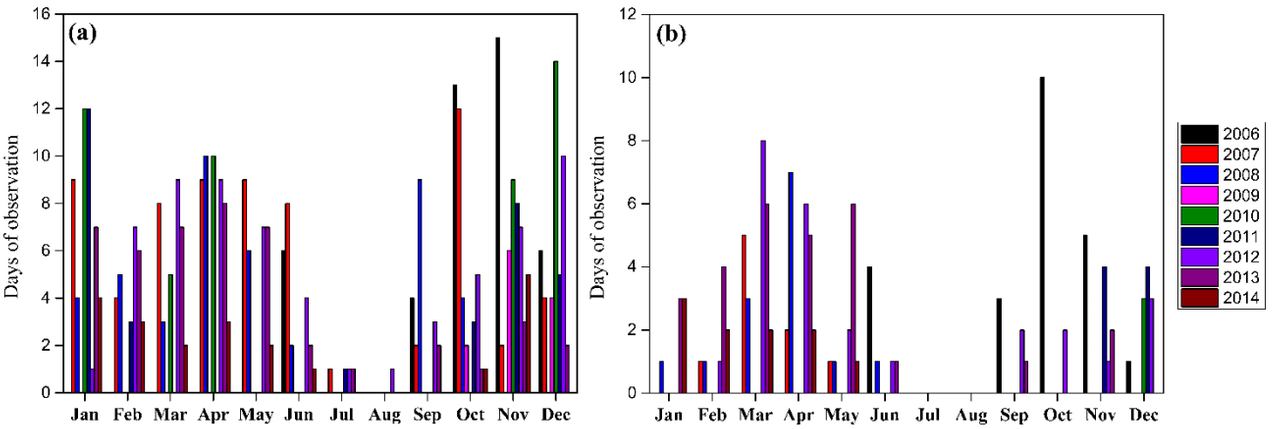

Fig. 4.4. LiDAR observations from ARIES, Nainital site during 2006-2014 for **(a)** all (cloudy, cloud-free, and mixed conditions), and **(b)** only the cloud-free conditions.

Basic principle

The basic principle involved in all three LiDAR systems are same, which can be expressed in terms of LiDAR equation as (*Bangia et al*., 2011):

$$P(r) = \frac{KP_o\beta(r)\exp\left[-2\int_0^R \alpha(r)dr\right]}{R^2} \quad (4.2)$$

where, $P(r)$ is the instantaneous backscattered signal power at time t from range (height) r, P_o is the transmitted LASER power, K is the LiDAR constant that includes receiver optical efficiency η, collecting area (A) of the primary mirror of receiving telescope, and the range resolution ($c\tau/2$, where c and τ are velocity of light and pulse duration of the LASER beam, respectively). The term A/r^2 is the solid angle subtended by the primary mirror at a given range. $\beta(r)$ and $\alpha(r)$ are the backscattered and extinction coefficients, respectively, which includes the contributions from both aerosols and molecules, given by:

$$\alpha(r) = \alpha_{aer}(r) + \alpha_{mol}(r), \text{ and}$$
$$\beta(r) = \beta_{aer}(r) + \beta_{mol}(r) \quad (4.3)$$

where, subscript (*aer)* and (*mol)* indicate aerosols and molecules, respectively.

The extinction $\alpha_{mol}(r)$, contributed by molecules is expressed as:

$$\alpha_{mol}(r,\lambda,p,T) = \frac{8\pi^3(n_{air}^2-1)^2}{3\lambda^4 N_s^2} F(\lambda,r) N_s \frac{T_0 p(r)}{p_0 T(r)} \quad (4.4)$$

where, the values of the pressure, $p(r)$ and temperature, $T(r)$ are taken from the COmmittee on SPAce Research (COSPAR) International Reference Atmosphere (CIRA) 1986 standard atmosphere model (*Rees et al*., 1990) deduced for the site, p_0 and T_0 are standard pressure and temperature, respectively, n_{air} denotes the refractive index of air, r is the height, λ is the LiDAR wavelength, N_s is the molecular number density and is considered as 2.54743×10^{25} m^{-3} (*Sagar et al.*, 2004). The term $F(\lambda, r)$ is the King factor for the depolarization of air at wavelength, λ and height, r expressed as:

$$F(\lambda, r) = \frac{6+3\gamma}{6-7\gamma} \quad (4.5)$$

where, γ is the depolarization factor taken as 0.035 for ARIES LiDARs.

The molecular backscatter coefficient $\beta_{mol}(r)$ is estimated by considering the theoretical molecular LiDAR ratio, $S_{mol} = \alpha_{mol}(r)/\beta_{mol}(r)$ as $8\pi/3\,\mathrm{sr}$ (constant), under the condition of zero molecular absorption. Various techniques are there to solve equation (4.2) (*Klett*, 1981; *Fernald*, 1984; *Sasano and Nakane*, 1984). In the present work, Fernald method is used in the analysis, which is expressed as (*Fernald*, 1984):

$$\beta_{aer}(r)+\beta_{mol}(r)=\frac{X(r)\exp[-2(S_{aer}-S_{mol})]\int_{r_c}^{r}\beta_{mol}(r)dr}{\frac{X(r_c)}{\beta_{aer}(r_c)+\beta_{mol}(r_c)}-2S_{aer}\left\{\int_{r_c}^{r}X(r)\exp[-2(S_{aer}-S_{mol})\int_{r_c}^{r}\beta_{mol}(r')dr']dr\right\}} \quad (4.6)$$

where, $X(r)$ is the range normalized signal, given by $P(r)r^2$ and r_c is the reference height, S_{aer} is the LiDAR ratio due to aerosols, which is discussed in details, in the later portion of this thesis.

4.1.3. Automatic Weather Station

The AWS system is installed in the campus of ARIES, Nainital at approximately 29.21°N, 79.27°E, ~1790 m amsl. It is the latest technology based compact, modular, and rugged system that facilitates continuous monitoring of near surface meteorological parameters like temperature, humidity, pressure, rainfall, solar radiation, wind speed and direction. The location of the AWS station alongwith the elevation map of the surrounding regions, is shown in **Fig. 4.5**.

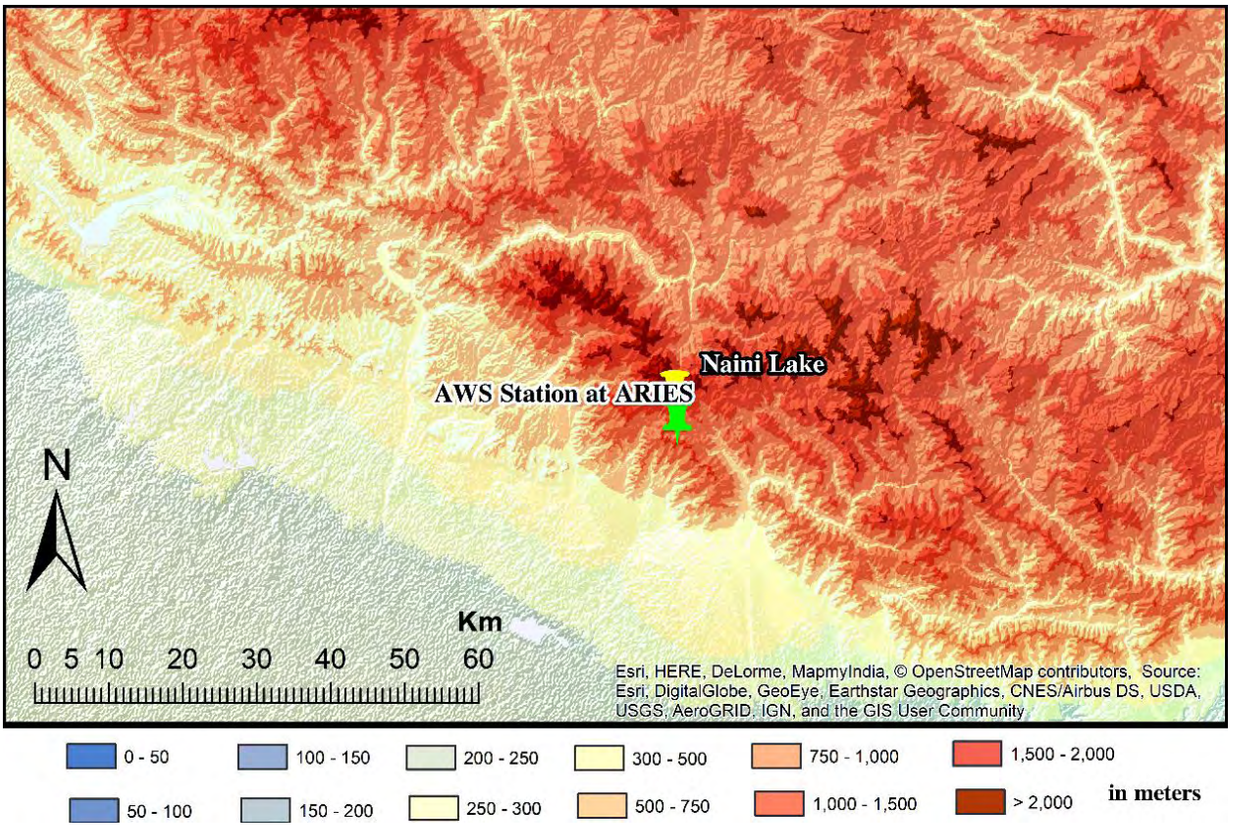

Fig. 4.5. Elevation map showing the **l**ocation of AWS station at ARIES, Nainital.

The heart of the system is its data logger, comprising of main processor, peripheral devices and interfaces for communicating and collecting data from the meteorological sensors in its in-built memory. The sampling of sensor data is done at equi-spaced time intervals set in the data logger, which can be changed as per the user requirements. Communication with the remotely located master desktop and display screen is accomplished over an Ethernet connection via File Transfer Protocol (FTP) server. The master desktop hosts the Network Management Software (NMS) application for further processing. The final data is displayed at about every 15 minutes interval to the display screen for general public. **Fig. 4.6** shows the pictorial view of the installed AWS system, and the front view of display screen, together with the NMS application running on master desktop.

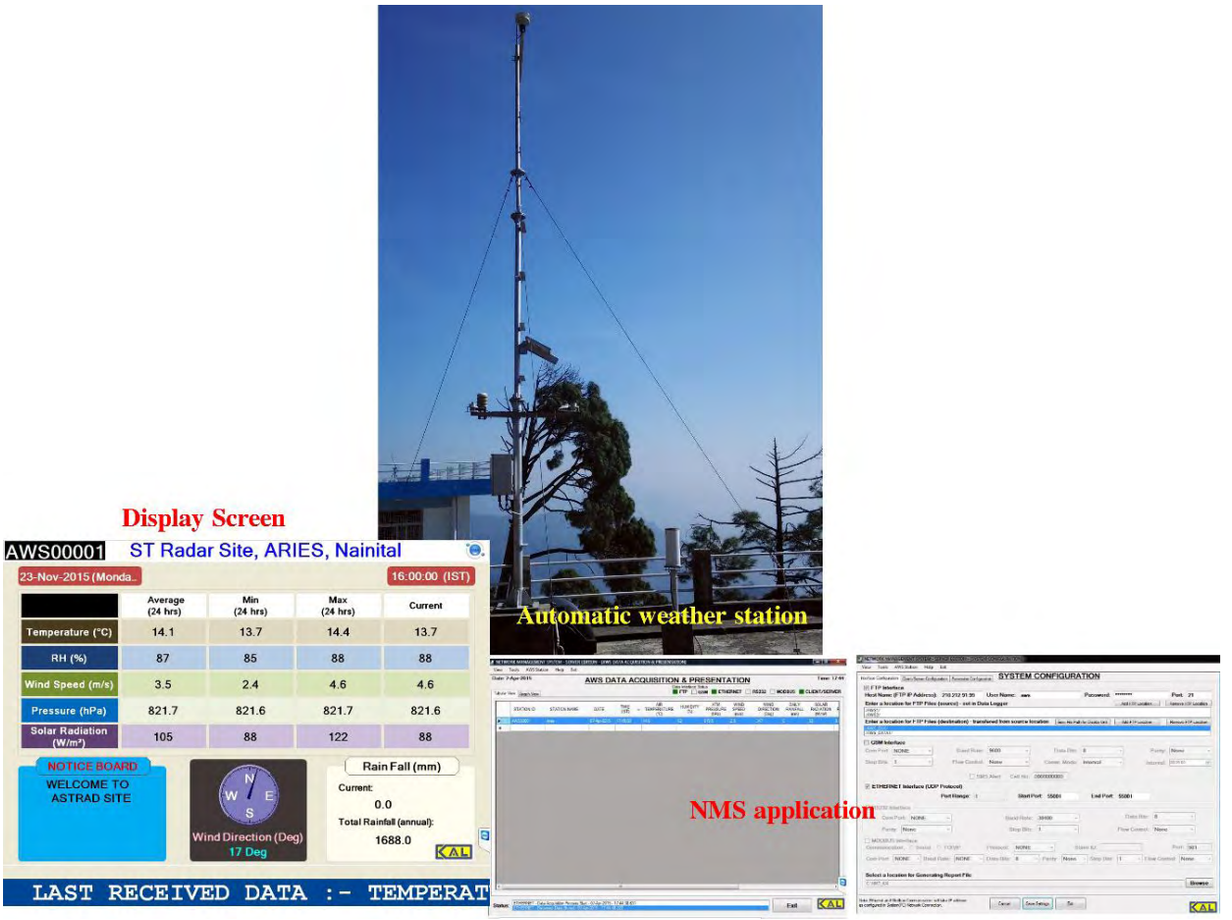

Fig. 4.6. AWS system at ARIES, Nainital.

The details on the sensors, and their accuracies, that are installed on the AWS tower is provided in **Table 4.3**.

Table 4.3: Technical specification of AWS sensors at ARIES, Nainital.

Air Temperature		
Sensor type	Platinum Resistance Thermometer (PRT)	
Range	-40 to +85 ºC	
Accuracy	0.05 ºC	
Resolution	0.01 ºC	
Relative Humidity		
Sensor type	capacitive	
Range	0 to 100%	
Accuracy	± 2%	
Resolution	0.1%	

Atmospheric Pressure		
Sensor type	ceramic Micro Electro-Mechanical Systems (MEMS)	
Range	100-1200 hPa	
Accuracy	±0.2 hPa	
Resolution	0.01 hPa	
Wind speed		
Sensor type	Ultrasonic	
Range	0-60 m/s	
Accuracy	± 2%	
Resolution	0.01 m/s	
Wind direction		
Sensor type	Ultrasonic	
Range	0-359°	
Accuracy	± 2%	
Resolution	1°	
Pyranometer (total Solar radiation)		
Sensor type	Multi-junction Thermopile	
Range	0 to +2000 W/m^2	
Accuracy	± 3 % FS	
Resolution	1 W/m^2	
Rainfall		
Sensor type	Tipping Bucket	
Accuracy	± 3 %	
Resolution	better than 0.5 mm	

4.1.4. Radiosonde

Background

Accurate measurements on vertical structure of the meteorological parameters such as pressure, temperature, humidity, and wind, plays crucial role in dispersion, transportation and accumulation of the atmospheric pollutants, and their study is extremely important for weather prediction, environmental pollution, upper-air climate change, model validation etc. The radiosonde is standard in-situ tool for obtaining the profiles of these parameters upto ~ 30 km vertical in the atmosphere, with sufficient accuracy or degree of confidence as compared to satellite observing systems. The lightweight radiosonde, equipped with meteorological sensors, signal-processing electronics, and a radio transmitter unit, is transported to atmosphere with the help of a rubber

balloon, filled with fixed mass of helium/hydrogen gas. In order to avoid free-fall and jerks, a parachute and unwinder/dereeler are put in between the radiosonde and rubber balloon. The balloon acts as a constant pressure device, which expands its volume, V during ascends, according to the ideal gas equation: $pV = nRT$, where p and T are the ambient pressure and temperature, respectively. The term n is the number of moles of helium/ hydrogen gas, and R (= 8.314 J/mol-K) is the universal gas constant. Sounding typically reaches ~30 km in height before the balloon bursts due to very low temperature in the upper atmosphere.

The radiosonde is also equipped with a low noise Global Positioning System (GPS) device to gather the height and position information of the radiosonde in sky. There are two radio frequency bands specified by the International Telecommunication Union (ITU) i.e. 400.15–406 MHz (band-1) and 1668.4–1700 MHz (band-2) that are used worldwide for transmitting the meteorological data. The ground system is mainly composed of directional antenna (generally Yagi-Uda), Low Noise Amplifier (LNA), modem, a radio receiver, and a computer/laptop. Antenna is used to receive the radio transmission sent from radiosonde, LNA is for pre-amplification of signal, radio receiver is for processing the received signal, modem is for the demodulation of data, and a computer is used for recording the information demodulated by modem.

Radiosonde observations from ARIES, Nainital

The first radiosonde observation from ARIES, Nainital was made on 18 June 2008 using Vaisala make RS80 radiosonde, in collaboration with PRL, Ahmedabad (**Fig. 4.7**).

The regular (on a weekly basis) radiosonde launches from ARIES, Nainital was started since January, 2011, with iMet-1 RSB radiosondes (*Wierenga and Parini*, 2005) attached to a 1.2 kg (or 2 kg, when used with ozonesonde) rubber balloon. The size and weight of radiosonde is ~ 260 g and 18 cm × 9 cm × 9 cm (H × L × B). The iMet-1 RSB radiosonde at ARIES uses band-1, which can be tuned to one of the 8 frequencies in 400.15-406 MHz frequency range. The details on meteorological sensors used in iMet-1 RSB radiosonde is given in **Table 4.4**.

Apart from regular observations, the observations using Vaisala RS92-SGP radiosonde (**Table 4.4**), were also made four times a day (at about 0 hrs, 6 hrs, 12 hrs, and 18 hrs UTC), during a 10-month (June 2011 to March 2012) Indo-United States (US) field campaign - Regional Aerosols Warming Experiment (RAWEX)–Ganges Valley Aerosol Experiment (GVAX), which was conducted at ARIES jointly by the US Department of Energy (DOE) and Indian Space Research

Organization (ISRO) (e.g. *Moorthy et al*., 2016; *Naja et al*., 2016; *Singh et al*., 2016), alongwith the involvements from institutions like ARIES, Indian Institute of Science (IISc), Argonne National Laboratory, North Carolina State University, and Pacific Northwest National Laboratory (*Kotamarthi*, 2010, 2013).

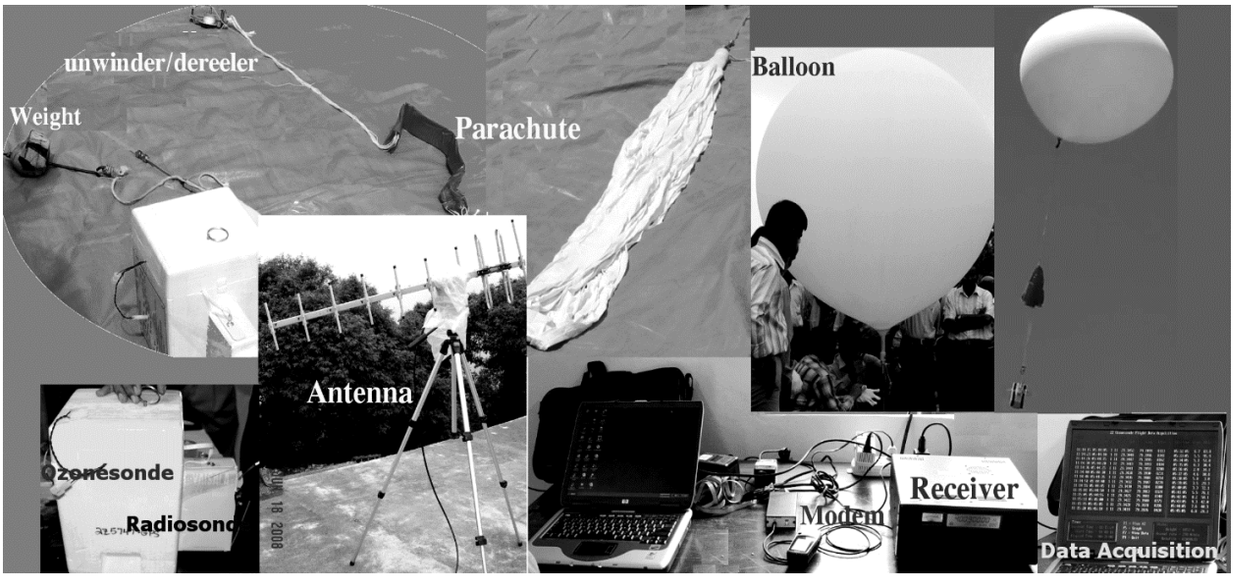

Fig. 4.7. Snapshots of the first radiosonde launch from ARIES, Nainital.

Table 4.4: Technical specifications of the meteorological sensors provided in iMet-1 RSB and Vaisala RS92-SGP radiosondes.

	iMet-1 RSB	**Vaisala RS92-SGP**
Air Temperature sensor		
Type	Bead thermistor	Capacitive wire
Range	-95 to +50 ºC	-90 to +60 ºC
Resolution	< 0.01 ºC	0.1 ºC
Accuracy	±0.3 ºC	±0.5 ºC
Response time	2 sec (1000 hPa)	< 4 sec (1000 hPa)
Humidity sensor		
Type	Capacitive polymer	Thin film capacitive polymer, heated twin sensor
Range	0 to 100 % RH	0 to 100 % RH

Resolution	< 0.1 % RH	1 % RH
Accuracy	±5 % RH	±5 % RH
Response time	2 sec at 25°C 60 sec at -35°C	< 0.5 sec at 20°C < 20 sec at -40°C
Pressure sensor		
Type	Piezoresistive silicon	Capacitive silicon
Range	2 to 1070 hPa	3 to 1080 hPa
Resolution	< 0.01 hPa	0.1 hPa
Accuracy	±0.5 hPa for < 400 hPa ±1.8 hPa for 400-1070 hPa	±0.6 hPa for 3-100 hPa ±1 hPa for 100-1080 hPa
Response time	< 1 sec	< 1 sec
GPS		
Altitude accuracy	±15 m	±20 m
Position accuracy	±10 m	±10 m
Wind velocity accuracy	±1 m/s	±0.15 m/s std. dev. of differences between two soundings
Wind direction accuracy	≤ ±5° for wind speeds < 14 m/s, and ≤ ±2° for wind speeds > 14 m/s	2° std. dev. of differences between two soundings, wind speed above 3 m/s

Radiosonde observations from Delhi station for intecomparison

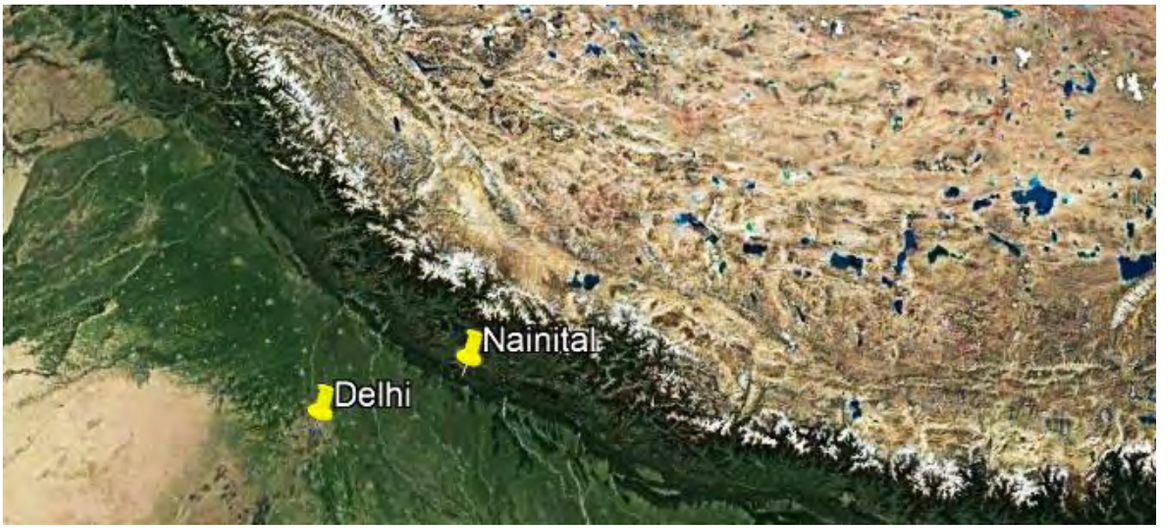

Fig. 4.8. Geographical locations of the stations – Delhi, and Nainital.

The radiosonde data for a highly polluted urban-industrial city i.e. Delhi (*Lodhi et al*., 2013), available at the University of Wyoming's Department of Atmospheric Science public repository (weather.uwyo.edu/upper air/sounding.html) is also analyzed in the present work, and compared with the observations made from ARIES, Nainital. Delhi (28.58°N, 77.20°E, elevation: 216 m amsl) is located towards southwest at ~ 230 km (aerial) from Nainital. The geographical location of the selected two stations are shown in **Fig. 4.8**.

The sources of errors associated with the comparison between radiosonde launches from Nainital and Delhi stations are mainly due to (a) temporal gap between the observations, (b) horizontal separation between the observing stations, and (c) differences arising due to types and accuracies of sensors used in the measurement. The error source (c) is not taken into account in the present work, however, error sources (a) and (b) are minimized here, by selecting the observing station i.e. Delhi closest to Nainital, and by considering only those observations, that offer the best temporal matching (±1 hr) with the radiosonde observations from Nainital, during the period of investigation. **Table 4.5** summarizes the number of radiosonde observations available from Nainital station during June 2011 – March 2012, and the corresponding observations from Delhi station.

Table 4.5: The number of radiosonde observations available from Nainital during June 2011 – March 2012, together with the number of coincident radiosonde observations (±1 hr) from Delhi.

Seasons	**Months**	**Nainital**	**Delhi**
		No. of observations	**No. of observations coincident (±1 hr) to (A)**
		(A)	**(B)**
monsoon	June-2011	13	7
	July-2011	118	55
	Aug-2011	112	56
post-monsoon	Sep-2011	118	59
	Oct-2011	117	60
	Nov-2011	114	59
winter	Dec-2011	120	59
	Jan-2012	122	56
	Feb-2012	114	54
pre-monsoon	Mar-2012	121	59

It is necessary to mention that the wind measurements from radiosonde for Nainital site during June - August 2011 are available only for 4 coincident days, and hence not considered in the present comparison.

4.1.5. ST RaDAR

Background

While radiosonde have been giving the vertical profiles of meteorological parameters like temperature, humidity, winds, however, they possess some limitations. They give a temporal snapshot of these parameters along the line of ascent, and due to cost implications associated with a single radiosonde launch, they cannot be used on a continuous basis. The contemporary science scenario in the atmospheric dynamics, especially in the troposphere and lower part of the stratosphere, requires setting up of a state-of-the-art system that monitors the atmosphere round the clock. This is achieved using the atmospheric RaDARs, which generally operates in VHF and UHF bands (*Woodman and Guillen*, 1974; *Strauch et al.*, 1984), and widely used to investigate structure and dynamics of the troposphere, stratosphere and mesosphere. **Table 4.6** provides the list of some directly and derivable parameters obtained from atmospheric RaDARs.

Table 4.6: List of some direct and derivable parameters obtained from the atmospheric RaDARs.

Directly measurable parameters		
1.	Wind parameters	The two orthogonal horizontal wind components (zonal and meridional) and the vertical wind component, together with wind spped and direction
2.	Turbulence	The width of the Doppler spectra give the estimates of turbulence parameters
3.	RaDAR reflectivity	It is obtained directly from the received signal strengths
Derivable parameters		
1.	Brunt Vaisala frequency and temperature profile	The Brunt Vaisala frequency signifies the atmospheric stability, and can be derived from temporal spectrum of the vertical wind velocity. From the altitude profile of the Brunt Vaisala frequency, the temperature profile can be derived using the method devised for convective stability conditions (*Röttger*, 1986; *Revathy et al*., 1996; *Mohan et al*., 2001).
2.	Horizontal divergence	The horizontal divergence (D) can be derived from vertical velocities obtained from RaDAR using different methods, namely, the kinematic, adiabatic and the vorticity methods (*Cifelli et al*., 1996; *Satheesan and Murthy*, 2005).
3.	Vorticity	The vorticity can be derived using the high resolution wind measurements from RaDAR (*Kudeki and Rastogi*, 1992).
4.	Momentum fluxes	The vertical flux of horizontal momentum of the different atmospheric waves can be derived from the wind components (*Vincent and Reid*, 1983)

The atmospheric RaDAR basically works on the Doppler principle which was introduced by Austrian mathematician and physicist Christian Andreas Doppler in 18th century (*Roguin,* 2002). The principle states that if there is a relative motion between the source of waves and an object encountering the waves, the frequency measured at that object will be different from that at the source. If the object is approaching the source, the frequency will be higher; if it is receding, the frequency will be lower. The amount of frequency change, called the Doppler shift (f_d), is directly proportional to the relative radial velocity (V_r) between the source and object and inversely proportional to the wavelength (λ). Here, the source is the atmospheric RaDARs and the object is the refractive index irregularities that scatters the waves. The advection of scatterers causes the Doppler shift expressed in Hz, as:

$$f_d = \frac{-2V_r}{\lambda} \tag{4.7}$$

where, V_r is the radial velocity (m/s) of scatterers along the antenna beam, and f_d is the Doppler shift (Hz). The negative sign indicates the positive radial velocities corresponding to motion away from the RaDAR, where the frequency is lower.

The atmospheric RaDARs detect echoes from turbulence-induced irregularities and fluctuations in the radio refractive index of atmosphere (which is the function of temperature, humidity, and electron density). The gradients in radio refractive index give rise to a very little backscatter of the incident electromagnetic waves and since they get mixed well due to turbulence and moves with the wind, they are used as an effective tracers of wind velocity, which essentially characterizes the atmospheric dynamics. In general, the radio refractive index for the troposphere, stratosphere and mesosphere at VHF and UHF bands is (*VanZandt et al*., 1978):

$$n - 1 = \frac{3.73\times10^{-1}e}{T^2} + \frac{77.6\times10^{-6}P}{T} - 40.3\frac{n_e}{{f_o}^2} \tag{4.8}$$

where, n is the refractive index, P is the atmospheric pressure (mb), e is the partial pressure of the water vapor (mb), T is the absolute temperature (°K), n_e is the ionospheric electron density (m^{-3}), and f_o is the RaDAR operating frequency (Hz).

One of the simpler equation of RaDAR theory is the RaDAR range equation that gives the relation between the received backscattered signal level and other parameters like transmit peak power, aperture, volume reflectivity etc. The basic form of RaDAR equation is:

$$P_r = \frac{P_t A_e \pi c \tau \eta F_1}{128 R^2 \alpha_t \alpha_r \alpha_a} \tag{4.9}$$

where, P_t = transmitter peak power (watt), A_e = effective area of antenna (m^2), $P_t A_e$ is power aperture product (~ 1×10^8 Wm^2) which is required to be high for better sensitivity of the system, c is the velocity of light (= 3×10^8 m/s), τ is pulse width (sec), η is the RaDAR volume reflectivity (m^2/m^3) , F_1 is loss due to filtering (~ 1dB), R is the range (m), α_t is the transmit loss (~ 1dB), α_r is the receive loss (~1.2 dB), and α_a is the two-way attenuation due to atmosphere.

The received backscattered signal from the clear air is directly proportional to the RaDAR volume reflectivity, η, which is related to the volume averaged refractivity turbulence structure constant, C_n^2 as follows (*Otterson*, 1969; *Singh et al*., 2008):

$$\eta = 0.38 C_n^2 \lambda^{-1/3} \tag{4.10}$$

where, λ is the RaDAR wavelength (m).

The refractivity turbulence structure constant, C_n^2 values, in general lies between 10^{-12} $m^{-2/3}$ and 10^{-19} $m^{-2/3}$ (*Rao et al*., 1996; *Singh et al*., 2008) at different layers of atmosphere that corresponds to η variation from 3.35×10^{-13} m^{-1} (-124.7 dB) and 3.35×10^{-20} m^{-1} (-194.7 dB). Further, the RaDAR volume reflectivity, η and hence the C_n^2 is directly related to Signal to Noise Ratio (SNR) at any given range (*VanZandt et al*., 1978; *Rao et al*., 1996), expressed as:

$$SNR = \frac{P_r}{k T_s B} \tag{4.11}$$

$$T_s = \frac{T_a}{\alpha_r} + \frac{T_{tr}(\alpha_r - 1)}{\alpha_r} + T_R$$

where, k is Boltzmann's constant (1.3807×10^{-23} J/°K), B is the effective noise bandwidth of the RaDAR (Hz), T_s is the system noise temperature (°K) which includes the sky noise component, the

component due to ohmic losses and the amplifier's noise figure. T_a is the antenna noise temperature (°K), T_{tr} is the transmission line temperature (°K), and T_R is the receiver noise temperature (°K).

RaDAR system at ARIES, Nainital

There are different types of VHF and UHF band atmospheric RaDARs, and among them, the VHF band Mesosphere-Stratosphere-Troposphere (MST) and Stratosphere-Troposphere (ST) RaDARs are the excellent remote sensing tools for high resolution measurements (temporal: 10 min or less, vertical: ~ 75 m – 500 m) of the atmospheric winds, turbulence, waves, stability, troposphere-stratosphere exchange processes, precipitation, and other phenomenon throughout the troposphere and up to the Mesospheric heights. To fill the gap of such systems in the Himalayan region, one ST RaDAR has been installed at ARIES, Nainital, which is a monostatic, active, coherent, pulsed Doppler RaDAR, for obtaining the vertical profiles of wind and its three components namely the zonal wind (U), meridional wind (V) and vertical wind (W) up to ~18 km height on a continuous basis, with good vertical and temporal resolutions. The location of this only RaDAR in the Himalayan region is expected to offer the ample of opportunities for studying the mountain waves, turbulence, structure and formation of clouds and precipitating systems over the mountainous region, and to some extent, it will emerge as a robust tool in building up a credible database for verification of regional climate models dealing with mountain meteorology, and numerical weather predictions.

The ARIES ST RaDAR is also called as Aries ST RADar (ASTRAD). After successful demonstration of its down-scaled version (comprising of 49 transceivers), so called Mini-profiler, at 17.28° N, 78.34° E in Hyderabad (**Fig. 4.9**), the installation and testing of ASTRAD system at ARIES, Nainital was started in 2013, which is in the process of testing the hardware and validation of its data products (mainly the winds) before commissioning.

The intermittent test observations from ASTRAD was started since 2014, and the data were collected in a progressive manner using 49 (one cluster), 147 (three clusters) and 343 (seven clusters) transceivers, and currently, the system is ready to conduct the test observations with its full capacity i.e. with the twelve clusters (588 transceivers). The number of days, ASTRAD system was operated in the test observation modes during 2014-2018 is shown as vertical bars in **Fig. 4.10**.

Fig. 4.9. Mini-profiler site at 17.28° N, 78.34° E in Hyderabad.

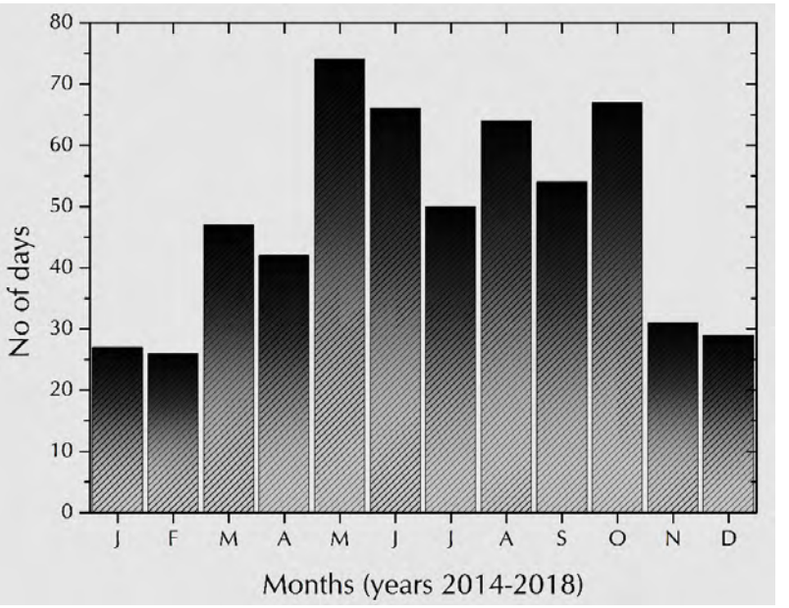

Fig. 4.10. Month-wise statistics of ASTRAD observations from ARIES, Nainital during 2014-2018.

The ASTRAD system employs 588 solid state Transmit-Receive Modules (TRMs) each connected to individual 3-element Yagi antenna elements, placed in an equilateral triangular grid fashion, forming circular aperture array, with an inter-element spacing of 0.7λ. The main advantage of this active array RaDAR is that the phase of the signal transmitted from individual Yagi's are electronically controlled at low power level, and hence fast dynamic behaviour of the atmosphere can be observed with the system. The inherent advantage of Yagi antenna elements is that because

of its reflector, extra ground plane is not required, and a single Yagi provides high gain and negligible coupling between the adjacent Yagi's in an array. A clutter fence is installed along the periphery of the antenna array to minimize the strength of the clutter return from the nearby hills. The snapshots of the major sub-sections of ASTRAD is shown in **Fig. 4.11**, and **Table 4.7** provides the detailed technical specifications of the system.

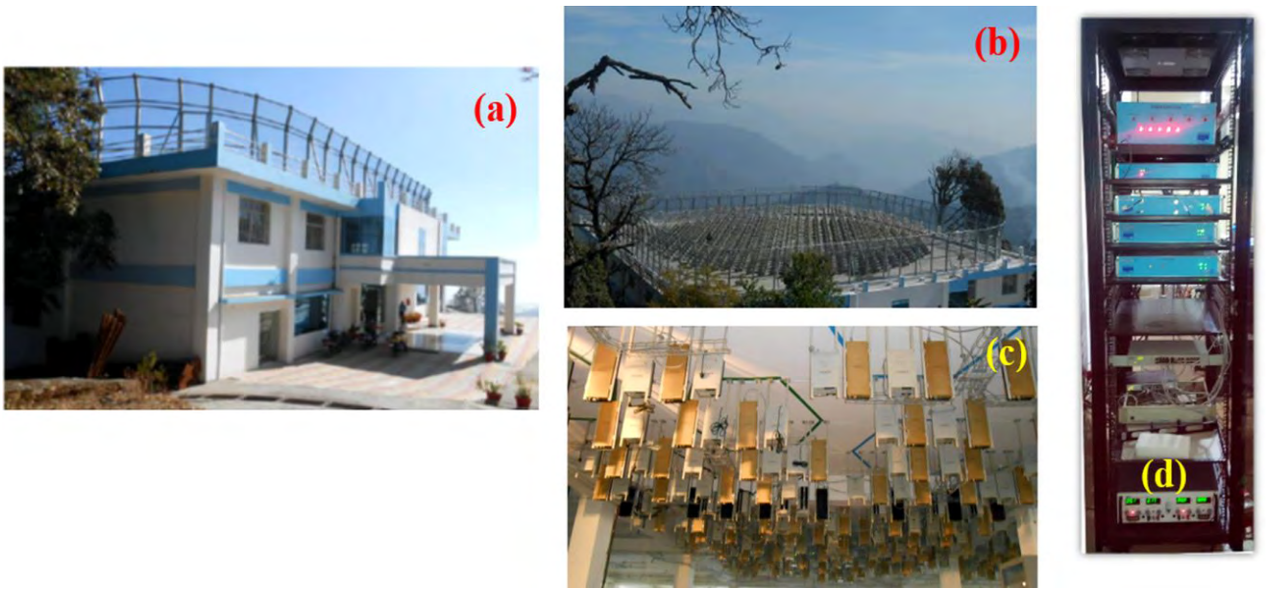

Fig. 4.11. ASTRAD facility at ARIES, Nainital: **(a)** building and clutter fencing at its roof-top, **(b)** antenna array, **(c)** transmit-receive modules, **(d)** digital subsystems.

ASTRAD produces vertical profiles of the orthogonal horizontal (U and V) and vertical wind by measuring the radial velocity (V_r) of the scatterers as a function of range on three or five antenna beam positions (**Fig. 4.12**). One antenna beam is pointed towards zenith and the other two or four beams are pointed off-zenith (at selected scan angle in 1° - 30° range, in 1° step resolution) with orthogonal azimuths. The beam steering to orthogonal directions is achieved electronically by controlling the phase shifters placed in the individual TRMs, such that the phase gradient between successive modules is equal and corresponds to the desired steering angle.

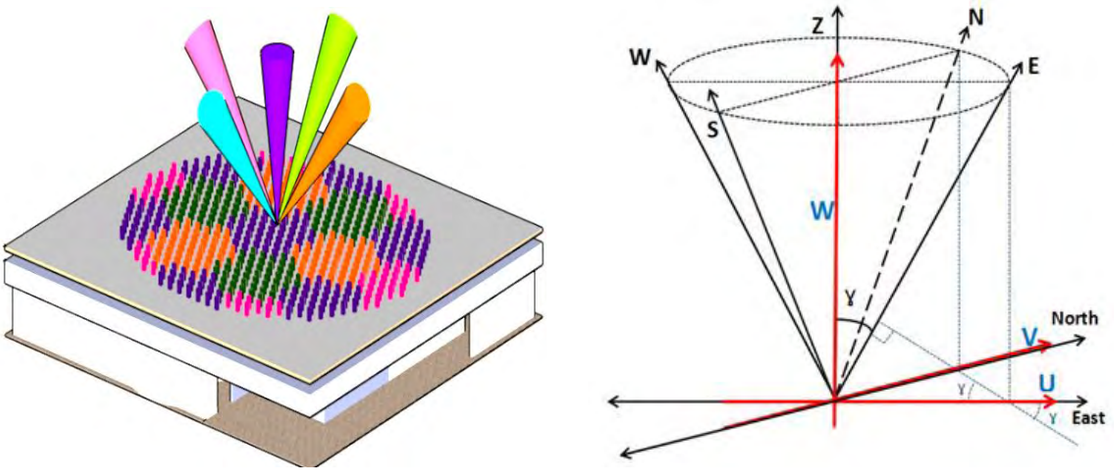

Fig. 4.12. Antenna beam positions in ASTRAD. The beam directions are denoted as Z (zenith), N (north), S (south), E (east), and W (west) beams, and the horizontal and vertical velocities are represented as U (zonal), V (meridional), and W (vertical).

Table 4.7: Technical specifications of ASTRAD system at ARIES, Nainital.

Parameters	**Specifications**
RaDAR system	Active phased array, pulsed Doppler VHF band
Operating frequency	206.5 MHz, 5 MHz bandwidth
Operating modes	Doppler Beam Swinging (DBS), Spaced Antenna Drift (SAD)
Peak Power Aperture product	~ 1×10^8 Wm^2
Height Coverage	~ 0.5 km - 18 km above ground level (AGL)
Height resolution	75 m -300 m (typical)
Horizontal wind velocity	0.1 m/s - 70 m/s
Vertical wind velocity	0.1 m/s - 30 m/s
Time resolution	~ 10 min for full profile
Beam width	~ 3°
Scan angle	upto 360° (azimuth), upto 30° (elevation) in 1° step
Array type	Active, planar phased array
Aperture	Circular, equilateral triangular grid, installed in 30 m × 30 m area on the roof-top
Array element	588 numbers of 3-element Yagi antenna
Inter-element spacing	0.7λ
Array Gain	~ 34 dB (typical)
Transceiver type	Coherent, solid-state Transmit-Receive modules (TRMs)
Number of TRMs	588
Total peak power	~ 235 KW

Recovery time	< 4 µs
Duty ratio	12.8 % max
Pulse repetition frequency	250 Hz – 8000 Hz
Pulse width	0.5 – 64 µs uncoded 2 - 64 µs coded with baud of 0.5 and 1 µsec
Dynamic range	~ 70 dB
Intermediate frequency (IF)	70 MHz
Digital receiver channels	4
No. of coherent integration	upto 1024 (programmable)
No. of spectral averaging	upto 10
No. of FFT points	upto 1024 (programmable)
Data storage format	binary, NetCDF

The received backscattered signals after amplification in the receive chain of the TRMs are combined in power combiners to provide the combined received signal for extraction of Doppler information in the digital receiver, which contains the high speed Field Programmable Gate Arrays (FPGAs), and dedicated embedded processors. Digital receiver, after performing analog to digital conversions, extracts the inPhase (I) and quadPhase (Q) signals at baseband level, which are then decoded, in the case of coded transmission, and coherently integrated in time domain to improve the SNR. When the complex time series (I + *j*Q) is transformed into the frequency domain, its finite length introduces side-lobes in the Doppler spectrum. The spectral leakage from these side-lobes increases the noise level across the spectrum's entire width. To correct this, the data is weighted with a window function (e.g. Hamming, Hanning, Blackman, Kaiser) to smooth the abrupt edges in the time series. The transformation from time to frequency domain is done using standard Fast Fourier Transform (FFT) algorithm in near-real time (*Farley*, 1985). Spectral averaging (incoherent integration) is then performed on the power spectrum to further enhance the SNR. The power spectrum containing signal is obtained after subtracting the noise power density, which is estimated using an objective method (*Hildebrand and Sekhon*, 1974). The three spectral moments (M_o, M_1 and M_2), that represents signal strength, the weighted mean Doppler shift and variance in the Doppler spectrum respectively, are then computed through numerical integration (*Woodman*, 1983). By measuring the Doppler shift in the frequency of the return signal for each range resolution cell, the radial velocity (V_r) of the scatterers, and hence the wind components (U, V, and W) at a given height is estimated and displayed on the real time (RT) display. The Doppler spectra are also stored

in the desktop for offline processing, where necessary processing and quality checking (e.g. clutter removal, smoothing, averaging etc.) is performed in the data, at the stages starting from the raw IQ level to final wind estimation. **Fig. 4.13** shows the basic signal processing flow diagram of ASTRAD, after the received signal enters the digital receiver.

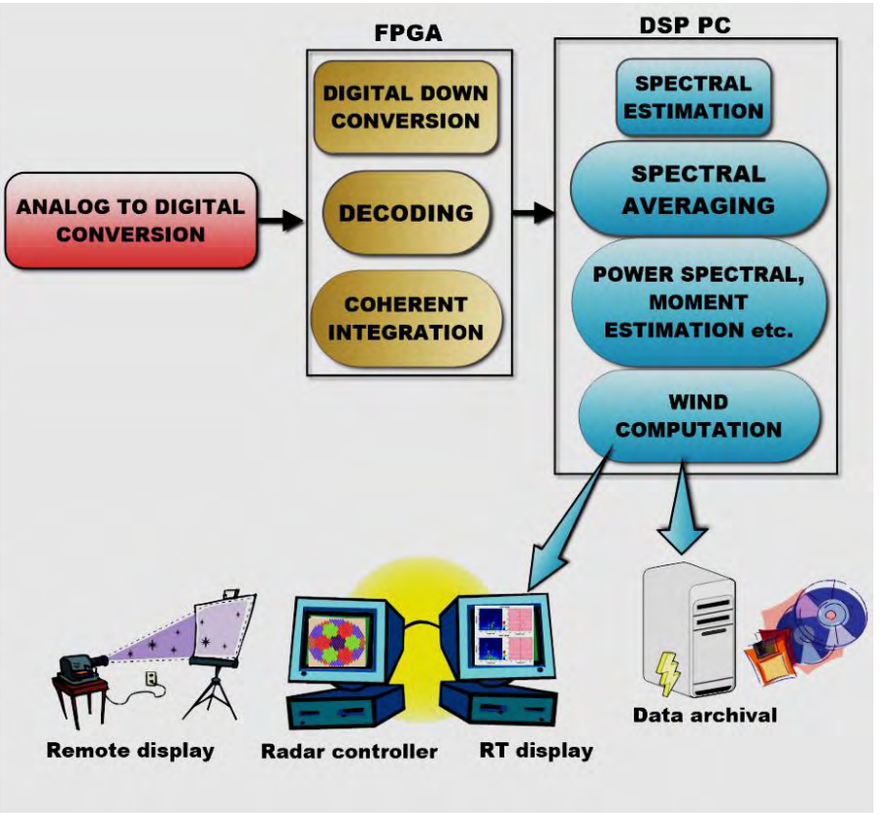

Fig. 4.13. Signal processing steps performed in the ASTRAD digital subsystems.

4.2. Satellite remote sensing products

4.2.1. MODIS

MODIS is a key Earth observing instrument launched aboard NASA's Terra (MOD) and Aqua (MYD) satellites on 18 December 1999 and 4 May 2002 respectively (*Savtchenko et al.*, 2004). Terra's orbit around the Earth is so timed that it passes from north to south across the equator (descending node) in the morning, while Aqua passes south to north over the equator (ascending node) in the afternoon. MODIS satellite passes over the Nainital region twice a day and specifically, Terra crosses between 10:00 – 11:00 hrs LT, while Aqua between 13:00 – 14:00 hrs LT. MODIS Terra and Aqua satellites view the entire Earth's surface in every 1 to 2 days, acquiring data since

March 2000 for Terra, and July 2002 for Aqua in 36 spectral bands between 0.4 and 14.4 μm. The acquired MODIS data are available in the hierarchy of levels (level-1 to 4) and grouped in four broad disciplines – land, atmosphere, ocean and cryosphere. The collections are also defined in MODIS data that represent the versions of MODIS data production algorithm (*Savtchenko et al.,* 2004*; Remer et al.,* 2005). In the present work, level-2 MODIS aerosol collections (C5.1 and C6.0) and active fire location product (C6.0) available under atmosphere and land disciplines respectively are used.

The latest level-2 MODIS aerosol product collections C5.1 and C6.0 over land and ocean are based on two algorithms, namely the Deep Blue (DB) and Dark Target (DT) (*Remer et al.,* 2005*; Levy et al.,* 2013*; Bilal et al.,* 2016). DT has separate algorithms for land and ocean, whereas DB is for the land retrieval only. Both C5.1 and C6.0 contains the standard 10 km spatial resolution MODIS Terra (MOD04_L2) and Aqua (MYD04_L2) retrievals. To cater the need of resolving the local aerosol gradients and regional features in a much precise manner, the MODIS C6.0 production includes the DT aerosol product with 3 km spatial resolution under both Terra (MOD04_3K) and Aqua (MYD04_3K) platforms. Recent studies revealed that the MODIS 3 km land product is less reliable and requires continued evaluation in contrast to the standard 10 km product (*Remer et al.,* 2005*; Levy et al.,* 2013*; Remer et al.,* 2013*; Nichol and Bilal,* 2016*; He et al.,* 2017). Studies were carried out on the validation of MODIS 10 km aerosol retrievals over land with the ground based measurements, and over ocean with the shipborne measurements (*Remer et al,* 2002*; Remer et al.,* 2005*; Wang et al.,* 2011*; Sayer et al.,* 2013). Majority of the cited studies have found reliable and good agreements of the 10 km retrievals with ground based measurements. Therefore, here 10 km MODIS level-2 latest C6.0 (DT and DB) and C5.1 (DT) with quality flag 3 were chosen for assessment and comparison with the ground truth over Nainital region.

For one of the case studies presented, the MODIS C6.0 standard active fire location product MCD14ML is extracted from NASA Fire Information for Resource Management System (FIRMS) database which is produced using the most up-to-date algorithms in the form of monthly files containing the geographic location, date, brightness temperature, updated Fire Radiative Power (FRP), fire type and the confidence levels for each fire pixel detected by the Terra and Aqua MODIS sensors. The confidence estimate is expressed in percentage and is classified as 0% - 29 % for low, 30% - 79% for nominal, and 80% - 100% for high fire-events (*Giglio et al.,* 2003*; Giglio,* 2005).

4.2.2. CALIPSO

CALIPSO was launched in April 2006 under a joint mission of NASA and the French space agency, Centre National d'Etudes Spatiales (CNES). It is equipped with a dual wavelength (550 and 1064 nm) polarization LiDAR system referred as CALIOP for providing the long term database of global aerosol vertical profiles (*Winker et al.,* 2009, 2010). The CALIOP LASER transmitter is a diode-pumped Nd:YAG LASER that emits simultaneous co-aligned pulses at 532 and 1064 nm. The LASER generates optical pulses of ~20 ns long with 110 mJ of energy at both the wavelengths. The receiver sub-systems measures the backscattered signal intensity at 1064 nm and the two backscattered orthogonal polarization components at 532 nm (*Winker et al.,* 2009, 2010*; Hunt et al.,* 2009).

At present, the researchers worldwide, are utilizing the CALIPSO products to a great extent in order to understand the impact of aerosol and cloud on the Earth's radiation budget. The CALIPSO/CALIOP (*ver. 3 and 4.10*) aerosol products used in this thesis are:

- *Level-1B* product:
  temporal resolution: 0.05 sec, vertical and spatial resolution: 30 m (0 - 8.2 km) and 333 m
- *Level-2* products:
  - Aerosol profile (temporal resolution: 5.92 sec, vertical and spatial resolution: 60 m × 5 km)
  - Aerosol layer (temporal resolution: 0.74 sec, spatial resolution: 5 km)
  - Vertical Feature Mask (VFM) product (temporal resolution: 0.74 sec, vertical and spatial resolution: 30 m (up to 8.2 km) and 333 m)

4.2.3. DARDAR

NASA A-train satellite mission (e.g. CloudSat, CALIPSO, and MODIS) provides a simultaneous multi-sensor view of clouds and radiation (*L'Ecuyer and Jiang.,* 2010). In the present study, the potential of its two most popular and widely used satellites – CALIPSO (*Winker et al.,* 2009, 2010) and CloudSat (*Stephens et al.,* 2002) is explored. The CALIPSO operates at 532 nm and 1064 nm, while the W-band nadir-pointing RaDAR onboard CloudSat operates at 94 GHz (about 3.2 mm wavelength). The CloudSat RaDAR is more sensitive to thick clouds, and in contrast, the CALIPSO LiDAR signals can probe the thin clouds but gets attenuated by thick cloud layers (*Winker et al.,* 2009, 2010*; Stephens et al.,* 2002).

The combination of CloudSat RaDAR and CALIPSO LiDAR, so called raDAR/liDAR (DARDAR) is a state-of-the-art multi-sensor extraction that not only provides vertical cloud information but also offers the view on both thick and thin clouds as well (*Delanoë and Hogan,* 2008, 2010*; Ceccaldi et al.,* 2013; *Kumar et al*., 2019). It was developed by Drs. Julien Delanoë and Robin Hogan at Department of Meteorology in the University of Reading (*Delanoë and Hogan, 2008, 2010*). The product is derived using the variational (or varcloud) method (*Delanoë and Hogan,* 2008), applied on the combination of the CloudSat raDAR reflectivity (dBZ_e) and CALIPSO parallel and perpendicular attenuated backscatter (β) and retrieves the profiles of visible extinction (σ), ice-water content (*IWC*) and effective radius (r_e) (*Delanoë and Hogan, 2008,* 2010).

In addition to the characterization of cloud types, the combination of LiDAR (CALIPSO) backscatter and RaDAR (CloudSat) reflectivity in DARDAR also forms the basis for distinguishing different forms of precipitation. The backscattered signal in LiDAR gets intensified due to large cross-sectional area of the precipitation particles, mainly liquid droplets. In contrast, the CloudSat is highly sensitive to the precipitation-size particles with signal detectability range and accuracy as -30 to + 40 dBZ and about 1 dBZ, respectively (*Tanelli et al*., 2008), and hence the precipitation related information is mainly inferred using CloudSat. The information on light to moderate rain and snow, together with the drizzle are captured with high degree of accuracy through CloudSat (*Stephens et al*., 2002; *Sassen and Wang*, 2008), however, the estimates from CloudSat impedes during heavy rainfall that causes strong attenuation in the backscattered raDAR echoes (*Sassen and Wang*, 2008). The DARDAR version 2.0 (most recent version) products (**Table 4.8**) available at Interactions Clouds Aerosols Radiations Etc (ICARE) Thematic Centre are used as the primary data for clouds and precipitation studies in this work.

Table 4.8: DARDAR by-product details.

Products	**version**	**Description**	**Resolution**	
			Horizontal	**Vertical**
CSTrack (CloudSat Track) • CAL-LID-L1 • CAL-LID-L2-VFM • CLOUDSAT-2B-CLDCLASS • CLOUDSAT-2B-GEOPROF	ver.0.2.3	Multi-sensor extractions co-located with the CloudSat footprints	~1.1 km	60 m (-1.92 km to 40.02 km)

DARDAR_MASK	ver.2.0	CALIPSO/CloudSat combined vertical categorization mask	~1.1 km	60 m (-1.02 km to 25.08 km)
DARDAR_CLOUD	ver.2.0	Cloud variables retrieved from CALIPSO/ CloudSat	1.4 km	60 m (-1.02 km to 25.08 km)

4.2.4. TRMM

TRMM, often referred as 'flying rain gauge' is a space mission for monitoring and studying the three-dimensional tropical and sub-tropical rainfall and the associated energy (latent heat) budget. It was launched from the Tanegashima Space Center, Japan in November, 1997, jointly by the NASA and the Japan Aerospace Exploration Agency (JAXA) (*Kummerow et al.,* 1998, 2000; *Adler et al.,* 2000). The satellite carries the complementary suite of active and passive instruments like Precipitation RaDAR (PR), TRMM Microwave Imager (TMI), Visible and Infrared Scanner (VIRS), Clouds and the Earth's Radiant Energy System (CERES), and the Lightning Imaging Sensor (LIS). These instruments either function individually or in combination with one another (*Huffman et al.,* 2007). The PR, operating at 13.8 GHz, is the key TRMM instrument and the first rain RaDAR in space that measures three dimensional rainfall distribution over the land and ocean. This Ku-band PR, with its minimum detectable signal level of about 17 dBZ, and with the uncertainties of about 1.5 dBZ (below 0°C isotherm) and about 2 dBZ (above 0°C isotherm), is capable of estimating moderate to heavy precipitation, however its high wavelength (~ 22 mm) limits its capability to detect the light rain (< 0.7 mm/hr), solid precipitation and drizzle entirely (*Kummerow et al.,* 1998).

The TRMM PR Multi-satellite Precipitation Analysis (TMPA) is designed to combine precipitation estimates from various satellite systems and land surface precipitation from rain gauges. This primary merged microwave infrared product is computed at a 3-hourly temporal and 0.25° x 0.25° spatial resolution (*Huffman et al.,* 2007). The TMPA is computed as two products - an experimental real-time monitoring product that is produced nine hours after collection (TMPA_RT), and a post-real-time research-quality product (TMPA_3B42) that becomes available about ten to fifteen days after the end of every month (*Huffman et al.,* 2007). In this work, ver. 7 of the research-quality product i.e. TRMM/TMPA_3B42 is used for rainfall estimation. In addition, the monthly TRMM product – TRMM/TMPA_3B43 ver. 7 is also used. This product is created using TRMM-adjusted merged microwave-infrared precipitation rate (in mm/hr) and Root-Mean-Square (RMS)

precipitation-error estimates. The key specifications of the selected product are - spatial coverage:(-50°N to 50°S; -180°E to 180°W), temporal coverage: 01 January 1998 to present, with spatial and temporal resolution is 0.25° x 0.25°, and 1 month, respectively.

4.2.5. AIRS

The Atmospheric Infrared Sounder (AIRS) onboard NASA's Aqua satellite provides the estimates of atmospheric temperature and water vapor at a spatial resolution of 1° × 1° (*Parkinson*, 2003). AIRS ver. 6 is the most current retrieval algorithm since the launch of AIRS instrument (*Olsen et al*., 2013), and its monthly standard physical retrieval (AIRX3STD, level-3), available at Goddard Earth Sciences Data and Information Services Center (GES DISC), is used in this work for comparison of its temperature data with the re-analysis models.

4.2.6. Multi-sensors

The Absorbing Aerosol Index (AAI) near the ultra-violet range over the Himalayan region is retrieved from Tropospheric Emission Monitoring Internet Service (TEMIS) which is the part of Data User Programme (DUP) of the European Space Agency (ESA). From TEMIS, the Multi-Sensor Absorbing Aerosol Index (MS-AAI) data record (ver. 1.7) with 1° x 1° resolution from the measurements using Total Ozone Mapping Spectrometer (TOMS), Global Ozone Monitoring Experiment (GOME)-1, Scanning Imaging Absorption Spectrometer for Atmospheric CHartographY (SCIAMACHY), OMI, GOME-2A and GOME-2B instruments for the period January 1980 to December 2017 is considered in this study (*Tilstra et al*., 2011, 2013). It is to be noted that there exists a two-year gap in the data from June 1993 to May 1995. OMI flies on the NASA's EOS Aura platform since 15 July 2004, and its level-3 monthly data (ver. 1.7) with 1° x 1° resolution is also used for the period 2005-2017 in the study.

4.3 Ancillary products

4.3.1. Re-analysis products

The records on the atmospheric variables are usually generated by accumulating the regular measurements made in different temporal and spatial scales and hence introduces the inhomogeneity that limits their usefulness in studying the long-term variations in climate. To overcome this, re-analysis products have been established. The re-analysis products are produced

from the available atmospheric observations and dynamic models, and uses modern data-assimilation systems to reprocess the observations taken over the past several decades. There are number of re-analysis products available on the global scale such as National Centers for Atmospheric Prediction - National Center for Atmospheric Research (NCEP-NCAR) re-analysis (NNR), ERA-40, ERA-Interim, Modern-Era Retrospective analysis for Research and Applications (MERRA) etc. (*Decker et al.,* 2012). These re-analysis data sets have now became an important source of information for conducting studies on climate variations (*Dee et al.,* 2011, 2014) and for assessing the climate models (*Gleckler et al*., 2008; *Zhao et al*., 2013; *Bender et al*., 2018).

In the present study, following re-analysis products are used to describe the general synoptic conditions, and the horizontal/vertical and temporal distribution of the prevailing meteorological conditions over the study area:

(1) **MERRA-2**: It is one of the latest re-analysis product released by NASA Global Modeling and Assimilation Office (GMAO), and is based on the EOS satellite observations (*Bosilovich et al.*, 2016). Its most updated version i.e. ver. 5.12.4 is used in this work. For surface temperature its M2TMNXSLV and M2TMNXLND data products, and for ascertaining the sources of dust, the most recent version of aerosol diagnostic data (M2T1NXAER) are used. Further, MERRA-2 data products are also used for understanding the carbon monoxide emission, snow depth over glaciated surface, and snowfall over the Himalayan region.

(2) **ERA-Interim**: The 6-hourly ERA-Interim product is produced from the available atmospheric observations and dynamic models (*Dee et al.,* 2011, 2014). ERA-Interim parameters used in this study are the stored products, except the U and V components of wind that are computed from the stored vorticity and divergence fields that are scaled by cosine of the latitude i.e. U*cos*(*lat*) and V*cos*(*lat*).

(3) **GLDAS**: The surface temperature and albedo data with 0.25° X 0.25° spatial resolution, obtained from Global Land Data Assimilation System (GLDAS) ver. 2.1 Noah land surface model L4 (*Rodell et al*., 2004; *Beaudoing and Rodell*, 2016) are utilized for product inter-comparison, and in the context of demonstrating changes in glaciers and snow depth over the Himalayan region.

4.3.2. Air mass trajectory model

To trace the sources of air masses over the study region, the backward trajectory analysis is done using NOAA Hybrid Single Particle Lagrangian Integrated Trajectory (HYSPLIT) model (*Draxler and Hess,* 1997, 1998). The model utilizes several meteorological parameters like rainfall, humidity, temperature and solar radiation flux for computing the air mass trajectories at different height levels. The trajectory analysis basically characterizes the air masses and their origin or source of production, in order to understand the impact on meteorological conditions and the aerosol transport (*Draxler and Hess,* 1997, 1998*; Stein et al.,* 2015).

4.3.3. Digital elevation data

The Global 30 Arc-Second Elevation (GTOPO30) data set is used for preparing the elevation profiles in this thesis. The horizontal grid spacing in GTOPO30 dataset is 30 arc seconds (~ 1 km) and is derived from multiple sources of topographic information, compiled at the United States Geological Survey (USGS)/ Earth Resources Observation and Science (EROS) Data Center (EDC) and made available from the Land Processes Distributed Active Archive Center (LP DAAC).

4.4 Methodologies

4.4.1. Assessment of aerosol retrievals from MODIS and CALIPSO satellites

4.4.1.1. Data selection

Out of the data sets collected from the ground based LiDAR and AERONET measurements over ARIES, Nainital, during the period 2008- 2012, common days of reliable measurements with best temporal match were selected. Based on the LiDAR profiles, the selected data were further screened for clear sky conditions. In this process the usable data sets turned out to be 37, and considered for the analysis.

In order to match with the identified 37 days, the selection of MODIS data sets is done on the basis of closest overpass to the site and the availability of AERONET data during the overpass. The details on the number of spatially and temporally coincident data sets (*N*) so obtained is given in **Table 5.2** of the next chapter in this thesis. To achieve a valid comparison between AOD values measured from MODIS and AERONET instruments, a well-known spatio-temporal averaging technique is adopted (*Ichoku et al.,* 2002) and multiple metrics were utilized to quantify the results. Taking into account the mean MODIS AOD values within 20 km × 20 km and 30 km × 30 km grid

and AERONET AOD averaged over ±30 minutes and ±15 minutes, various cases on spatio-temporal combinations were examined and the levels of agreement were established.

MODIS being the passive remote sensor provides a single columnar value of aerosol parameter, which lacks the information of aerosol vertical distribution, a rather important parameter to quantify aerosol effects in the atmosphere. In this context, the CALIPSO satellite products were also evaluated and used in the BL height estimation and for the case studies on the evolution and transport of aerosols. In order to understand the associated changes (vertical features and aerosol sub-types) in the two versions (ver. 3 and 4.10) of CALIPSO data over the complex Himalayan terrain, level-2 VFM profiles available within the grid of ± 0.5° ranging from 28.86° - 29.86° N and 78.96° - 79.96° E for the period August 2006- April 2017 were analysed. The results in the form of confusion matrix are presented and discussed in relevance to the changes in the feature types and aerosol sub-types between ver. 3 and ver. 4.10 data. Further, to evaluate the AOD values from two versions of CALIPSO with AERONET, a total of 23 data sets were identified based on the criteria of high Cloud Aerosol Discrimination (CAD) score (between -35 and -100), the presence of 5 or more valid vertical profiles up to 4.5 km altitudes within the horizontal distance of ~ 100 km from the site, and the availability of coincident AERONET measurements within ± 30 minutes of the closest CALIPSO ground track.

For the period October 2006 – December 2014, 54 good cases of AOD measurements both from the MODIS Terra DB C6.0 and CALIPSO (within 100 km) were identified, and the same were utilized in the products inter-comparison. The selection procedure is based on the screening and coincidence constraints, and the sequence is as follows:

- To account for the best temporal match between the CALIPSO and MODIS satellite overpasses, only the day-time CALIPSO profiles were considered where the time difference between two observations is within 3 hours.
- For MODIS, the averaged AOD values (550 nm) with quality flag 3, measured within 30 km × 30 km from the site were considered.
- For CALIPSO, the average of the column AOD values (532 nm) reported in CALIPSO level-2 aerosol layer product is used. The selection criteria set for the AOD is: CAD score (between -35 to -100), Extinction QC 532 flag (0 or 1), column optical depth uncertainty (between 0 and 0.5 ×

AOD), CALIOP initial LR = final LR, surface elevation > 1200 m, and the horizontal averaging ≤ 80 km (*Young and Vaughan,* 2009*; Vaughan et al.,* 2016).

4.4.1.2. Retrieval error and wavelength conversions

The EEs associated with AERONET measured AOD (τ) and the corresponding MODIS retrievals are $EE_{AERONET}$ = ± 0.01 to ±0.02 and EE_{MODIS} = ± (0.05+0.15τ), respectively (*Holben et al.,* 1998*; Eck et al.,* 1999*; Remer et al.,* 2005; *Levy et al*., 2013). Similarly, the EE associated with CALIPSO measurement is $EE_{CALIPSO}$ = ± (0.05+0.4τ) (*Winker et al.,* 2009). The uncertainties in the AODs measured with AERONET are wavelength (λ) dependent and consititutes ± 0.01 for λ > 440nm and ± 0.02 for shorter wavelengths (*Holben et al.,* 1998, 2001).

MODIS and AERONET measure AOD at two different wavelengths 550 and 500 nm respectively, and to make a valid comparison between the two, AOD at 500 nm is converted to AOD at 550 nm by taking into account the AE provided by AERONET in the wavelength range of 440 - 870 nm, using the relation as follows (*Eck et al.,* 1999):

$$\tau_{required} = \tau_{measured} \times \left[\frac{\lambda_{required}}{\lambda_{measured}} \right]^{-AE} \tag{4.12}$$

where, $AE = -\dfrac{\log\left[\dfrac{\tau_{\lambda_1}}{\tau_{\lambda_2}}\right]}{\log\left[\dfrac{\lambda_1}{\lambda_2}\right]}$, τ_{λ_1} and τ_{λ_2} are the AOD values at wavelengths λ_1 and λ_2.

Similar analogy is used to make the comparison of CALIPSO (532 nm) with AERONET. In all the wavelength conversions, it is assumed that the errors introduced were negligible.

4.4.1.3. Performance parameters used in product assessments

To evaluate the performance of different products, the following statistical parameters were computed on *N* coincident data sets:

(i) Mean Bias Error (MBE) = $\dfrac{\sum(\tau_{Satellite} - \tau_{AERONET})}{N}$, is the measure of overall bias error and the values > 0 indicate overestimation, whereas the values < 0 represent underestimation of the satellite retrievals with the ground truth.

(ii) Average Error Ratio (AER) = $\frac{\sum(\tau_{MODIS} - \tau_{AERONET})}{N} \times \frac{1}{EE}$, is the measure of the comparison between the actual error and the Expected Error (EE) limits. |AER| ≤ 1 is the good match, and |AER| > 1 represents the poor match. In case of satellite data, AER< 0 represents underestimation of the measurement, and AER > 0 reveals overestimation.

(iii) Root Mean Square Error (RootMSE) – It is the root mean square of the error in the regression, computed as the square root of the reduced Chi-square i.e. $\sqrt{Reduced\ \chi^2}$. It provides the variability/standard deviations of the data from the regression line. Lower the value of RootMSE, better will be the agreement between the regression and the data.

(iv) Percentage Mean Relative Deviation (MRD) = $\frac{100}{N}\sum_{i=1}^{N}\frac{\left|M_{version2} - M_{version1}\right|}{M_{version2}}$, is the measure of mean divergence of the data version 2 ($M_{version2}$) from the version 1 ($M_{version1}$).

(v) Percentage EE (%EE) = Percentage of values falling within EE limits. If out of N values, M values falls within the EE limits, then $\%EE = \frac{M}{N} \times 100$.

(vi) Standard Deviation (SD) – It is a measure of how spread out a data is, and is equal to the square root of the variance. Mathematically, for N samples (X_1, X_2, ... X_N), $SD = \sqrt{\frac{\sum_{i=1}^{N}(X_i - \bar{X})^2}{N-1}}$, where, $\bar{X}$ is the mean value of N samples.

(vii) Standard Error of Mean (SEM) = $\frac{SD}{\sqrt{N}}$, and is the measure of the variability associated with estimating a mean.

(viii) Correlation: It a statistical technique that shows how strongly the pair of variables are related to each other. There are several different correlation techniques but the Pearson's or product-moment correlation is most common. For two measurements X and Y the correlation coefficient is given by the covariance of X and Y divided by the product of their standard deviation. Its value lies between -1 to +1.

4.4.2. Utilization of the aerosol retrievals: estimation of LR and BL height

4.4.2.1. LR estimations

The LR for any single wavelength ground-based LiDAR is a key parameter that needs to be known for the retrieval of aerosol vertical profiles. Basically, it is the ratio of aerosol extinction coefficient (α_{aer}) and the aerosol backscatter coefficient (β_{aer}) that is linked to the regional aerosol characteristics like shape, size and composition. A-priori hypotheses for LR in the range between 20 to 100 sr is quite common, but LR computed by constraining the AOD from LiDAR through AERONET or MODIS measurements can be the better choice than former (*He et al.,* 2006; *Leon et al.,* 2009). In the later approach, initially the LiDAR Range-Corrected Signal (RCS) is processed for AOD computation with a fixed LR, which then undergoes several iterations to produce an adjusted LR at a point where the difference between LiDAR derived AOD (τ_{LiDAR}) and the AOD retrieved from AERONET ($\tau_{AERONET}$) or MODIS (τ_{MODIS}) measurements is minimal. Similar approach is adopted here to find out the best LR values for the three LiDAR systems operated in night-time under clear-sky conditions during different seasons. Along with the intermittent observations made using the LiDAR systems, the collocated AERONET measurements from ARIES site for the period of 2008- 2012 is used in this case. The AERONET observation were made in two phases – each during April 2008 - February 2011 (Nainital station) and August 2011 - March 2012 (ARM_Nainital station). AERONET provides the high quality data on a wider scale across the globe, so the methodologies adopted here, can be utilized by larger science community.

To estimate LR, at first the RCS obtained from LiDAR measurement is processed for obtaining the aerosol extinction profile with a fixed LR and system constants. The obtained extinction profile is then subjected for integration to obtain AOD value from LiDAR data. Then by using an iterative method, the initial LR value is changed in steps of 0.01 sr for minimizing the difference between τ_{LiDAR} and $\tau_{AERONET}$ (or τ_{MODIS}). The adjusted range-independent LR values, where the τ_{LiDAR} showed the best match within the tolerance of ±0.5 %, are considered to be the final LR. To account for any discrepancies between day and night-time AOD measurements from AERONET and the ground based LiDAR, about 95% of the data sets were so chosen that the diurnal variations in AOD and AE (440-870 nm) fall in the limits of ± 0.05 and ± 0.2, respectively (*Amiridis et al.,* 2011). Such a bound is employed to ensure that the intrusion of aerosol from other locations is almost insignificant and the aerosol loading remains nearly the same during day and night over the site.

The LiDAR AOD in LR retrieval process has been computed using the relation:

$$\tau_{LiDAR,532} = \int_{z_0}^{z_1} \alpha_{aer}(z)dz + \int_{z_1}^{z_2} \alpha_{aer}(z)dz \quad (4.13)$$

where, z_0 = height at which the LiDAR system is installed, z_1 = height at which complete overlap occurs (150 m, 300 m and 90 m considered for the three LiDAR systems at ARIES, respectively), and z_2 = upper height limit considered for the columnar AOD retrievals (assumed as 4.5 km above ground level). Considering the uniform distribution of aerosols between z_0 to z_1, it is assumed that for the three LiDAR systems, the maximum of 7.5 %, 15 % and 5 % of the AOD values, respectively are confined within the respective overlap regions.

4.4.2.2. BL height estimation

The BL height is an important meteorological parameter that determines the extent to which the dispersion of pollutants, heat and moisture take place, and is very useful parameter for weather, climate and pollution studies (*Monks et al.,* 2009). It is one of the fundamental parameter in numerical simulations of regional meteorology and air quality. In this context, an accurate determination of BL height, using different data sources over the complex high altitude site, where the upslope and downslope airflows vary with time, is of great interest.

From ARIES, Nainital, the radiosonde launches were conducted four times a day during 2011-2012 (*Singh et al.,* 2016), so taking this an advantage, and considering the fact that BL depth can be derived from the radiosonde (*Seibert et al.,* 2000*; Singh et al.,* 2016) and CALIPSO data (*Jordan et al.,* 2010*; McGrath Spangler and Denning,* 2012), an attempt is made to estimate and compare the BL height computed from the in-situ radiosonde observations and near coterminous CALIPSO level-1B data (< 100 km overpass distance; ver. 4.10). To ascertain cloud-free cases, the parameters (signal intensity at the surface, depolarization ratio, color ratio and vertical features) from CALIPSO level-1B and 2 data products are examined for the period June 2011 - March 2012. After discarding the cloud contaminated profiles, a total of 10 day-time cloud-free CALIPSO profiles, in the temporal match (< 2 hours) with the radiosonde observations were identified and selected for BL height estimation. The day-time cases were selected to avoid the influence of the residual layer and heavy surface inversion (*Su et al.,* 2017).

To estimate the BL heights from radiosonde, the vertical gradient method is used for the Potential Temperature (PT) and Specific Humidity (SH), that is expressed as:

$$\frac{dX(y_i)}{dy} = \frac{X(y_{i+1}) - X(y_i)}{y_{i+1} - y_i} \tag{4.14}$$

Here, $X(y_k)$ is used to represent the PT or SH values at altitude y_k, where k represents the height intervals i up to 3.2 km amsl in vertical, that is selected on the basis of the characteristics studied over Nainital (*Singh et al.,* 2016). The BL height is identified as the location of the maximum vertical gradient for PT and SH changes (*Seibert et al.,* 2000*; Seidel et al.,* 2010).

To retrieve the BL height from CALIPSO, two methods, namely the threshold (*Melfi et al.,* 1985*; Jordan et al.,* 2010) and Wavelet Covariance Transform (WCT) (*Brooks,* 2003*; Compton et al.,* 2013) are used. With the threshold method, the BL height is determined by finding the steepest gradient in total aerosol backscatter coefficient profiles (CALIPSO level-1B). In WCT method, the Haar wavelet and the Mexican hat wavelet functions (*Brooks*, 2003) are frequently used for BL height estimation from the atmospheric LiDAR profiles. Possibly other available wavelet functions produces large discrepancies in BL estimate. The Haar wavelet function has been selected in the present work because it distinguishes even a small-scale transitions efficiently as compared to the Mexican hat wavelet function.

Computing WCT using Haar function is equivalent to a joint low-pass filtering and differentiation process. For BL height computation, the Haar function is applied to the total aerosol backscatter coefficient profile, and its first maxima where the sharpest decrease in the total aerosol backscatter coefficient occurs is taken up as the BL height (*Baars et al*., 2008). The implementation of WCT method is described using two equations (*Gamage and Hagelberg,* 1993*; Brooks*, 2003):

$$W_f(a,b) = \frac{1}{a}\int_{z_b}^{z_t} \beta'_{total,532}(z)\psi\left(\frac{z-b}{a}\right)dz \tag{4.15}$$

$$\text{and, } \psi\left(\frac{z-b}{a}\right)=\begin{cases}+1; & \left(b-\frac{a}{2}\right)\le z<b\\ -1; & b\le z\le\left(b+\frac{a}{2}\right)\\ 0; & \text{elsewhere}\end{cases} \tag{4.16}$$

where, a = dilation parameter (spatial extent); b = vertical translation i.e. altitude at which the wavelet function is centered; $\beta'_{total,532}(z)=$ CALIPSO level-1B total aerosol backscatter coefficients as the function of altitude; $W_f(a,b)=$ wavelet covariance transform as a function of dilation and translation; $\psi\left(\frac{z-b}{a}\right)$ is the Haar wavelet function, described as a symmetrical square wave with positive and negative going amplitudes; z_t and z_b are the top and bottom altitudes of $\beta'_{total,532}(z)$. The dilation 'a' and translation 'b' adjusts the location and shape of the wavelet function. The value for 'a' is $n\Delta z$, where n = 2, 4, 6,…. and Δz is the vertical resolution of the backscatter profile.

For retrieval of BL height with high degree of accuracy using the WCT method, it is essential that the dilation, 'a' should be chosen carefully, and must be sufficient enough to distinguish the transitions from small-scale variations in $\beta'_{total,532}(z)$ (*Brooks*, 2003), and the translation 'b' is to chosen in between two discrete points to ensure the symmetry in **equation 4.15**. At small dilation, due to the spurious gradients and noisy $W_f(a,b)$ profile, it becomes very difficult to estimate the correct BL height, and at extremely high dilation value, the BL height becomes too high or sometime may even get missed. Therefore, the BL height estimated from the mean profile of wavelet covariance transform, $<W_f(a,b)>$, generated across the mid-range of dilation values, is considered as the optimum BL height in the present work, which is expressed as:

$$<W_f(b)>=\frac{1}{n}\sum_{i=1}^{n}W_f(a_i,b) \tag{4.17}$$

The final BL height is *max* $<W_f(b)>$, for $z_b < b < z_t$. This approach of selecting and averaging multiple wavelet dilation values will reduce the bias in the final BL height estimation. An example demonstrating the sensitivity analysis and the selection of appropriate dilation range for a typical CALIPSO level-1B (ver. 4.10) total aerosol backscatter coefficients profile of 16 June 2011 is shown in **Fig. 4.14(a-d)**. As evident in the shown figure, the profile of $W_f(a,b)$ becomes smoother with the increase in dilation *a*.

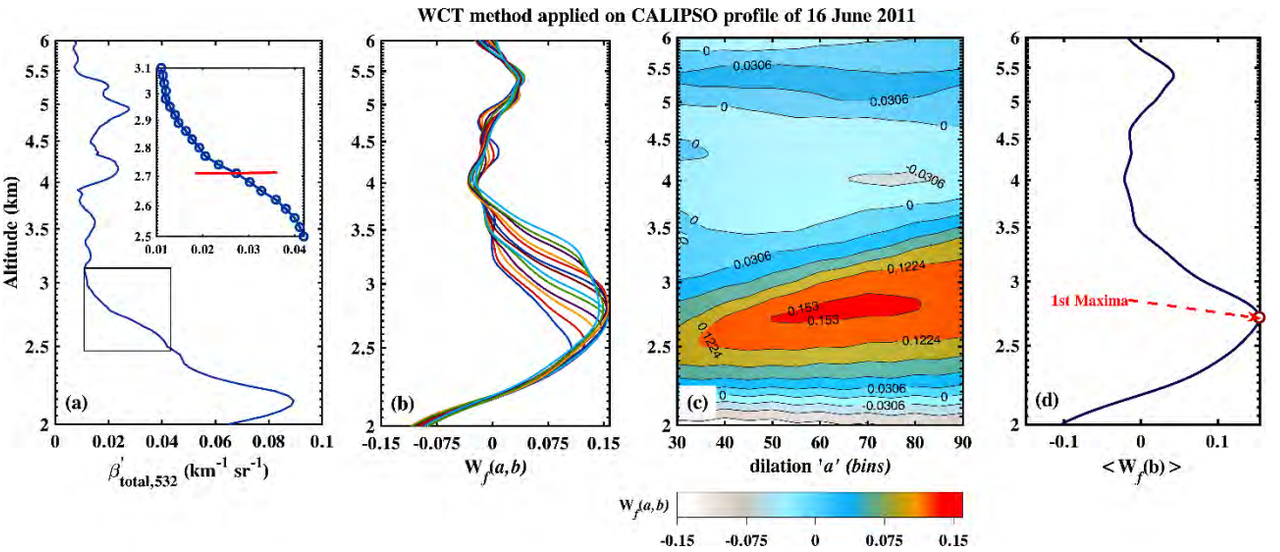

Fig. 4.14. (a) CALIPSO level 1B total aerosol backscatter coefficient (an average of the profiles lying within 100 km coincidence circle of the closest CALIPSO overpass) of 16 June 2011 (~13:15 hours LT); **(b)** and **(c)** are its wavelet covariance transform, $W_f(a,b)$ over the range of dilation '*a*' from 0.9 to 2.7 km in 30 m steps (bins 30 to 90); **(d)** Mean profile of the wavelet covariance transform, represented as $< W_f(b) >$, generated across the range of 50 to 80 bins. The location showing the first maxima from the surface upward is the final estimated BL height.

4.4.3. Absorbing aerosols

The absorbing aerosols like dust, smoke, black carbon and volcanic ash can modulate the cloud properties, photochemical processes, and atmospheric stability (*Koren et al*., 2008; *Mishra et al*., 2014; *Lee and Wang*, 2015). In the present era, numerous datasets collected through satellites, ground stations and computational models exist that describes the state of the past and present Earth's atmosphere, and serves as the basis to model projections. However, these massive resources are under-utilized in the climatological investigation of the aerosols, especially over the complex mountainous regions, where they get trapped and accumulated in the foothills or surrounding

spaces. One such mountainous region posing serious concerns from climate perspective is the 'third pole' on Earth i.e. the Himalayas (*Immerzeel et al*., 2013; *Pant et al*., 2018), where the local winds, complex terrains and orography have strong interactions with the air masses. The undue interventions from these pollutants modify the rate of atmospheric heating and modulates the properties and lifetime of neighbouring clouds and atmospheric stability (*Penner et al*., 2003; *Koren et al*., 2008; *Torres et al*., 2013; *Lee and Wang*, 2015). These modifications are possibly affecting the hydrological cycle indirectly by eventually melting the 'steady water tower' of glaciers and snow packs of this region (*Messerli et al*., 2004; *Viviroli et al*., 2007, 2011). To some extent, they are also responsible for increase in the extreme weather and climate events (drought, flood, cloud bursts, etc.) leaving, colossal losses and trauma.

Himalayan environment is characterized by large variability, which complicates efforts to use short data records for the study therefore, the long term climatological study from multiple satellites data sources is very essential. Considering the same, this work pursues the study on the seasonal and monthly climatology on the absorbing aerosols over the Himalayan region with an emphasis on the major pollutant – dust, by making use of the updated and long-term data obtained from multiple sensor measurements of Aerosol Index (AI). The AI is the key parameter used to distinguish between absorbing and non-absorbing aerosols. The AI is positive for absorbing and negative for non-absorbing aerosols like sulphate (H_2SO_4) or nitrate (HNO_3) aerosols. The AI values, almost equal to zero are mainly due to cloud presence (*Mironova et al*., 2008).

4.4.4. Precipitation and clouds distribution over NSI region

Due to varied and complex topography of the NSI region, covering the major part of IGP as well as the Himalayas, it possess the large variability in the meteorological parameters particularly the rainfall pattern. Rainfall is the predominant form of precipitation which is responsible for spatial and temporal distribution of runoffs, soil moisture and groundwater reserves, and its intensity affects the frequency of droughts and floods. Hence, it is important to study the rainfall pattern over this region, for which, the latest ver. 7 (released in late 2012) of the TRMM Multi-satellite Precipitation Analysis (TMPA) 3B42 data product (with resolution 0.25° X 0.25°) is analyzed for the period of almost two decades (1998-2016). Although none of the satellite based rainfall data is free from bias, however, this product has reported relatively low bias (*Tan et al.,* 2015), hence, used in the present study.

Rainfall over the NSI region is mainly controlled by two major atmospheric circulations – southwest monsoon (June – September), and the western disturbances during December - March. These two contrasting periods - (i) June-July-August-September (JJAS), and (ii) December-January-February-March (DJFM) encompassing the southwest monsoon and active periods of western disturbances, respectively over the NSI region, are hence taken up for seasonal study on precipitation and clouds.

The DARDAR CSTrack CLOUDSAT-2B-CLDCLASS v.0.2.3 product contains CloudSat level 2 based classification of eight different cloud types - cirrus (*Ci*), altostratus (*As*), altocumulus (*Ac*), stratus (*St*), stratocumulus (*Sc*), cumulus (*Cu*), nimbostratus (*Ns*), and deep convective (*DC*) (i.e., cumulonimbus) (*Wang and Sassen*, 2001). In addition, the product also provides the classification on precipitation types – liquid precipitation, solid precipitation and (possible) drizzle. These information on clouds and precipitation types are available at CloudSat footprints with the resolution of ~1.1 km (horizontal) and 60 m vertical (over -1.92 to 40.02 km), and the same data product is used to understand the spatial distribution, and seasonal variability of different types of cloud (up to 18 km from the mean sea level) and precipitation, prevailing over the NSI region during the period 2007 – 2016. The provided information will be helpful in quantifying the feedback provided by the clouds in the earth–atmosphere system and in radiation and latent heat calculations. The *St* cloud type is not taken into account due to its negligible frequency of occurrence over this region. The analysis is subjected to the identified daytime (between 06:30 - 07:40 UTC) data records of 163 days (2007), 126 days (2008), 142 days (2009), 147 days (2010), 53 days (2012), 94 days (2013), 121 days (2014), 133 days (2015), and 89 days for the year 2016, amounting to be a total of 1,068 days. The cloud type information for the year 2011 is not taken into account in the investigations, due to very less data records (30 days). The TRMM 3B42 ver. 7 product combines the rain gauge and passive satellite observations to estimate the 3-hourly rain rate at a spatial grid resolution of 0.25° x 0.25°. The coincident days and collocated TRMM observations over NSI available at 06:00 UTC and 09:00 UTC (an average of these two temporal observations per day), providing the best spatial and temporal match with DARDAR (06:30 - 07:40 UTC) are considered in the precipitation estimates.

It is to mention that the studied years have different days of data records, hence to make a valid comparison of the cloud types on an annual scale, at first, the matrices are generated for individual cloud types, say x_{ijk}, where, x represents the cloud type, i represents year numbers (2007-

2016, excluding the year 2011), j represents the height bins at every 60 m vertical intervals from the surface to 18 km, and k is the accumulated counts of x in each height bins. The individual cloud type data, x_{ijk}, is then normalized throughout the height range with the maximum value of k obtained individually for the study period.

4.4.5. ASTRAD system: waveform generation, interference removals, and data validation

4.4.5.1. Implementation of Pulse compression technique

An ideal pulsed RaDAR transmits a short pulse of high magnitude, which is then detected by the receiver after some delay. The receiver may receive several smaller pulses reflected from the different scattering points within the target. The intervals between these smaller pulses defines the resolution (ΔR), which can be resolved prior to the reflection from two close scattering points. Brandon described the limit on ΔR that the peak power from a transmitter is usually limited and for the given peak transmit power, maximum range coverage (R) with desired SNR can be achieved by lengthening the pulse, i.e. sacrificing with ΔR (*Brandon*, 1973). For some problems however both maximum R and smaller ΔR are needed, which in turn poses the requirement of impractical values of power from the transmitter, which are unacceptable in most systems. To circumvent such requirements, the pulse compression coding technique is used in RaDAR application, in which the codes are superimposed onto the carrier wave. The technique allows RaDAR to achieve data acquisition with maximum range coverage with smaller ΔR and high SNR, at reasonable power levels. In this research work, an attempt is made to demonstrate the usefulness of pulse compression technique in the context of atmospheric RaDARs through Graphical User Interface (GUI) based approach that will save a lot of time spent on computer programming and/or constructing any hardware assemblies for demonstration purposes. The functionality of this developed GUI tool in LabVIEW and MATLAB environment is discussed in Chapter 5.

The relevant theory on RaDAR waveforms, coding schemes, and their properties are provided below.

1. *Pulsed waveform*

Almost all the pulsed waveforms with constant amplitude and phase (or frequency) are in the form:

$$u(t) = e^{j\varphi(t)} rect\left[\frac{t}{\tau_p}\right] \tag{4.18}$$

where, τ_p is the PW, and $rect\left[\frac{t}{\tau_p}\right] = \begin{cases} 1, & 0 \le t \le \tau_p \\ 0, & elsewhere \end{cases} rect\left[\frac{t}{\tau_p}\right]$

The generation of pulse compression waveform for any RaDAR applications involves the two fundamental parameters of the RF waves:

- *Bandwidth*: The RF carrier will have a particular set of frequencies, with some minimum and maximum range. The total amount of frequency spectrum used by a channel is known as the RF bandwidth.
- *Modulation*: Waves are sinusoidal in nature defined by their properties of amplitude, frequency and phase. With these three properties they can carry information on the sine or cosine waves. This process is known as modulation.

In this work, the operating frequency of ASTRAD is chosen as the carrier frequency i.e. 206.5 MHz with 5 MHz bandwidth. The type of modulation used in the analysis and front-end GUI creation is phase modulation, which occurs when the amplitude and frequency remains constant but the phase within the carrier frequency changes over a small range. A change in phase (polarity or direction of wave travel) is related directly to the digital information comprising the transmitted information.

2. *Coding schemes*

In the atmospheric RaDAR application, two different types of binary phase codes are popular – Barker codes, and the complementary codes.

Barker codes have been used in the RaDARs deployed for ionospheric incoherent scatter measurements, where the correlation time of the scattering medium is substantially longer than the full-uncompressed length of the transmitted pulse (*Barker*, 1953; *Damtie et al.*, 2007). The decoding involves adding and subtracting voltages. If the scattering centers move a significant fraction of the RaDARs wavelength between the time of arrival of first and last baud of the pulse,

the compression process may fails. The Barker code offers good pulse compression, and easy decoding, however, it suffers from fairly unacceptable side-lobe suppression. In addition, the Barker sequences are only available for the length of 2, 3, 4, 5, 7, 11 and 13 bauds (**Table 4.9**). Due to these disadvantages, Barker codes have limited utility in the atmospheric RaDAR application.

Table 4.9: Barker codes of **lengths** 2 to 13.

Code Length	**Sub pulse phases, $\varphi(t)$**
2	$\{0, \pi\}$ or $\{0, 0\}$
3	$\{0, 0, \pi\}$
4	$\{0, 0, \pi, 0\}$ or $\{0, 0, 0, \pi\}$
5	$\{0, 0, 0, \pi, 0\}$
7	$\{0, 0, 0, \pi, \pi, 0, \pi\}$
11	$\{0, 0, 0, \pi, \pi, \pi, 0, \pi, \pi, 0, \pi\}$
13	$\{0, 0, 0, 0, 0, \pi, \pi, 0, 0, \pi, 0, \pi, 0\}$

The complementary codes are another form of the binary phase codes that comes in pair (*Golay*, 1961). They are decoded by matched filter / delay line combination whose impulse response is time reverse of the pulse. The two pulses encoded with the complementary pair have the property that their side-lobes are equal in magnitude but opposite in sign, so when the outputs are added, the side-lobes cancel out, leaving only the central peak. As far as complementary codes are concerned, there is still one main restriction i.e. the phase changes introduced by the target must vary only on a time scale much longer than the Inter-Pulse Period (IPP). This restriction has prevented the use of this code in military applications and in incoherent scatter from ionosphere, where the Doppler shifts are too large. But for the very small Doppler shifts associated with the atmospheric RaDAR (e.g. ASTRAD), the use of complementary codes for pulse compression is fully compatible. However, the selection of most suitable complementary code pairs must be decided based on several performance measures like merit factor, discrimination, quality factor, Integrated Side-lobe Level (ISL) and Peak Side-lobe Level (PSL), discussed elsewhere (*Kumar et al*., 2012).

3. *Complementary codes and their properties*

Golay defined a pair of complementary codes as two equally long finite sequences of two kinds of elements with the property that the number of pairs of like elements with any given separation in one sequence is equal to the number of pairs of unlike elements with the same

separation in the other sequence (*Golay*, 1961). Here an example of complementary pairs: *A* = {-1, -1, -1, 1, -1, -1, 1, -1} and *B* = {-1, -1, -1, 1, 1, 1, -1, 1} is used to clarify the definition, as illustrated in **Fig.4.15** in which, each code has a length of 8 bits, and the two kinds of elements are 1 and -1. In the code sequences binary '1' represents 0° phase and binary '-1' represents 180° out of phase. '*L*' is used to denote a pair of like elements and '*U*' as a pair of unlike elements in code *A* or *B*. For the given separation of 2, it is shown that code *A* has one pair of unlike elements and four pairs of like elements, and code *B* has four pairs of unlike elements and one pair of like elements. Any other separations (0, 1, 3, and so forth) can be used to check the property of the pair of complementary codes. The given code pairs remain complementary pairs, if they are reversed, or the two kind of their elements are interchanged, or their elements at even orders are altered. Further, longer complementary code pairs can be generated through appending and interleaving operations.

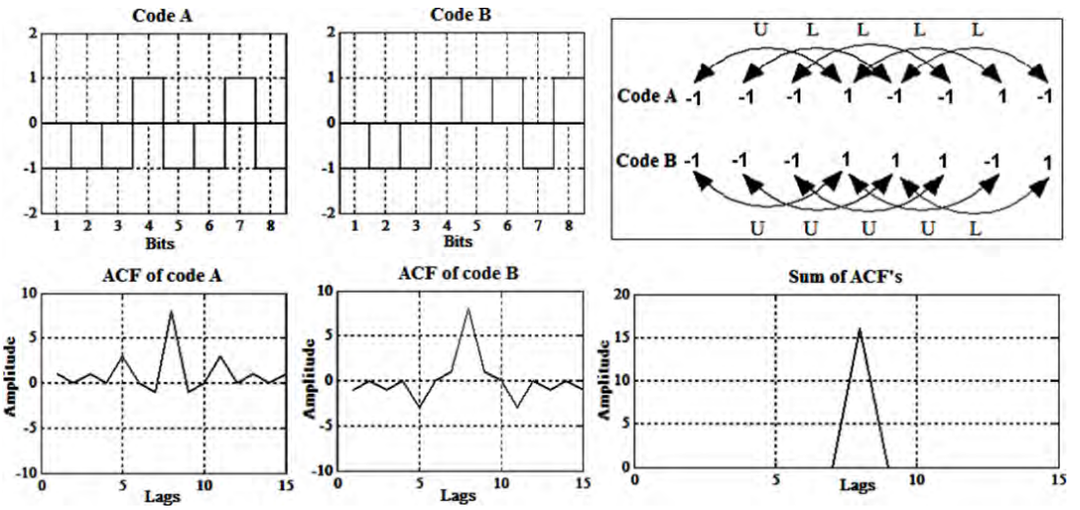

Fig.4.15. Complementary code sequences, *A* = {-1, -1, -1, 1, -1, -1, 1, -1} and *B* = {-1, -1, -1, 1, 1, 1, -1, 1} and their properties.

The complementary sequences are governed by two major correlation properties that forms the basis of pulse compression in RaDAR applications (*Hussain*, 2008).

i. The complementary codes come in a pair of two binary sequences of the same length whose Auto-Correlation Functions (ACFs) have side-lobes equal in magnitude but opposite in sign. The sum of these ACFs gives a single ACF with the peak of twice the original length and zero elsewhere. For any two complementary sequences A_T and B_T of length *N*, it holds:

$$R_{A_T}(\tau) + R_{B_T}(\tau) = \begin{cases} 2N, & \tau = 0 \\ 0, & \tau = \pm 1, \pm 2, \ldots . \pm (N-1) \end{cases} \quad (4.19)$$

where, $R_{A_T}(\tau)$ and $R_{B_T}(\tau)$ represent the ACFs of A_T and B_T with lags τ. This property plays a key role in the atmospheric RaDAR application when the sequences A_T and B_T are used in the phase modulation of two successive transmit Radio Frequency (RF) pulses separated by the IPP, respectively.

ii. The transmitted complementary sequences A_T and B_T of length *N*, and the received sequences A_R and B_R of the same length holds the relation:

$$R_{A_T A_R}(\tau) + R_{B_T B_R}(\tau) = 0, \text{ for } \tau = \pm 1, \pm 2, \ldots . . \pm (N-1) \quad (4.20)$$

where, $R_{A_T A_R}(\tau)$ represents the correlation between A_T and A_R, and $R_{B_T B_R}(\tau)$ represents the correlation between B_T and B_R.

4. *Complementary coded waveform generation*

If $A_T = \{a_1, a_2, a_3, \ldots . . a_N\}$ and $B_T = \{b_1, b_2, b_3, \ldots . . b_N\}$, where, $a_i, b_i \in \{-1, +1\}$ for $1 \leq i \leq N$, then the coded transmitted RaDAR signal is represented as:

$$\begin{aligned} Tx(t) &= Tx_{A_T}(t) + Tx_{B_T}(t - IPP) \\ &= \left(\sum_{i=1}^{N} a_i \, rect\left(\frac{t - i\tau}{PW}\right)\right) \cos(\omega_c t) + \left(\sum_{i=1}^{N} b_i \, rect\left(\frac{t - IPP - i\tau}{PW}\right)\right) \cos(\omega_c (t - IPP)) \end{aligned} \quad (4.21)$$

where, the width of each pulse (bit) in a code is called baud width (τ), and the number of bits in the code is referred as baud length (*N*). The pulse width (*PW*) is computed as $N \times \tau$. The angular frequency, $\omega_c = 2\pi f_c$, *IPP* = Inter pulse period or Pulse Repetition Time (*PRT*), and $rect()$ is the rectangular function.

Let us consider the 16-bit complementary code pairs, A_T = { 1, 1, 1, -1, 1, 1 , -1, 1, 1, 1, 1, -1, -1, -1, 1, -1} and B_T = { 1, 1, 1, -1, 1, 1, -1, 1, -1, -1, -1, 1, 1, 1, -1, 1}. These code pairs are modulated on the carriers waves $cos(\omega_c t)$ and $cos(\omega_c(t\text{-}IPP))$, to form the coded pulse compression waveforms. **Fig. 4.16(a-b)** shows the resulting transmit signals coded with the code sequences A_T and B_T, respectively. In this case, f_c, the carrier frequency is chosen as 206.5 MHz which is the ASTRAD operating frequency, IPP as 125 μs, *N* as 16-bit, and baud width, τ as 1 μs. In addition, **Fig. 4.16c** shows the Power Spectral Density (PSD) of the two codes A_T and B_T. The transmit RF signal in a given IPP is available only during the pulse width duration where its phase is altered

according to the first code A_T, and after some blanking period, the system waits for the return signals until the start of the next cycle of IPP, where code B_T is used for coding. In practical RaDAR operation, generally four *IPP* cycles are used for reliable coded transmission, and the coding sequence follows A_T, B_T, A_T' and B_T', where, A_T' and B_T' are the complements of A_T and B_T, respectively. The same sequence is repeated in the next four *IPP* cycles and so on, as long as the RaDAR transmission continues.

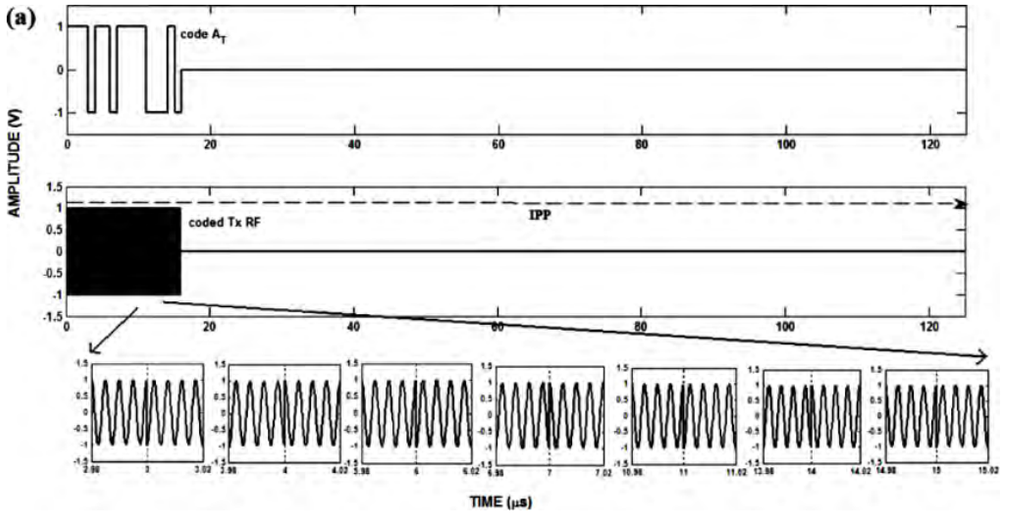

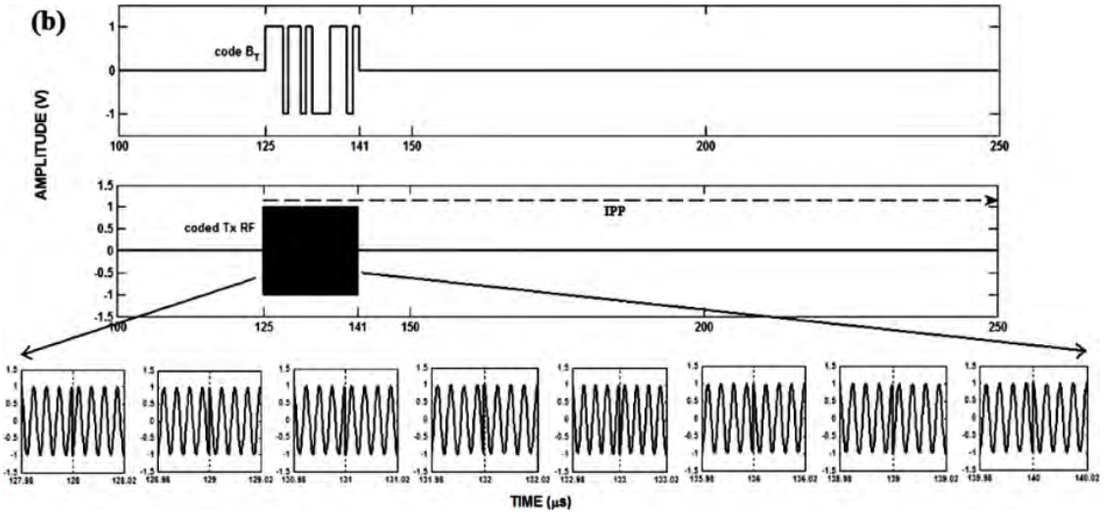

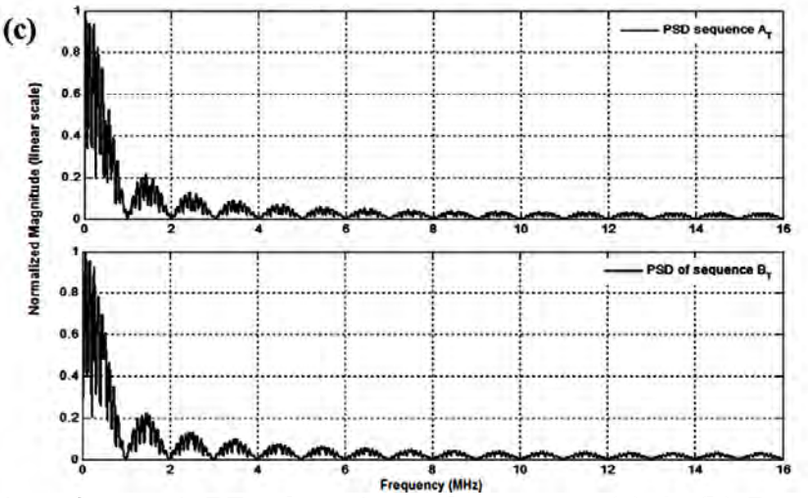

Fig.4.16. Modulation of transmit RF pulse using code sequence **(a)** A_T **(b)** B_T , and **(c)** the Power Spectral Density of these code pairs.

To band-limit the transmission, coded RF signals are generally passed through the Infinite-Impulse Response (IIR) digital bandpass filtering stage. The reason behind the choosing IIR filter is that it is quite common in atmospheric Radar and it is computationally more efficient to implement than a comparable Finite Impulse Response (FIR) filter. **Fig. 4.17(a-b)** shows the pulse shapes, rise time, fall time and overshoots for the two successive coded RF signals, modulated with the same 16-bit complementary sequences A_T and B_T, respectively.

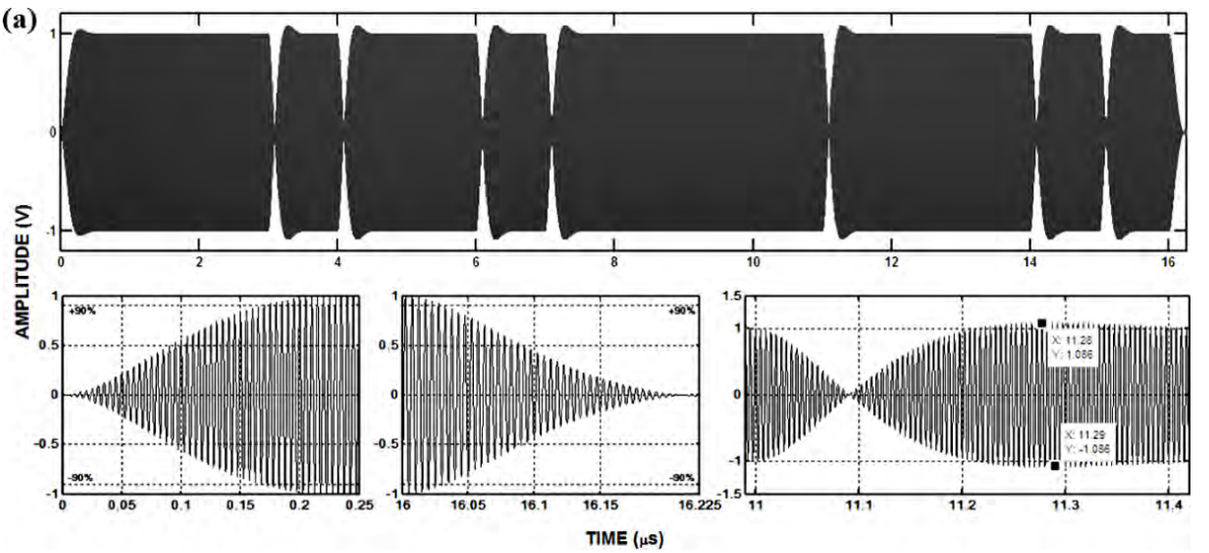

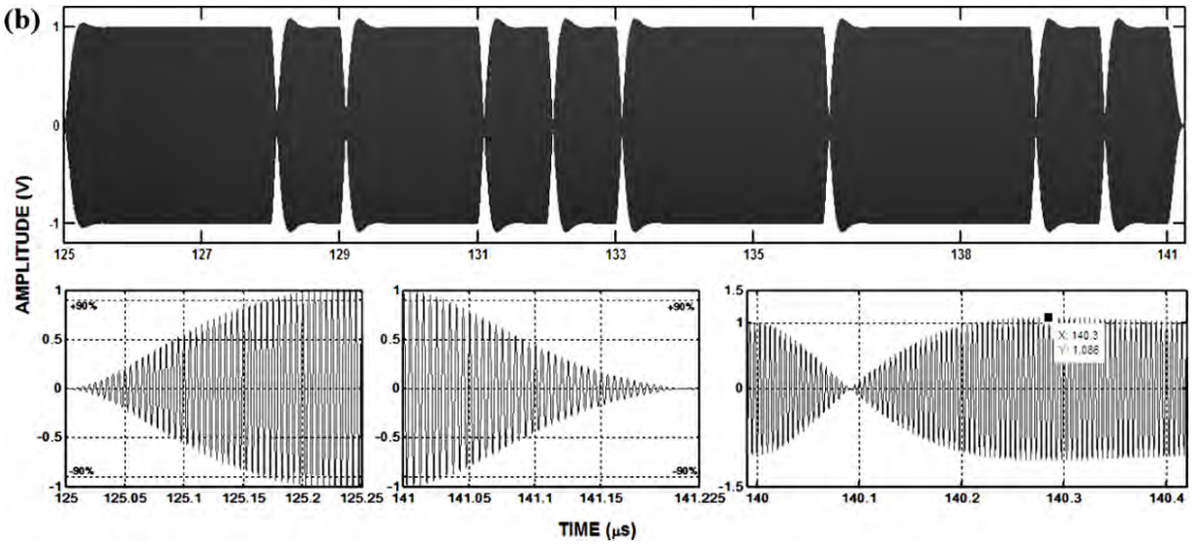

Fig. 4.17. Pulse shapes, rise time, fall time and overshoots of the coded transmit RF pulse using code sequence **(a)** A_T, and **(b)** B_T

The received signal $Rx(t)$ in RaDAR is the time-shifted (delayed by t_o) replica of the transmitted signal $Tx(t)$ plus the additive noise $n(t)$, given by:

$$Rx(t) = Tx(t - t_o) + n(t) \tag{4.22}$$

In this equation, $Tx(t)$ is expressed by equation (4.21). The noise and Doppler shifts ($f_d = 1/t_o$) may causes the ACFs of the complementary pairs to lose their ideal properties, resulting in the undesired side-lobes not being completely cancelled out, in actual RaDAR application. These leftover side-lobes may suppress the detection from small targets or may cause false target detection. One possible approach to mitigate such problems to arise in the atmospheric RaDAR is proper selection of the complementary code pairs. The good pair is one that has very high merit factor and discrimination, and extremely low ISL and PSL (*Kumar et al.*, 2012).

4.4.5.2. Radio frequency interference and clutter removals

The quality of profiles in any atmospheric RaDARs often get degraded due to conglomeration of unwanted echoes originating from non-atmospheric and fixed targets, in the form of Radio frequency Interference (RFI) and Zero-Doppler Clutter (ZDC). Some of the clutter and interference sources are shown in **Fig. 4.18**.

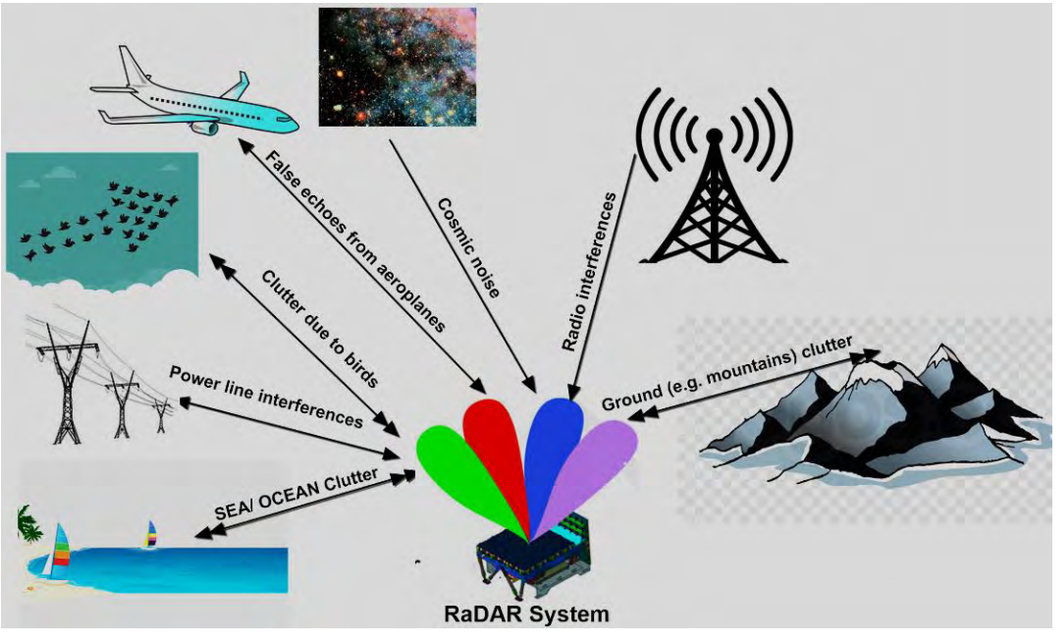

Fig.4.18. Major sources of interferences for atmospheric RaDARs.

The ZDC appears as a line of strong returns at zero-Doppler, extending throughout the range bins in the Doppler profile, and possibly it may arises primarily due to the undesired echoes, resulting when the skirts of low level side-lobes of the antenna array illuminates the stationary artefacts or hard targets like surrounding terrains, mountains, buildings etc. (*Sato and Woodman*, 1982). The RFI often arises due to the presence of undesired wireless communication channels active in the nearby regions of the RaDAR site, or from the nearby power lines. Both these phenomenon's outweighs, and thereby overwhelms, the desired Doppler detection from the atmospheric targets. Moreover, the characteristics of clutters, in general, are location dependent, and hence it is essential to determine the most ideal methodology for eliminating these undesired interferences from the Doppler spectra, to avoid fallacy in the signal detection. Further, the practical implementation of the devised methodology in the application software is a crucial step, and should essentially be worked out, especially during the commissioning phase of any RaDAR.

Significant efforts in the hardware aspects have been put to minimize the contributions from these undesirable sources, and at the same time, several robust algorithms or schemes were suggested in the signal processing by the researchers for the RaDARs operating at ~ 50 MHz and ~ 400 MHz frequency bands (e.g. *May and Strauch*, 1998; *Lehmann and Teschke*, 2001; *Anandan and Jagannatham*, 2013), however, the performance checking of these algorithms on ASTRAD

observations, or any profilers operating ~ 200 MHz bands, have never been checked so far. Therefore, an initial attempt in this direction is made in this work on few sample Doppler spectra obtained from ASTRAD, and the results are discussed in the next Chapter of this thesis.

4.4.5.3. Validation of the wind measurements from ASTRAD observations

Radiosonde observations are often considered as a means of verifying the observations made by other collocated systems. Therefore, the wind measurements from the radiosonde observations from ARIES, Nainital is used to achieve meaningful validation of the zonal (U) wind, meridional (V) wind, and wind speed estimated from the ASTRAD observations. During the process of validation, the following points have been considered:

i. The consistency in the ASTRAD data is checked by comparing the same beam frames obtained during the first scan cycle with the corresponding frames in the next scan cycle and so on. If the differences between them exceeds certain threshold values, then the frames are discarded.
ii. To eliminate outliners in the data, the raw radial velocities obtained from ASTRAD are averaged for every 15-20 min intervals.
iii. To account for temporal differences between the wind observations from the Radiosonde and ASTRAD, the time averaging interval of ASTRAD data was centered at the middle time of the radiosonde launch.
iv. To account for the differences in their spatial resolutions, the height resolution of the radiosonde observation is brought to the RaDAR resolution, and the data were extrapolated accordingly.

Chapter 5

RESULTS AND DISCUSSIONS

CHAPTER 5
RESULTS AND DISCUSSIONS

5.1. Studies on atmospheric aerosols – their variations, evaluation, utilization, and transport

5.1.1. Seasonal variations in aerosol optical parameters over the study region

Aerosols are highly variable components of the Earth's atmosphere, and they influence the climate directly by scattering and absorbing the incoming solar radiation, and indirectly by modifying the microphysical and hence the radiative properties, amount and lifetime of clouds (*Hansen et al.,* 1997*; Haywood and Boucher,* 2000*; Lohmann and Feichter,* 2005*; Ming et al.,* 2010*; Lau et al.,* 2010*; Wang,* 2013*; Lee and Wang,* 2015; *Boucher et al.,* 2013, 2015*; Banerjee et al.,* 2018). Their presence in large volume has an adverse effect on human's health, and leads to poor visibility, acidic deposition, and changes in the Earth's radiation balance (*Lippmann et al.,* 2000*; Ruzer and Harley*, 2004; *OECD,* 2014). During past, inadequate measurements on the temporal and spatial variations in aerosols, together with their limited understanding on the optical and microphysical properties, pose large uncertainties in quantifying their impacts on the Earth's climate system. Over the last few decades, the advent of satellite technology such as MODIS, MISR, OMI, CALIPSO etc., together with the establishment of ground based AERONET networks, and field studies/ research campaigns, have greatly enhanced our level of understanding on the distribution and properties of aerosols (e.g. *Holben et al*., 1998, 2001; *Veefkind et al*., 2000; *Wang et al*., 2000; *Torres et al*., 2002a, 2002b; *Savtchenko et al*., 2004; *Remer et al*., 2005; *Young and Vaughan*, 2009; *Winker et al*., 2010; *Wang*, 2013; *Solanki and Singh*, 2014; *Satheesh et al*., 2017; *Kumar et al*., 2018), but not up to the desired level, particularly at regional scales (*IPCC*, 2007; *Srivastava et al*., 2012). Furthermore, the aerosol measurements from both satellite and ground-based tools are limited over the complex mountainous terrains, having several sensitive ecosystems and landscapes of regional and global significance such as the pristine Himalaya.

Knowledge on the sources and size distribution of aerosols is essential in order to study the radiative effects, and also to understand the health impacts due to the pollutant particles. However, this study deals with the distribution of aerosols over the Himalayan region, which have gained serious concern as a result of seasonal transport of various forms of pollutants. The AERONET based aerosol observations from ten stations located in the region under study, namely, Nainital, Pantnagar, Kanpur, New Delhi, Lahore, Gual Pahari, Gandhi College, Jaipur, Lumbini, and Pokhara are subjected for investigation. The present analysis in the direction of understanding the optical, and physical/ chemical properties of aerosols to different air mass origins and local aerosol sources, and their spatio-temporal characteristics, may serves as the crucial input for modeling and prediction on air quality and climate system of the mountainous region.

The details regarding the stations subjected for investigation, are covered in the previous chapter. The seasonal variations in the aerosol volume size distribution for these stations are presented in **Fig. 5.1**. The figure shows the bi-modal size distribution of aerosols (*Schuster et al.*, 2006) at these stations during all the seasons.

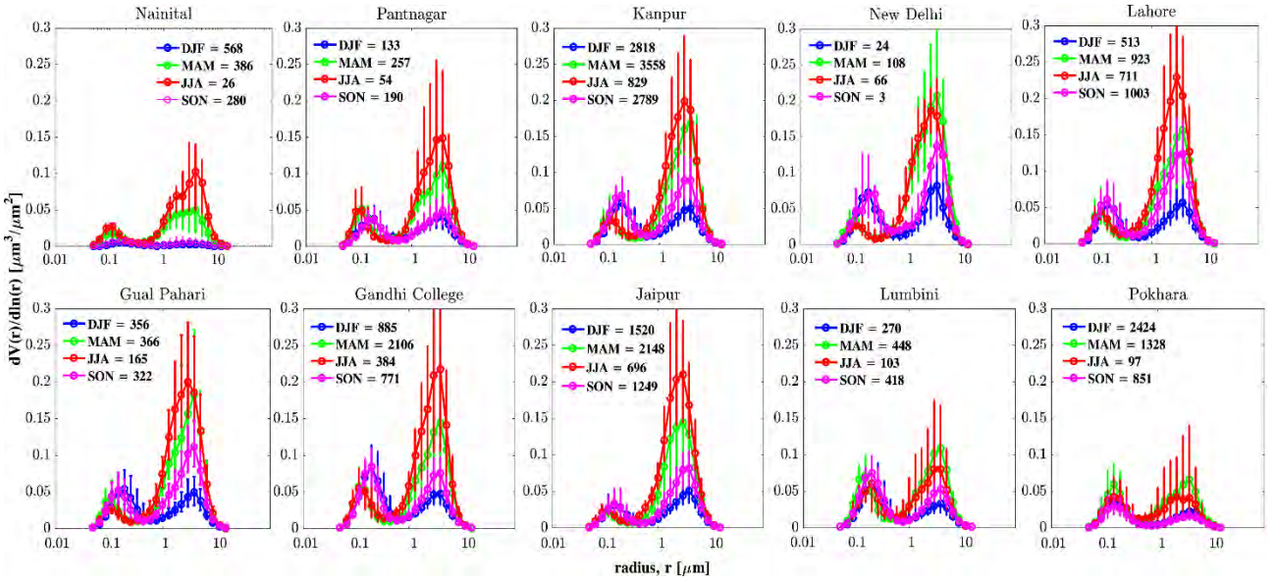

Fig. 5.1. Seasonal variation of aerosol volume-size distribution for ten AERONET stations in the Himalayan region.

The bi-modal log-normal function is the most suitable approach for representing the fine and coarse mode particle size distributions (e.g. *Eck et al.*, 1999; *Dubovik et al.*, 2002; *Schuster et al.*, 2006). Although, the volume concentrations shown in **Fig. 5.1** exhibits few differences over each

stations, however, their shapes are analogous across all the seasons. Further, **Table 5.1(a)** shows the seasonal means±SD of fine, coarse, and total AOD at 500 nm for these stations, alongwith the mean±SD FMF values. From **Table 5.1(a)** it seems that the AOD and FMF values are zero bounded and not Gaussian distributed, therefore, their median and interquartile range (IQR), which is defined as the difference between 75th and 25th percentiles, are also computed (**Table 5.1(b)**).

Table 5.1: AOD (fine mode, coarse mode, and total) at 500 nm, and FMF for ten AERONET stations in the Himalayan region: **(a)** Seasonal mean±SD.

Station	*Seasons*	*fine mode AOD*	*coarse mode AOD*	*total AOD*	*FMF*
Nainital	DJF	0.08±0.07	0.01±0.02	0.09±0.07	0.84±0.15
	MAM	0.15±0.11	0.15±0.14	0.30±0.19	0.52±0.20
	JJA	0.16±0.07	0.16±0.08	0.32±0.10	0.50±0.15
	SON	0.09±0.06	0.02±0.03	0.11±0.07	0.85±0.15
Pantnagar	DJF	0.44±0.22	0.06±0.08	0.51±0.22	0.85±0.18
	MAM	0.29±0.18	0.25±0.13	0.54±0.23	0.52±0.15
	JJA	0.35±0.26	0.23±0.18	0.58±0.33	0.63±0.21
	SON	0.52±0.34	0.06±0.05	0.59±0.35	0.87±0.11
Kanpur	DJF	0.56±0.34	0.08±0.07	0.64±0.33	0.83±0.15
	MAM	0.24±0.13	0.33±0.21	0.57±0.26	0.44±0.16
	JJA	0.28±0.20	0.40±0.31	0.68±0.34	0.44±0.24
	SON	0.62±0.36	0.11±0.09	0.73±0.33	0.81±0.17
New Delhi	DJF	0.66±0.48	0.07±0.03	0.73±0.49	0.87±0.06
	MAM	0.23±0.10	0.38±0.16	0.62±0.20	0.38±0.11
	JJA	0.26±0.30	0.37±0.17	0.63±0.32	0.39±0.18
	SON	0.68±0.22	0.15±0.04	0.83±0.21	0.80±0.10
Lahore	DJF	0.46±0.37	0.09±0.07	0.55±0.38	0.79±0.13
	MAM	0.25±0.15	0.32±0.22	0.57±0.29	0.45±0.15
	JJA	0.35±0.26	0.44±0.24	0.79±0.30	0.43±0.19
	SON	0.55±0.44	0.18±0.11	0.73±0.42	0.69±0.18
Gual Pahari	DJF	0.57±0.36	0.08±0.09	0.65±0.37	0.85±0.16
	MAM	0.25±0.14	0.34±0.16	0.59±0.24	0.42±0.13
	JJA	0.22±0.19	0.42±0.22	0.64±0.27	0.36±0.18
	SON	0.47±0.33	0.16±0.08	0.63±0.30	0.69±0.21
Gandhi College	DJF	0.78±0.44	0.07±0.05	0.85±0.43	0.89±0.11
	MAM	0.35±0.21	0.27±0.14	0.62±0.26	0.56±0.17
	JJA	0.33±0.21	0.35±0.29	0.69±0.33	0.52±0.24
	SON	0.65±0.37	0.08±0.09	0.73±0.35	0.85±0.15
Jaipur	DJF	0.30±0.24	0.08±0.06	0.39±0.24	0.75±0.16
	MAM	0.14±0.07	0.28±0.15	0.42±0.17	0.35±0.14
	JJA	0.17±0.10	0.40±0.18	0.58±0.20	0.31±0.15
	SON	0.33±0.29	0.11±0.08	0.44±0.27	0.68±0.20
Lumbini	DJF	0.73±0.46	0.06±0.04	0.79±0.47	0.90±0.08
	MAM	0.54±0.29	0.23±0.11	0.77±0.31	0.67±0.14
	JJA	0.37±0.27	0.26±0.40	0.63±0.49	0.66±0.21
	SON	0.71±0.41	0.04±0.02	0.75±0.41	0.92±0.06

Pokhara	DJF	0.34±0.25	0.03±0.02	0.38±0.25	0.88±0.08
	MAM	0.49±0.41	0.14±0.10	0.62±0.43	0.74±0.15
	JJA	0.23±0.19	0.07±0.09	0.30±0.24	0.77±0.15
	SON	0.28±0.21	0.02±0.02	0.30±0.21	0.90±0.08

(b) Seasonal [median, interquartile range (IQR)].

[*median, interquartile range*]					
Station	*Seasons*	*fine mode AOD*	*coarse mode AOD*	*total AOD*	*FMF*
Nainital	DJF	[0.06, 0.06]	[0.006, 0.01]	[0.07, 0.07]	[0.90, 0.20]
	MAM	[0.12, 0.10]	[0.11, 0.11]	[0.24, 0.23]	[0.51, 0.28]
	JJA	[0.15, 0.09]	[0.14, 0.10]	[0.32, 0.12]	[0.50, 0.23]
	SON	[0.07, 0.07]	[0.005, 0.02]	[0.09, 0.10]	[0.92, 0.17]
Pantnagar	DJF	[0.42, 0.27]	[0.03, 0.05]	[0.47, 0.23]	[0.93, 0.09]
	MAM	[0.24, 0.19]	[0.21, 0.13]	[0.50, 0.27]	[0.51, 0.21]
	JJA	[0.27, 0.29]	[0.20, 0.27]	[0.54, 0.51]	[0.60, 0.37]
	SON	[0.42, 0.42]	[0.05, 0.06]	[0.50, 0.42]	[0.91, 0.15]
Kanpur	DJF	[0.49, 0.46]	[0.06, 0.07]	[0.57, 0.43]	[0.90, 0.20]
	MAM	[0.20, 0.15]	[0.29, 0.22]	[0.52, 0.31]	[0.42, 0.22]
	JJA	[0.21, 0.18]	[0.36, 0.31]	[0.63, 0.36]	[0.38, 0.33]
	SON	[0.58, 0.49]	[0.08, 0.11]	[0.68, 0.42]	[0.88, 0.23]
New Delhi	DJF	[0.55, 0.52]	[0.06, 0.04]	[0.62, 0.55]	[0.87, 0.11]
	MAM	[0.21, 0.15]	[0.36, 0.19]	[0.60, 0.24]	[0.38, 0.14]
	JJA	[0.19, 0.10]	[0.34, 0.23]	[0.57, 0.34]	[0.32, 0.10]
	SON	[0.76, 0.31]	[0.15, 0.06]	[0.92, 0.29]	[0.84, 0.05]
Lahore	DJF	[0.35, 0.41]	[0.08, 0.06]	[0.44, 0.42]	[0.82, 0.17]
	MAM	[0.20, 0.14]	[0.28, 0.21]	[0.51, 0.34]	[0.44, 0.18]
	JJA	[0.26, 0.19]	[0.41, 0.24]	[0.74, 0.34]	[0.38, 0.19]
	SON	[0.40, 0.48]	[0.16, 0.15]	[0.62, 0.46]	[0.71, 0.29]
Gual Pahari	DJF	[0.49, 0.46]	[0.04, 0.05]	[0.55, 0.45]	[0.92, 0.13]
	MAM	[0.21, 0.17]	[0.31, 0.20]	[0.57, 0.31]	[0.41, 0.21]
	JJA	[0.17, 0.07]	[0.39, 0.25]	[0.60, 0.31]	[0.30, 0.11]
	SON	[0.42, 0.41]	[0.16, 0.14]	[0.59, 0.35]	[0.74, 0.37]
Gandhi College	DJF	[0.72, 0.56]	[0.05, 0.04]	[0.77, 0.54]	[0.94, 0.09]
	MAM	[0.31, 0.26]	[0.25, 0.21]	[0.60, 0.38]	[0.54, 0.26]
	JJA	[0.27, 0.23]	[0.32, 0.41]	[0.69, 0.39]	[0.47, 0.42]
	SON	[0.59, 0.46]	[0.05, 0.06]	[0.68, 0.41]	[0.91, 0.15]
Jaipur	DJF	[0.23, 0.22]	[0.07, 0.06]	[0.32, 0.23]	[0.77, 0.22]
	MAM	[0.12, 0.07]	[0.26, 0.17]	[0.40, 0.20]	[0.32, 0.18]
	JJA	[0.15, 0.08]	[0.37, 0.21]	[0.53, 0.25]	[0.27, 0.15]
	SON	[0.22, 0.27]	[0.11, 0.11]	[0.37, 0.26]	[0.68, 0.33]
Lumbini	DJF	[0.60, 0.69]	[0.04, 0.06]	[0.63, 0.71]	[0.94, 0.08]
	MAM	[0.49, 0.39]	[0.21, 0.14]	[0.75, 0.42]	[0.69, 0.20]
	JJA	[0.32, 0.33]	[0.11, 0.20]	[0.53, 0.56]	[0.72, 0.26]
	SON	[0.64, 0.48]	[0.04, 0.02]	[0.68, 0.48]	[0.94, 0.05]
Pokhara	DJF	[0.27, 0.23]	[0.03, 0.02]	[0.31, 0.23]	[0.90, 0.11]
	MAM	[0.37, 0.38]	[0.11, 0.11]	[0.52, 0.43]	[0.76, 0.21]
	JJA	[0.19, 0.21]	[0.04, 0.06]	[0.23, 0.28]	[0.78, 0.18]
	SON	[0.22, 0.22]	[0.02, 0.01]	[0.24, 0.21]	[0.93, 0.09]

From **Fig. 5.1a-b**, it is evident that the seasonal average particle size distribution is characterized by two modes, namely the fine and coarse modes. It is seen that the fine mode particles is near 0.15 µm and the coarse mode particles is lying between 1-10 µm for all the stations, with very high volume concentration of coarse mode particles reaching close to 0.2 $\mu m^3/\mu m^2$ or above for Kanpur, New Delhi, Lahore, Gual Pahari, Gandhi College, and Jaipur, during pre-monsoon and monsoon. The overall pattern of aerosol size distributions over these stations are similar, characterized as bi-modal log-normal distribution with prominent peak in coarse mode, particularly during monsoon and pre-monsoon seasons, suggesting dust-dominated environment. Further, the coarse mode concentrations over the Himalayan stations - Nainital, Lumbini, and Pokhara are about two times lower than the above-mentioned IGP stations, and about 1.5 times lower than the foothill station, Pantnagar.

During monsoon and pre-monsoon, the coarse mode particles (primarily from long-range transports) are dominant in the IGP regions, that includes Gual Pahari (FMF as 0.36±0.18 and 0.42±0.13, respectively) (*Hyvarinen et al*., 2010), New Delhi (FMF as 0.39±0.18 and 0.38±0.11, respectively) (*Srivastava et al*., 2012, 2014), and Kanpur (FMF as 0.44±0.24 and 0.44±0.16, respectively) (*Tripathi et al*., 2005; *Ram et al*., 2016). On the other hand, the fine mode particles in these regions are dominant during post-monsoon and winter, with average FMF of ~ 0.77 and ~0.85, respectively. During winter, the northern India experience western disturbances, moving from west to east, leading to intense fog, haze, and cold waves in the region, that contributes to significant increase in AOD value (*Kumar et al*., 2015; *Alam et al*., 2018). The high concentration of fine mode aerosols over IGP during post-monsoon is mainly due to biomass burning, and continental aerosols.

Generally, high altitude locations have lower AODs and the densely populated, low-altitude urban and industrialized locations have higher AODs, and the same is evident here when the AOD values between Nainital (a high altitude site) and the nearby low-land industrial station, Pantnagar are inter-compared. During post-monsoon and winter, the AOD values is ~ 5 times higher in Pantnagar than Nainital, and ~ 1.5 time higher during pre-monsoon and monsoon. The lower AOD at Nainital may be attributed to the BL dynamics as the site is in the free troposphere and free from any local sources due to the presence of the surrounding mountains, that acts as barrier to aerosol transport from the IGP region (*Dumka et al*., 2014). The FMF value at both these stations are high (> 0.8) during post-monsoon and winter, confirming the dominance of fine mode aerosols, while

during pre-monsoon and monsoon, the dust activities peaks, as inferred from the low FMF values (0.5 - 0.63) over these regions.

At Gandhi College, the fine-mode aerosols are dominant during post-monsoon and winter, with FMF values as 0.85±0.15 and 0.89±0.11, respectively. During pre-monsoon and monsoon, mixed type of aerosols (i.e. mixture of both fine and coarse-mode) are present, with the fine mode and coarse mode AOD values are closer to each other. For Jaipur station, the dominance of the coarse mode particles, mainly dust, is evident from **Table 5.1** during pre-monsoon and monsoon with FMF values as 0.35±0.14 and 0.31±0.15, respectively. During these seasons, the influx of dust over this region is not only from the Thar desert, but also from the far away locations in the west or northwest, mainly from Afghanistan/Iran and Middle-Eastern peninsular regions. The contribution of fine mode particles in post-monsoon and winter is mainly of the continental origine, and the atmosphere in Jaipur is stable during winter with total AOD lowest (0.39±0.24) than other season (*Verma et al*., 2015, 2017).

The highest aerosol loading in Lahore is observed during monsoon (total AOD: 0.79±0.30), while the lowest in winter (total AOD: 0.55±0.38), with the dominance of coarse (FMF: 0.43±0.19) and fine mode (FMF: 0.79±0.13) aerosols, respectively. The occurrence of peak AOD with coarse mode dominance during pre-monsoon and monsoon is mainly attributed to mineral dust transported from the Thal, Dasht, and Thar deserts (*Ali et al*., 2014), while the low AOD values in winter is mainly due to local vehicular and industrial/urban emissions, house-hold fires, and crop residue burning (*Alam et al*., 2012; *Ali et al*., 2014).

In Lumbini, the total AOD values are on higher side (> 0.6) with FMF > 0.65, during all the seasons. The dominant fine mode aerosols throughout the seasons could be due to nearby pollutants (that includes the contribution from industrial and vehicular emissions, biomass burning from cooking activities and agro-residue burning) and regional (IGP region) biomass burning (*Rupakheti et al*., 2017, 2018). The build-up of haze due to burning of rice paddy residue during post-monsoon and its intensification by winter over the major portion of western India and eastern Pakistan could be thought as the major contributor for extremely high FMF value (> 0.9) in Lumbini. The coarse mode AOD is highest during pre-monsoon and monsoon, indicating the additional contribution from desert dust originating mainly from the Thar desert. In Pokhara, the aerosol loading during pre-monsoon showed highest variability with the total AOD values of 0.62+/-0.43. A substantial fraction of coarse mode particles are seen over this station during pre-monsoon (FMF value as

0.74+/-0.15) and monsoon (FMF value as 0.77+/-0.15), while the post-monsoon and winter are dominated by the fine mode aerosol particles (*Xu et al*., 2014), with FMF values as 0.90+/-0.08 and 0.88+/-0.08, respectively (*Aryal et al*., 2015).

5.1.2. Assessment of satellite aerosol retrievals – MODIS and CALIPSO

5.1.2.1. Assessment of MODIS collections with coincident AERONET measurements

To make an assessment of MODIS collections (C5.1 and C6.0), four cases on spatio-temporal comparisons were considered. In the first two cases, the average of MODIS AOD within 20 km × 20 km from ARIES, Nainital are compared with the average AOD from AERONET within (a) ±30 minutes and (b) ±15 minutes, and in the latter two cases, the average of MODIS AOD within 30 km × 30 km are compared with the average AOD from AERONET within (c) ±30 minutes and (d) ±15 minutes of the closest Terra/Aqua overpass occurrences. From the statistics on the four spatio-temporal combinations, as given in **Table 5.2**, case (c) is found to perform better with almost all the metrics in good agreement as compared to other three cases. Since, MODIS Terra shows high Pearson correlation (R ~0.90), Spearman correlation (S ~0.9), and high %EE (~62) in comparison to Aqua (R ~0.75, %EE ~54) with ground based AERONET measurements. Therefore, one has to essentially decide upon the most suitable collection of Terra retrievals out of C5.1 DT, C6.0 DT and C6.0 DB.

Table 5.2: Statistical summary on AOD (550 nm) comparison between the MODIS and AERONET retrievals for the four spatio-temporal cases. All the correlations shown are significant at the 0.05 level (2-tailed).

		Case-(a)	**Case-(b)**	**Case-(c)**	**Case-(d)**
MODIS Terra DT: C5.1, C6.0 DB: C6.0	*N*	24	24	27	27
	Pearson Correlation (mean±SD±SEM)	0.90±0.05±0.03	0.89±0.05±0.03	0.90±0.04±0.02	0.90±0.03±0.02
	Spearman Correlation (mean±SD±SEM)	0.87±0.05±0.02	0.87±0.05±0.02	0.90±0.02±0.01	0.89±0.01±0.01
	RootMSE (mean±SD)	0.068±0.02	0.069±0.02	0.067±0.01	0.068±0.02
	%EE (mean±SD)	52.8±17.4	48.6±17.3	61.7±15.5	56.8±17.1
	MBE (mean±SD)	0.052±0.04	0.052±0.04	0.054±0.04	0.054±0.04
	AER (mean±SD)	0.13±0.14	0.14±0.16	0.105±0.10	0.12±0.13

MODIS Aqua DT: C5.1, C6.0 DB: C6.0	*N*	22	21	22	22
	Pearson Correlation (mean±SD±SEM)	0.72±0.06±0.03	0.66±0.02±0.01	0.75±0.06±0.04	0.69±0.04±0.02
	Spearman Correlation (mean±SD±SEM)	0.67±0.08±0.05	0.61±0.08±0.05	0.72±0.10±0.06	0.69±0.10±0.06
	RootMSE (mean±SD)	0.081±0.003	0.089±0.003	0.084±0.006	0.093±0.004
	%EE (mean±SD)	57.5±2.6	53.9±14.6	54.5±9.1	51.5±13.8
	MBE (mean±SD)	0.057±0.03	0.056±0.03	0.059±0.03	0.055±0.03
	AER (mean±SD)	0.102±0.06	0.12±0.10	0.12±0.08	0.13±0.11

For the reasonable assessment with the ground truth, the study in case (c) is extended for 174 coincident AOD measurements available during 2008-2010. Each of the three collections is subjected to one-one line comparison with AERONET AOD values as shown in **Fig. 5.2**. From the figure, it is evident that MODIS Terra C5.1 DT showed high Pearson correlation (R ~0.92) and low RootMSE (~ 0.087), thereby reflecting lowest variability, whereas, MODIS Terra C6.0 DB demonstrated the highest percentage of MODIS AOD values falling within the defined EE (±0.05±0.15τ) boundary (%EE ~77.01). However, MODIS Terra C6.0 DT is showing good correlation (R ~0.90), but the least %EE (~45.98) among all.

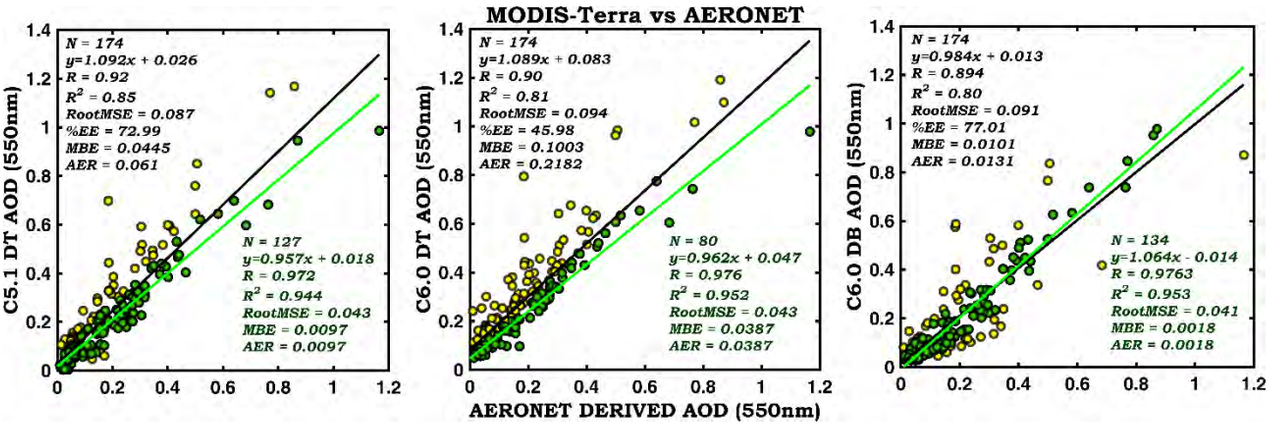

Fig.5.2. Scatter plot with one-one line comparison for MODIS Terra and AERONET AOD measurements; green + yellow = complete, green = for values within %EE.

Based on the %EE values, a total of 127, 80 and 134 data points respectively for C5.1 DT, C6.0 DT and C6.0 DB are found to be within EE limits, which are further subjected to statistical

analysis. The statistics confirms that the MODIS Terra C6.0 DB is the best choice among others. MBE and AER values for the three collections are found to be positive, indicating the overestimation of MODIS AOD as compared to the ground based AERONET measurement. The overestimation may be attributed to the huge spatial differences in measurements, as the ground-based AOD measurement through AERONET is a point observation, whereas the MODIS retrievals of AODs are over 10 km x 10 km at each instance. Owing to the large spatial coverage, the MODIS retrieved AOD may get influenced due to the presence of small clouds, geographical locations etc.

5.1.2.2. Inter-comparison of CALIPSO product versions

CALIPSO mission announced the release of its level 1B ver. 4.00 data product in November 2014 and, level 1B and 2 ver. 4.10 during November 2016, however, the two differ only in the ancillary data sets used in their computations. In comparison to the earlier ver. 3.xx (that includes ver. 3.01 to ver. 3.04), the quality in ver. 4.10 release is enhanced with the inclusion of the updated Digital Elevation Map (DEM) from CloudSat and high-quality MERRA-2 product (*Vaughan et al.*, 2016). Study on a global scale has reported that the MRDs in the total attenuated backscatter ($\beta'_{532,total}(r)$) provided in ver. 4.xx (4.00 and 4.10), tends to be positive in comparison to the preceding ver. 3.xx products, however, deviations are higher for night as compared to the day time observations (*Zhang and Wu*, 2016). To assess the changes in latest data product at regional scale, three CALIPSO overpasses within ~100 km are used for comparative study as presented in **Table 5.3**.

Table 5.3: Statistical comparison on different versions of CALIPSO level-1B product.

	Total Attenuated Backscatter 532, $\beta'_{532,total}(r)$			
	Mean bias ($Mm^{-1}sr^{-1}$)		**MRD** (%)	
	v4.1-v3	**v4.1-v4.0**	**(v4.1-v3)/v3**	**(v4.1-v4.0)/v4.0**
30 Mar 2012 (Day)	0.71	0.04	7.1	0.34
10 Nov 2011 (Night)	0.39	0.02	7.8	0.39
9 Dec 2010 (Night)	0.12	0.04	1.6	0.52

For the days mentioned in this table, $\beta'_{532,total}(r)$ values are higher in level-1B ver. 4.xx than ver. 3.xx, and the relative mean bias and MRD are highest in ver. 4.10 than ver. 3.xx and ver. 4.00

products. Increasing the DEM resolution from 30 to 15 arc seconds in ver.4.10, an enhancement in surface detectability is also seen. For the number of detected surfaces, the MRDs between ver. 4.10 and earlier version i.e. ver. 3 are found to be ~1.25 % (30 March 2012) during day-time, and during night-time, it is ~ 2.42 % (10 November 2011) and ~ 2.53 % (9 December 2010). Further analysis on the DEM surface elevation data for all the CALIPSO overpasses (206 nights and 153 days) that occurred within the region extending to 1° in all the four directions from the site during the period 2011-2015 is made. Study using the valid 6510 (night-time) and 4644 (day-time) LASER footprints on the Earth's surface within defined region for the given period revealed that for the number of detected surfaces, the MRD between ver. 4.10 and ver. 3.xx is ~3.41 % with more deviation during night (~3.47 %) than during day (~3.33 %).

In going from CALIPSO ver. 3 to ver. 4.10, major code and algorithm modifications were implemented, e.g. improved data filtering strategies, changes in the calibration algorithms for both 532 nm and 1064 nm, and the revised Probability Density Functions (PDFs) in CAD algorithm. To highlight some of the associated changes due to modifications in ver. 4.10, a typical CALIPSO level 2 VFM profile of 10 May 2008 (~02:00 hrs Local Time (LT)) is processed, and the vertical features as well as the aerosol sub-type classifications are extracted, as shown in **Fig. 5.3(a-b)**.

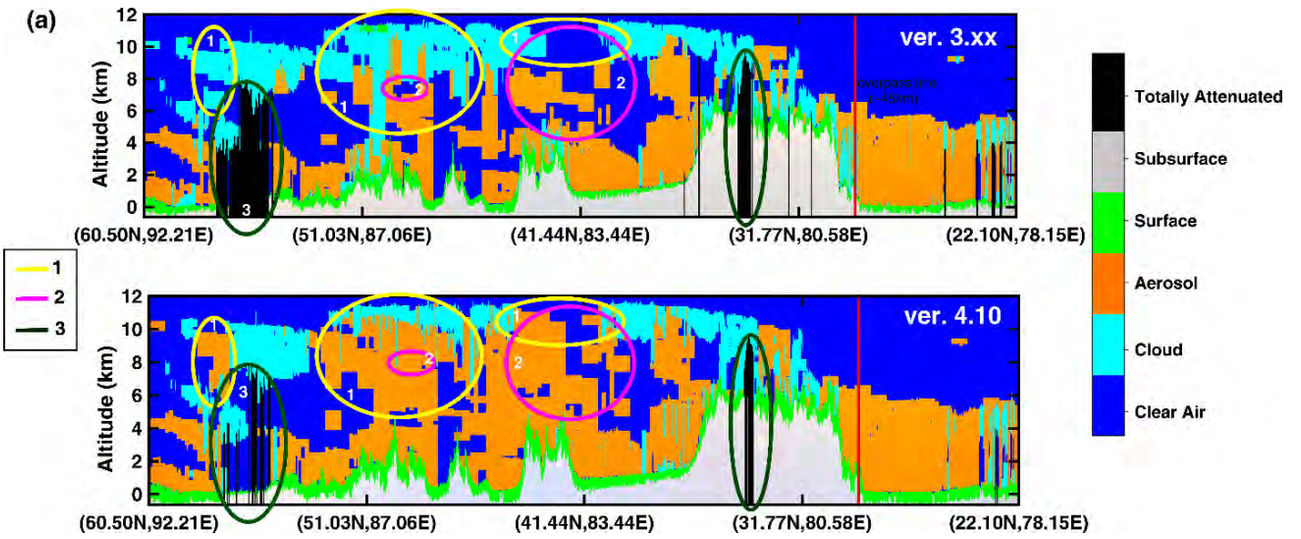

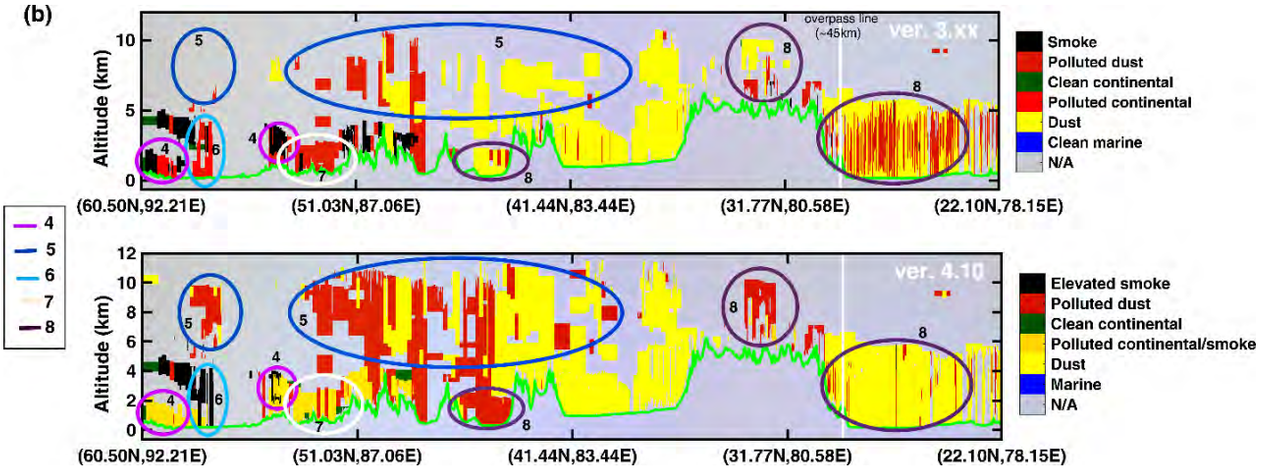

Fig. 5.3. CALIPSO (ver. 3.xx and ver. 4.10) derived **(a)** vertical feature mask, and **(b)** aerosol sub-type classification images of 10 May 2008 (~02:00 hrs LT) transact.

The major changes in the CALIPSO versions are labelled as 1-8 in **Fig. 5.3(a, b)**, whose details are presented in **Table 5.4**.

Table 5.4: Summary of the changes in the CALIPSO ver. 4.10 in relevance to **Fig. 5.3(a, b)**

Label #	Description
1.	Some of the cloud layers in ver. 3.xx are converted to aerosols in ver. 4.10.
2.	In ver. 4.10, there is an increase in the number of layers reported.
3.	Few additional surfaces are detected in ver. 4.10 as compared to ver. 3.xx.
4.	The nomenclatures from 'polluted continental' and 'smoke' in ver. 3.xx has been changed to 'polluted continental/smoke' and 'elevated smoke', respectively in ver. 4.10.
5.	Enhancement in the lofted dust and polluted dust classifications is noticed in ver. 4.10 as compared to ver. 3.xx.
6.	Few polluted continental classifications in ver. 3.xx has been changed to elevated smoke in ver. 4.10.
7.	Few polluted dust cases in ver. 3.xx have been reported as polluted continental/smoke in ver. 4.10.
8.	Few dust cases in ver. 3.xx have been converted to polluted dust in ver. 4.10.

To investigate the changes in vertical features provided by two CALIPSO versions, an analysis is performed by extracting the Feature Classification Flag (FCF) of each detected layer from the level-2 VFM data files for the CALIPSO transacts within the defined geographical region of 28.86°-29.86° N and 78.96°-79.96° E with Nainital almost its center for the period of August

2006 - April 2017. The vertical feature type, with a confidence level of at least 'medium' i.e. 50 ≤ |CAD score| < 70 for aerosol and cloud layers (confirmed using FCF bits 4 and 5), is obtained by decoding the FCF bits 1-3 in decimal form (*Vaughan et al.,* 2016). The changes w.r.t. ver. 3, as observed in ver. 4.10 are explained by constructing a confusion matrix as given in the **Table 5.5.** The confusion matrix shows the comprehensive statistical comparison of the changes in the vertical feature type classifications provided by CALIPSO's ver. 3 and ver. 4.10 products within a coincidence box around Nainital. The overall agreement between ver. 3 and ver. 4.10 in this case is computed by summing the samples which remained unchanged (e.g. clear air – clear air, cloud - cloud) divided by the total number of samples expressed in percentage, and is found to be 94.64 % when a total of 437 day and night-time profiles were taken into account. The level of disagreement between ver. 3 and ver. 4.10 is ~1 % higher in the night-time profiles **(Table 5.6)** as compared to the day-time profiles (**Table 5.7**).

Table 5.5: Confusion matrix showing the 'Tropospheric feature type' expressed in percentage, as obtained from 437 day and night-time CALIPSO VFM profiles, with rows representing the classification using ver. 3 and the columns representing the classification using ver. 4.10.

DAY+NIGHT		**Feature Type, ver. 4.10**						
		invalid	**clear air**	**cloud**	**tropospheric aerosol**	**surface**	**no signal/ totally attenuated**	**TOTAL**
Feature Type, ver. 3	**invalid**	**Nil**	Nil	Nil	Nil	Nil	Nil	0
	clear air	Nil	**97.44 %**	0.40 %	1.84 %	0.30 %	0.02 %	23414038
	cloud	Nil	3.32 %	**87.62 %**	6.09 %	1.92 %	1.05 %	1821564
	aerosol	0.04 %	5.89 %	1.17 %	**90.54 %**	2.35 %	0.01%	3679968
	surface	Nil	0.27 %	0.36 %	0.69 %	**98.55 %**	0.13 %	1057769
	no signal/totally attenuated	0.01 %	9.31 %	0.48 %	1.14 %	1.75 %	**87.31%**	5721878
	TOTAL	2092	23626671	1765319	3945937	1333610	5021588	**35695217**
Overall Agreement between ver. 3 and ver. 4.10 = 94.64 %								

It is observed that about 6 % of the 'cloud' in ver. 3 is converted to 'tropospheric aerosols', and a few 'cloud' or 'aerosol layers' (~ 4 %) are converted to 'surface' in ver. 4.10. Furthermore, ~10 % of the features that were 'totally attenuated' ('no signal') due to opaque clouds, aerosols, and/or stratospheric layers in ver. 3 are classified as 'clear air'/ 'aerosol'/ 'cloud' or as 'surface' in ver. 4.10. The surface detection scheme in ver. 3.xx is based on the general purpose top-down detection scheme that relies on the significant positive excursions in the backscatter signal,

however, the technique sometime during multi-layer scenes and/or highly turbid atmospheres gets fail and leads to signal attenuation. The problem is attended in ver. 4.10 by implementing the derivative-based peak finding algorithm for the surface detection. Hence, the observed additional surface detections in ver. 4.10 may be attributed to this changes in the layer detection schemes between ver. 3 and ver. 4.10. In addition, the detection of extra surfaces in ver. 4.10 primarily happened due to the increase in the DEM resolution from 30 to 15 arc seconds.

Table 5.6: Confusion matrix showing the 'Tropospheric feature type' expressed in percentage, as obtained from 218 night-time CALIPSO VFM profiles, with rows representing the classification using ver. 3 and the columns representing the classification using ver. 4.10.

NIGHT only		**Feature Type, ver. 4.10**						
		invalid	**clear air**	**cloud**	**tropospheric aerosol**	**surface**	**no signal/ totally attenuated**	**TOTAL**
Feature Type, ver. 3	**invalid**	**Nil**	Nil	Nil	Nil	Nil	Nil	0
	clear air	Nil	**96.43 %**	0.43 %	2.90 %	0.24 %	Nil	7423842
	cloud	Nil	1.26 %	**89.83 %**	5.47 %	2.52 %	0.92 %	700504
	aerosol	Nil	4.20 %	1.54 %	**91.21 %**	3.04 %	0.01%	1762829
	surface	Nil	0.10 %	0.30 %	0.51 %	**98.86 %**	0.23 %	390295
	no signal/totally attenuated	Nil	7.94 %	0.67 %	1.40 %	2.29 %	**87.70 %**	2072168
	TOTAL	0	7406806	703659	1892190	522096	1824887	**12349638**
Overall Agreement between ver. 3 and ver. 4.10 = 93.92 %								

Table 5.7: Confusion matrix showing the 'Tropospheric feature type' expressed in percentage, as obtained from 219 day-time CALIPSO VFM profiles, with rows representing the classification using ver. 3 and the columns representing the classification using ver. 4.10.

DAY only		**Feature Type, ver. 4.10**						
		invalid	**clear air**	**cloud**	**tropospheric aerosol**	**surface**	**no signal/ totally attenuated**	**TOTAL**
Feature Type, ver. 3	**invalid**	**Nil**	Nil	Nil	Nil	Nil	Nil	0
	clear air	Nil	**97.90 %**	0.40 %	1.35 %	0.32 %	0.03 %	15990196
	cloud	Nil	4.62 %	**86.23 %**	6.48 %	1.54 %	1.13 %	1121060
	aerosol	0.08 %	7.44 %	0.82 %	**89.93 %**	1.72 %	0.01%	1917139
	surface	Nil	0.37 %	0.39 %	0.79 %	**98.38 %**	0.07 %	667474
	no signal/totally attenuated	0.01 %	10.08 %	0.38 %	0.99 %	1.45 %	**87.09 %**	3649710
	TOTAL	2092	16219865	1061660	2053747	811514	3196701	**23345579**
Overall Agreement between ver. 3 and ver. 4.10 = 95 %								

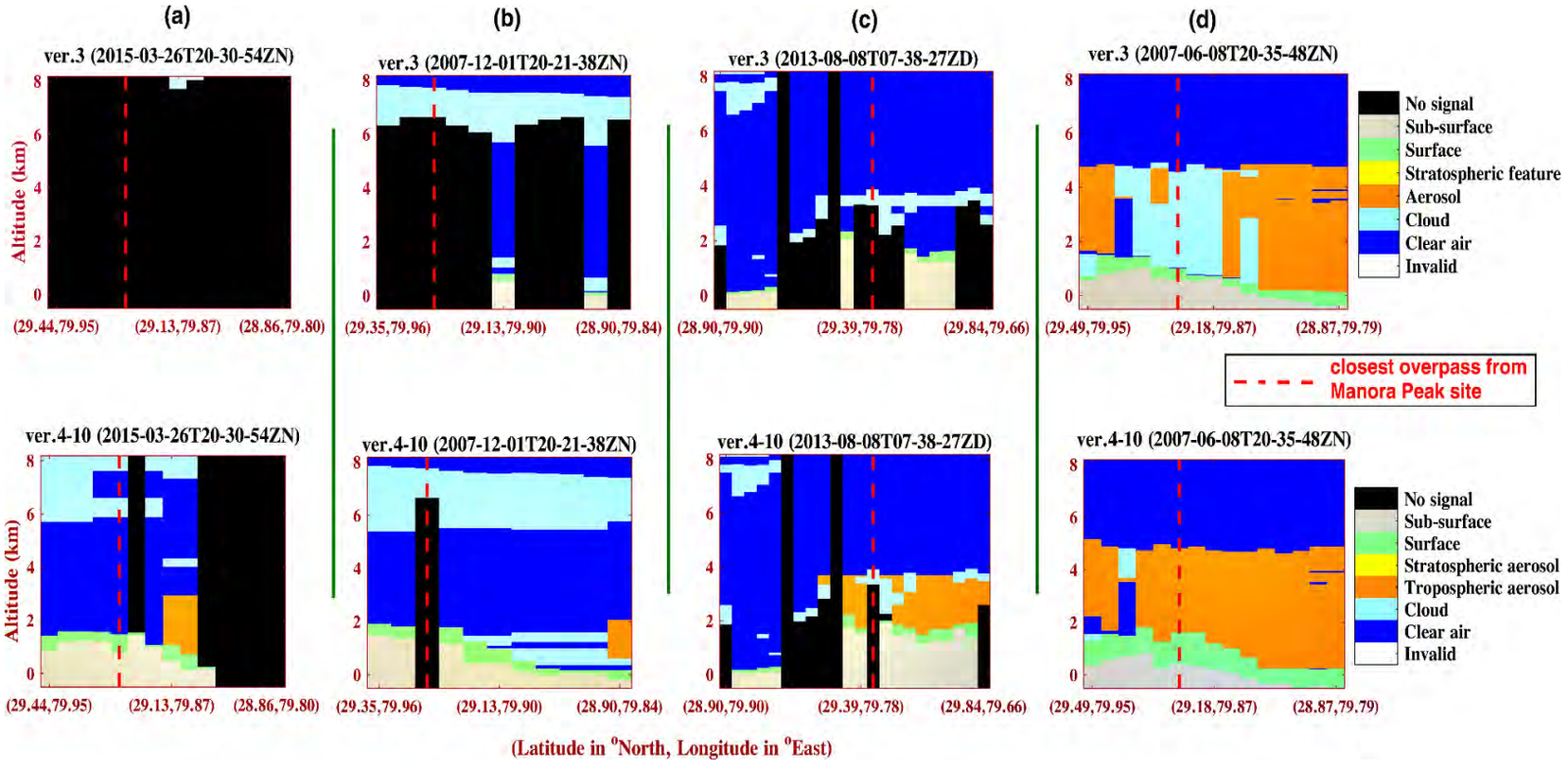

Fig. 5.4. CALIPSO (ver. 3 and 4.10) derived vertical feature types for **(a)** 26 March 2015, 20:30 UTC (~02:00 hrs. LT), **(b)** 01 December 2007, 20:21 UTC (~01:50 hrs. LT), **(c)** 08 August 2013, 07:38 UTC (~13:08 hrs. LT), and **(d)** 08 June 2007, 20:35 UTC (~02:05 hrs. LT), for the altitudes between -0.5 km to 8.2 km.

To illustrate some of the major changes in the vertical features between the CALIPSO versions, four typical transacts on 26 March 2015, 01 December 2007, 08 August 2013, and 08 June 2007 were selected, and the results are presented in **Fig. 5.4(a-d)**. It can be inferred from the figure that in ver. 4.10 there is an enhancement in the feature detection (**Fig. 5.4a-c**) as compared to ver.3. Surface detection is typically higher in ver. 4.10 as compared to ver. 3, and the same is evident in the figure. It is also visible that some of the 'clouds' and 'clear air' features in ver. 3 are changed to 'tropospheric aerosols' in ver. 4.10 (**Fig. 5.4c-d**).

Together with the information on feature types, the CALIPSO VFM product also provides the breakdown of the atmospheric layers including the feature sub-types of aerosols and clouds (*Omar et al.*, 2009). For the same period, the aerosol sub-types were investigated over the defined region. The VFM product ver. 4.10 identifies the seven major aerosol sub-types based on the geographical location, surface elevation, surface type, attenuated backscatter, color ratio and the volume depolarization ratio. These seven different aerosol sub-types in ver. 4.10 are - clean marine, dust, polluted continental/smoke, clean continental, polluted dust, elevated smoke and dusty marine (*Vaughan et al.*, 2016).

In comparison to the aerosol sub-type classifications defined in ver. 3, it is found that the nomenclatures for two sub-types were re-defined and one additional sub-type is included in product ver. 4.10. The change in the nomenclatures from 'polluted continental' and 'smoke' in ver. 3 to 'polluted continental/smoke' and 'elevated smoke', respectively in ver. 4.10 are to overcome the misclassification observed under certain circumstances as reported in earlier studies (*Powell et al.*, 2009; *Adams et al.*, 2012). This change in the nomenclature also eliminates the uncertainties associated with the discrimination between smoke and polluted continental aerosol within the planetary boundary layer. The inclusion of 'dusty marine' in ver. 4.10 is to distinguish it from the clean marine aerosol, and is applicable for the cases where the marine aerosols are contaminated with dust and anthropogenic pollution. Since CALIOP is an elastic backscatter LiDAR, therefore, to accomplish the above-mentioned changes in the aerosol sub-types, the LRs corresponding to these sub-types have also been updated, as portrayed in **Fig. 5.5**, which also shows the frequency of the aerosols sub-types identified by the two CALIPSO product versions over the defined region during August 2006 – April 2017.

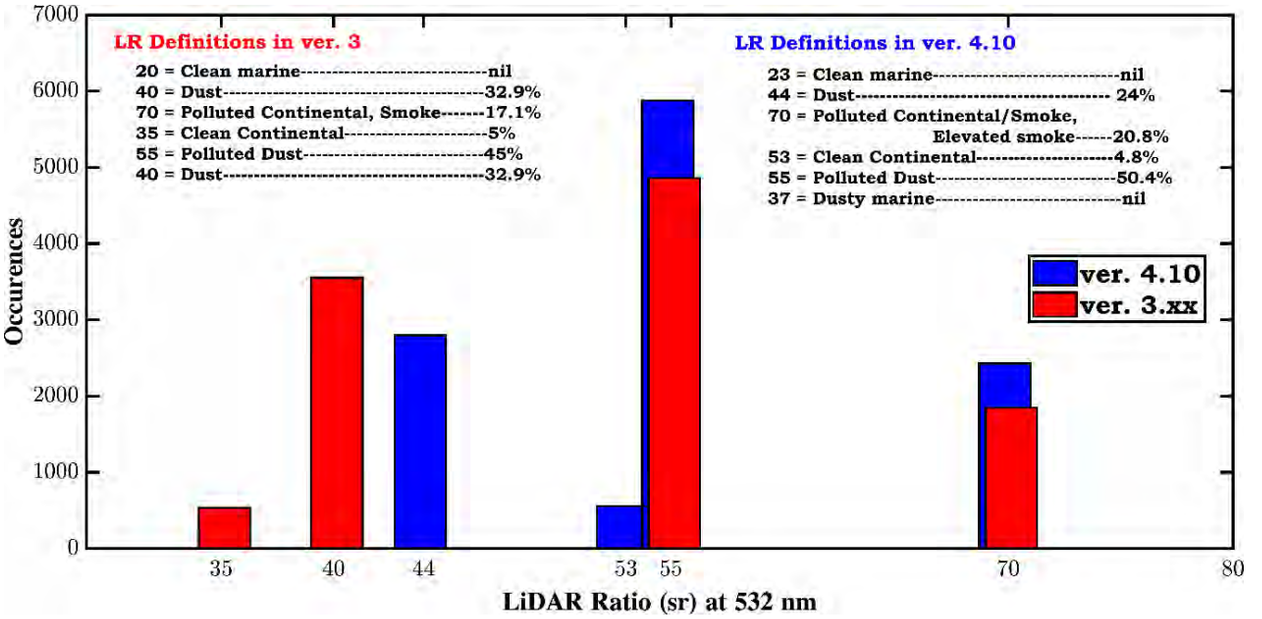

Fig. 5.5. Aerosol sub-types and 532 nm LiDAR ratio identified by the CALIPSO product ver. 3 and 4.10 over the geographical region of 28.86°-29.86° N and 78.96°-79.96° E for the period of August 2006- April 2017.

To further understand the changes over the defined region, the FCF bits 10-12 that defines the aerosol sub-types are decoded after confirming the feature type as aerosol with the quality assurance level as "high" (FCF bit 13) in both the CALIPSO versions. The confusion matrix is formed (**Table 5.8**) to show the changes in the aerosol sub-types retrieved using ver. 3 and ver. 4.10 data. In the case of aerosol sub-type the overall agreement between the two versions is found 68.62 %, for a total of 437 day and night-time VFM profiles. The level of disagreement is ~9.5 % higher in night-time (**Table 5.9**) profiles as compared to that of day-time (**Table 5.10**).

From **Table 5.8**, it is seen that in ver. 3, the sub-types identified as 'dust' (~23.5 %), 'smoke' (~ 24 %) and 'polluted continental' (~25.5 %) have now become 'polluted dust' in ver. 4.10. The major portion of 'clean continental' (~ 42.5 %) in ver. 3 are converted to 'polluted continental/smoke' in ver. 4.10. About 28.7 % of 'smoke' and ~ 65.2 % of 'polluted continental' in ver. 3 are changed to 'elevated smoke' and 'polluted continental/smoke' in ver. 4.10. All these changes in aerosol sub-types can be attributed to the major revisions done in the aerosol retrieval and classification algorithms of ver. 4.10 data release, as mentioned in the data quality summary (https://www-calipso.larc.nasa.gov/resources/calipso_users_guide/qs/cal_lid_l2_all_v4-10.php).

Table 5.8: Confusion matrix showing the 'Aerosol sub-type' expressed in percentage, as obtained from 437 day and night-time CALIPSO VFM profiles, with rows representing the classification using ver. 3 and the columns representing the classification using ver. 4.10.

DAY + NIGHT		Aerosol sub-type, ver. 4.10								
		not determined	clean marine	dust	polluted continental /smoke	clean continental	polluted dust	elevated smoke	dusty marine	TOTAL
Aerosol sub-type, ver. 3	not determined	**Nil**	Nil	Nil	Nil	Nil	Nil	Nil	Nil	0
	clean marine	Nil	**Nil**	Nil	Nil	Nil	Nil	Nil	Nil	0
	dust	Nil	Nil	**75.50 %**	0.65 %	0.13 %	23.43 %	0.29 %	Nil	1047178
	polluted continental	Nil	Nil	0.39 %	**65.24 %**	1.40 %	25.51 %	7.46 %	Nil	187050
	clean continental	Nil	Nil	0.13 %	42.47 %	**29.60 %**	12.16 %	15.63 %	Nil	31266
	polluted dust	Nil	Nil	13.20 %	6.15 %	0.69 %	**77.62 %**	2.34 %	Nil	1688253
	smoke	Nil	Nil	0.80 %	45.89 %	0.59 %	23.98 %	**28.73 %**	Nil	514944
	others	Nil	Nil	Nil	Nil	Nil	Nil	Nil	**Nil**	0
	TOTAL	0	0	1018494	482243	27937	1730721	209296	0	**3468691**
Overall Agreement between ver. 3.xx and ver. 4.10 = 68.62 %										

Table 5.9: Confusion matrix showing the 'Aerosol sub-type' expressed in percentage, as obtained from 218 night-time CALIPSO VFM profiles, with rows representing the classification using ver. 3 and the columns representing the classification using ver. 4.10.

NIGHT only		Aerosol sub-type, ver. 4.10								
		not determined	clean marine	dust	polluted continental /smoke	clean continental	polluted dust	elevated smoke	dusty marine	TOTAL
Aerosol sub-type, ver. 3	not determined	**Nil**	Nil	Nil	Nil	Nil	Nil	Nil	Nil	0
	clean marine	Nil	**Nil**	Nil	Nil	Nil	Nil	Nil	Nil	0
	dust	Nil	Nil	**69.57 %**	0.66 %	0.23 %	29.40 %	0.13 %	Nil	465719
	polluted continental	Nil	Nil	0.45 %	**59.44 %**	2.02 %	27.42 %	10.66%	Nil	126799
	clean continental	Nil	Nil	0.12 %	31.38 %	**38.29 %**	8.40 %	21.81%	Nil	22405
	polluted dust	Nil	Nil	16.11 %	5.81 %	1.50 %	**73.52 %**	3.06 %	Nil	775916
	smoke	Nil	Nil	0.31 %	39.33 %	0.86 %	28.59 %	**30.91 %**	Nil	281949
	others	Nil	Nil	Nil	Nil	Nil	Nil	Nil	**Nil**	0
	TOTAL	0	0	450493	241436	26315	824652	129892	0	**1672788**
Overall Agreement between ver. 3.xx and ver. 4.10 = 63.70 %										

Table 5.10: Confusion matrix showing the 'Aerosol sub-type' expressed in percentage, as obtained from 219 day-time CALIPSO VFM profiles, with rows representing the classification using ver. 3 and the columns representing the classification using ver. 4.10.

DAY only		Aerosol sub-type, veer 4.10								
		not determined	**clean marine**	**dust**	**polluted continental /smoke**	**clean continental**	**polluted dust**	**elevated smoke**	**dusty marine**	**TOTAL**
Aerosol sub-type, ver. 3	**not determined**	**Nil**	Nil	Nil	Nil	Nil	Nil	Nil	Nil	0
	clean marine	Nil	**Nil**	Nil	Nil	Nil	Nil	Nil	Nil	0
	dust	Nil	Nil	**80.25 %**	0.64 %	0.04 %	18.64 %	0.42 %	Nil	581459
	polluted continental	Nil	Nil	0.26 %	**77.44 %**	0.10 %	21.47 %	0.73 %	Nil	60251
	clean continental	Nil	Nil	0.17 %	70.53 %	**7.62 %**	21.68 %	Nil	Nil	8861
	polluted dust	Nil	Nil	10.73 %	6.44 %	0.004 %	**81.10 %**	1.72 %	Nil	912337
	smoke	Nil	Nil	1.41 %	53.82 %	0.26 %	18.41 %	**26.10 %**	Nil	232995
	others	Nil	Nil	Nil	Nil	Nil	Nil	Nil	**Nil**	0
	TOTAL	0	0	568001	240807	1622	906069	79404	0	**1795903**
Overall Agreement between ver. 3.xx and ver. 4.10 = 73.20 %										

Fig. 5.6(a-d) illustrates some of the major changes in the aerosol sub-types between ver. 3 and ver. 4.10 for the CALIPSO transacts on 12 May 2016, 24 April 2015, 09 September 2006, and 29 April 2016. As seen from **Fig. 5.6a**, some of the 'dust' sub-type is changed to 'polluted dust' in ver. 4.10, along with the appearance of new layers of 'polluted dust', 'elevated smoke' and 'polluted continental/smoke' (**Fig. 5.6b-d**). The inclusion of these additional sub-types seems to be valid because they are the dominant sources of pollutants over the studied region as shown in earlier studies (*Badarinath et al.,* 2006*; Pant et al.,* 2006*; Solanki et al.,* 2013*; Kazuo, T.,* 2014*; Ojha et al.,* 2014*; Vijayakumar et al.,* 2016).

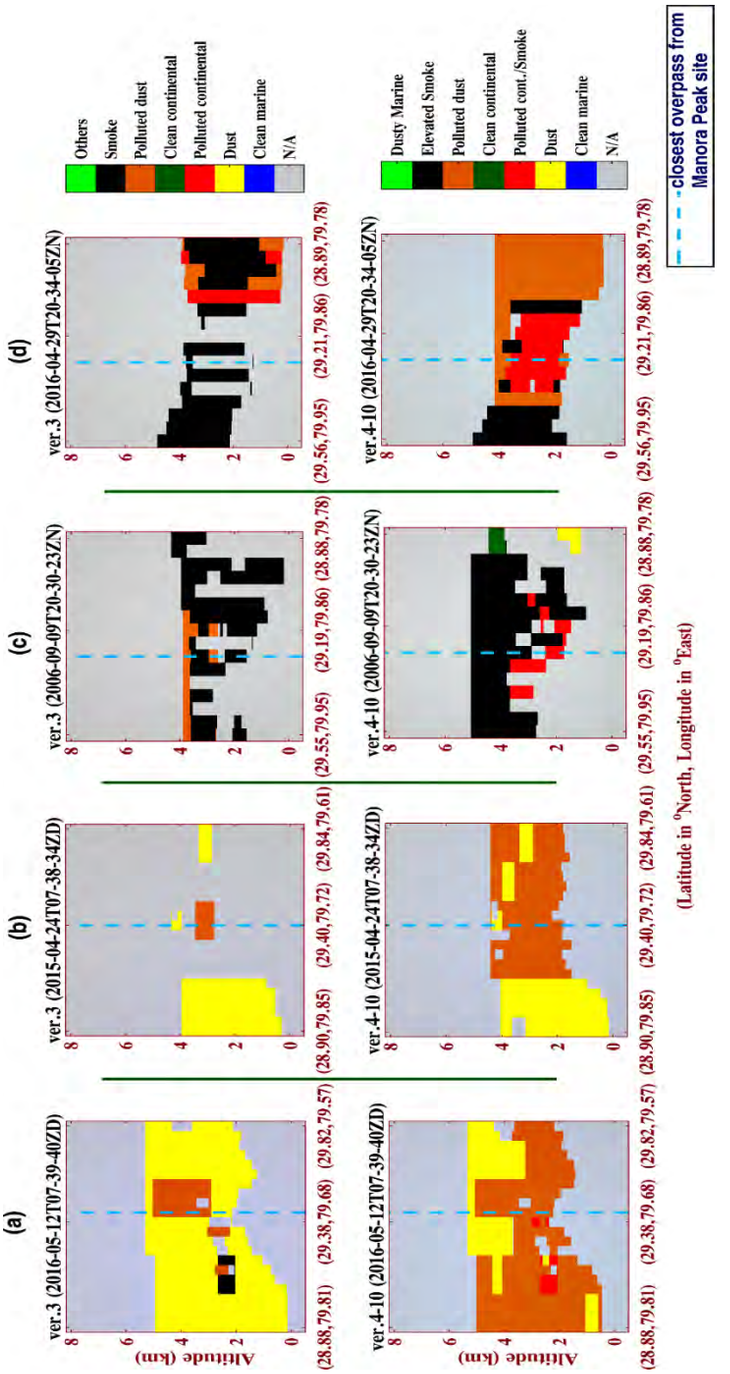

Fig. 5.6. CALIPSO (ver. 3 and 4.10) derived aerosol sub-types for **(a)** 12 May 2016, 07:39 UTC (~13:09 hrs. LT), **(b)** 24 April 2015, 07:38 UTC (~13:08 hrs. LT), **(c)** 09 September 2006, 20:30 UTC (~02:00 hrs. LT), and **(d)** 29 April 2016, 20:34 UTC (~02:04 hrs. LT), for the altitudes between -0.5 km to 8.2 km.

5.1.2.3. Evaluation of CALIPSO with AERONET measurement

It is noted from the previous sub-sections that the CALIPSO ver. 4.10 has shown significant changes in the data quality, hence further attempt is made to evaluate the columnar AOD retrievals of CALIPSO with AERONET AOD measurements. Within 100 km distance from the site, a total of

23 valid overpasses were observed between 2008 - 2012, which were coinciding with the day-time AERONET measurements and subjected for the statistical analysis as shown in **Fig. 5.7**.

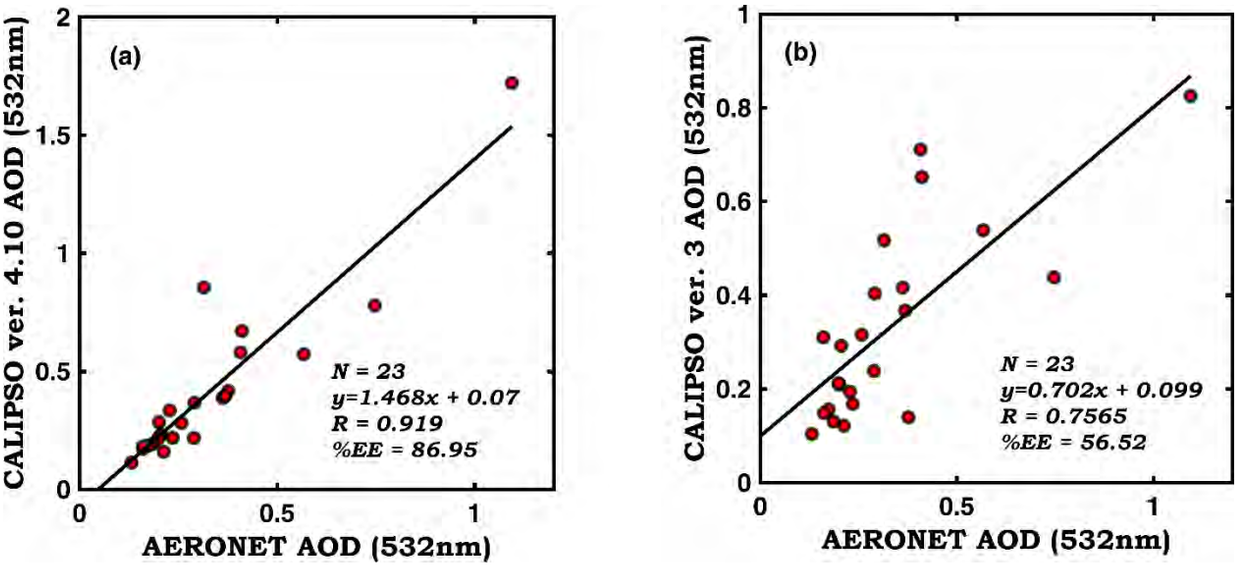

Fig. 5.7. Scatter plot with one-one line comparison for AERONET AOD and **(a)** CALIPSO ver. 4.10, **(b)** ver. 3 column AOD measurements for 23 valid overpasses observed between 2008 - 2012.

Result shows that AOD from CALIPSO ver. 4.10 is highly correlated with AERONET AOD (R ~0.92) and having high %EE (~86.95) whereas for ver. 3 it turned out to be relatively low correlation (R ~0.76) with EE value of ~56.52%. The evaluation of the two versions has revealed that the CALIPSO ver. 4.10 is significantly improved and enhanced version, particularly over the region of this study.

5.1.2.4. Comparison of MODIS Terra (C6.0 DB) and CALIPSO (ver. 3 and 4.10)

Previous sub-sections have revealed that the AOD values provided by MODIS Terra C6.0 DB and CALIPSO ver. 4.10 are in better agreements with the ground truth, therefore, with this background, it will be interesting to inter-compare these satellite products as well (*Kittaka et al.* 2011*; Redemann et al.*, 2012*; Bibi et al.*, 2015). The CALIPSO ver. 4.10 is most recent product being explored on the regional scale, particularly, over the Himalayan region. Hence, to assess the

improvements reported in ver. 4.10 over the established and widely used CALIPSO ver. 3, both the versions are compared with MODIS AOD as given by **Fig. 5.8**.

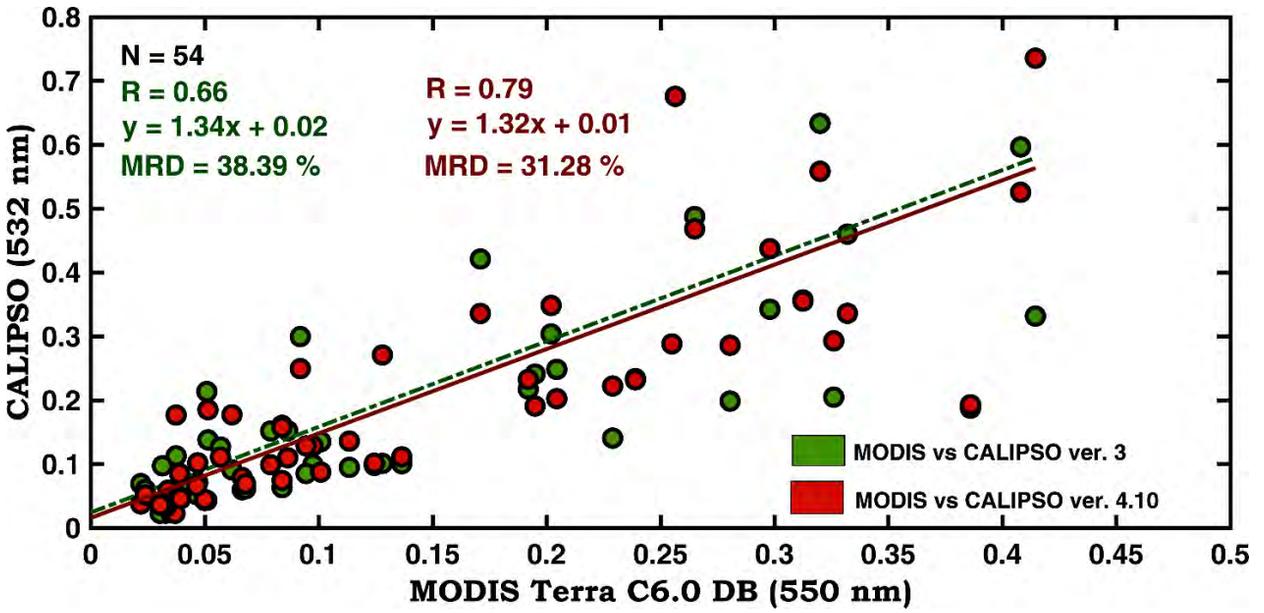

Fig. 5.8. Scatter plot with one-one line comparison for the AOD from MODIS Terra C6.0 DB and CALIPSO (ver. 3 and 4.10).

The AOD retrievals from CALIPSO product ver. 4.10, demonstrated better Pearson's correlation (R ~0.79) and reduced MRD (~ 31.3%) with MODIS AOD, as compared to the CALIPSO ver. 3. In addition, the RMS deviation and MBE in the AOD values between CALIPSO product ver. 4.10 and MODIS Terra C6.0 DB (~0.12 and ~0.06, respectively), are comparatively lower, in comparison to that observed between CALIPSO product ver. 3 and MODIS Terra C6.0 DB (~0.18 and ~0.07, respectively). These matrices indicate that the AOD retrievals from CALIPSO ver. 4.10 can be used in synergy with MODIS Terra C6.0 DB, over the complex Himalayan region. In general, the correlation values estimated between MODIS and CALIPSO are relatively lower as compared with the AERONET measurements individually. This may be attributed to certain limitations and uncertainties associated with the sensors depending upon the prevailing weather conditions (e. g. clouds), solar radiation, geographical locations, instrument calibration, coincidence circle, collocation criteria etc. (*Redemann et al.*, 2012).

5.1.3. Utilization of the satellite (MODIS and CALIPSO) based aerosol retrievals

5.1.3.1. Estimation of LR using AERONET and MODIS

The LR computed for the three LiDAR systems operated at ARIES, Nainital during 2008 - 2012, by using the AOD values retrieved from AERONET and MODIS Terra collections, is represented by box plot together with the statistics in **Fig. 5.9**. The horizontal line inside the box is the median value of LR for various data sets.

The LR values computed through ground truth range from about 10 to 45 for various systems, and the same while computed through three collections of MODIS Terra, it is found to vary between 6 and 52. However, LR values in all the combinations are found to be lower (< 16) during December-January and higher (> 43) in the months of spring and summer months (March and May). From the figure, it may be noticed that median LR computed using Terra C5.1 DT (LR~22) and C6.0 DB (LR~18) are closer to that of AERONET (LR~21), as compared to Terra C6.0 DT (LR~35) which is quite high and showing a maximum LR of 52.

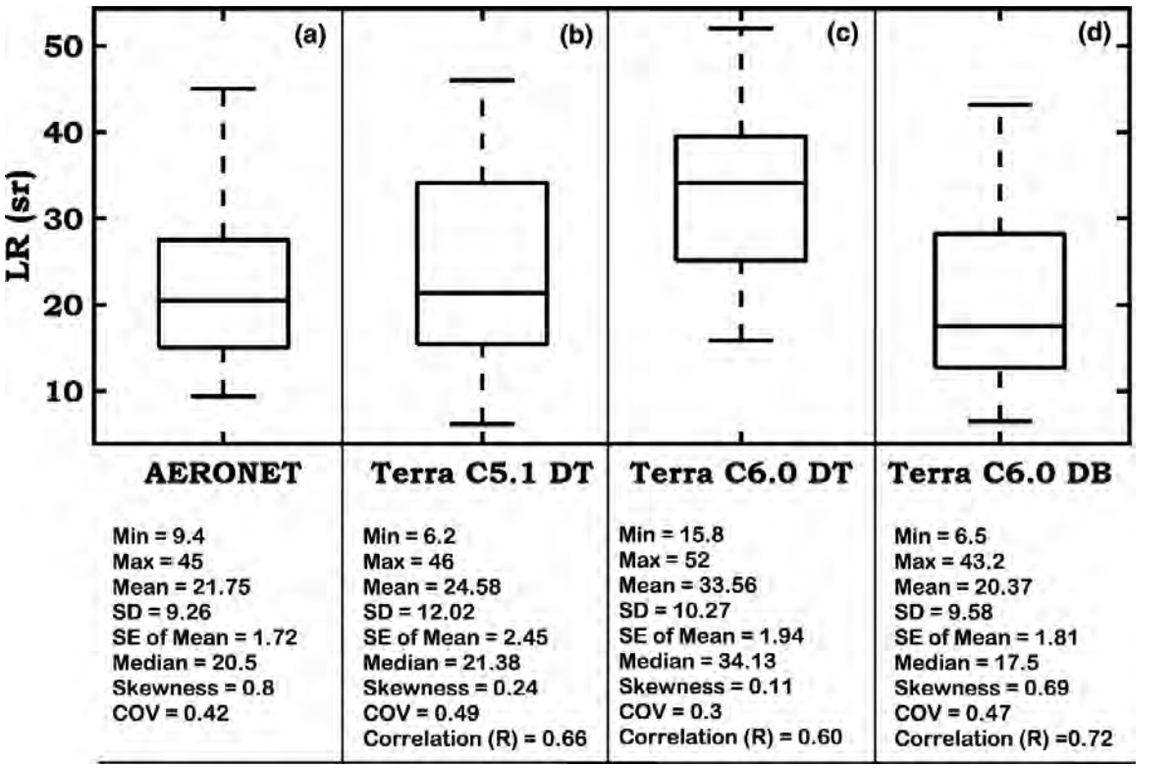

Fig. 5.9. LR box plot and statistics derived using LiDAR and **(a)** AERONET, **(b)** MODIS Terra C5.1 DT, **(c)** MODIS Terra C6.0 DT, and **(d)** MODIS Terra C6.0 DB.

The Pearson's correlation coefficient is estimated in reference to LR using AERONET, for all three Terra collections as shown in **Fig. 5.10(a-c)**, and C6.0 DB, among all, is found to be highly correlated (R~0.72) with AERONET. Here, the non-zero and positive intercepts in the plots represents the bias that could be associated with the differences in the AOD values obtained from AERONET and MODIS (due to different methodology/ retrieval algorithms), that were used in the iteration process for LR computation.

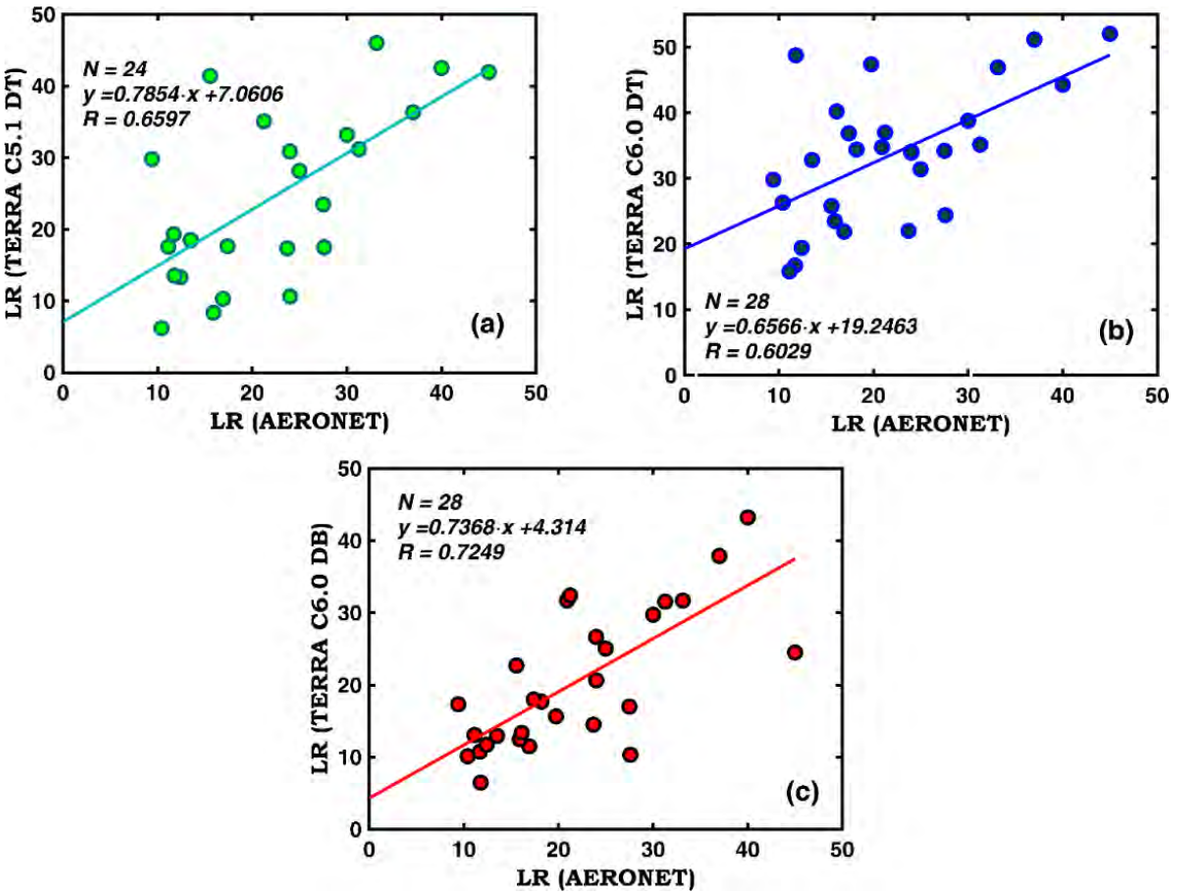

Fig. 5.10. Scatter plot with one-one line comparison for AERONET LR and **(a)** MODIS Terra C5.1 DT, **(b)** MODIS Terra C6.0 DT, and **(c)** MODIS Terra C6.0 DB.

5.1.3.2. Estimation of BL height using Radiosonde and CALIPSO

In order to make use of the evaluated CALIPSO ver. 4.10 data sets, here an attempt is made to estimate the boundary layer height and compared with the in-situ radiosonde measurements from

the site. **Fig. 5.11(a-d)** shows the typical BL height computed using the radiosonde (PT and SH-gradient methods) and CALIPSO (threshold and WCT methods) observations for 16 June 2011 at ~ 11:30 hrs and ~ 13:15 hrs LT, respectively. **Fig. 5.11e** shows the total aerosol backscatter coefficient profile obtained from CALIPSO for 16 June 2011 on which the threshold and WCT methods are applied (**Fig. 5.11c-d**).

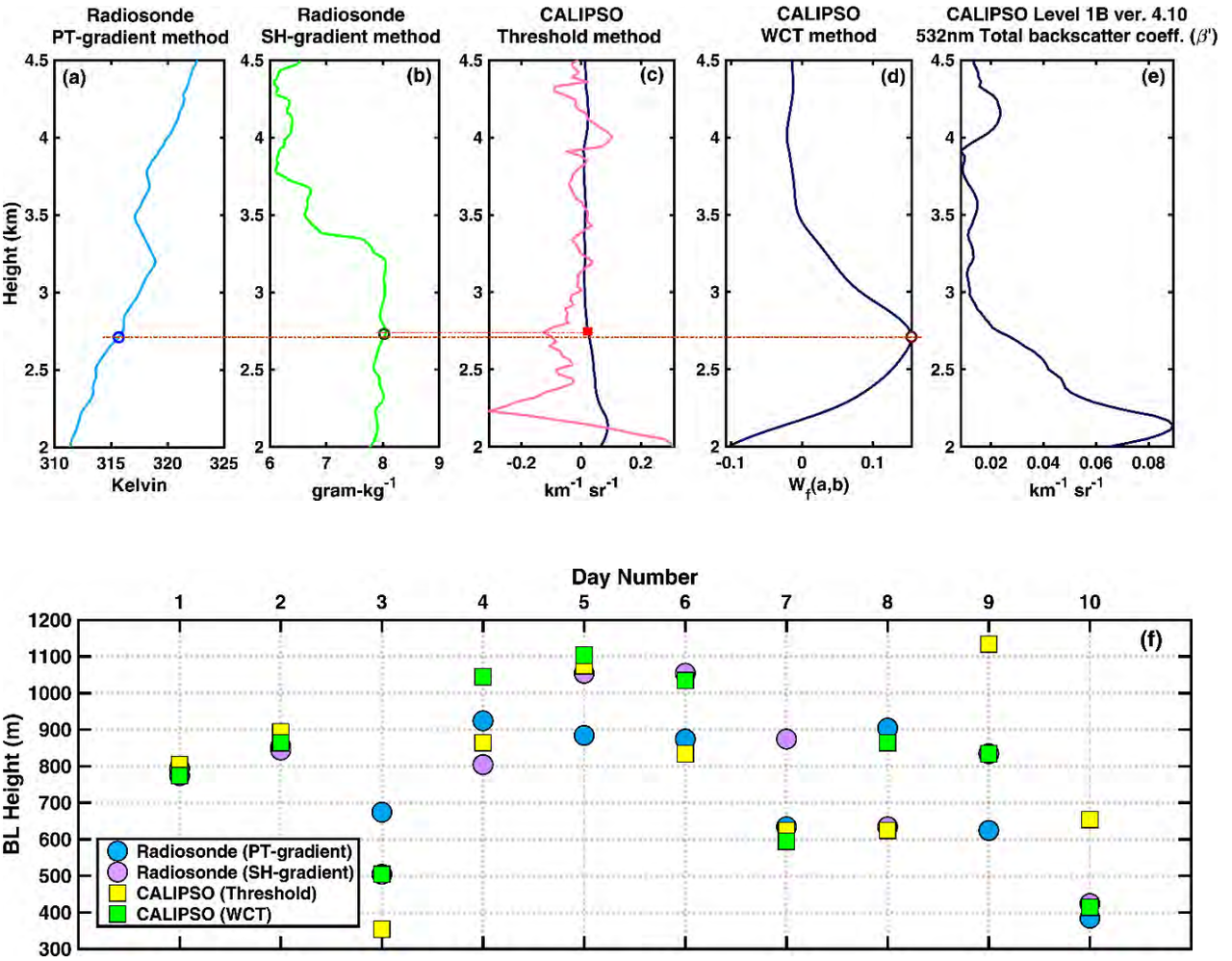

Fig. 5.11. Typical radiosonde profiles (16 June 2011, ~11:30 hrs.) of **(a)** potential temperature, **(b)** specific humidity with BL height marked by circle; BL height estimated from CALIPSO (ver. 4.10 level-1B) using **(c)** threshold, and **(d)** WCT methods that were applied on **(e)** the total aerosol backscatter coefficient profile (an average of the profiles lying within 100 km coincidence circle of the closest CALIPSO overpass) of 16 June 2011 (~13:15 hrs. LT); **(f)** BL heights obtained from radiosonde (PT and SH-gradient methods) and CALIPSO (threshold and WCT methods) for the 10 studied days.

From the study location (ARIES, Nainital), which is a complex terrain, the BL height is not expected to evolve beyond 1.2 km AGL (*Singh et al*., 2016), therefore most of the time one looks for its estimation within 2 km AGL for a given location. However, above this height and up to ~ 5 or 6 km amsl, the wind pattern usually changes (referred as wind transition zone) that leads to the interaction with different air masses, that sometime causes rapid fall in the air temperature, for e.g. in the shown case of 16 June 2011, the air temperature fell down rapidly to 8°C (~3.5 km) from 12.5°C (~ 3.2 km). This rapid fall in temperature introduces the sharp gradient in the potential temperature (θ) as evident in **Fig. 5.11a** at ~ 3.2 km. The potential temperature is is related as $\theta = T\left(\frac{P_0}{P}\right)^{R/c_p}$, where, T is the absolute temperature at pressure P, P_0 is a standard reference pressure, R is the gas constant, c_p is specific heat capacity, R/c_p= 0.286 for air. However, as we go up in the atmosphere the air temperature T decreases as per the standard lapse rate whereas P has exponential decrease.

Fig. 5.11f shows the decent agreement between the BL height derived from the radiosonde and CALIPSO. A recent study (*Singh et al.,* 2016) over the complex terrain of ARIES, Manora peak has revealed that, with radiosonde, the SH-gradient method for BL height estimation is the good choice. However, SH and PT-gradient methods (radiosonde) were utilized, to compare the CALIPSO derived BL height. It is evident from the figure that 90% BL heights from SH-gradient method matches (within ±50 m tolerance) with CALIPSO derived BL heights. In 70% of the cases, a reasonably good agreement between the SH-gradient (radiosonde) and the WCT (CALIPSO) methods is seen, whereas in 90 % of the cases, the WCT derived BL height is very well matching with the radiosonde derived BL height using either of the methods (PT and SH-gradient). This suggests that with CALIPSO, the WCT method works well and could be the best choice for BL height computation over the complex terrain such as ARIES, Nainital, and complements the SH-gradient method used in the BL height retrieval with radiosonde observation. Moreover, a number of studies across the globe have also proved the effectiveness of WCT method in BL height estimation (*Brooks,* 2003*; Compton et al.,* 2013).

The use of CALIPSO data in estimating the BL height over typical sites where ground based measurements are difficult to conduct, could be one of the paramount importance, for the studies related to the vertical transport of pollutants and their dispersions. Additionally, there are other

model products like WRF (*Hegarthy et al*., 2018), MERRA-2 and ECMWF (*Palm et al*., 2005; *McGrath Spangler and Denning*, 2012) that may also be used in conjunction with CALIPSO for PBL height detection and evaluation.

Further, it is established that the BL heights from the CALIPSO profiles computed using the WCT method shows high degree of accuracy and offers larger adjustability than the threshold method. With this background a long term seasonal statistics on the BL heights were estimated using the CALIPSO data (December 2006- May 2017) for the two contrasting seasons – DJF and MAM, averaged over the geographical boundary 26-36°N and 72-86°E, where the major portion of north India is confined, as shown in **Fig. 5.12(a, b)**. For this study only the daytime observations were considered to avoid the influences from residual layer. The errors associated with clouds were also nullified by considering only the cloud-free profiles obtained from CALIPSO.

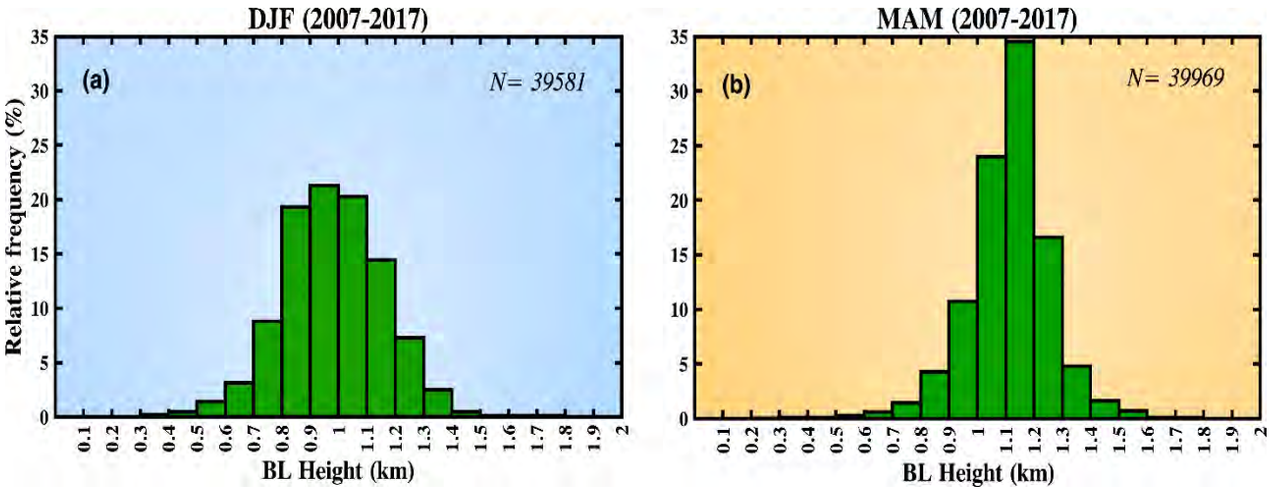

Fig. 5.12. Frequency distribution of average BL heights over 26-36°N and 72-86°E from CALIPSO satellite data of 11 years (2007 - 2017) for **(a)** winter season i.e. December-February (DJF), and **(b)** for spring/summer season i.e. March – May (MAM).

Fig. 5.12(a, b) reveals that the BL heights over the studied region tends to be on the higher side during MAM, as compared to the winter season. Similar finding is reported on a local scale from ARIES Nainital site based on the studies conducted using the ground based RaDAR wind profiler measurements (*Singh et al.*, 2016).

5.1.4. Aerosol transport studies based on synergic ground and satellite observations

5.1.4.1. AERONET measurements

As discussed in the previous section, it is observed that low LR mainly belong to the winter and high LR to the spring and summer, however, post-monsoon month of November witnesses the transport of pollutants originating from the agricultural fire activity in the nearby western part of the country and may contribute to high LR values. In order to study the dynamics, the data sets available from ground and satellite based measurements are explored over this region. In the process, three suitable cases in coincidence to the CALIPSO overpass days (**Table 5.3**) were picked up 9 December 2010 (9D10), 10 November 2011 (10N11) and 30 March 2012 (30M12), and investigated thoroughly for the source of production, and their transport. To understand the aerosol loading and mode of particles, the AERONET measurements from the study site (ARIES, Nainital) is utilized for the above mentioned days. **Fig. 5.13(a-c)** shows the diurnal variations in the AERONET measured AOD (500 nm), temporal variation of AE in the wavelength band of 440 - 870 nm ($AE_{440-870}$) along with columnar water vapor content derived from 935 nm channel for the above mentioned study days. The AE is an indicator of average aerosol concentrations which are broadly distributed between fine and coarse mode particles, where each mode has a characteristic size distribution, chemical composition, and optical properties. $AE \leq 1$ and $AE > 1$ indicate the presence of coarse and fine mode aerosols, respectively. $AE > 1.5$ is an indication of intensive fine mode aerosols.

AOD values observed are least on 9D10, overall high on 30M12 and in between the two on 10N11. However, a strong diurnal variability in the afternoon hours (06:00-08:00 UTC, LT = UTC +05:30 hrs) is observed on 30M12 and 10N11 in AOD and columnar water vapour with an increasing trend that approaches to a maximum thereafter. Since the site is located at the ridge top, therefore enhancement in the AOD values on these days may be due to the dominance of slope winds, flowing during daytime hours that would have brought the aerosols and the pollutants from the adjoining plains and nearby valleys to the site. Past studies over the site have also reported that AOD and aerosol black carbon mass concentrations are generally on the higher side during afternoon in comparison to the morning hours due to plain-to-mountain and mountain-valley circulations (*Pant et al*., 2006; *Dumka et al*., 2014).

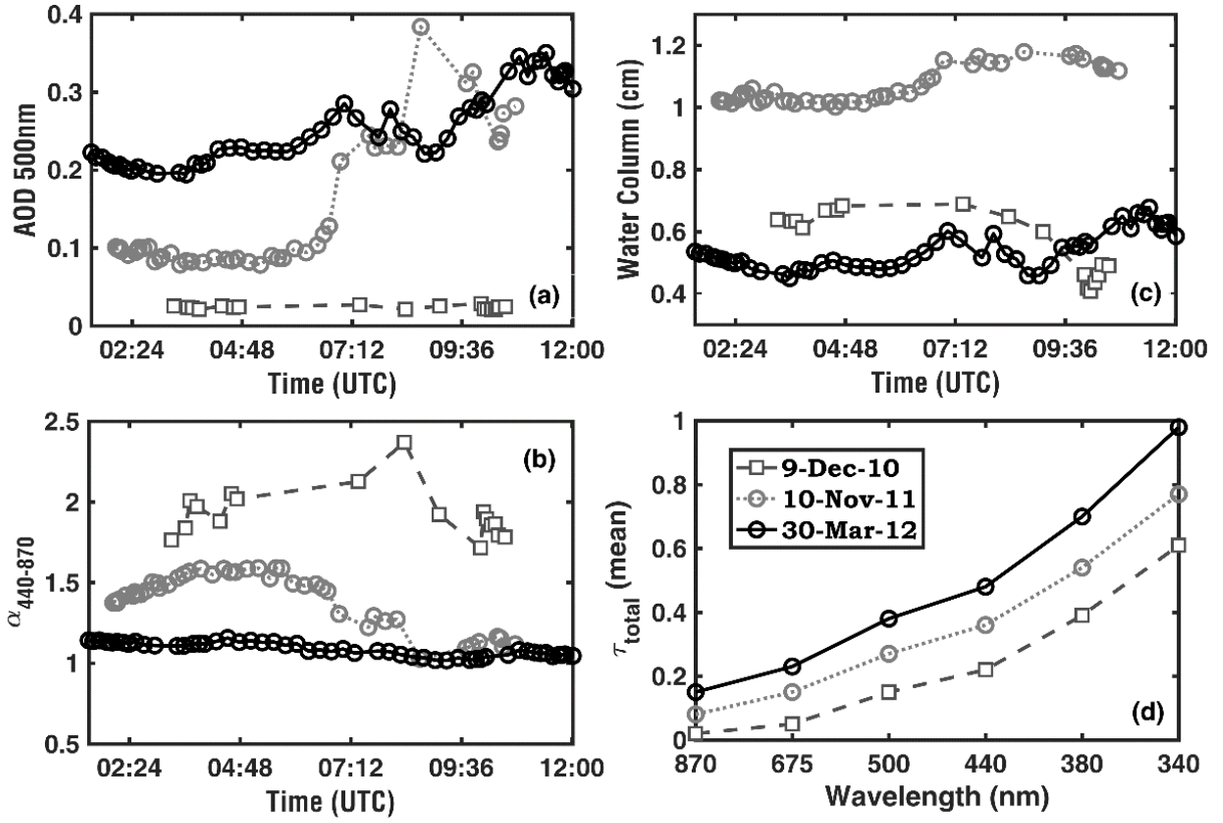

Fig. 5.13. AERONET measured **(a)** AOD at 500 nm, **(b)** AE at 440-870 nm, **(c)** columnar water vapor content, and **(d)** total aerosol optical thickness in the spectral range from 340 - 870 nm, for 9 December 2010, 10 November 2011 and 30 March 2012.

On 10N11, a sudden increase in AOD (0.09 to 0.38) and columnar water vapour (1.0 to 1.2 cm) is noted after 07:00 UTC, also at the same time AE, although high (~1.34 ± 0.25), but showed the decreasing trend (1.59 to 1.03). An extremely high value of columnar water vapor, along with high AOD and AE (>1) on 10N11 may be understood as the presence of anthropogenic particles in the atmosphere with the tendency to attract moisture into condensation. Similarly, on 30M12 (a summer day), the maximum enhancement in AOD from 0.19 to 0.35 with AE (~1.07 ± 0.07) may be attributed to the long range transport of coarse mode particles that are usually associated with the dust. The volume particle size distribution derived from the AERONET inversion algorithm for 10N11 and 30M12, is given by **Fig. 5.14**, which has a bimodal nature, and clearly shows the presence of fine and coarse mode particles on these respective days. The aerosol size distribution data for 9D10 was not available, and hence missing in this figure. The aerosol particles with radius ranging from 0.05 to 0.6 μm are considered as fine (case of 10N11), while those greater than 0.6 μm

are considered as coarse (case of 30M12) (*Dubovik et al*., 2002). The dominance of a particular mode in the aerosol distribution curve is governed by the factors such as geographical location, season, production sources and their abundance. The detailed description on the source apportionment and nature of the aerosol particles for these days are discussed in great details in the sub-sections. On 9D10, the AOD values are quite low with peak value of ~0.03 at 09:30 UTC, until then there exists an opposite trend between the AOD and columnar water vapor. The rapid rise in the AE between 08:00 and 09:00 UTC is also seen on 9D10, which surpasses even a maximum of 2. This extremely high AE value indicates the presence of intensive fine mode particles that might have been produced elsewhere and transported to the site by winds. To understand the mechanism behind extremely low AOD and extremely high AE on 9D10, a thorough investigation is also included in the subsequent section as one of the case study. The total optical thickness ($\tau_{total} = \tau_{aerosol} + \tau_{Rayleigh} + \tau_{Gases} + \tau_{cloud}$) typically decreases with increasing wavelengths, and the same is noticeable in **Fig. 5.13d**. On 30M12, the total optical thickness variations within the spectral range from 340 to 870 nm are highest as compared to the other two days. The total optical thickness variations on 10N11 are also on the higher side, and on 9D10 it is found to be the lowest.

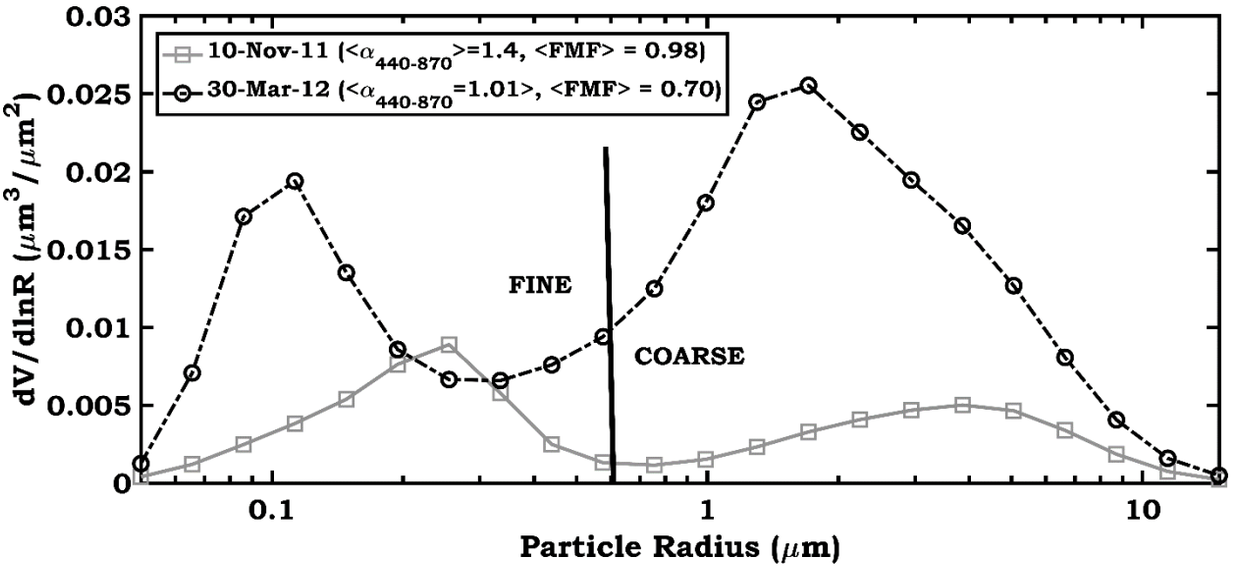

Fig. 5.14. AERONET derived volume particle size distributions at ARIES, Nainital for 10 November 2011 and 30 March 2012.

It is interesting to note enhanced columnar water vapor content on 10N11 than other study days (**Fig. 5.13c**), which could be due to the dominant fine mode particles (e.g. smoke plumes) in the atmosphere. In general, the anthropogenic sources, mainly emanating smoke is thought to be hydrophobic, but there have been reports of high water vapor content within the smoke plumes (e.g., *Clements et al*., 2006; *Parmar et al*., 2008). Further investigation performed in this direction suggested associations with the cyclone Keila, which developed over the Arabian Sea during 28 October - 3 November 2011, and moved west to west-northward and ended up in increasing the moisture over a large region including our site of observation. To understand the connection, the variations in the 6-hourly Total Column Water (TCW) in cm, is studied for the region 0-40°N and 55-100°E during 26 October– 12 November 2011. **Fig.5.15(a-t)** shows the temporal variations in TCW during the circulation phase of Keila.

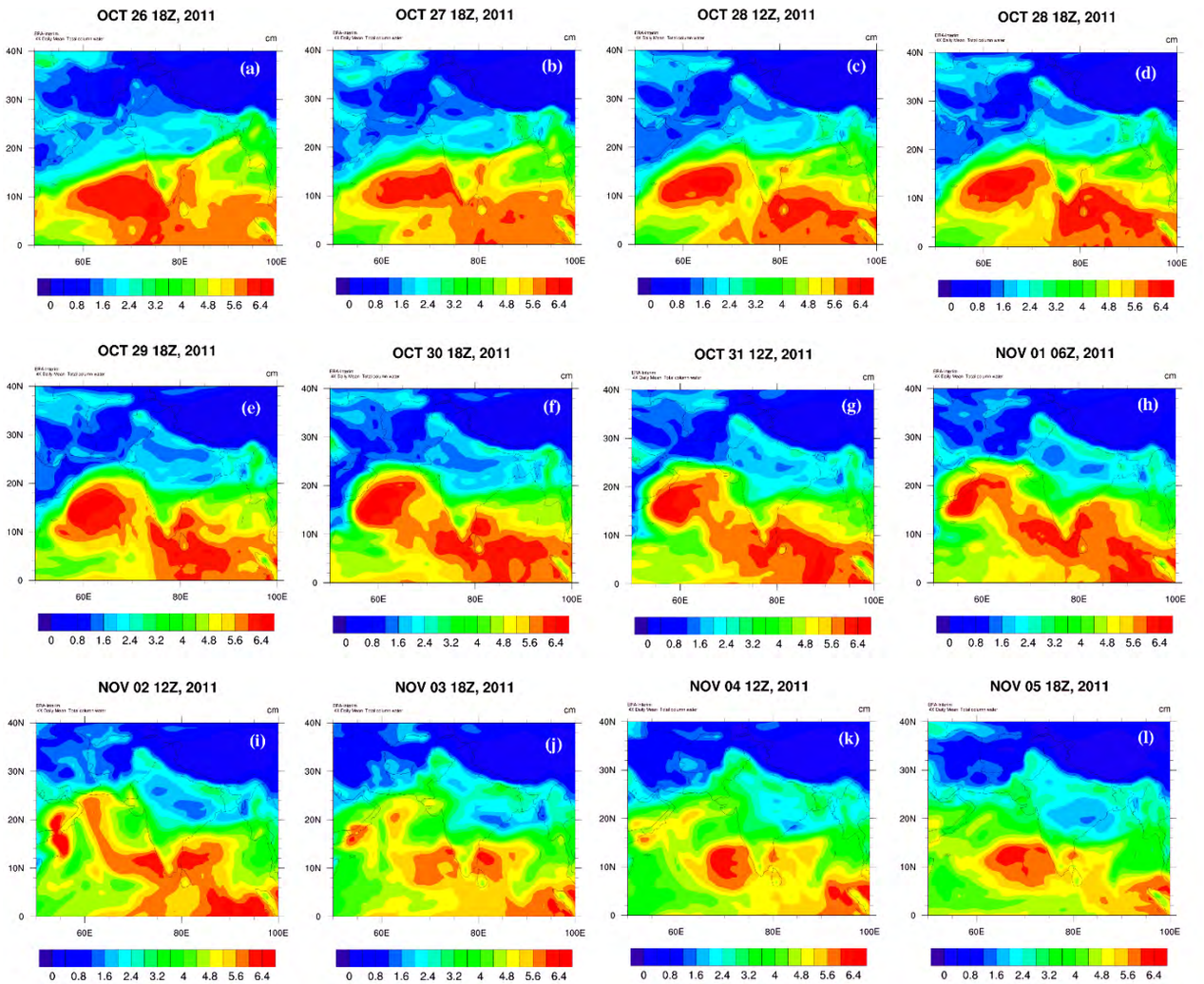

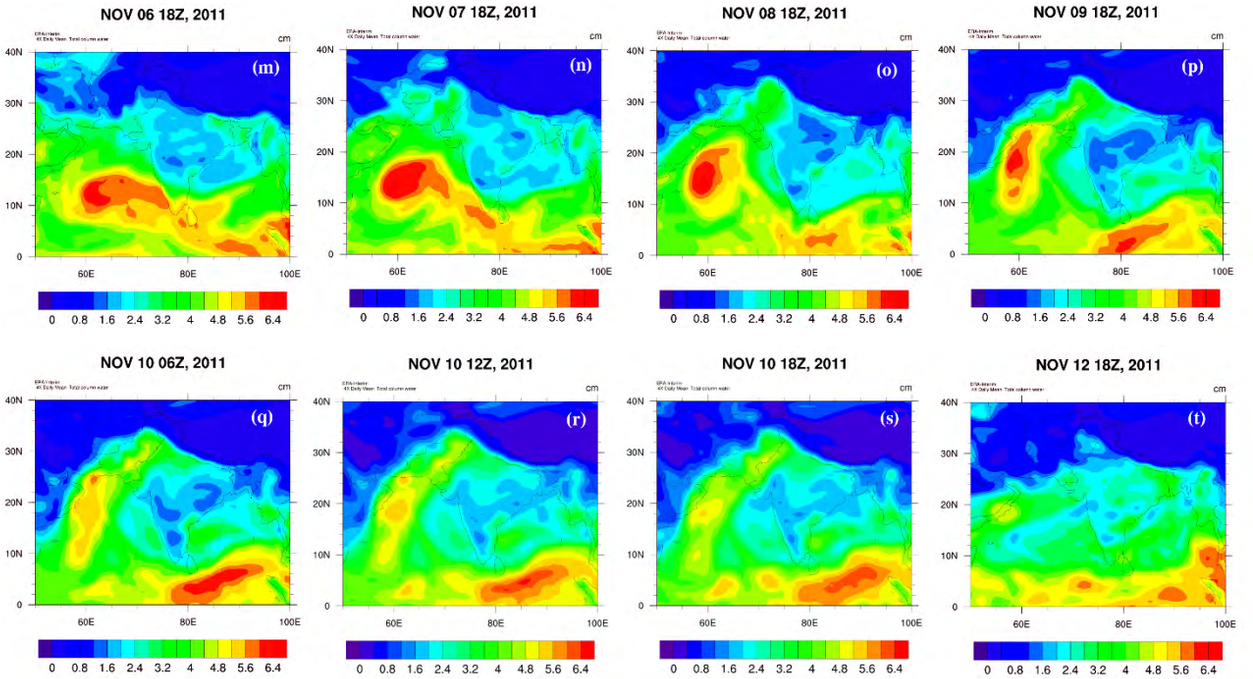

Fig. 5.15.(a-t) Variation in total column water (in cm) w.r.t. the circulation of cyclone Keila for the region 0-40°N and 55-100°E during 26 October– 12 November 2011 obtained from 6-hourly ERA-Interim product.

The cyclonic circulation that formed south-eastern sector of the Arabian Sea moved west-north-westward during 26-27 October 2011 (**Fig.5.15(a-b)**), and on 28 October 2011, the strong low pressure persists in the central parts of Arabian Sea (**Fig.5.15(c-d)**). During 29-30 October 2011 (**Fig.5.15(e-f)**), the low pressure showed signs of intensification and the cyclonic circulation move towards Oman in the north-west direction. On 31 October 2011 (**Fig.5.15(g)**), it persists near Oman and adjoining Yemen. On 1 November 2011 (**Fig.5.15(h)**), the storm continued over west central Arabian Sea with slight intensification. On 2 November 2011 (**Fig.5.15(i)**), the deep depression further get intensified in to cyclone Keila and moved closer to the Oman coastline, and on the same night, it made landfall over southern Oman. On 3 November 2011 (**Fig.5.15(j)**), the cyclone weakened into deep depression over the same area and started moving towards south-eastern side during 4-5 November 2011 (**Fig.5.15(k-l)**). On 6 November 2011 (**Fig.5.15(m)**), it again started moving towards west-northwestward, while during 7-8 November 2011 (**Fig.5.15(n-o)**), it moves with a much lower intensity towards northern and north-western portion of India. This results in enhanced increase in TCW over Gujarat, Rajasthan and Punjab on 9 November 2011 (**Fig.5.15(p)**), and subsequently on 10 November 2011 (**Fig.5.15(q-s)**), there is an increase in TCW

over the southern slopes of Himalaya and including the study site, and by 12 November 2011 (**Fig.5.15(t)**) the complete cyclonic circulation settled down, with the reduction in the TCW value.

5.1.4.2. Case study on the continental transport of smoke plumes (10 November 2011)

In order to ascertain the dominance of fine or coarse mode of aerosols, the FMF value is utilized as an indicator from AERONET and MODIS measurements. The FMF values of 0 and 1 represent the purely coarse and purely fine mode particles respectively, and practically, the value lies in between the two. For the case of 10N11, mean FMF observed from AERONET is 0.98, and from MODIS Terra it is 0.89, hence, confirming the major contribution from anthropogenic sources. Considering the fact that Nainital is surrounded by high mountain ranges of central Himalayas from east, west and north, the transport of fine mode particles from the foothills and adjacent plains (which is the open south side), to this region is most likely to take place due to general tendency of upslope flows that develop in the mountainous terrain during day-time (*Pant et al*., 2006; *Solanki et al*., 2016).

To investigate the type of aerosols prevailing over the site on 10N11, ver. 4.10 of CALIPSO/CALIOP level-1B total attenuated backscatter ($\beta'_{total,532}(r)$), together with level-2 VFM data product which is able to classify the aerosol sub-type, are analyzed. **Fig. 5.16(a-b)** shows the CALIPSO profiles of $\beta'_{total,532}(r)$ and the aerosol sub-type, respectively for the overpass that occurred on 10N11 at about 20:40 UTC (~02:10 hrs. LT of 11 November 2011) over the region [(44.12°N, 84.33°E), (17.32°N, 77.03°E)]. The minimum distance between the site and CALIPSO overpass is found to be ~44.6 km. It is noticeable that the presence of aerosol type over the region is marked by the prevalence of polluted continental/smoke and polluted dust, however, the concentration is dominated with fine mode particles. The fine mode particles resulting from the agricultural burning in the north-west region could be transported in the form of smoke plumes to the Himalayan foothills and higher altitudes (*Badarinath et al*., 2006).

Therefore, to assign a source to the production of smoke, MODIS C6.0 active fire product MCD14ML in the surrounding regions of site for the period 1-10 November 2011 are studied. The occurrences of the fire-events with nominal (30-79 %) and high (80-100 %) confidence levels are taken into account for analysis as presented in **Fig. 5.17**, whereas the low confidence cases have been neglected, in order to reduce the uncertainty in result.

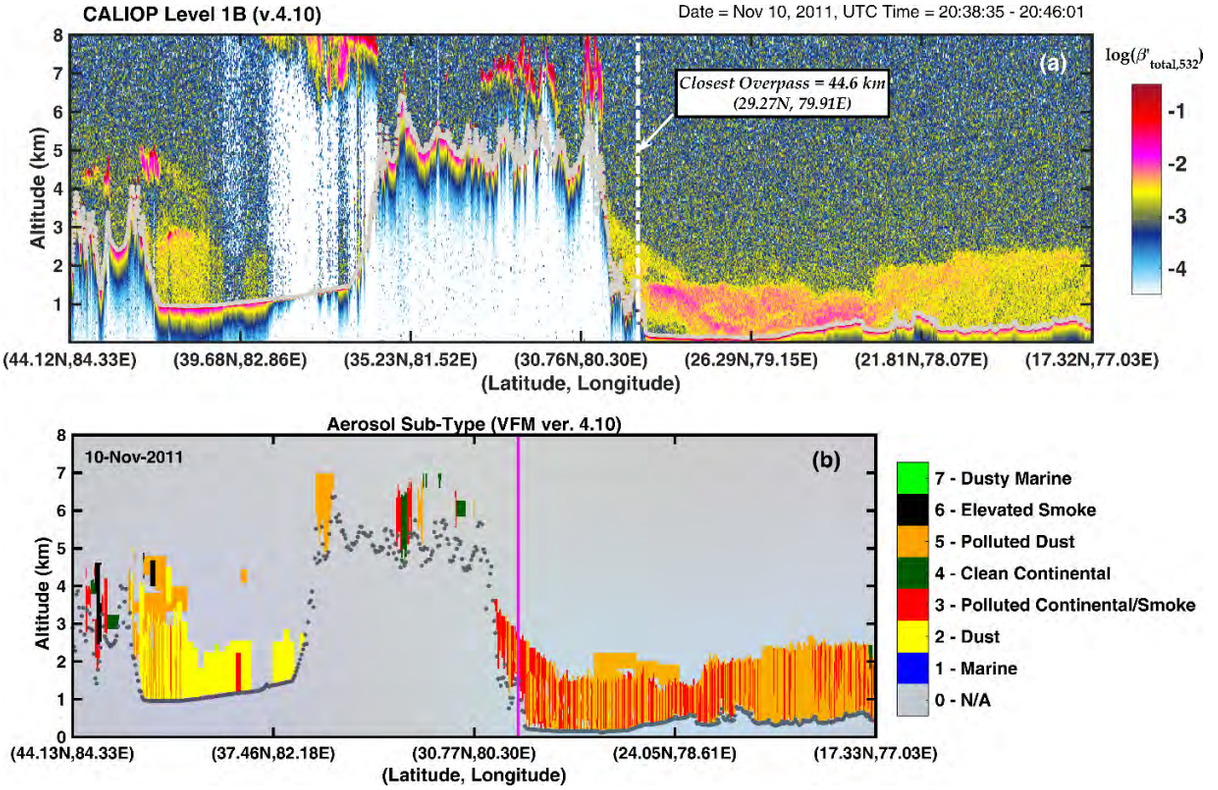

Fig. 5.16. CALIPSO (ver. 4.10) profile of the **(a)** vertical distribution of 532-nm total attenuated backscatter ($\beta'_{total,532}(r)$) from level-1B, and **(b)** the corresponding aerosol sub-type plots using level-2 VFM product ver. 4.10 for 10 November 2011 at 20:38:35 – 20:46:01 UTC (i.e. 02:08:35 - 02:16:01 hrs LT of 11 November 2011).

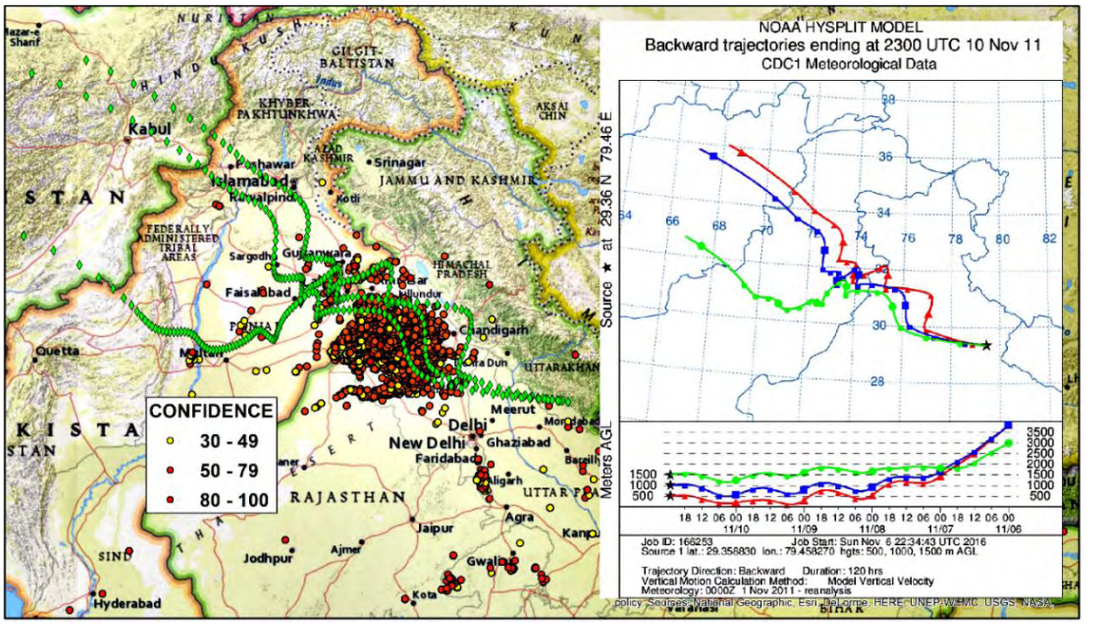

Fig. 5.17. Region showing fire occurrences during 1-10 November 2011, along with the 5-days HYSPLIT back-trajectories of air mass ending at the study site.

The MODIS fire data reveals the strong fire-event occurrences during 1-10 November 2011 over Punjab and northern Haryana states of India. The statistics on the fire-events that occurred in these states (27.39°N – 32.32°N, 73.55°E – 77.36°E) during 1-10 November 2011 is presented in **Table 5.11**, which clearly demonstrate significant fire-events (N_{Aqua} = 4827 and N_{Terra} = 434, where N is the number of fire counts), with mean/maximum FRP of 18.2±14 MW/ 197.5 MW (Aqua) and 12.4±9.3 MW/ 83.8 MW (Terra).

Table 5.11: Fire-event statistics over Punjab and Haryana (27.39°N – 32.32°N, 73.55°E – 77.36°E) during 1-10 November 2011 as observed with MODIS Aqua and Terra satellites.

<table>
<tr><td colspan="2" rowspan="2">No. of fire-events</td><td colspan="2">Aqua: 4827</td></tr>
<tr><td colspan="2">Terra: 434</td></tr>
<tr><td colspan="2">Confidence Level</td><td colspan="2">FRP (MW)</td></tr>
<tr><td rowspan="2">0-29 %
(low fire)</td><td>Aqua: 4.5%</td><td rowspan="2">Mean</td><td>Aqua: 18.2±14</td></tr>
<tr><td>Terra: 0.9%</td><td>Terra: 12.4±9.3</td></tr>
<tr><td rowspan="2">30-79 %
(nominal fire)</td><td>Aqua: 80.5%</td><td rowspan="2">Max</td><td>Aqua: 197.5</td></tr>
<tr><td>Terra: 92.8%</td><td>Terra: 83.8</td></tr>
<tr><td rowspan="2">80-100 %
(high fire)</td><td>Aqua: 15%</td><td rowspan="2">Min</td><td>Aqua: 3.8</td></tr>
<tr><td>Terra: 6.3%</td><td>Terra: 3.8</td></tr>
</table>

The intense fire episodes in Punjab and Haryana are mainly attributed to the agriculture based burnings, as during post-monsoon season, the farmers of these states, before sowing the seeds, generally, fertilize and/or clear their fields by burning the residues/ leftover straws of last cropping. Although the fire events cannot be truly linked to agriculture based burning, there could be some other fire sources like industries etc. However, considering the fact that both the states have strong agricultural base with more than 60 % of agricultural lands, the information may be useful in the present context of increased AOD and high concentration of fine mode aerosol particles on 10N11. Past studies have reported that more than 65 % of the annual fire-events occurring in these areas come from agriculture based burnings and mainly during March-May and October-December (*Singh and Panigrahy*, 2011; *Vijayakumar et al*., 2016).

To understand in a broader sense, long term MODIS fire data (MCD14ML) for the November month of 2011-2015 are analyzed further over the major portion of northern India, as shown in **Fig. 5.18(a-e)**.

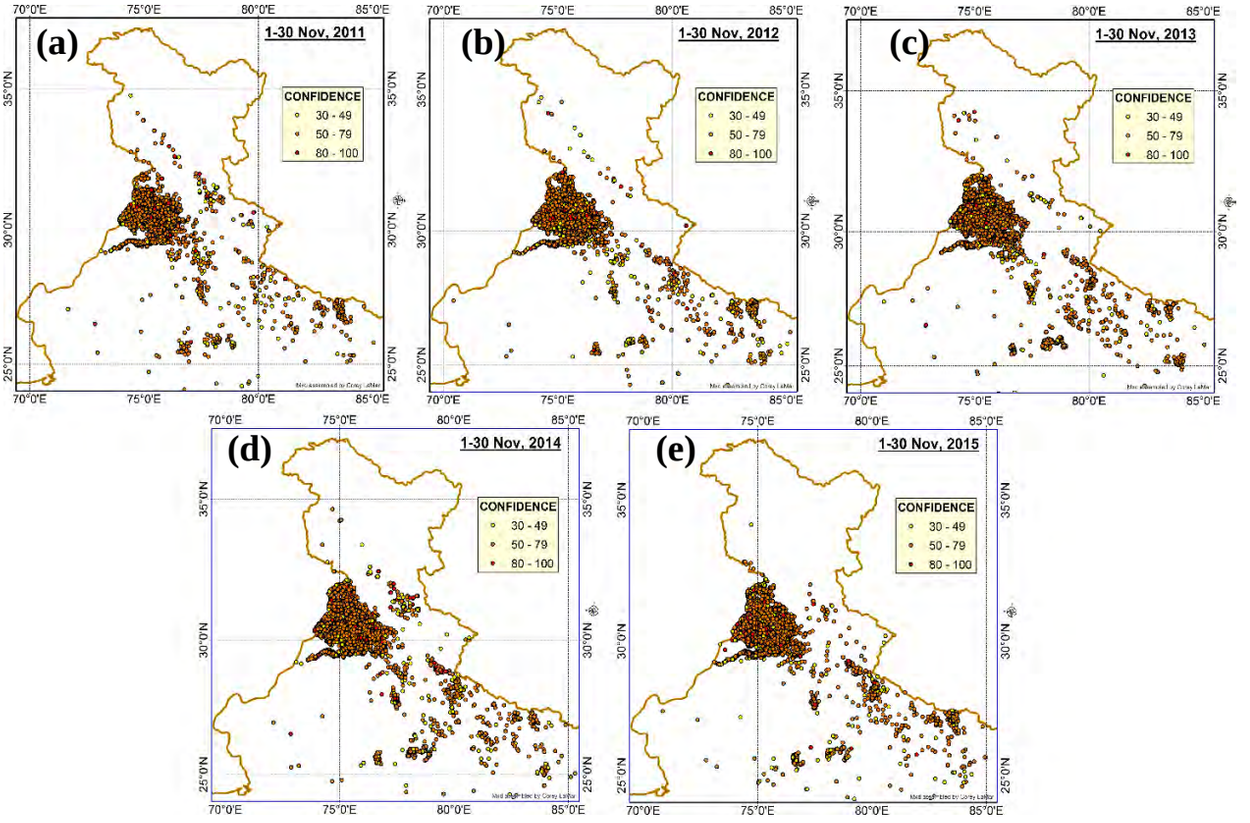

Fig. 5.18. MODIS reported **(a)-(e)** fire events for the November month of 2011-2015 over the major portion of northern India.

Fig. 5.18(a-e) revealed that the occurrence of fire episodes in northern India is a continued practice, and such episodes are intense in Punjab and Haryana regions located in the geographical boundary 27.39°N – 32.32°N and 73.55°E – 77.36°E, than other north Indian states. The total number of fire counts (nominal and high confidence levels) and the radiated power associated with detected fires over these two states during the period 2011-2015 for the month of November is shown in **Fig. 5.19**, which further ascertains that the continued fire activities since last 5-years are consistently high in these states during November with significant number of fire counts (nominal and high) and high magnitude of FRP.

The type of aerosol and the sources of production have been assigned using the ground and satellite based measurements as mentioned in the previous paragraphs. Further to confirm the transport of smoke plumes originating from the aforementioned regions, 5-days air mass backward trajectories analysis using HYSPLIT model is carried out. The trajectories between 0.5 and 1.5 km above ground level are drawn and projected over the fire density plot as displayed in **Fig. 5.17**, which indicate the transport of smoke plumes from Punjab and northern Haryana over the site. The

prevailing wind at the site during 1-10 November 2011 was near-westerly and north-westerly, and the same is confirmed from the 6-hourly vertical slices (between 800 to 400 hPa pressure levels) of zonal, meridional and vertical (Omega) wind velocities provided by ERA-Interim.

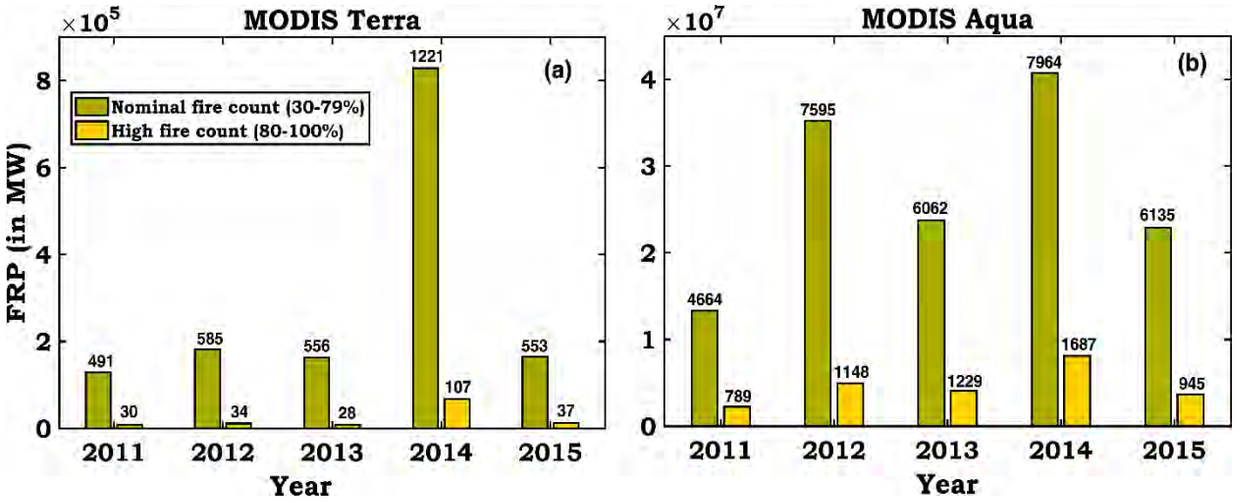

Fig. 5.19. Punjab and Haryana states (27.39°N – 32.32°N, 73.55°E – 77.36°E): MODIS reported nominal and high fire count (in numbers, at the top of each bar), total Fire Radiative Power for the fire events reported during November months (2011-2015) for MODIS **(a)** Terra, and **(b)** Aqua satellites.

Fig. 5.20(a-c) shows the mean zonal, meridional, and vertical wind patterns (00 hrs, 06 hrs, 12 hrs, and 18 hrs) obtained from ERA-Interim product over 29°N-30°N, 79°E-80°E during 1-10 Nov 2011. ERA-Interim adopts the meteorological convention for winds with zonal component positive for westerly wind (west to east) and meridional component positive for southerly wind (south to north).

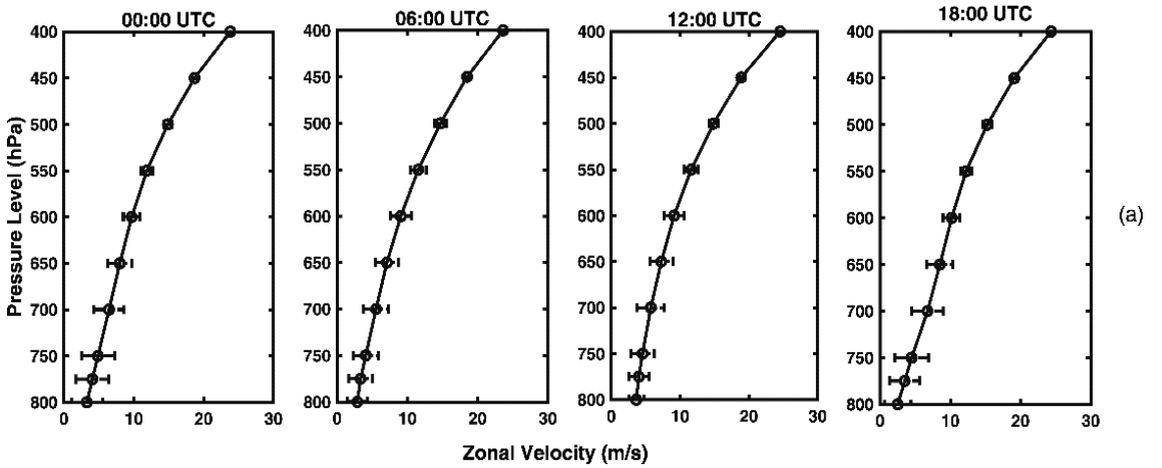

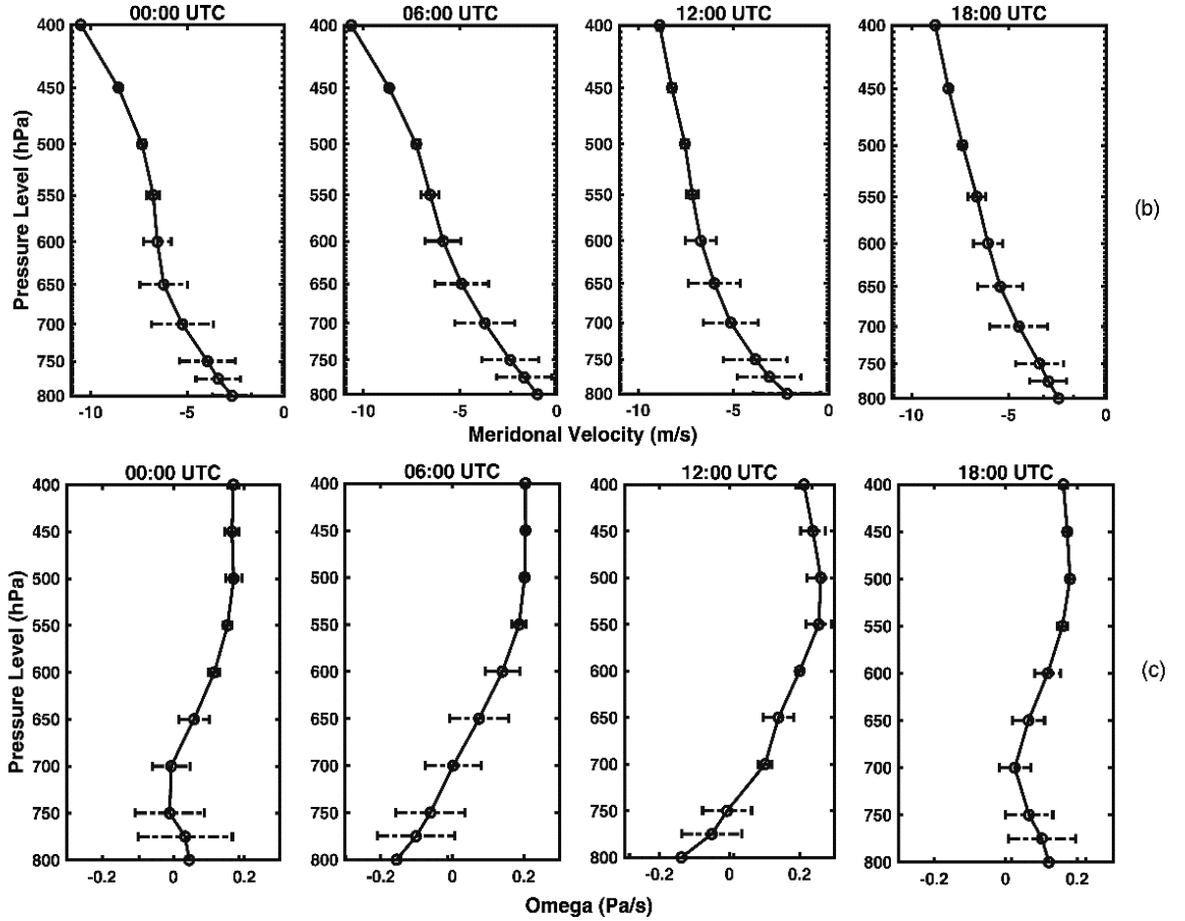

Fig. 5.20. ERA-Interim 6-hourly averaged **(a)** zonal, **(b)** meridional, and **(c)** omega wind velocities between 800 to 400 hPa pressure levels during 1-10 Nov 2011 over 29°N-30°N, 79°E-80°E.

The smoke plumes basically consisting of fine mode particles are lifted up and with the prevailing winds subsequently gets transported to the surrounding regions and towards high altitude locations in the Himalayas, which are confirmed with LiDAR observations and satellite measurements over the site under study. Very often such emanated smoke plumes, together with the urban and industrial pollutions reach the southern slopes of Himalaya and contributes to the formation of haze (*Ramanathan and Ramana*, 2005) in the Himalayan region as evident in **Fig. 5.21(a-c)**. The LiDAR observations on 2 November 2011 (20:00 – 23:30 hrs LT) from ARIES, Nainital (**Fig. 5.21a-b**) is clearly displaying the high concentration of aerosol in the atmosphere up to about 2 km above the site, and the mean aerosol extinction and AOD for 2 km column is found to be 0.16±0.03 km^{-1} and 0.34±0.02 respectively. The LiDAR observation is in agreement to the image captured from MODIS Terra satellite (**Fig. 5.21c**) on 3 November 2011 (~ 05:15 hrs LT)

showing a cover of dense haze above the site which is spreading over the southern valley and foothills of Himalayas.

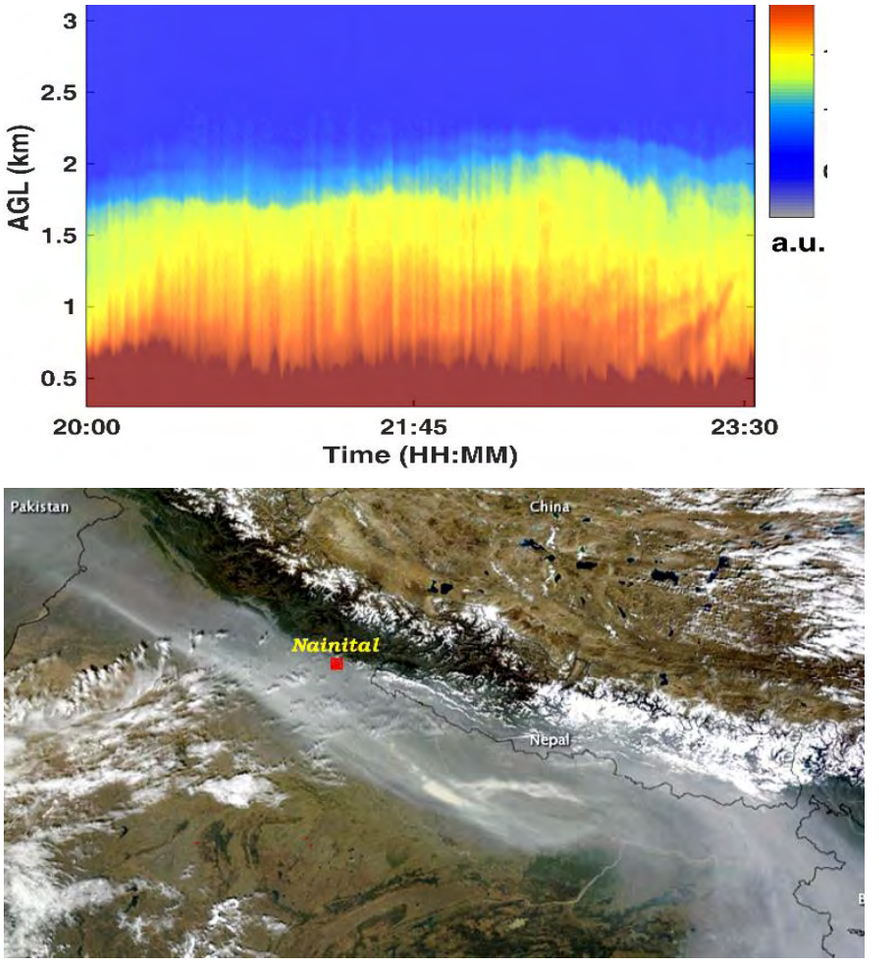

Fig. 5.21. (a) Height-time contour plot of the LiDAR Range-corrected signal of 2 November 2011 (20:00 – 23:30 hrs. LT) from Manora peak; Vertical and temporal resolutions are 15 m and 120 sec respectively, (b) corresponding aerosol extinction profile showing mean and standard deviation for the profiles captured between 20:00 – 23:30 hrs on 2 November 2011, and (c) MODIS Terra satellite image of 3 November, 2011 at ~ 05:15 AM local time showing the haze stretching from Pakistan south-eastward to Bangladesh (NASA image courtesy MODIS Rapid Response Team at NASA GSFC. Caption by Michon Scott.).

Besides the production of haze, the negative consequence of crop residue burning and transport of smoke plumes are mainly - the increase in production of greenhouse gases, health hazards, atmospheric aerosol loading, changes in the air quality and impact on environment at

regional and continental scales (*Andreae and Merlet*, 2001*; Streets et al.*, 2003*; Pope and Dockery*, 2006*; Estrellan and Iino*, 2010*; Jain et al.*, 2014*; Long et al.*, 2016). Among the by-products of agricultural burning, CO is the most active component to contribute in both air pollution and climate change, and particularly, plays a critical role in reducing the OH concentrations. It has the residence time of even more than 60 days and gets easily transported to long distances. It also affects methane (CH_4), carbon dioxide (CO_2), and tropospheric ozone (O_3). Considering such an important role of CO, it is vital to understand its distribution during fire episodes and variability in the atmosphere (*Ding et al*., 2015). The CO emissions associated with the observed high confidence fire episodes for November (2011 - 2015) are presented in **Fig. 5.22** and found in agreement with the fire counts and FRP, however, the highest values of about $3.4x10^{-9}$ kg $m^{-2}s^{-1}$ and $2.3x10^{-9}$ kg $m^{-2}s^{-1}$, are observed during 2012 and 2014 respectively over the agriculture dominated regions of Punjab and northern-Haryana.

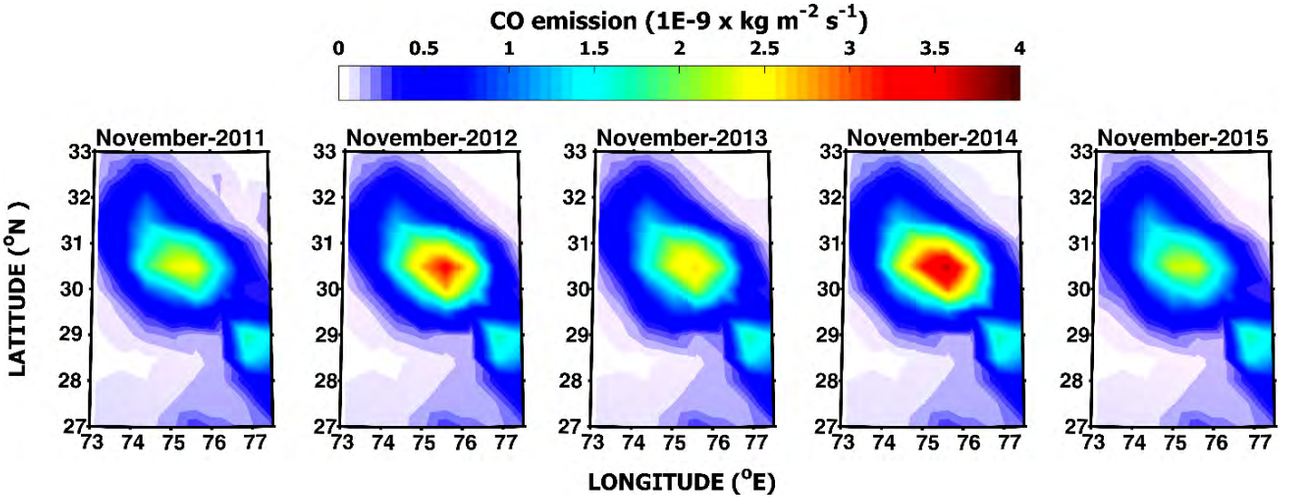

Fig. 5.22. Punjab and Haryana states (27.39°N – 32.32°N, 73.55°E – 77.36°E): Monthly carbon monoxide emission (ENSEMBLE) in kg m^{-2} s^{-1} obtained from MERRA-2 for November months (2011-2015).

The tropospheric ozone has not shown significant enhancement in the emission hence not presented here. The transported CO reaching to the surrounding regions and high altitude locations in the Himalayas, may affect the human health by creating respiratory problems, help developing the heart diseases, and reduces the efficiency of vital organs (*Pope and Dockery*, 2006; *Ding et al*., 2015). Considering the negative consequences of crop residue burning and to preserve the

environment for future generation, it become essential that the community, especially the farmers of Punjab and northern Haryana should be made aware of the negative consequences of crop residue burning. Through awareness campaigns, government initiatives, viable schemes and training programmes, they should be trained for the sustainable agricultural practices by which they can reduce their environmental footprints.

5.1.4.3. Case study on the long range transport of dust (30 March 2012)

The source apportionment and the nature of aerosols over the site on 30M12 is investigated using the ground LiDAR and the satellite based CALIPSO measurements. The LiDAR RCS plot shown in **Fig. 5.23a** depicts two separate aerosol layers each within and above the local boundary layer (*Singh et al*., 2016). The layer closer to the ground dissipates and tends to settle in the late evening hours, with the appearance of an elevated aerosol layer intensifying after ~ 22:00 hrs. However, the elevated layer above the boundary layer at about 2 km also intensifies and continues to be there. The dissipation of the aerosol layer closer to ground is primarily due to the strengthening of the down slope winds over mountainous topography, whereas the elevated aerosol layer formation together with the dominance of coarse mode particles on 30M12 confirms the long range transport over the site and surrounding region.

The signature of the elevated layer is also evident in the mean aerosol extinction profiles obtained from both the CALIPSO and LiDAR measurements (**Fig. 5.23b and c**). The AOD values reported by the two different CALIPSO versions are 0.367±0.03 (ver. 3) and 0.395±0.01 (ver. 4.10), and found to be in good agreement with ground based AOD measurements using LiDAR (0.349±0.02) and AERONET (0.393±0.05). The AOD values retrieved with MODIS Aqua and Terra are 0.337 ± 0.14, and 0.296 ± 0.024, respectively. CALIPSO provides the time constrained observations of aerosol vertical distributions, whereas the ground based LiDAR provides information on the evolution of the distribution over a location. The difference in the peak of extinction profiles retrieved from LiDAR and CALIPSO observations as shown in **Fig. 5.23c** and **d** could be due to the factors like - spatial and temporal mismatches, poor signal-to-noise ratios, large sensor-to-target distances, horizontal inhomogeneity's in aerosol conditions, limitations associated with their transmission i.e. downward-looking (CALIPSO) vs. upward-looking (LiDAR), selection/ assumption of the constants e.g. LiDAR ratio, and the differences in their screening algorithms, calibration methods etc. (*Hunt et al*., 2009; *Powell et al*., 2009; *Solanki and Singh*, 2014; *Kumar et*

al., 2018). In **Fig. 5.23d**, the CALIPSO VFM product evidently demonstrates the dominance of coarse mode particles due to the intrusion of dust over the site and the surrounding regions and provides a fair classification of several aerosol sub-types, each represented by the different color codes as shown.

Elevated aerosol layer formation over the central Himalayas is generally observed during spring aided by the strong synoptic north-westerly wind flow, transporting dust from arid regions of Thar desert, Middle-East and North Africa. The transportation of dust over the longer distances is usually episodic and mainly occurring in favourable meteorological conditions. Time averaged plot for dust column mass density in **Fig. 5.24a** evidently exhibits the prevailing high concentration of aerosol and dust, on 30M12, mainly over north-west Africa, north-east part of Saudi Arabia and Iran.

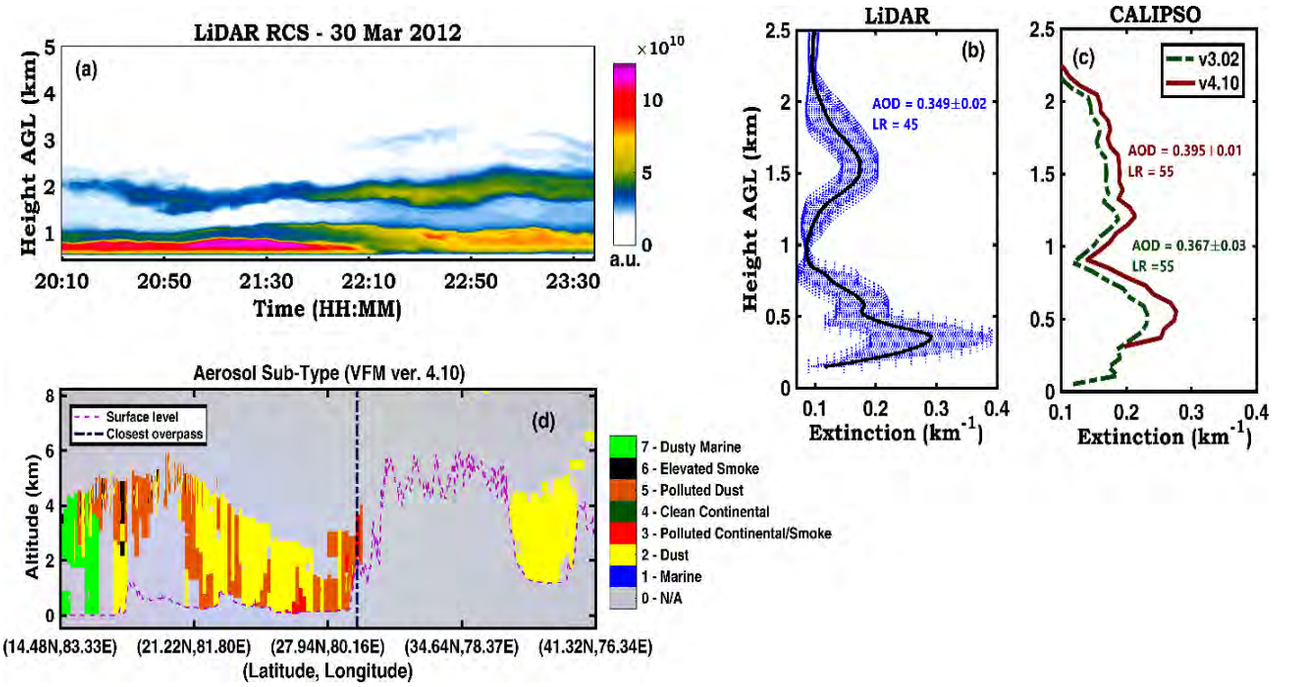

Fig. 5.23. Temporal vertical profile of the **(a)** LiDAR range-corrected signal (RCS) for the observation on 30 March 2012 (20:10 to 23:40 hrs. LT) from Manora peak; Unit: arbitrary (a.u.); Vertical and temporal resolutions are 15 m and 120 s, respectively, **(b)** the corresponding LiDAR derived average aerosol extinction profile, **(c)** CALIPSO (ver. 3.02 and ver.4.10) measured aerosol extension profile (average of the valid profiles with CAD score < -35 available within ~100 km horizontal distance; profile vertical resolution is 60 m) of 30 March 2012 (~13:35 hrs. LT), and **(d)** the corresponding aerosol sub-type plot using level-2 VFM product ver. 4.10 for 30 March 2012.

The dominant mechanism behind the lifting of aerosol and dust is basically intense solar radiation during summer that gives rise to the strong convection. Especially, over the arid regions, coarse mode particles rise up with the thermals (warm air parcels) and reach up to higher altitudes in the lower troposphere, which then are further transported to distant locations depending upon the horizontal winds at different altitudes. This may be clearly seen in the trajectory plot (**Fig. 5.24b**) that the synoptic wind flow between 0.5 and 2.3 km is north-westerly to near westerly and bringing in the aerosols and dust that has been lifted up somewhere else in the west as described above.

In order to understand the impact of transport of coarse aerosols and dust to the Himalayan region, in a much better way, the geographical boundary of study is extended to 28–34° N and 78–98° E, where the major portion of central Himalaya (India, Nepal and Tibet) is confined. The idea behind selecting the aforementioned region is to elucidate upon the effect of dust loading over the central Himalayan glaciers and snow cover, as very limited studies are available particularly focussing over this spectacular and dramatic region (*Ren et al*., 2006; *Xu et al*., 2010; *Mal et al.*, 2016). During the recent past, the region has encountered a number of damages due to natural disasters like - the devastating earthquake of April 2015 which killed more than 8,000 people (*Mendoza et al*., 2016), and flash flood incident of Kedarnath in June 2013 which resulted in more than 10,000 killings (*Dobhal et al*., 2013).

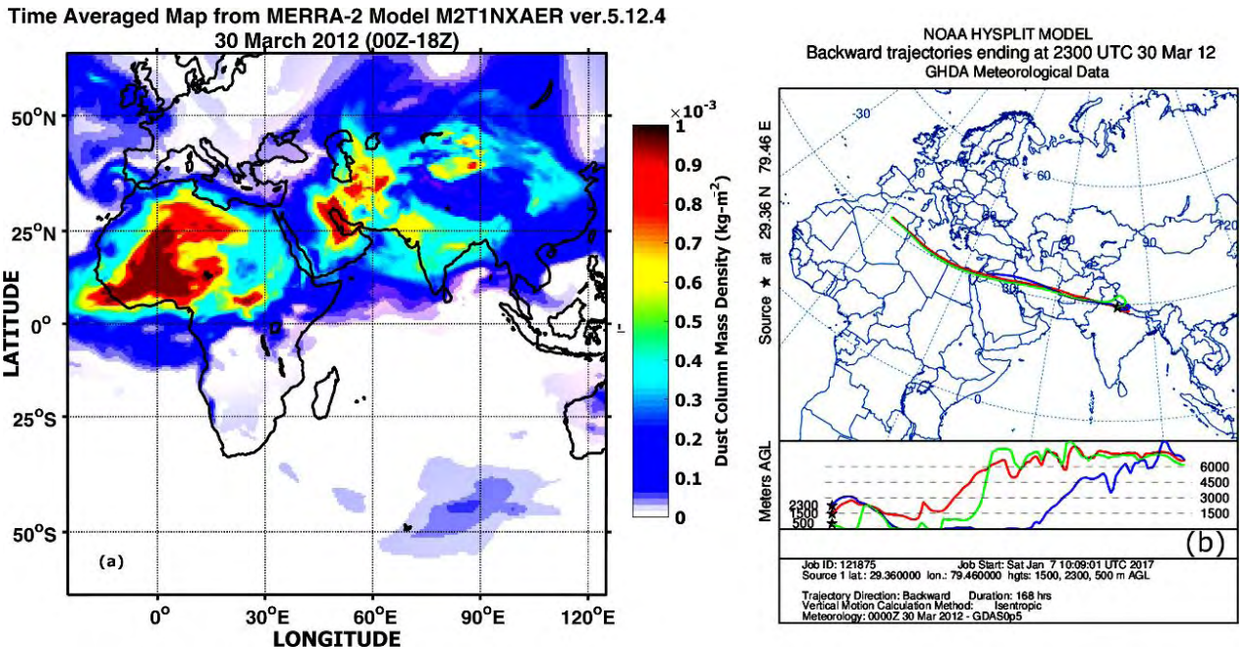

Fig. 5.24. (a) Time averaged plot of MERRA-2 based dust column mass density (in kg m^{-2}), and **(b)** 168 hrs HYSPLIT back-trajectories for 30 March 2012 showing the transport of air mass to the site.

The spring and summer mainly witnesses the long range transport, therefore, to investigate the presence of dust over a wider region, the data set on dust column mass density for all available days of March month of each year during 2011-2015 is subjected to analysis and the time series maps for the monthly mean dust density over the region specified are produced as shown in **Fig. 5.25**. The highest column mass density (~ 4 x 10^{-4} kg m^{-2}), which is an indicative of dust loading, is observed in March 2012, as compared to the other years. The average AOD (550 nm) for March 2012 is also higher than the other years, with MODIS C6.0 Terra DB, DT and combined DB-DT mean values of 0.38±0.32, 0.43±0.31, and 0.37±0.17, respectively.

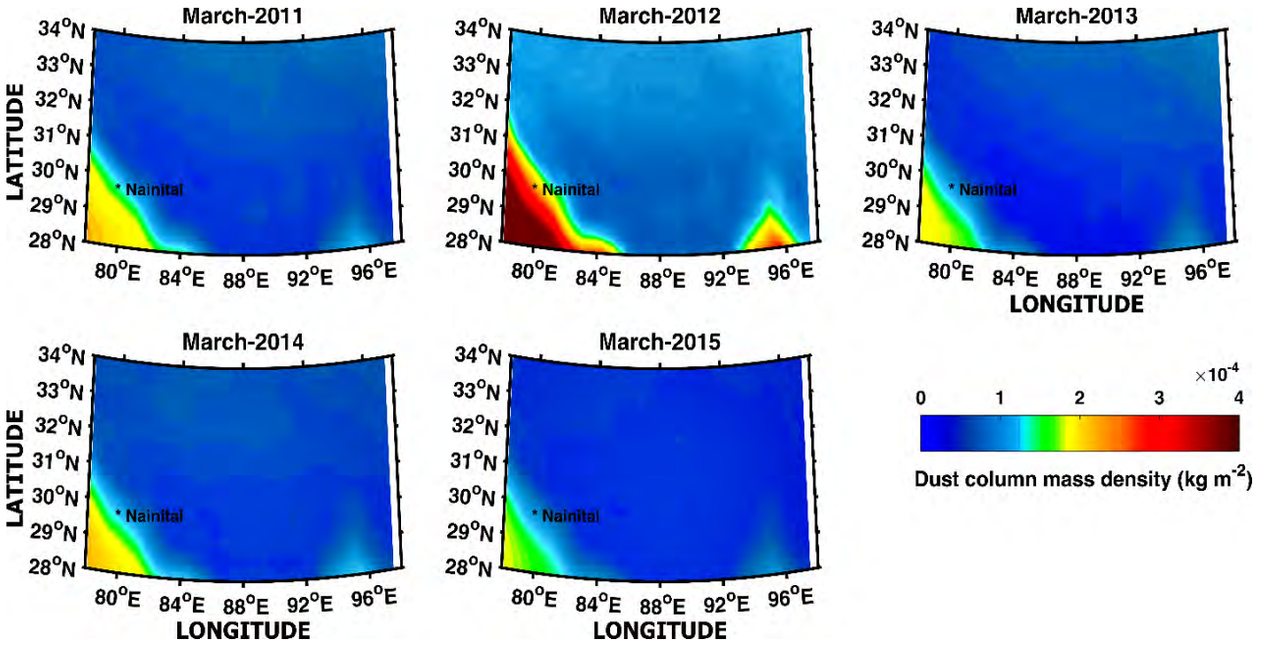

Fig. 5.25. Average dust column mass density, in kg m^{-2} (MERRA-2: 0.5° x 0.625° resolution) over 28–34° N and 78–98° E during March (2011 – 2015).

To examine the effect of dust transport on the glaciated surface during March (2011-2015), the snow depth over the glaciated surface (from MERRA-2) at the same spatial resolution as used for dust column mass density i.e. 0.5° x 0.625° is studied. Consequently, the corresponding snow depth over glaciated surface as seen in **Fig. 5.26** is found to be at the lowest level for March 2012. In March 2015 the snow depth over glaciated surface is ranging from 0.4 - 0.8 m in the region 28–34° N and 78–86° E, due to the obvious reason that the corresponding average dust column mass density has been at the lowest levels. The possible mechanism suggests that the clouds forming in

the presence of dust contain small droplets and produce little precipitation by drop coalescence (*Rosenfeld et al*., 2001) and hence leads to the inhibited snow fall.

The major portion of the defined region is covered with snow throughout the year, and the loading of the transported dusts nearby or over the snow covers may alters the surface albedo and hence, allows more absorption of solar radiation which in turn may raise the rate of melting of the snow cover. As an impact, the waning of glaciers, change in the seasonal snowfall pattern, and early stream runoff may take place, which disturbs the ecosystem of the Himalayan region. Furthermore, the accumulation of desert dust over the foothills and Himalayan slopes may produce the detrimental impacts on rainfall and surface radiative balance (*Aoki et al*., 2006; *Duchi et al*., 2014). The accrual of dust and other pollutants over the mighty Himalayan region, transported from distant locations are also responsible for the growing extreme weather events over the region to some extent.

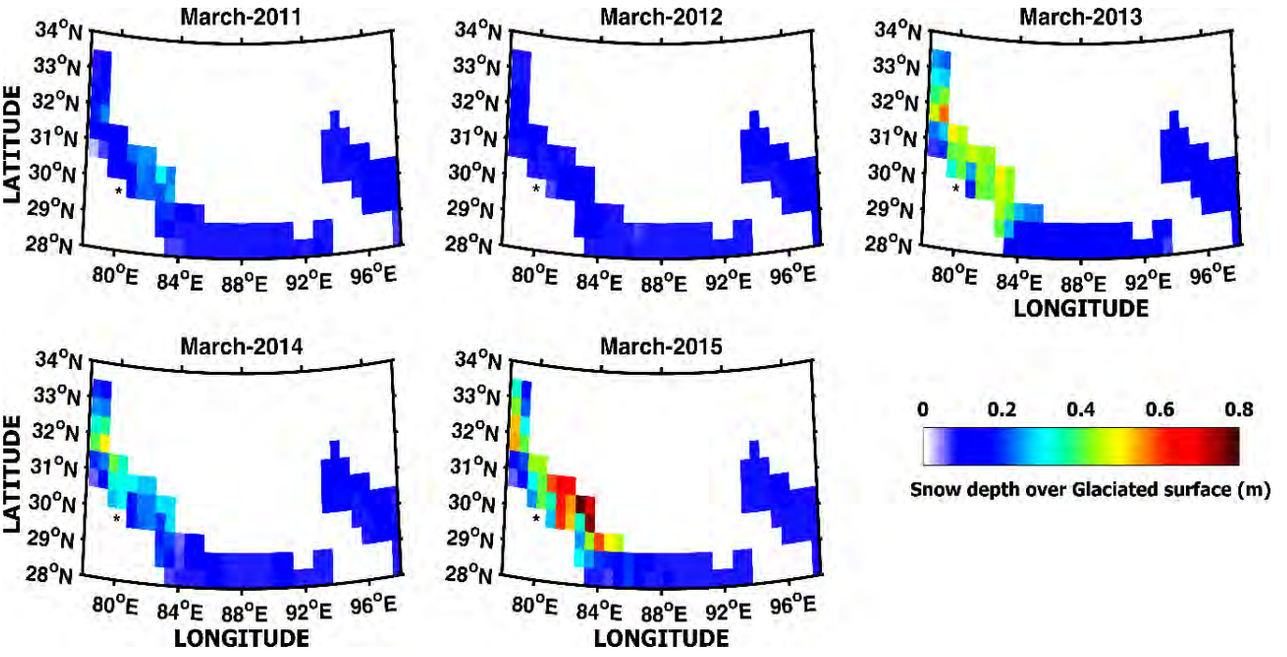

Fig. 5.26. Average snow depth over glaciated surface, in m (MERRA-2: 0.5° x 0.625° resolution) over 28–34° N and 78–98° E during March (2011 – 2015).

The mean albedo computed from GLDAS model, over the glaciated surface during March 2011 and 2013-2015 is found to be as high as ~70-75% that may be inferred from **Fig. 5.27** indicating relatively lower impact on the snow cover as compared to the March 2012. In general, the typical value of the Albedo from the clean and dry snow lies between 80 % and 95 %. Contrary

to this, average Albedo over the glaciated surfaces during 2012 is found to be less than 55%, thereby implying that more than 45-50% of the incoming solar radiation is absorbed. As an impact the surface including the snow packs may become warmer and the anomalous snow melting can occur. The adverse effect of the change in the snow cover, essentially over Himalayan region should be looked upon as such occurrences might influence the phasing of the seasonal cycle and also trigger the abnormal change in the parameters like atmospheric temperature, precipitation, cloud formations, soil moisture and polluted runoffs.

To show the impact of aerosols on glaciated surface and the snow fall, a regression analysis is performed between these parameters and the dust column mass density over a period of 1980-2017. Line regression as given by **Fig. 5.28(a, b)** elucidates that snow depth cover and snow fall are negatively correlated with dust column mass density. However, the impact of dust is more severe on snow depth cover as compared to the snow fall, as discussed in earlier section as well. The analysis extricates that in addition to the dust loading in the atmospheric column, as the dust settles on the snow, it adversely affect the snow due to its property of absorbing radiation and creating a heating impact, more than affecting the cloud formation mechanism.

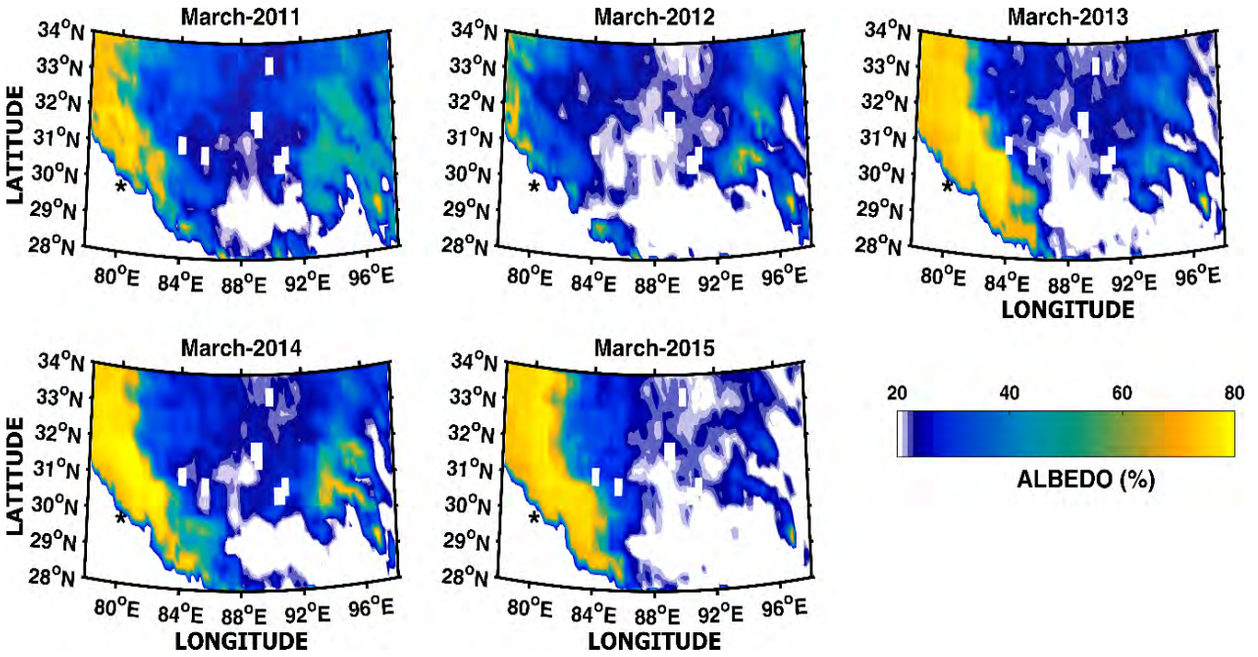

Fig. 5.27. Surface albedo distribution over 28–34° N and 78–98° E, in percentage (GLDAS model: 0.25° x 0.25° resolution) during March (2011 – 2015).

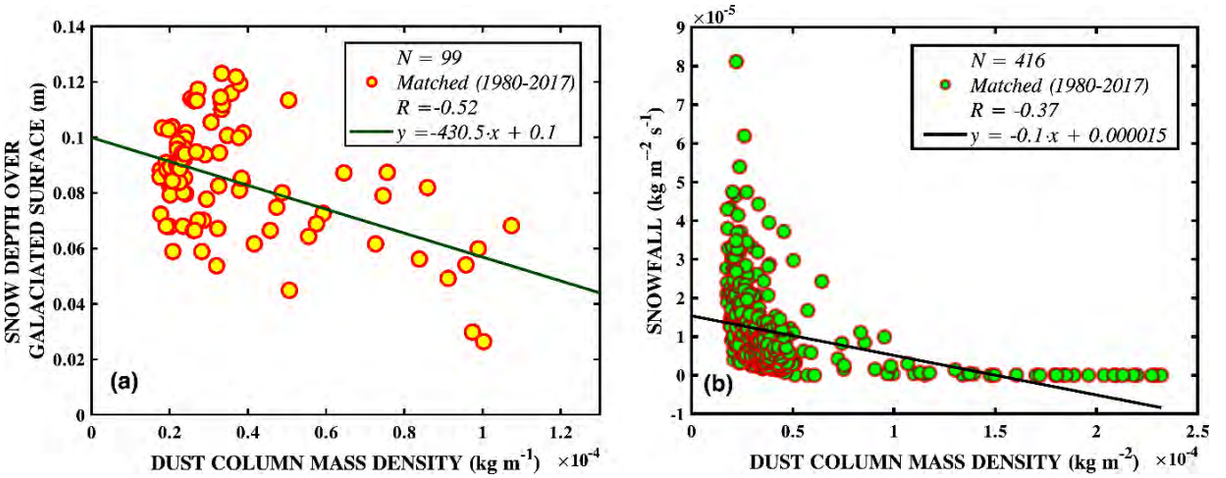

Fig. 5.28. Line regression plot showing the relation between monthly Dust column mass density and **(a)** monthly Snow depth over glaciated surfaces, **(b)** monthly Snowfall, obtained from MERRA-2 data sets for the period 1980-2017 over 28–34° N and 78–98° E.

5.1.4.4. Case study on the dominance of ultra-fine aerosol particles (9 December 2010)

The aerosol variations are inherently linked with the meteorological parameters such as temperature, humidity, wind speed etc. and the presence of hygroscopic particles at occasions may lead to the formation of clouds as well. In contrast to the episodes of continental and long range transport of aerosols, one such case observed on 9D10, is discussed here. The diurnal cycle of AOD at 500 nm (**Fig. 5.13a**) does not show any pronounced variability, and AOD values remain low and almost same over the day. However, the AE increases with the advancement of day and reaching to a maximum in the afternoon about 01 hrs. LT, and thereafter decreases until evening (**Fig. 5.13b**). It indicates that the influence of the transport of aerosols mostly of fine and, coarse mode nature is negligible. Hence, the ultra-fine particles of local origine under high humidity conditions seems to be contributing in the formation of localized cloud on the day, which during evening hours dissipates and moisture settles down, thereby, marking a very low water column as shown by (**Fig. 5.13c**).

The CALIPSO/CALIOP total attenuated backscatter profile (**Fig. 5.29a-b**) on 9D10 confirms the existence of a thin cloud during midnight (20:43 UTC) at ~3 km altitude in the nearby areas of the study site.

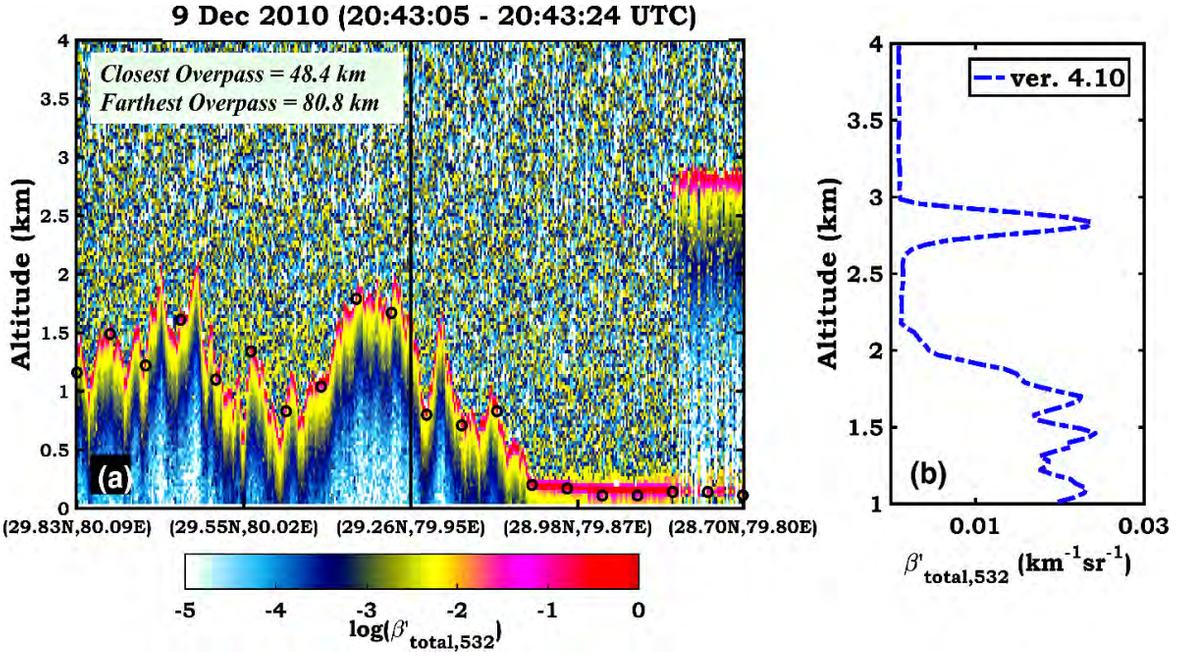

Fig. 5.29. CALIPSO **(a)** vertical distribution (log scale), and **(b)** average profile (linear scale) of 532-nm total attenuated backscatter ($\beta'_{532,total}(r)$) for the overpass distance up to 80.8 km observed on 9 December 2010 during 20:43:05 to 20:43:24 UTC.

To check for the diurnal pattern, the meteorological parameters obtained from ERA-Interim data for the closest co-ordinate (29.5°N, 79.5°E) between 800-400 hPa pressure levels, corresponding to the vertical structure up to about 7 km are examined and presented in **Fig. 5.30**, which shows the mean and SD of 6-hourly temperature, humidity, wind velocity and cloud water contents for 9D10. ERA-Interim has adopted the meteorological convention for winds with U component positive for eastward wind (west to east) and, V component positive for northward wind (south to north). The RH depicts wide variations between 700-600 hPa (around 3 km to 4.2 km), showing the high and low values of 72.2 % (06:00 UTC) and 0.3% (12:00 UTC), respectively. The negative trend in the vertical velocity (omega) with pressure level on this date confirms the rising motions that have played an important role in the formation of cloud as observed in **Fig. 5.30**, with cloud index and a maxima in liquid water content between 3 and 4 km. Moreover, the zone of uplifts in coincident with the high RH is very favourable for convective cloud development as evident in the vertical profiles of cloud water contents (both liquid and ice).

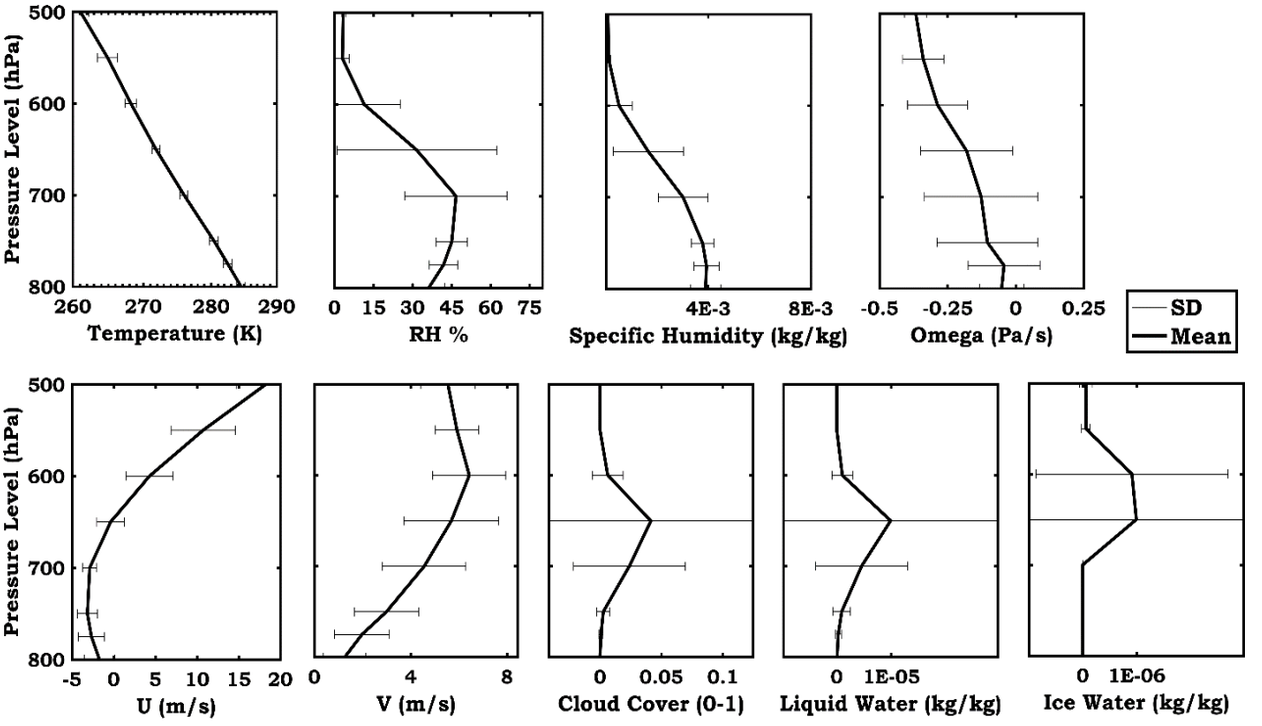

Fig. 5.30. Meteorological conditions on 9 December 2010 derived from ERA-Interim 6-hourly re-analysis product for the coordinate (29.5°N, 79.5°E).

5.2. Climatological study on the absorbing aerosols over the Himalayan region

5.2.1. Seasonal and monthly climatology on dust

More than one-third of the global land masses are occupied by large deserts e.g., the Sahara, Arabian, Atacama, Thar, Karakum, Taklamakan and Gobi deserts. These desert areas are the source for emission of ~2000 Mt of dusts into the atmosphere, ~1500 Mt of depositions on the land surface, and ~500 Mt over the oceans (*Tegen and Fung*, 1994; *Shao et al*., 2011), which are responsible for scattering, reflecting and absorbing solar radiation and other effects of the radiation, and hence contributing to the global warming (*IPCC*, 2013). With this background, the seasonal dust distribution scenario over the global (land only) is deduced using the long-term MERRA-2 re-analysis data, and shown (**Fig. 5.31**) as the mean (1980-2017) dust column mass density for the four distinct seasons – winter (DJF), summer/spring (MAM), monsoon (JJA), and post-monsoon (SON). The figure clearly shows that the arid and semi-arid regions, in particular the Middle East, Saharan Africa, and Mongolia hosts the largest dust source throughout the four seasons, and hence contributing to global dust emission at a great extent (*Middleton and Goudie*, 2001; *Washington et al*., 2003; *Ginoux et al*., 2012; *Schepanski*, 2018).

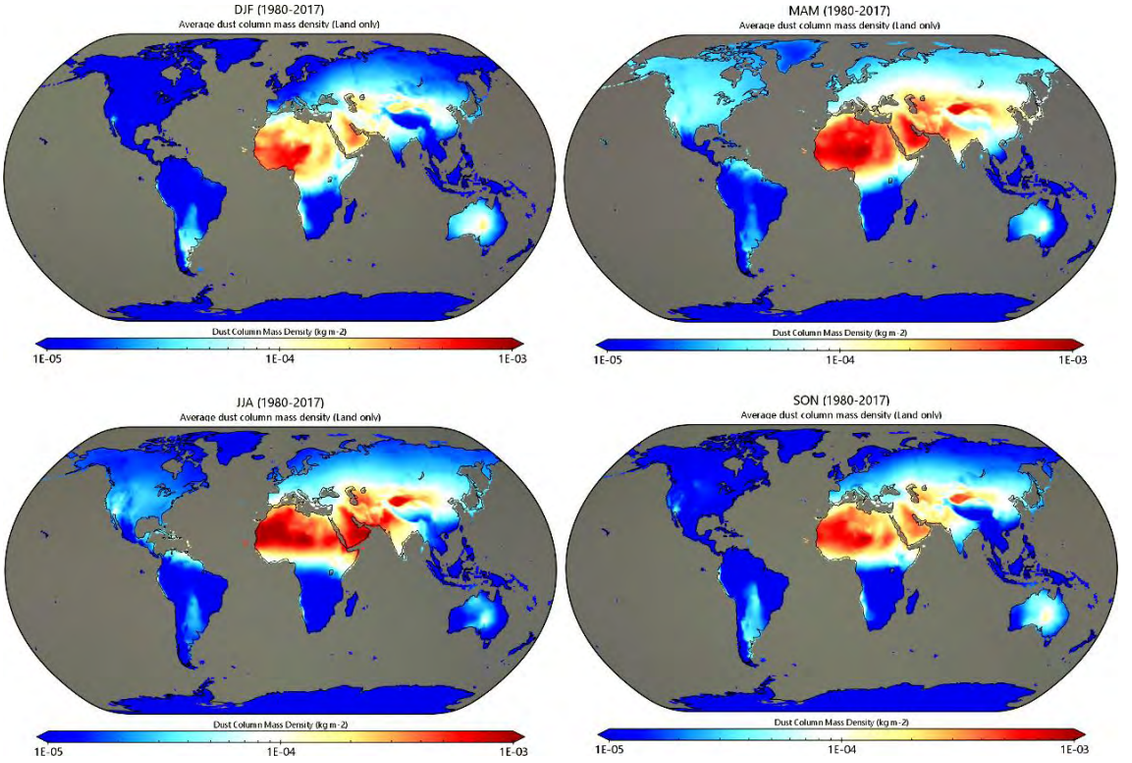

Fig. 5.31. Seasonal global mean (1980-2017) dust column mass density (kg m^{-2}) from MERRA-2 (0.5° x 0.625°) over the globe (land only) for the four seasons - DJF, MAM, JJA, and SON.

The accrual of dust and other pollutants over the Himalayan region are also responsible for growing extreme weather events to some extent (*Pant et al*., 2018; *Krishnan et al*., 2019). **Fig. 5.32** presents the corresponding mean plots of dust column mass density using MERRA-2 re-analysis data, for the Himalayan region, where the major portions are covered with snow throughout the year, and the burden of dusts nearby or over the snow covers may alters the surface albedo and hence, allows more absorption of solar radiation which in turn may raise the rate of melting of the snow cover. As an impact, the changes in the seasonal snowfall pattern, the waning of glaciers, and early stream runoff may takes place that disturbs the ecosystem of the Himalayan region. Furthermore, the accumulation of desert dust over the foothills and the Himalayan slopes may produce the detrimental impacts on rainfall and surface radiative balance (*Aoki et al*., 2000; *Duchi et al*., 2014). The massive dust outbreaks during MAM and JJA from the northern China region, especially from the Taklamakan desert of Tarim Basin and the Gobi desert is clearly noticeable in **Fig. 5.32**. The intensification of dust activity is also observed in the north-western portion of Indian subcontinent alongwith the adjoining states of Pakistan and Afghanistan during these two seasons.

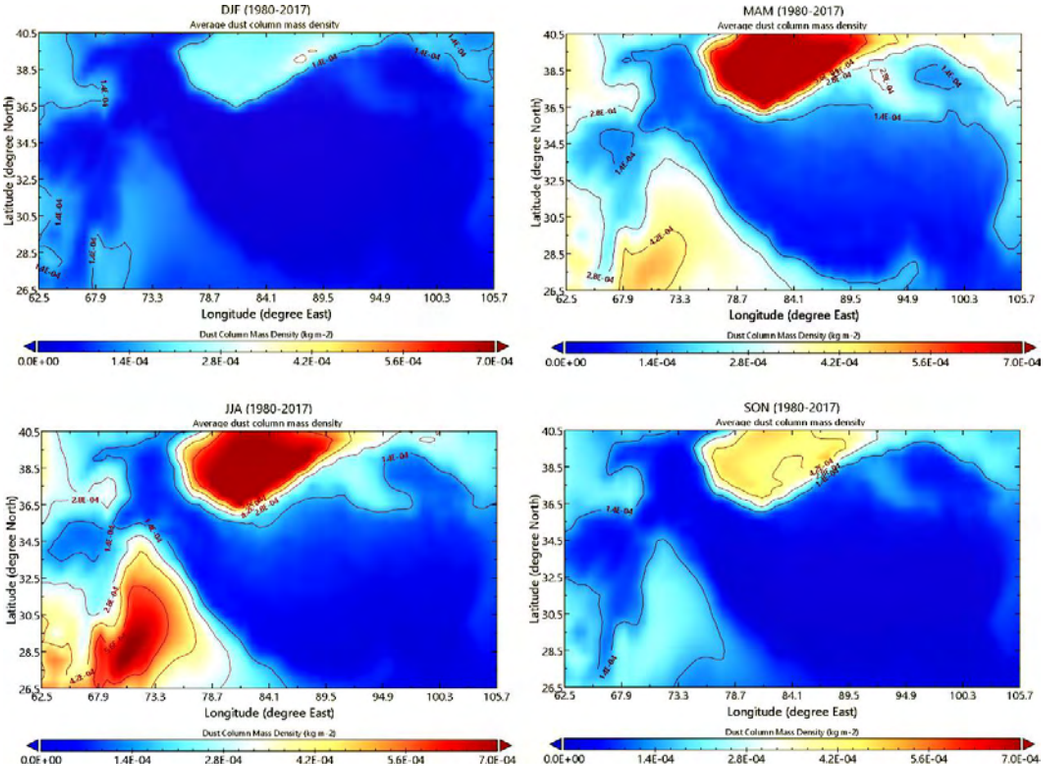

Fig. 5.32. Seasonal mean (1980-2017) of dust column mass density (kg m^{-2}) from MERRA-2 (0.5° x 0.625°) over the Himalayan region for the four seasons - DJF, MAM, JJA, and SON.

The analysis based on **Fig. 5.31** and **Fig. 5.32**, revealed that the average dust loading, over the globe and the Himalayan regions are highest during MAM. Together with this, JJA also experiences intense dust. The dust loading during MAM is observed as ~12.4 % and ~5.4 % more in comparison to JJA, across the globe and over the Himalayan regions, respectively. Further, on the basis of analysis using past 38 years of data record, it is inferred that the dusts over the Himalayan region have occupied nearly 8.5 % (JJA), 7.9 % (MAM), 6.4 % (SON), and 4.7 % (DJF) of the total volume of the global dust column mass density during the mentioned seasons.

To understand monthly variations in dust, the month-wise climatology (1980-2017) of dust column mass density from MERRA-2 is derived as shown in **Fig. 5.33a**, which clearly demonstrate the dust loading over the Tarim Basin and Thar desert, peaking during May and June, respectively. The influence from the Karakum desert of Turkmenistan is also noticed during April-July. The mean and SD of the dust column mass density (**Fig. 5.33b**) elucidates May and December as maxima and minima dust depositing months, respectively over the investigated region.

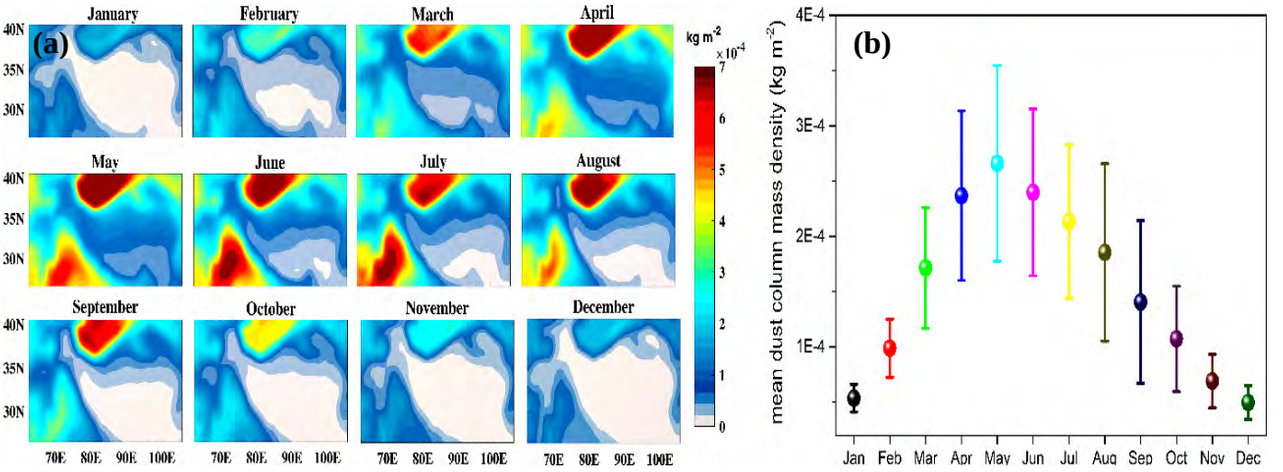

Fig. 5.33. (a) Month-wise climatology (1980-2017) of mean dust column mass density from MERRA-2 (0.5° x 0.625°**)** over the Himalayan region, and **(b)** the corresponding mean ± SD plot.

5.2.2. Seasonal and monthly climatology of absorbing aerosols

The dust particles falls under the category of the absorbing aerosols with AI value being positive, represented by AAI. The index AAI also denotes the contributions from other absorbing aerosol pollutants like smoke, black carbon etc., therefore with this background it is important to know the climatology of AAI as well. The TEMIS data record of AAI from multiple sensors i.e. MS-AAI ver. 1.7, is utilized here for plotting the seasonal climatology on global scale and over the Himalayan region, shown by **Fig. 5.34** and **Fig. 5.35**, respectively. Global mean AAI over is observed highest during JJA (~0.4), while over the Himalayan region, it is ~0.75 (highest) during MAM, and ~0.73 during JJA.

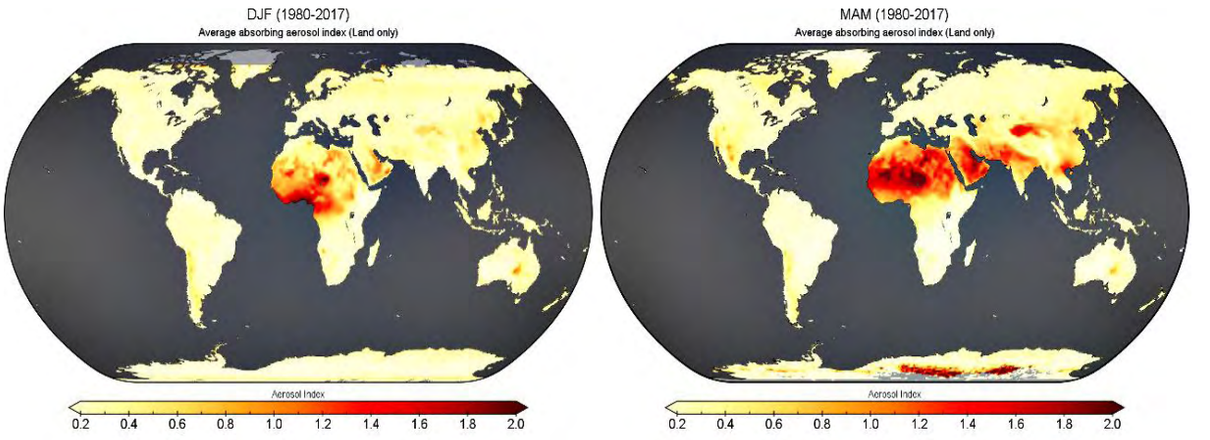

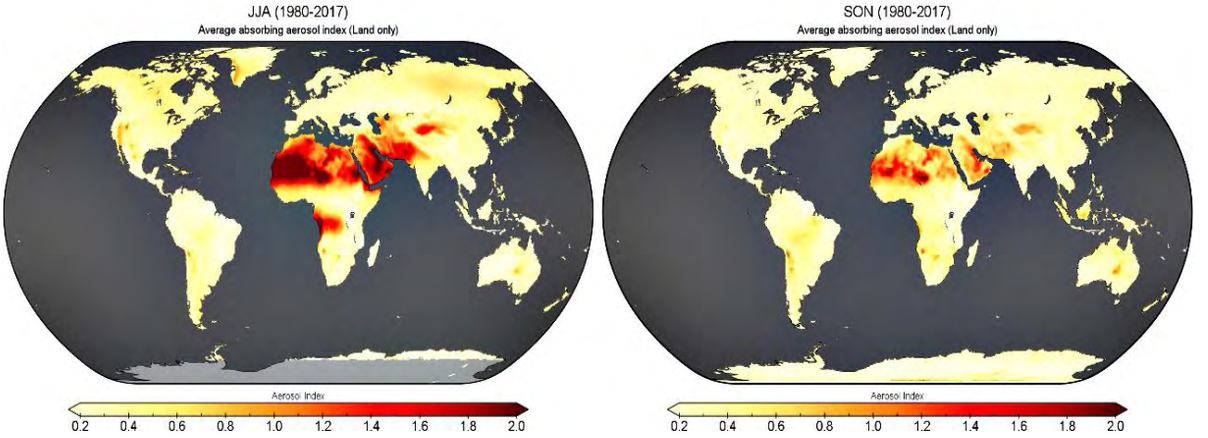

Fig. 5.34. The mean (1980-2017, excluding the period June 1993 - May 1995) absorbing aerosol index from multi-sensors over the globe (land only) for the four seasons - DJF, MAM, JJA, and SON.

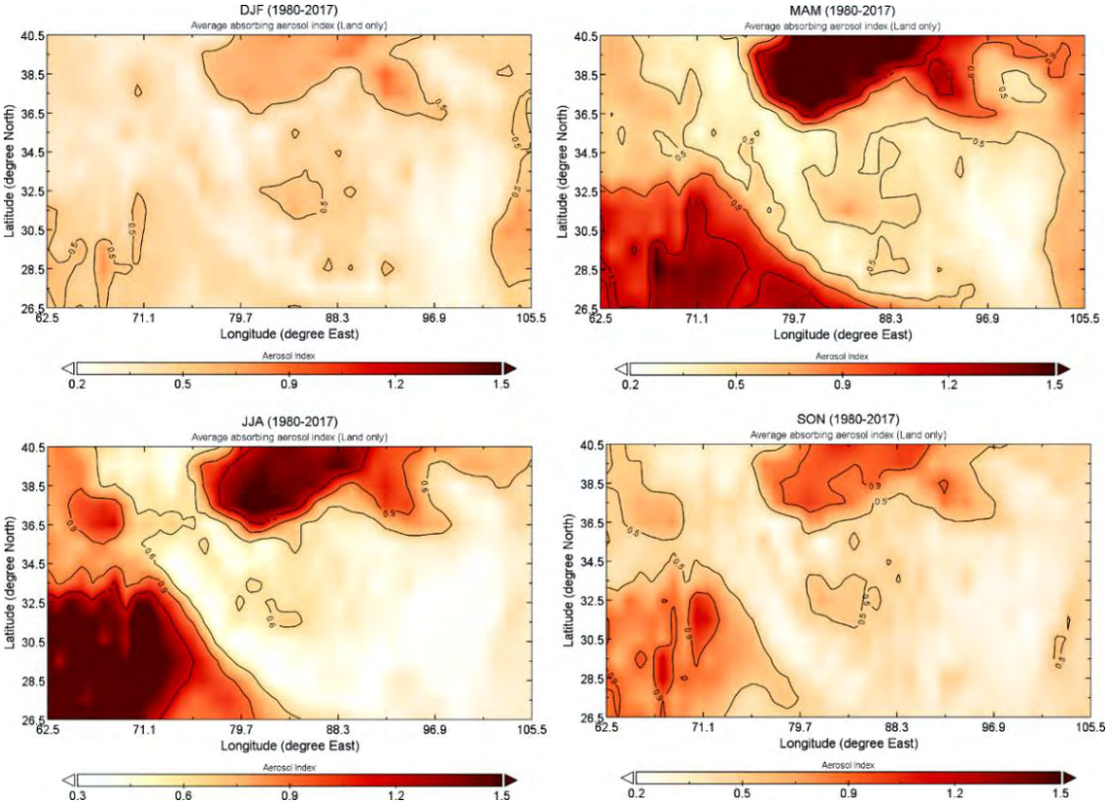

Fig. 5.35. The mean (1980-2017, excluding the period June 1993 to May 1995) absorbing aerosol index from multi-sensors over the Himalayan region for the four seasons - DJF, MAM, JJA, and SON.

The month-wise climatology of AAI over the Himalayan region is shown in **Fig.5.36a**, and the statistics that emerge from an analysis is shown as monthly mean±SD, minima, and maxima in **Fig. 5.36b**.

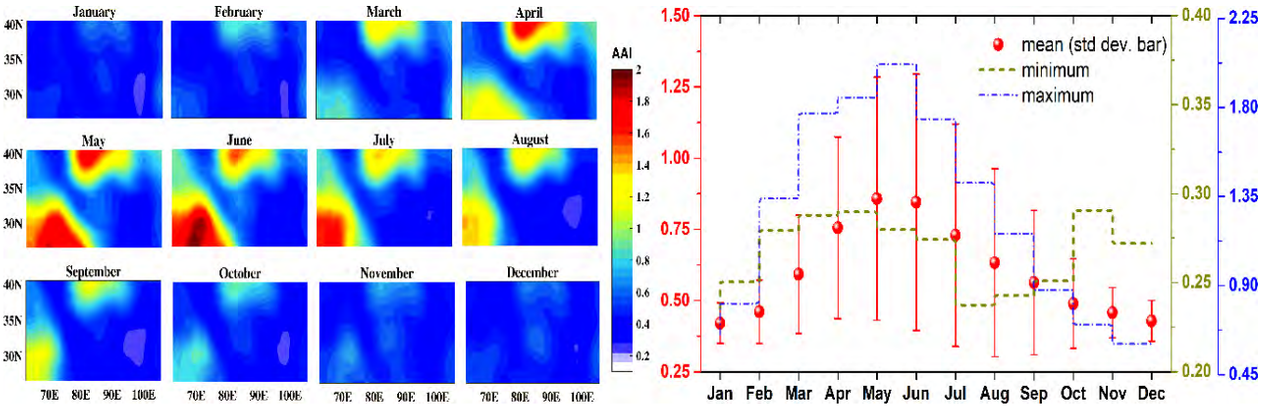

Fig. 5.36. (a) Month-wise climatology (1980-2017, excluding the period June 1993 to May 1995) of absorbing aerosol index from multi-sensors over the Himalayan region, and **(b)** the corresponding statistics.

5.2.3. Trend analysis on dust and other absorbing aerosols

The air quality over the Himalaya and its surrounding regions has received significant attention during the past few decades due to unprecedented overall economic growth, population, and rapid urbanization. The rapid increase in the concentration of pollutant from distinct sources over the Himalayan region has resulted in a large environmental impact and climate change. To analyse the trends of dust over the study region, the normalized monthly anomaly of the average dust column mass density (expressed in kg-m^{-2}) from MERRA-2 is derived for the last 38 years (1980-2017) as shown in **Fig. 5.37**. The figure also shows the top five month-year combinations with highest (positive anomalies) and lowest (negative anomalies) dust intrusions as compared to the remaining years of the same month, in tabular form.

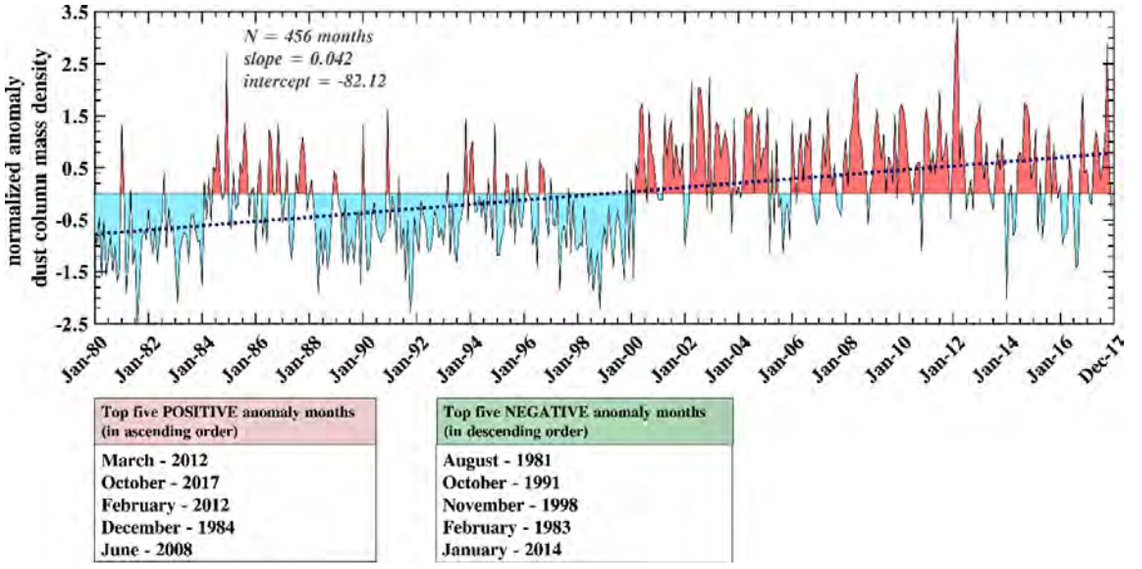

Fig. 5.37. The monthly anomaly for January 1980 through December 2017 of average dust column mass density from MERRA-2 (0.5° x 0.625°) over the Himalayan region. Each value is the monthly anomaly normalized by the standard deviation for the month.

The monthly anomaly of AAI for the same 38 years is deduced from MS-AAI ver. 1.7 data, as depicted in **Fig. 5.38**, which also shows the top five month-year combinations of the most positive and the most negative anomalies in the AAI as compared to the remaining years of the same month.

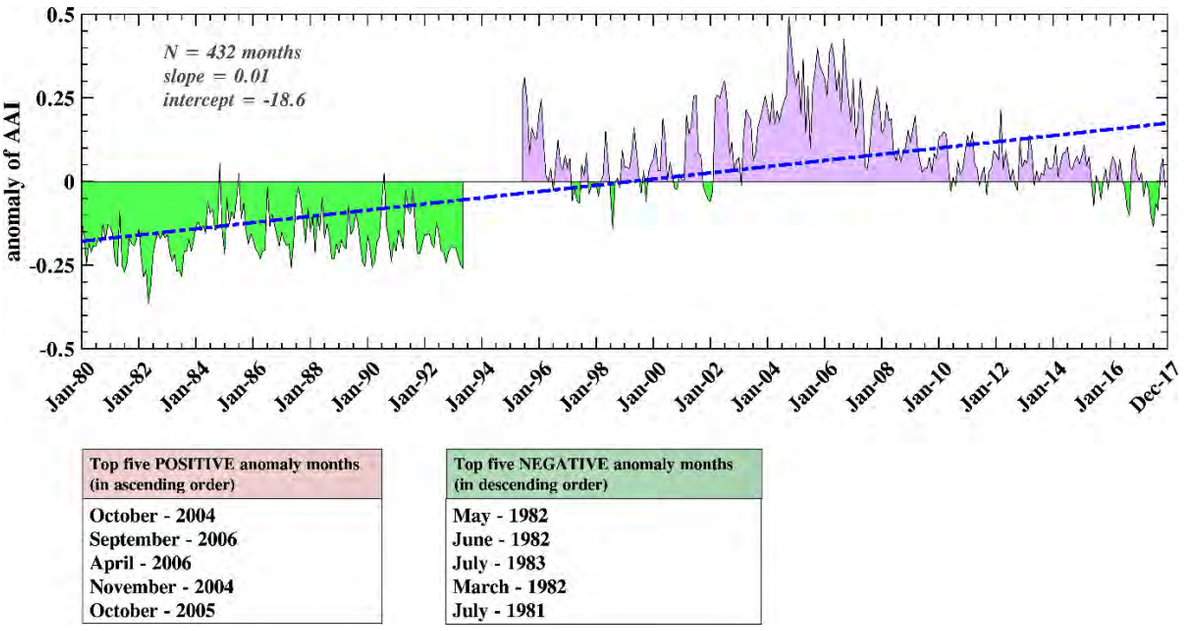

Fig. 5.38. The monthly anomaly for January 1980 through December 2017 of AAI (1° x 1°) obtained from MS-AAI v1.7 data over the Himalayan region. Note that the period June 1993 to May 1995 were not considered due to non-availability of data.

From **Fig. 5.37** and **Fig. 5.38**, it is evident that the pollutants (e.g. dust) over the Himalayan region is showing the rising trend in dust column density and AAI, however the slopes of the positive anomalies of AAI is negative beyond October 2004. The anomaly derived using the past 13 years (2005-2017) AAI data from OMI instrument shows the negative slope of -0.0083 and intercept as 16.55. The MS-AAI and OMI showed the anomaly peaks in AAI during October 2004 and May 2008, respectively.

5.3. Study on the distribution of clouds and precipitation over Northern India

5.3.1. Rainfall pattern

The rainfall data obtained from the TRMM satellite for the individual states in the NSI region during 1998-2016, is analyzed to compute the monthly mean rainfall (mm/day) characteristics, as shown in **Fig. 5.39**.

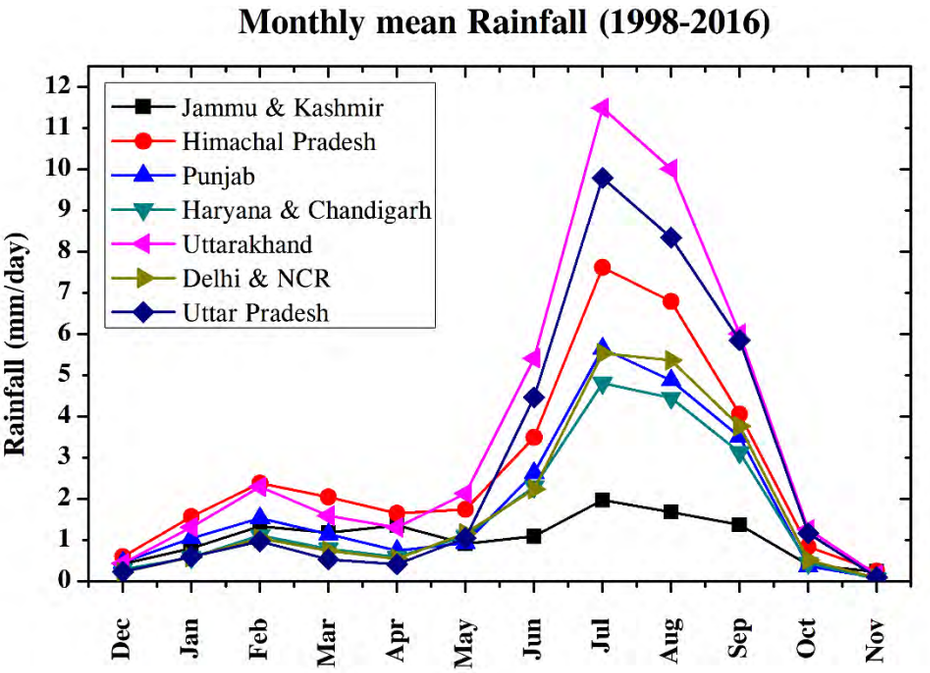

Fig. 5.39. Monthly mean (1998-2016) rainfall pattern (mm/day) obtained from TRMM for the northern states of India.

Fig. 5.39 reveals that the rainfall peaks during monsoon month of July in NSI region and dominates over Uttarakhand. Rainfall in Jammu & Kashmir is lowest and showing little variations as compared to the other states during all the months. Additionally, the amount of monthly mean

rainfall in Uttarakhand (~11.5 mm/day) is significantly higher than other states of northern India during June-September. In general, the onset of the southwest monsoon enters in the form of moist air currents which get deflected towards western Himalayas after hitting the eastern Himalayan ranges. It brings the monsoon rainfall in most of the regions of Uttarakhand and Uttar Pradesh by the mid of June and gets intensified by July (*Krishnamurthy and Shukla*, 2000; *Gadgil*, 2003). As the strength of monsoon winds carrying the moisture source decreases along the path of its travel from east to west, therefore, the north-western part of NSI, especially Jammu & Kashmir receives the last and the least rainfall during June - September as compared to other NSI states (*Goswami*, 1987*; Krishnamurthy and Shukla*, 2000*; Gadgil*, 2003*; Basistha et al.*, 2007*; Shrestha et al*., 2012; *Kothawale and Rajeevan*, 2017). Typically, monsoon in NSI continues till the end of September. The southwest monsoon as a whole contributes more than 70 % of the annual rainfall of India, and hence controls the water and agricultural resources of the country.

During winter (December - March), westerly winds associated with western disturbances originated in the Mediterranean region as extra-tropical cyclones, brings precipitation in the NSI states, sometimes resulting in heavy snowfall over higher reaches of Jammu & Kashmir, Himachal Pradesh and Uttarakhand (*Dimri et al.,* 2015). These western disturbances also brings rainfall during non-monsoonal months over the major portions of north and north-west India.

5.3.2. Vertical distribution of clouds

The classified cloud types do not have the same characteristics, and they do not get formed under the same conditions or in the same regions. Their impact on the hydrological cycle and weather are different, some of them produces precipitation on the ground and the others do not, and they also interact with the solar radiation differently. Therefore, to understand the long-term distribution patterns of different types of clouds (*Sc*, *Cu*, *Ac*, *As*, *Ns*, *Ci*, and *DC*) over the NSI region, the DARDAR product variable 'CLOUDSAT_Cloud_Scenario' is analyzed for the period 2007-2016. The analysis is limited to the identified 1068 days of day-time overpasses (between 06:30 - 07:40 UTC). It is to be noted that the cloud type information for the year 2011 is not taken into account in the present and the henceforth investigations, due to very less data records (30 days). **Fig. 5.40(a-g)** portrays the normalized distribution of seven different cloud types (*Sc*, *Cu*, *Ac*, *As*, *Ns*, *Ci*, and *DC*) over the NSI for the period 2007-2016.

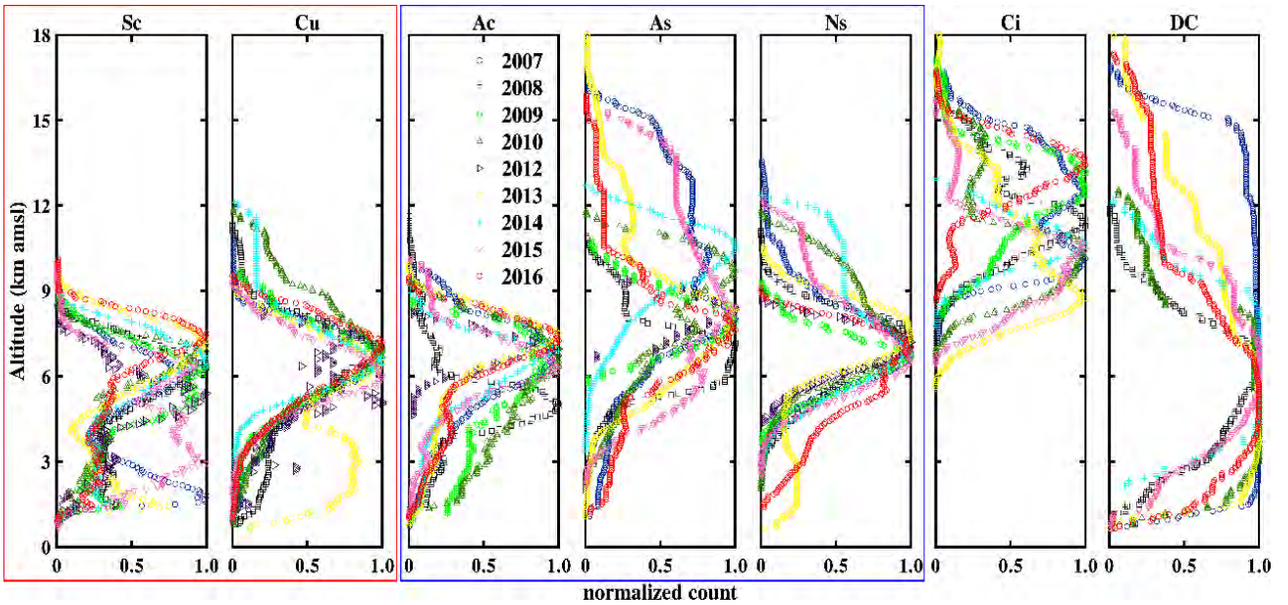

Fig. 5.40. Normalized distribution using DARDAR for **(a)** stratocumulus (*Sc*), **(b)** cumulus (*Cu*), **(c)** altocumulus (*Ac*), **(d)** altostratus (*As*), **(e)** nimbostratus (*Ns*), **(f)** cirrus (*Ci*), and **(g)** deep convective (*DC*) cloud types over the northern states of India for the period 2007-2016. Plots in the red box represents low level clouds, and those in the blue box are the middle level clouds.

Further, the statistics is computed, that revealed that the frequencies of *DC* clouds is high during 2007 (~22.2%) and 2013 (~14.7%), while the gloomy *Ns* clouds are on the higher side in 2014 (~15.2%) and 2015 (~13.1%). Both these cloud types have association with heavy precipitation, snow and severe weather events. The mean occurrences of low level clouds i.e. *Sc* and *Cu* are highest in 2015 (~14.1%) and 2013 (~16.4%), respectively, while the middle level clouds *Ac* and *As* have maximum mean occurrences in 2010 (~17.1%) and 2015 (~19.5%), respectively. The *Ci* appeared more in 2007 (~17.9%) and 2013 (~15.5%) in comparison to the remaining years.

5.3.3. Spatial distribution of clouds

Clouds occur frequently over the study region, and based on the investigation, its distribution (considering all the seven cloud types) over a decade (2007-2016) and during two seasons – JJAS and DJMF is deduced by accumulating the vertical granules representing any of the seven cloud scenes (*Sc*, *Cu*, *Ac*, *As*, *Ns*, *Ci*, or *DC*) between the surface to 18 km height over the grid box resolution of 1° × 1°, and the obtained result is shown in **Fig. 5.41(a-c)**. The multi-year (annual and seasonal) accumulation approach in this case is adopted to provide a better representation of cloud

statistics. Out of these seven studied cloud types, five of them (*Ns*, *Sc*, *Cu*, *Ac*, and *DC*) are categorized as precipitating clouds, and remaining two (*Ci*, and *As*) are non-precipitating clouds.

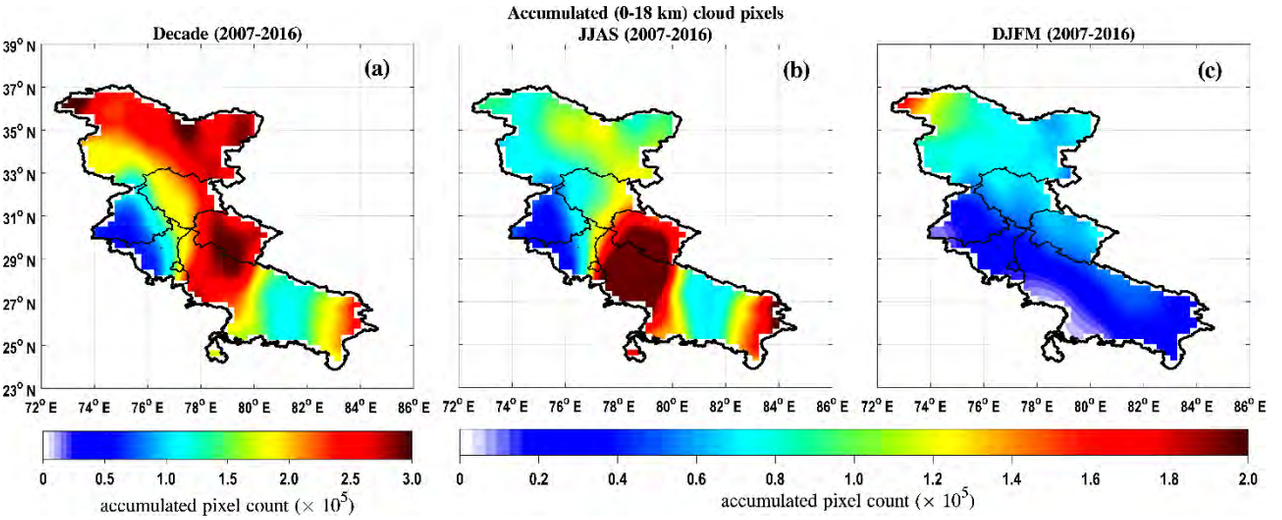

Fig. 5.41. Cloud (*Sc*, *Cu*, *Ac*, *As*, *Ns*, *Ci*, and *DC* altogether) distribution over the northern states of India, accumulated over the surface to 18 km height for **(a)** decade period 2007–2016, **(b)** season JJAS, and **(c)** season DJFM. The 'accumulated pixel count' in colour bar represents the total number of accumulated granules in each grid box.

The vertical profiles of the seven different cloud types shown in **Fig. 5.40** revealed their occurrences over NSI region, and so far it is also established that these clouds are distributed over the entire study zone (**Fig. 5.41**), and are more dominant over Uttarakhand, Himachal Pradesh, Jammu & Kashmir, and major portions of western Uttar Pradesh during JJAS as compared to DJFM seasons. Further, to understand the contribution of individual cloud types, an analysis is performed in obtaining their relative frequency distribution averaged on an annual and seasonal scales for the entire period of study, as depicted in **Fig. 5.42(a-u)**. The relative frequency, defined in percentage by the occurrence of an individual cloud type relative to all the cloud types being studied, has been adapted in this case. From **Fig. 5.42(a-u)**, it can be inferred that annual variation in '*DC*' and '*Ns*' cloud type follows similar pattern as observed during JJAS, and DJFM, respectively. The '*Ci*' cloud type is found to occur mainly in Uttar Pradesh, Punjab and Haryana at both annual and seasonal scales, however, its presence is also seen in Uttarakhand during the south-west monsoon season. The 'Ac' and 'Cu' cloud types marked their presence mainly over Punjab, and Jammu & Kashmir, respectively. Other two cloud types, i.e., '*Sc*' and '*As*' are also observed in most of the NSI regions.

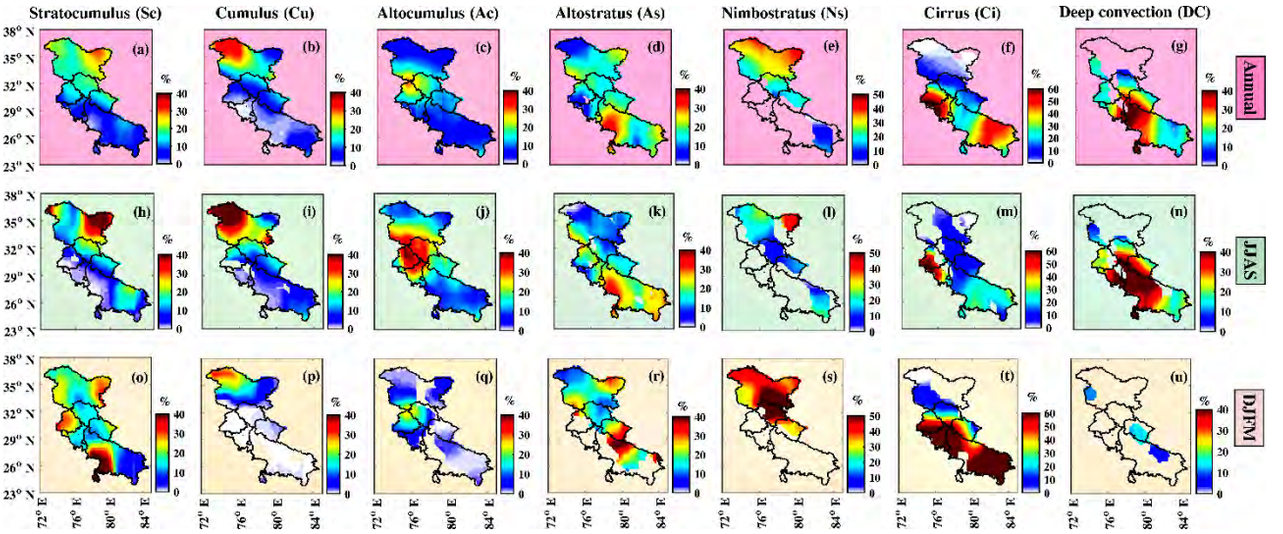

Fig. 5.42. Mean relative frequency distribution on **(a-g)** an annual, **(h-n)** season JJAS, **(o-u)** season DJFM scales for duration 2007-2016, of seven Cloud types (stratocumulus, cumulus, altocumulus, altostratus, nimbostratus, cirrus, and deep convective) over northern states of India, accumulated over the surface to 18 km height.

In the process of extracting the distribution pattern of individual cloud types over NSI region, the following relevant statistics were deduced:

i. During JJAS more than 50% of the clouds/annum appears, and DJFM season accounts for ~25% of the annual cloud occurrences.

ii. On an annual scale, the '*As*' cloud type showed maximum frequency of occurrence when compared with other cloud-types, and the order of occurrences over the last decade (2007-2016) followed: *As* (19.2%) > *Ns* (17.1%) > *DC* (15.8%) > *Ci* (14.9%) > *Sc* (13.8%) > *Cu* (11.2%) > *Ac* (8%).

iii. The most dominant cloud types over NSI region during JJAS and DJFM seasons are '*DC*' and '*Ns*', respectively.

iv. In JJAS season, the order of cloud occurrences followed: *DC* (24.6%) > *As* (20.5%) > *Ci* (13.6%) > *Cu* (12.2%) > *Ac* (11.5%) > *Sc* (10.8%) > *Ns* (6.8%).

v. During DJFM, the order is: *Ns* (32.8%) > *Ci* (21%) > *Sc* (16.3%) > *As* (16.1%) > *Cu* (7.5%) > *Ac* (4%) > *DC* (2.3%).

5.3.4. Concurrent occurrences of cloud types

There could be the possibility that at some instance more than one cloud type appears in a single vertical column. To quantify the same, the statistics on such concurrent occurrences over the NSI region is investigated for the seasons JJAS and DJFM (**Table 5.12**). From the table, it can be interpreted that during both the seasons, the mid level clouds (*Ac* and *As*) dominate the cloud regime, accompanying clouds at low level (*Sc* and *Cu*). The low and mid level (except *Ns*) clouds, together with the cirrus in isolation are very rare and on an average ~40 % of them are accompanied with the other cloud types. In JJAS, the *Ci* is found to appear maximum alongwith *Ac* (11.1 %) cloud type, while during DJFM, it appears most often alongwith *Sc* (23.4 %) cloud type. *Ns* and *DC* are found mostly isolated (more than 80 %), and their remaining volumes are mostly accompanied by *As* and *Ci* cloud types, respectively during both the seasons.

Table 5.12: Frequency of concurrent occurrences of different cloud types over NSI region during 2007-2016.

	Simultaneous occurrence frequency for JJAS in % for DJFM in %						
cloud type	*Sc*	*Cu*	*Ac*	*As*	*Ns*	*Ci*	*DC*
Sc	--	3.9 1.3	10.5 3.9	6.6 10	0.4 1.7	4.7 13.2	0.4 0.03
Cu	9 6.9	--	5.9 2.9	7.5 15.1	0.5 0.5	2.8 5.1	0.1 0.2
Ac	21.2 24.8	5.2 3.5	--	11.2 10.3	1.1 nil	10.8 10.9	0.6 0.3
As	18.1 26.7	9 7.7	15.1 4.3	--	1.9 7.7	5.2 13.1	0.4 nil
Ns	1.9 3.4	1 0.2	2.8 nil	3.6 5.8	--	0.2 0.3	nil nil
Ci	9.7 23.4	2.6 1.7	11.1 3	4 8.7	0.1 0.3	--	6.3 0.2
DC	2 1.9	0.3 2.1	1.5 3.1	0.8 nil	nil nil	14.7 7.3	--

5.3.5. Spatial distribution and frequency of precipitation

The variation in precipitation over the NSI region is further attempted for the same period i.e. 2007-2016 by making use of coincident TRMM and DARDAR retrievals. Alongwith the cloud type information (*Kumar et al*., 2019), DARDAR product provides the information on three precipitation

types - liquid precipitation, solid precipitation, and possible drizzle, and making use of this product, the frequency of occurrences of the individual precipitation types are derived for a decade and for the two seasons (JJAS and DJFM) as shown in **Fig. 5.43(a-c)**. For the above-mentioned period, the total rainfall (liquid precipitation) data from the TRMM, nearly coincident with the DARDAR retrievals are also analyzed to obtain the total rainfall distribution pattern for a decade, and for the two seasons, as portrayed in **Fig. 5.43(a-c)**.

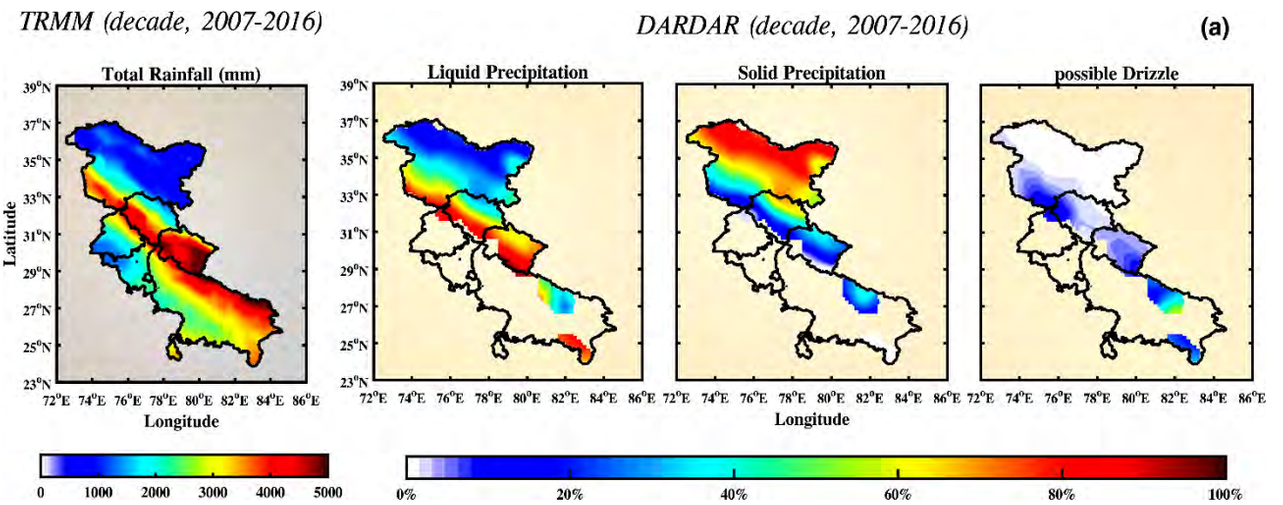

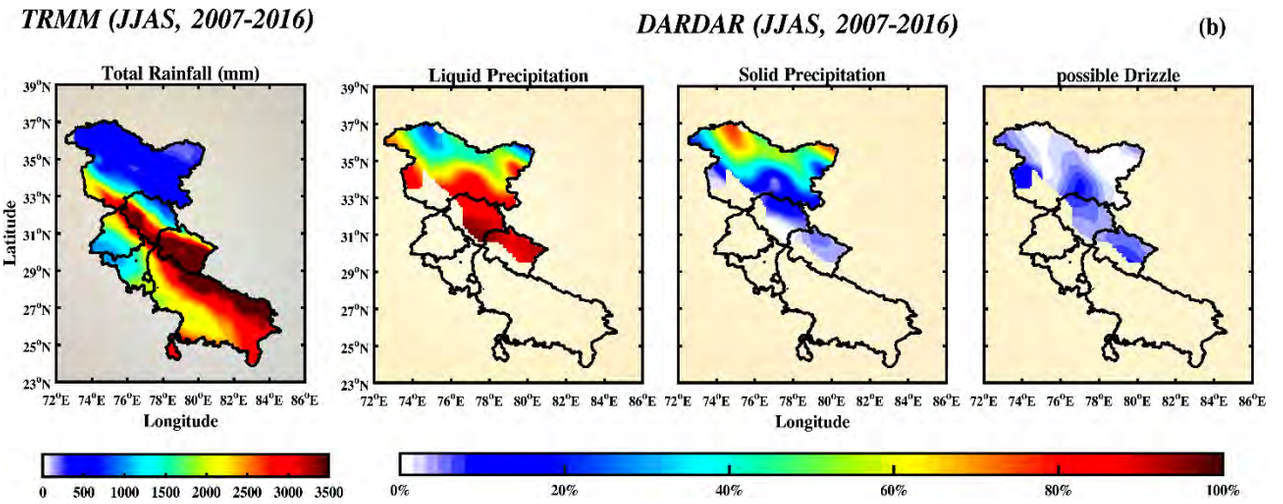

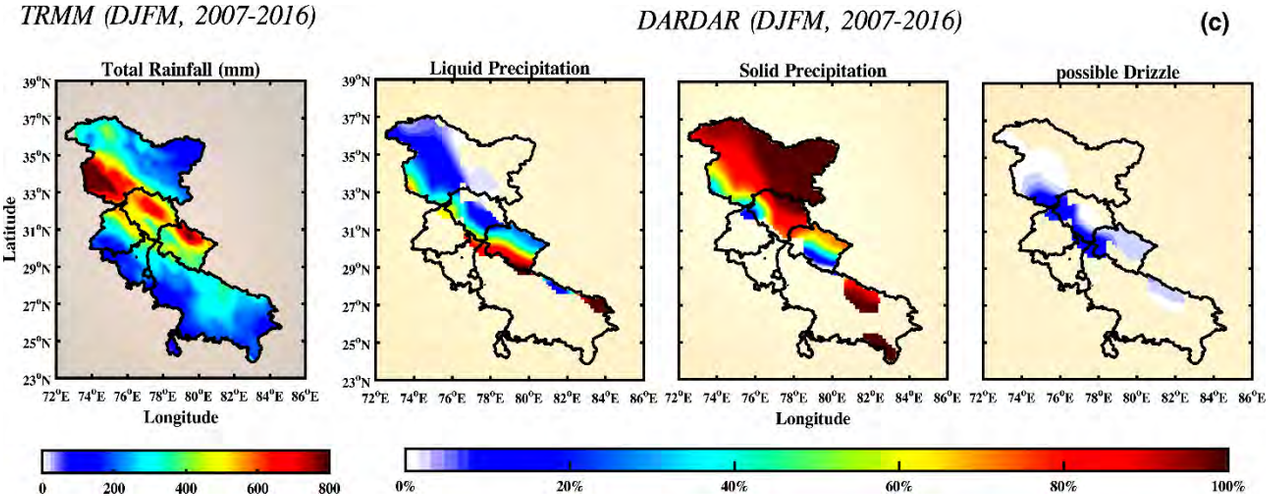

Fig. 5.43. Precipitation distribution and frequency of its types (liquid precipitation, solid precipitation, and possible drizzle) over the NSI region during **(a)** decade 2007-2016, **(b)** June-September, and **(c)** December-March, obtained from TRMM 3B42 and DARDAR products, respectively.

The key merits of using both the TRMM and DARDAR products for precipitation study in this research work is obtaining the two-fold information(s) – (i) compare and evaluate the two products as far as liquid precipitation (rainfall) is concerned, which can further be used in synergies to fill-the gaps in missed (undetected) regions, and (ii) identify the regions where the solid and liquid precipitations are dominant. As far as the liquid precipitation estimated using the TRMM and DARDAR is concerned, occasional differences is found in few states like Punjab and Haryana, however, this could be due to the differences in their operating frequency, sensitivities, dynamic range, and the uncertainties associated in their retrievals. From **Fig. 5.43(a-c)**, it is seen that both the TRMM and DARDAR identified maximum liquid precipitation in Uttarakhand, Himachal Pradesh, and few districts in the south-western part of Jammu & Kashmir over the last decade, especially during Indian summer monsoon. Rainfall resulting due to its interaction with the western disturbances is also observed in these states, however, it is found to be less significant, as compared to that observed during summer monsoon. Further, Jammu & Kashmir, Himachal Pradesh, and few portion of Uttarakhand receives the highest amount of solid precipitation (in the form of snow) over the decade (2007-2016), especially during the active months of western disturbances i.e. JJAS.

Precipitation occurs primarily in the form of rainfall (liquid precipitation) and snow (solid precipitation). Owing to the presence of Himalaya and the varied topography, different sub-portions of the NSI region experiences different precipitation climatology. Precipitation in this region is

mainly governed by the two dominant weather systems i.e. the southwest monsoon and the WDs. The study on the precipitation climatology over the NSI region for the period 2007-2016 (a decade) shown in **Fig. 5.43** revealed that in comparison to the other regions of NSI, the hilly portion of western and central Himalaya, comprising of Jammu and Kashmir, Himachal Pradesh, and Uttarakhand witnessed the highest precipitation, and there has been a substantial increase in the frequency of extreme weather events in these states in the last 30–40 years (International Disaster Database; http://www.emdat.be). The contributing factors for the higher precipitation over these areas could be the complex orography features andsynoptic-scale factors, and multiple-scale interactions over these hilly regions (*Rudari et al*., 2004; *Sen et al*., 2011). In addition, the increase in extreme weather events in the form of cloudbursts, flash floods, landslides etc. in these NSI states have strong connection to the land-use changesdue to man-made activities (e.g. urbanization, industrialization, deforestation, forest-fires) leading to the intensification of atmospheric processes and dynamics.

The heavy rainfall over the three NSI states - Jammu and Kashmir, Himachal Pradesh, and Uttarakhand, mainly occurs due to the interaction between the well-formed low pressure system of the south-west monsoon from east to west and the upper air westerly trough running from north-west regions to the east. However, several studies have reported significant decreasing trends in precipitation during monsoon (e.g. *Naidu et al*., 2009; *Singh and Mal*, 2014; *Kumar and Jaswal*, 2016), which is possibly linked to the warming over the Indian Ocean that weakens the southern oscillation and decreases the temperature gradients over south Asia (*Basistha et al*., 2009; *Naidu et al*., 2009). Furthermore, studies have reported mixed trends during active western disturbance months (winter)in these states (e.g. *Guhathakurta and Rajeevan*, 2007; *Kumar and Jain*, 2010; *Singh and Mal*, 2014; *Kumar et al*., 2015) and the winter warming has shifted the ratio of snowfall to rainfall towards increasing rainfall components, resulting in the uneven changes in the snowpack and snowmelt runoffs, and increase in their associated consequences (*Stewart*, 2009; *Madhura et al*., 2015).

Overall, the NSI region exhibits two salient features of precipitation that are - liquid precipitation / rainfall decreases westwards or north-westwards, while the solid precipitation increases westwards or north-westwards.

5.3.6. Associations between cloud and precipitation types

Variations in cloud fraction affect the microphysical processes in clouds, and may have a substantial influence on the occurrence and intensity of precipitation. Furthermore, different forms of precipitation (solid or liquid) have associations with the type of clouds present and vice versa. To quantify the same, an investigation is done using the retrieved information on the cloud (*Kumar et al*., 2019) and precipitation types over the NSI region for the period 2007-2016, and **Table 5.13** summarizes the associated precipitation for each cloud type on annual, and seasonal (JJAS and DJFM) scales.

Table 5.13: Frequency of different precipitation forms during the occurrences of individual cloud types on an annual and seasonal (JJAS and DJFM) scales for the period 2007-2016.

cloud type	temporal scales	total no. of occurrences (clouds)	total no. of co-occurrences (clouds + precipitation)	co-occurrence frequency		
				liquid precipitation	solid precipitation	possible drizzle
Sc	annual	1743589	847275 (48.6%)	38.6%	51.6%	9.8%
	JJAS	782543	376658 (48.1%)	62.3%	19.3%	18.4%
	DJFM	514998	236599 (45.9%)	12.8%	85.1%	2.1%
Cu	annual	1414916	888058 (62.8%)	43.5%	55.2%	1.3%
	JJAS	885048	484508 (54.7%)	61.0%	36.7%	2.3%
	DJFM	237339	185186 (78.0%)	5.5%	94.4%	0.1%
Ac	annual	1014998	49292 (4.9%)	50.7%	20.6%	28.7%
	JJAS	831354	46068 (5.5%)	48.6%	21%	30.4%
	DJFM	127016	2400 (1.9%)	100%	nil	nil
As	annual	2435075	4120 (0.2%)	35.4%	28.2%	36.4%
	JJAS	1480347	2960 (0.2%)	49.3%	nil	50.7%
	DJFM	509491	728 (0.14%)	nil	100%	nil
Ns	annual	2173183	1498461 (68.9%)	23.7%	76.0%	0.3%
	JJAS	491959	318225 (64.7%)	68.8%	29.7%	1.5%
	DJFM	1036049	780040 (75.3%)	11.2%	88.8%	nil
Ci	annual	1886175	nil	nil	nil	nil
	JJAS	987487	nil	nil	nil	nil
	DJFM	662512	nil	nil	nil	nil
DC	annual	2006733	1047553 (52.2%)	98.4%	1.6%	nil
	JJAS	1775933	914684 (51.5%)	99.8%	0.2%	nil
	DJFM	73303	36704 (50.1%)	86.4%	13.6%	nil

Based on the statistics presented in **Table 5.13**, it can be inferred that *Sc* clouds occurred highly in association with liquid precipitation during JJAS (62.3% of the total *Sc* cloud and

precipitation co-occurrences), and with solid precipitation during DJFM (85.1%). On the annual scale, its frequency is highest with solid precipitation (51.6%) as compared to the other forms of precipitation. Similar connections are noticed for *Cu* and *Ns* cloud types, with association of 61% and 68.8%, respectively to the liquid precipitation (JJAS). The association of *Cu* and *Ns* cloud types with solid precipitation during DJFM is observed as 94.4% and 88.8%, respectively. Both these cloud types showed the highest frequency of occurrences of solid precipitation (55.2% and 76%, respectively) when checked on the annual scale. On the other hand, the *DC* cloud type, which occurred more than 50 % with precipitation, showed its maximum frequency of occurrences with the liquid precipitation (> 85 %) in all the time scales. The concurrent occurrence of precipitation and cirrus clouds were not observed in any cases, and additionally, the middle level *Ac* and *As* cloud types also marked their least occurrences (< 6 % and ≤ 0.2 %, respectively) with precipitation in both the annual and seasonal scales.

5.4. Study on the meteorological parameters using remote sensing and in-situ measurements

5.4.1. Surface meteorology using AWS measurements

Surface meteorology plays an important role in air pollutants formation, dispersion, transport and dilution. Therefore, making use of the AWS data from ARIES, Nainital during January 2013 – December 2018, an understanding is developed on the variations in the near-surface meteorological variables - ambient temperature, relative humidity, pressure, rainfall, wind speed and wind direction. **Fig. 5.44(a-d)** shows the plots on the monthly variations in temperature, RH, pressure, and rainfall during the above period at ARIES, Nainital.

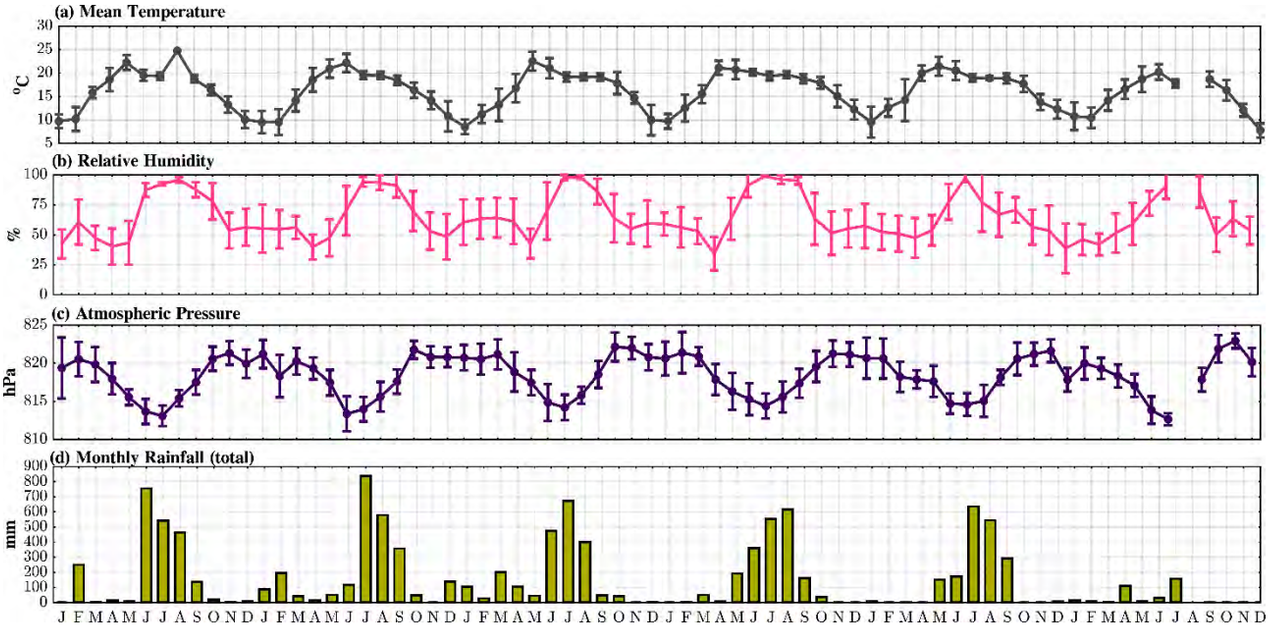

Fig. 5.44. Monthly variations in the average **(a)** temperature, **(b)** relative humidity, and **(c)** atmospheric pressure, and the variations in the **(d)** total rainfall at ARIES, Nainital obtained from AWS measurements during 2013-2018.

From **Fig. 5.44** it is inferred that during last 6 years (2013-2018), the temperature of the site varies from minimum (monthly average: 10.4°C ± 1.5°C) in winter (December to February) to maximum (monthly average: 20.1°C ± 1.7°C) during April to mid of June. The average variation in RH is 65 % ± 18 %, with minimum observed during April 2016 (monthly average: 34.3 %) and maximum in July 2016 (monthly average: 98.8 %). In July and August, the RH is found on much higher side (> 95 %) than other months. The atmospheric pressure varied from 812.6 hPa to 822.9 hPa during these 6 years, with highest during October-November, and lowest during June-July. The monsoon in this region generally begins from mid of June, gets intensified by the month of July, and continues till September. The study revealed that July received the highest average rainfall of 567 mm ± 226.7 mm, which accounts for ~ 30 % of the total annual rainfall. August is observed as the second highest rainfall month with 520.5 mm ± 87 mm of average rainfall. July 2014 and June 2013 are recorded as extreme rainfall months, with 837 and 755 mm of rain, respectively. The maximum surface wind speeds (> 6 m/s) were recorded during March – June, and on the other hand, the wind speed during winter (December-February) was found low with average intensity of ~ 2-3 m/s. To understand the wind behavior at the site, wind rose plots are generated from the reproduced hourly averages (computed from AWS data files logged at every 10 min) of wind speed and wind direction for the period 2015-2018. The wind measurements for the years 2013 and 2014

are not considered due to large discontinuities in wind data. Averaging of wind direction is done using the vector functions, which involves the computation of wind vectors ($\vec{u}$ and $\vec{v}$) from wind speed and direction values. **Fig. 5.45** shows the seasonal wind roses, aggregated by day and night hours to see the differences between their patterns. It is evident in the wind rose plots that nighttime has a much greater proportion of low wind speeds than the daytime hours at this monitoring location. The analysis revealed the dominance of westerly winds in all the seasons, except during winter when the wind pattern drifts towards northwesterly. During daytime of spring/summer seasons, signatures of strong south and southeasterly winds are also evident in the wind rose.

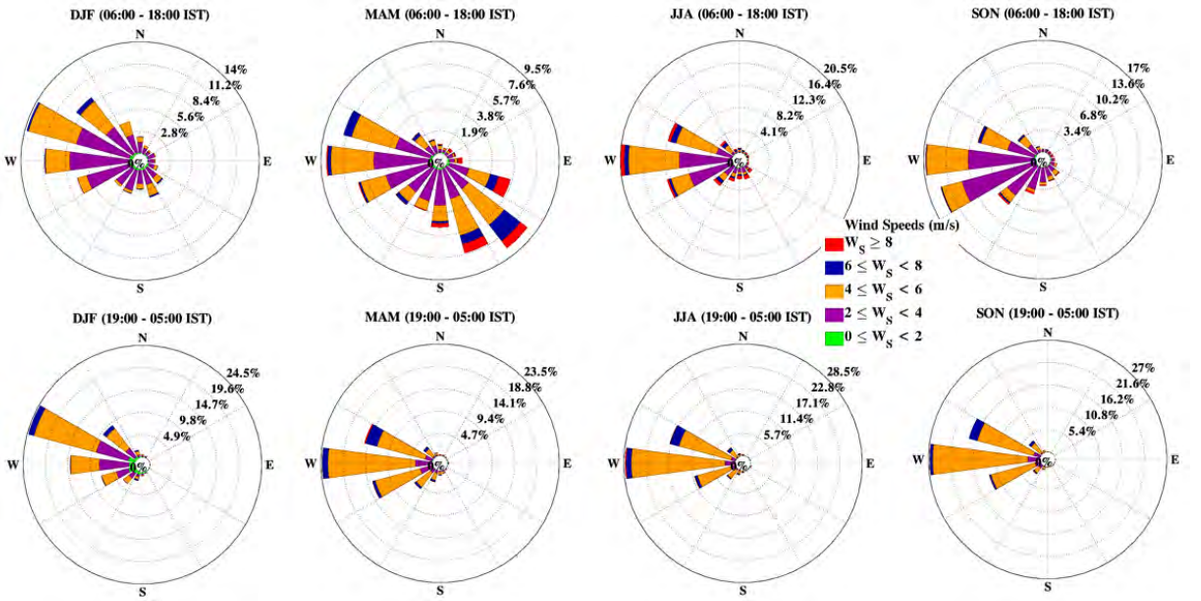

Fig. 5.45. Day (taken here as 06:00 – 18:00 IST) and night (taken here as 19:00 – 05:00 IST) wind roses for ARIES Nainital site, obtained from the AWS measurements over the period 2015-2018, during winter (DJF), spring/summer (MAM), monsoon (JJA), and autumn (SON).

It is worth to mention that the AWS site (**Fig. 4.5**) at ARIES is surrounded by rolling hills along the north, northwest and northeast sides, and steep valleys touching the Tarai regions towards its south and southwest. In addition to the geographic surroundings, the complex topography of the site is highly favorable to slope winds that consists of upslope and downslope winds during day and night times, respectively. The direct mechanic actions like orographic blocking from the surrounding hills and valleys, or complex actions like thermal inversions could lead to significant departures in the wind direction from what it would be expected, hence, without considering the

local effects, the AWS measurements of wind direction, may not be accurate or true representative, as far as the complex topography like ARIES, Nainital is concerned. Some of the local effects for a given wind direction could be minimized or avoided by including the low level upper air observations from the sensors placed on the meteorological towers at different levels, or through the measurements using the atmospheric RaDAR, a part of which is covered in this research work.

5.4.2. Long term changes in the surface temperature on local and regional scales

Due to the complex topography and limited ground based meteorological stations, it is very difficult to check and make time to time assessment of the hotspot locations in the Himalayan region, which are the main sources for the climate change in Himalaya. By making use of the long-term, high resolution measurements from satellite remote sensing tools and re-analysis models, a preliminary investigation in the direction of establishing a relation between surface temperature on local and regional levels in the Himalayan region, at monthly and seasonal scales is attempted here. The geographical grid boxes are defined as 29-30°N, 79-80°E for Nainital (local), and 26.5-40.5°N, 62.5-106°E for Himalaya (regional). The boundary defined for Nainital is basically the sub-set of the Himalayan boundary, however, they are separately defined in the present investigation to understand the effect of surface temperature and precipitation on local and regional levels.

Out of the available monthly data sets over the Himalayan region, it is found that the re-analysis data sets have more temporal coverage, and available at good spatial resolutions. For surface temperature, the latest versions of the re-analysis data from MERRA-2 (with spatial resolution of 0.5° × 0.625°) and GLDAS (with spatial resolution of 0.25° × 0.25°) are available from January 1980 – December 2017 i.e. 38 years, and from January 2000 – December 2017 i.e. 18 years, respectively. On the other side, the long term monthly surface temperature (daytime/ascending and nighttime/descending) records from AIRS (1° × 1°), a satellite remote sensor widely used for water vapour and temperature studies over the Himalayan region (*Prasad and Singh*, 2009; *Naja et al.,* 2016), is found for ~ 15 years till December 2017, and may be opted as a source for this investigation.

For the selection of surface temperature data among MERRA-2, GLDAS, and AIRS, for this study, a comparative statistical analysis is performed over the abovementioned latitude-longitude grids defined for the Himalaya, and MERRA-2 turned out to be best choice among the three data sets. For the matched period of data records, the correlation among these three data sets is found >

0.92, and highest correlation (R~0.99) is observed between MERRA-2 and AIRS surface temperature data sets. The absolute mean bias between MERRA-2 and AIRS is found < 1.2°K, with coefficient of variation in MERRA-2 (~0.029) is closer to 0.026 observed with AIRS, and 0.02 with GLDAS. Moreover, MERRA-2 data sets are available for the higher period than GLDAS and AIRS, and hence used here for further investigation.

To understand the long term monthly average mean, minimum, maximum, and trends in the surface temperature at Nainital and the Himalayan extents, the 2 m monthly surface temperature data obtained from MERRA-2 is analysed for the period of 38 years (1980-2017). The results obtained is summarized in **Table 5.14** and **Table 5.15** for both the regions. Here it is worth to mention that for the given period, the monthly surface temperature data for both regional and local scales are highly correlated with the Pearson's correlation value, R ~ 0.95, and hence indicating the regional representativeness of the Nainital location.

Table 5.14: Monthly mean, minimum, maximum, slope and intercepts in the monthly surface temperature (2 m) for Nainital and Himalayan regions, computed over the period 1980-2017 using MERRA-2 re-analysis model. Negative trends are highlighted in 'yellow' shades.

Months	Nainital temperature (°C)					Himalaya temperature (°C)				
	mean±std	minimum	maximum	slope	intercept	mean±std	minimum	maximum	slope	intercept
Jan	9.8±1.1	7.7	12.9	0.01	9.6	-4.0±0.9	-6.1	-2.5	0.01	-4.2
Feb	12.1±1.3	9.9	16.2	0.03	11.5	-1.5±1.3	-3.9	1.5	0.04	-2.2
Mar	16.8±1.3	14.3	19.4	0.02	16.4	3.7±1.0	1.8	5.9	0.04	2.8
Apr	22.5±1.4	19.7	22.3	0.01	22.2	9.5±0.8	7.5	11.0	0.03	9.0
May	26.5±1.2	22.5	28.2	0.004	26.2	14.3±0.7	13.0	15.9	0.02	13.9
June	27.3±1.4	23.9	29.5	-0.02	27.7	17.9±0.4	16.8	18.7	0.01	17.8
July	24.8±1.3	23.1	28.6	-0.04	25.5	19.2±0.4	18.4	20.0	0.01	19.1
Aug	23.4±0.6	22.5	26.1	-0.02	23.7	18.1±0.4	17.3	18.9	0.01	17.9
Sep	21.8±0.6	20.4	23.6	0.004	21.7	14.3±0.5	13.3	15.4	0.02	14.0
Oct	18.5±0.7	16.9	19.9	0.02	18.2	8.6±0.6	7.3	10.0	0.03	8.0
Nov	14.6±0.8	13.0	16.5	0.02	14.2	2.6±0.7	1.0	4.3	0.01	2.3
Dec	11.3±0.8	9.4	13.1	0.02	10.9	-2.2±0.8	-3.8	2.9	0.01	-2.4
overall	19.1±6.0	7.7	29.5	6E-4	19.0	8.4±8.1	-6.1	20.0	0.002	7.9

Table 5.14 clearly shows January as the coldest month in the Himalaya, including Nainital, while June and July are the hottest months in Nainital and Himalaya, respectively. The negative trend is clearly seen in temperature on local scale during monsoon season, in contrast to the steady positive trend (slope ~ +0.01) at regional level. Overall temperature trend is still positive at both the scales, hence confirming the net warming in the Himalayan region.

Table 5.15: The year-wise anomalies in the annual mean surface temperature for the past 38 years (1980-2017) over Nainital and Himalaya using MERRA-2 re-analysis model. The trends ≥ 0.5 are shaded in 'yellow', and that ≤ -0.5 are shaded in 'green'.

Nainital										
Year	**+0**	**+1**	**+2**	**+3**	**+4**	**+5**	**+6**	**+7**	**+8**	**+9**
1980	+0.01	-0.26	-0.96	-0.80	-0.07	-0.14	-0.42	+1.11	+0.45	+0.14
1990	+0.05	+0.21	+0.16	+0.21	+0.27	+0.12	-0.23	-0.84	-0.03	+0.69
2000	-0.19	+0.16	+0.53	-0.19	-0.12	-0.37	+0.31	-0.25	-0.52	+0.45
2010	+0.54	-0.74	-0.22	-0.45	+0.02	+0.03	+0.79	+0.54		
Himalaya										
Year	**+0**	**+1**	**+2**	**+3**	**+4**	**+5**	**+6**	**+7**	**+8**	**+9**
1980	-0.44	-0.55	-0.77	-0.64	-0.41	-0.11	-0.46	+0.28	+0.36	-0.50
1990	+0.14	-0.06	-0.47	-0.09	+0.19	-0.15	-0.23	-0.34	+0.54	+0.63
2000	+0.06	+0.34	+0.40	-0.02	+0.26	-0.19	+0.58	+0.23	-0.16	+0.24
2010	+0.35	-0.16	-0.56	+0.23	-0.05	+0.25	+0.85	+0.42		

The least-square linear regression trend on the temperature anomalies for the 38 years shown in **Table 5.15** revealed that in ~ 68 % of the years, both local and regional scales follows the correspondingly similar positive or negative trends in the surface temperature anomalies. The declining trends are seen during the initial 6-7 years at both local and regional scales, which gets reversed after 1987. Nainital experiences continuous rising trends since 1987, which continues till 1995. Somewhat similar pattern of declining-rising trend is also evident during 2011-2017 in this local scale, where 2011-2013 showing the falling trend, and rising trend henceforth. For the regional scale, such pattern is noticed during 1995-2002. The warmest year during the past 38 years is recorded as 1987 and 2016 for local and regional scales, respectively. To determine the overall trend in the annual variations in the surface temperature over regional and local scales, the anomaly values in the annual mean surface temperature (**Table 5.15**) are plotted in **Fig. 5.46**(**a** and **c**) for Himalaya and Nainital regions, respectively, and the corresponding regression lines are drawn. In these plots, positive anomaly indicates warming, while negative anomaly indicates cooling at the surface and the trends are statistically significant at 95% level. For further clarity, their residuals are also drawn to show departures of anomaly values from the baseline, shown by **Fig. 5.46b**, and **Fig. 5.46d**, respectively.

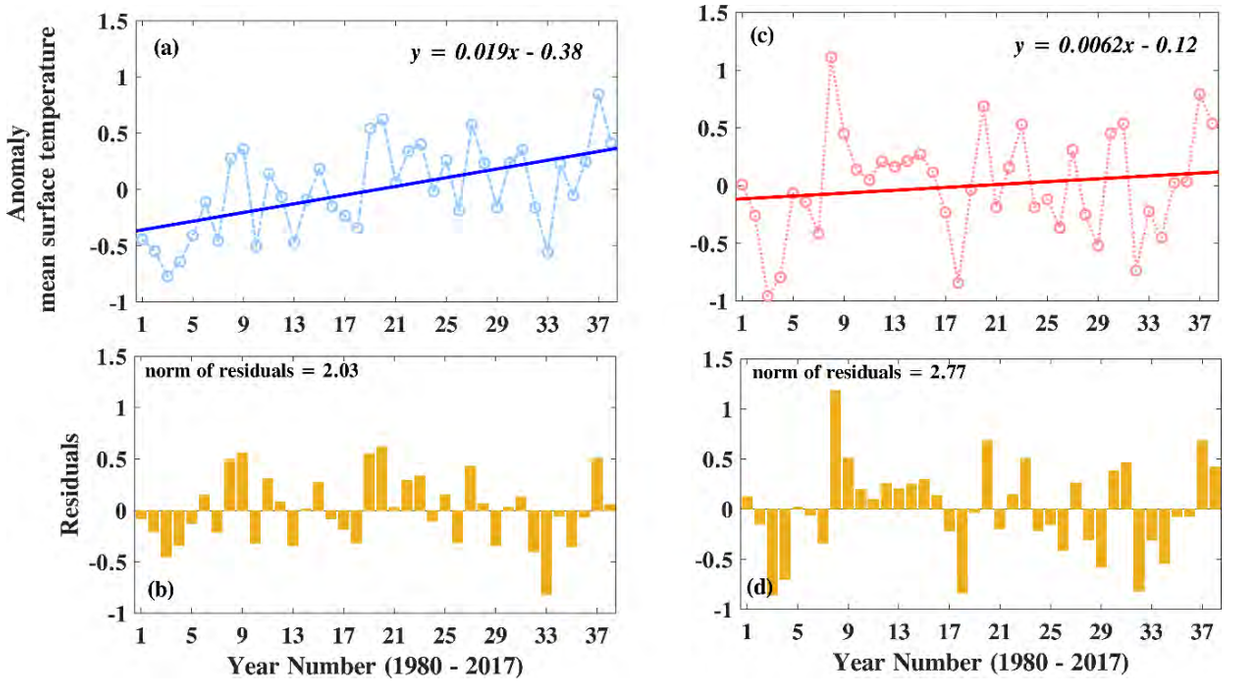

Fig. 5.46. Annual mean surface temperature anomalies for the period 1980-2017 over **(a)** Himalaya, and **(b)** Nainital, and their corresponding residual plots in **(c)** and **(d)** respectively. The years 1980 to 2017 are shown as year numbers 1 to 38.

Fig. 5.46. shows that that the trends in surface temperature at both regional and local scales are positive, with their slopes as +0.019 and +0.0062, respectively, and hence further confirming the warming of the Himalayan region. In addition to this, the rising trend in absorbing aerosols over the Himalayan region were also observed in the preceding section. Generally, aerosols, if present, tends to cool the surface by cutting-off the incoming solar radiation through absorption and scattering, which is known as the 'surface dimming' effect of aerosols. However, the positive anomalies observed both in the surface temperature and absorbing aerosols over the Himalayan region are opposite to this effect. Therefore, to explain the warming trend in surface temperature, trend in the cloud cover at pressure levels 700-400 mb is checked over the Himalayan region, for which the data is taken from MERRA-2 over the same 38 periods (1980-2017), as used in computing the trends in absorbing aerosols and surface temperature. Analysis revealed decreasing trend (slope = -0.00022, intercept = 0.0043) with 95% significance level in this mid-level cloud cover, which could possibly be due to the enhanced solar absorption by the absorbing aerosols (which have the general tendency of trapping the incoming solar radiation) in the atmosphere, which might have caused intensification in the evaporation of the cloud droplets and accelerated the cloud burning (aerosol

semi-direct effects). The decrease in the cloud cover greatly reduces the planetary albedo and allows access to more solar radiations to penetrate the troposphere and reach the surface. Hence, it may be said that the warming of the surface over the Himalayan region is not directly linked with the rising trend in absorbing aerosol, however, it is likely linked to the reduction of cloud amount in the atmosphere.

5.4.3. Vertical distribution of the meteorological parameters using radiosonde

From June 2011 to March 2012, there were regular radiosonde launches (4 times a day) from ARIES, Nainital. These radiosonde launches were made as a part of RAWEX–GVAX campaign, conducted during the above-mentioned period at ARIES, Nainital jointly by the government departments from US and India. The basic meteorological parameters that were measured are – atmospheric pressure, temperature, RH, wind speed (WS), and wind direction (WD). However, using these basic meteorological parameters there are other derived parameters such as dew point temperature, zonal and meridional components of the winds that are also utilized for atmospheric studies. The variations in the above-mentioned basic parameters on monthly and seasonal scales, and their comparison with the data obtained from AIRS satellite, MERRA re-analysis, and Weather Research and Forecasting (WRF) simulation have been already carried out (*Naja et al.*, 2016). The radiosonde observations were also used in boundary layer studies, and comparison with the ground based RaDAR Wind Profiler (RWP) and CALIPSO satellite retrievals (*Singh et al*., 2016; *Kumar et al*., 2018).

In this work, the radiosonde observations made from ARIES, Nainital during June 2011 – March 2012 are compared with the radiosonde data available from the nearby meteorological station Delhi. Only the near coincident observations (±1 hr) between the two stations are considered that include the 00 GMT and 12 GMT observations, that turned out to be 169 coincident observations during winter, 59 during pre-monsoon, 118 during monsoon, and 178 during post-monsoon. **Fig. 5.47** shows the mean vertical profiles of pressure, air temperature, RH, wind speed, and wind direction for Nainital and Delhi stations during these seasons. Nainital is about 2 km amsl, hence the measurements from Delhi are considered only above 2 km in order to maintain the uniformity in the pressure levels. The vertical profile of pressure agrees well and shows the expected exponential decrease in its level at both the stations, which are located around the same latitude (within ±1°). Temperature ideally decreases with altitude in the troposphere at a rate of

about 6.5°C/km, and then increases in the stratosphere, however, there appears some instantaneous variations in the temperature profile particularly in the lower atmosphere due to the dynamical aspects of the atmosphere, and the same is evident in the figure. The increase in temperature around 16 km and 18 km in case of Delhi and Nainital respectively is evident and represents the height of tropopause at that level. The differences in the height of tropopause may arise due to the geographical location of the two stations. Nainital is close to the mid latitude where the air masses from tropical and mid-latitude regions interact and may give slight rise to tropopause, however this needs to be understood in great detail and left for the future scope of study. RH is another important meteorological variable which affects the local weather and ecosystem to a great extent. In general, at this latitude the RH during monsoon is highest and falls mostly between 85-95%. **Fig. 5.47** depicts that the mean RH at 2 km for Delhi during winter, pre-monsoon, monsoon and post-monsoon are about 27 %, 26 %, 75 %, and 40 % respectively, while the corresponding RH for Nainital are 49 %, 43 %, 91 %, and 68 % respectively. The RH value at both the stations decreases with altitude, however, it starts decreasing rapidly after ~ 6 km, and goes down to less than 10 % beyond 10 km during winter and pre-monsoon at Nainital station. The differences in RH between the two stations is least (about 5%) during post-monsoon except at 2-4 km level where the differences exceed 20 %, while it is highest (even more than 10 %) during monsoon.

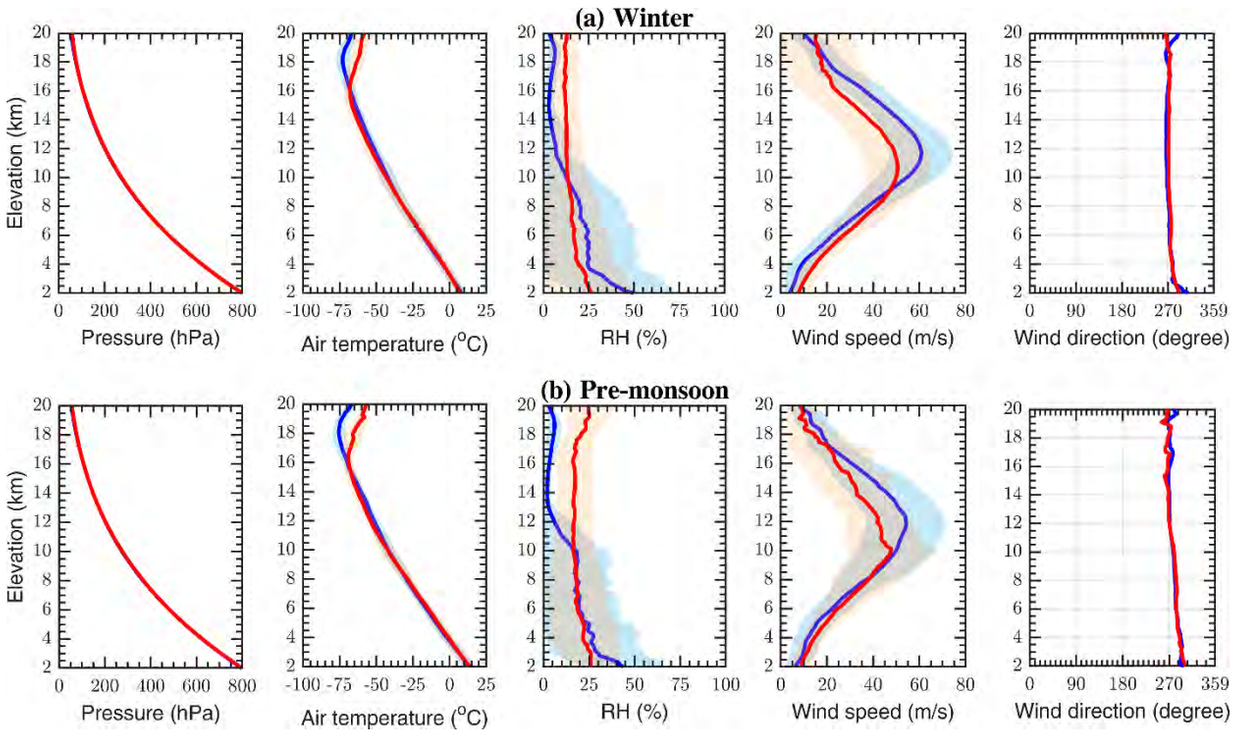

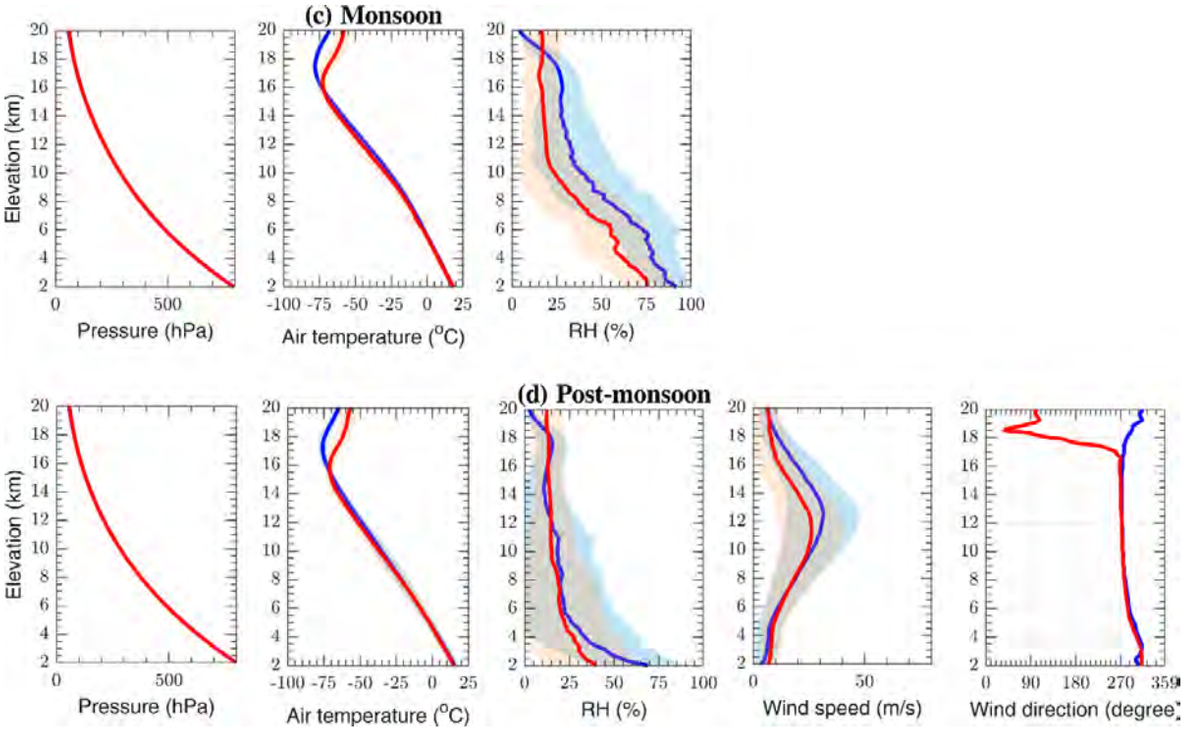

Fig. 5.47. Vertical profiles (2-20 km amsl) of pressure, air temperature, relative humidity, wind speed, and wind direction for Nainital (blue) and Delhi (red) stations obtained from radiosonde data during (June 2011 – March 2012, coincident within ±1 hr) the seasons **(a)** winter (December-February), **(b)** pre-monsoon (March-May), **(c)** monsoon (June-August), and **(d)** post-monsoon (September-November). The solid blue line and blue shades in the plot represents mean and SD profiles for Nainital, and the solid red line and red shades represents mean and SD profiles for Delhi station.

Surface winds basically changes with the season and vary from one latitude region to the other, however, the upper and lower level patterns by and large remains the same, except for monsoon season in the tropical region when the reversal of the winds take place. Wind speed between 2 km to about 10 km levels is observed slightly higher over Delhi than Nainital, beyond which the wind speed over Nainital becomes higher than Delhi station. Overall, the wind speed over Nainital is higher than Delhi station, with their maxima at ~ 12 km throughout the seasons, and then starts decreasing. The high wind speeds between 10 km and 13 km are basically the tropical easterly jets seen over both the stations. Wind speed at both the stations is found to be maximum during winter and minimum during post-monsoon. The dominant wind direction are found mostly westerly and northwesterly over the two stations, indicating the synoptic mean flow as evident in the wind rose plots shown in **Fig. 5.48**.

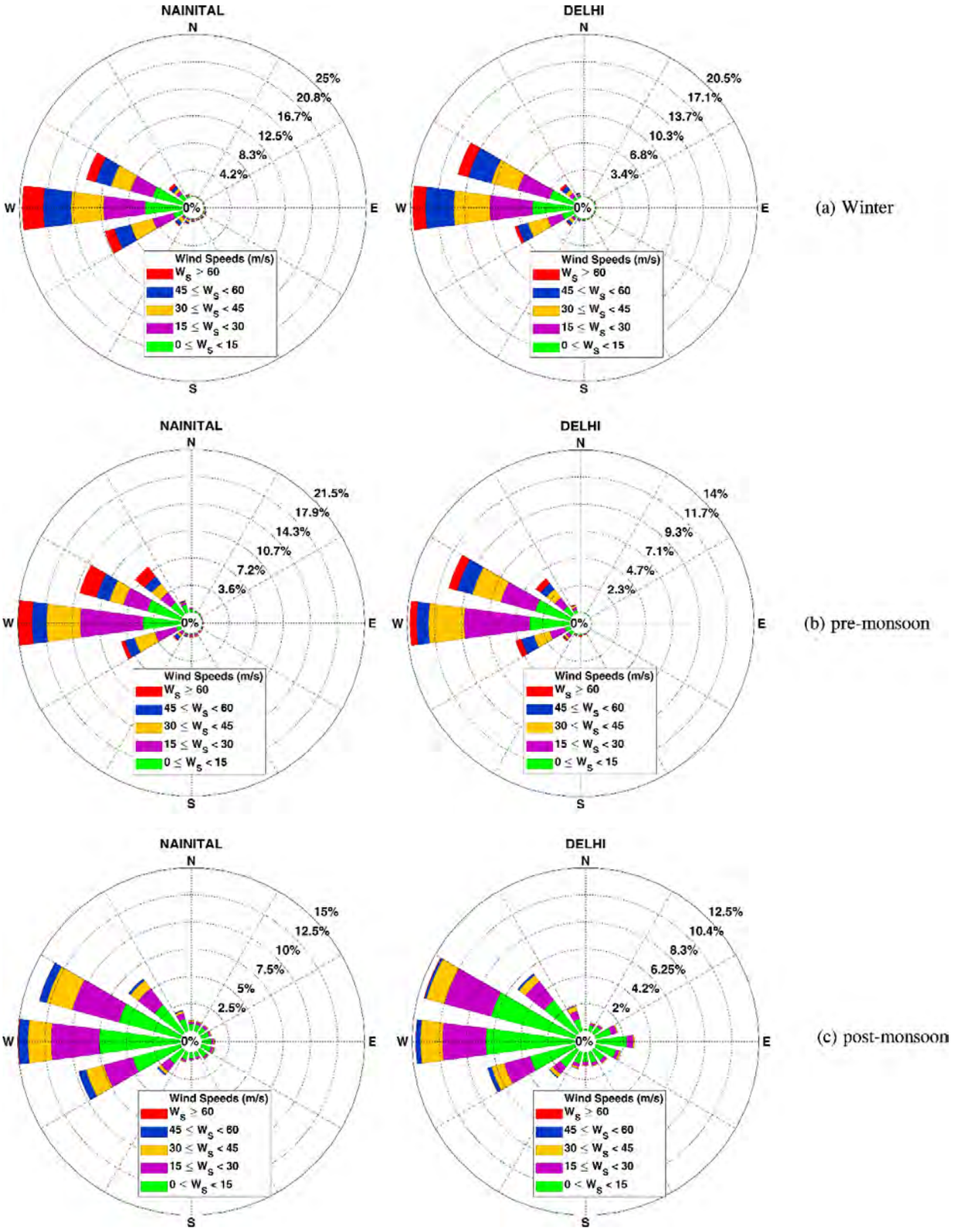

Fig. 5.48. Composite (2-20 km) seasonal wind rose plots for Nainital and Delhi stations obtained from radiosonde data during (June 2011 – March 2012, coincident within ±1 hr).

5.5. Preliminary studies pertaining to ASTRAD facility

5.5.1. GUI development on pulse compression technique

In atmospheric RaDAR including ASTRAD, maximum range coverage with smaller ΔR and high SNR at reasonable transmit power level is required, and to achieve this, pulse compression technique is introduced. This technique is performed in the atmospheric RaDARs, by modulating the complementary code sequences onto the pulsed carrier frequency during transmission, and on the other hand while reception, the same sequence of codes are used to correlate and combine the signals. This technique results in achieving the resolution (ΔR) of a short pulse at practically acceptable transmit peak power levels.

A GUI package has been developed in LabVIEW environment to demonstrate the pulse compression technique. The developed package is packed with an array of codes to perform many of the mathematical and signal processing functions related to transmission and reception of atmospheric RaDAR waveforms under coded and uncoded modes. The front-panel of the GUI is shown in **Fig. 5.49(a, b)**. It mainly comprises of two sub-sections – (1) control panel (**Fig.5.49a**), and (2) display panel (**Fig. 5.49b**).

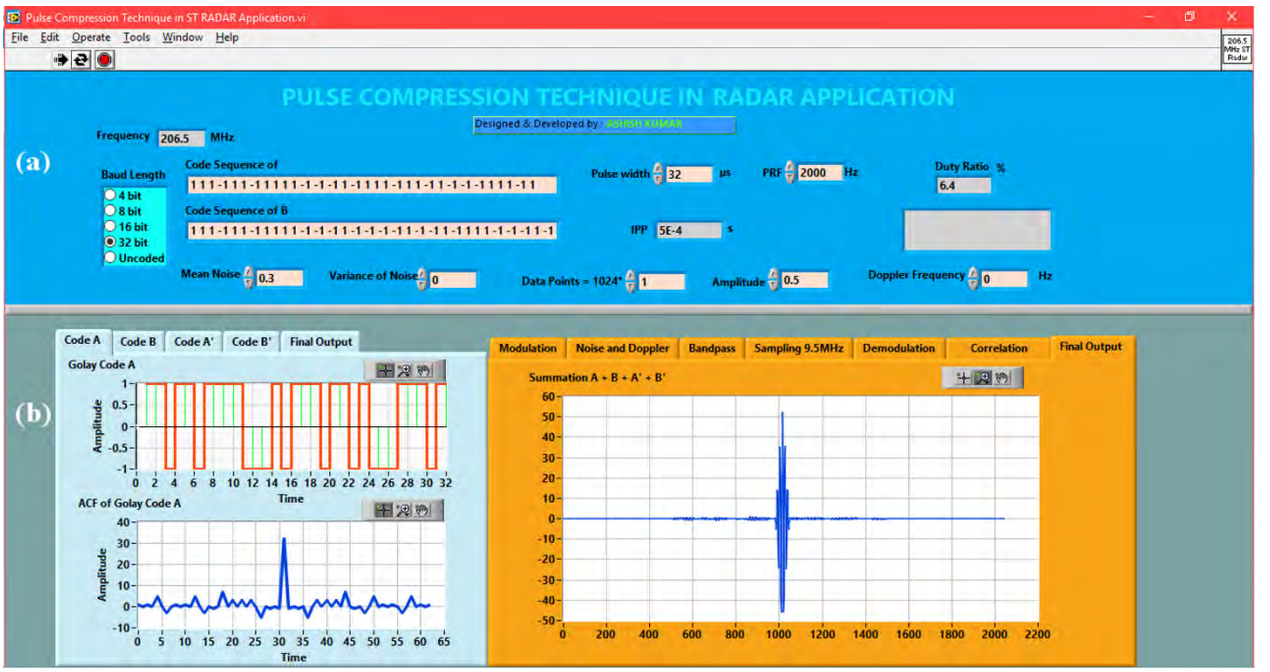

Fig. 5.49. (a) Control panel, and **(b)** display panel of the developed GUI for pulse compression technique.

The control panel is responsible for setting the simulation parameter required to initiate the RaDAR pulse compression waveform generation and processing, and **Table 5.16** explains the properties of the individual parameters of this panel.

Table 5.16: GUI control parameters.

Parameter	**Properties**
Frequency	This is the RaDAR operating frequency which is kept fixed as 206.5 MHz i.e. ASTRAD operating frequency.
Baud length	User can choose to modulate the given signal using 4, 8, 16, 32 bit codes, or without any modulation i.e. in uncoded mode.
Code sequences A and B	These fields shows the generated code sequences for A and B according to the baud length chosen, e.g. for 8 bit length, it will display A = {1 1 1 -1 1 1 -1 1} and B = {1 1 1 -1 -1 -1 1 -1}. For an uncoded sequence it will give a blank display.
Pulse width	This parameter is the time duration of a pulse, and can be chosen from 1 µs to 32 µs, in the step of 1 µs.
PRF	It is the number of pulses per unit time, and selected as any value from 250 Hz to 8000 Hz.
IPP	It is the inter-pulse period or the time between two consecutive pulses. IPP (=1/PRF) is displayed after specifying the PRF.
Duty Ratio	This displays the duty ratio once PRF and Pulse width is user defined. The duty ratio is basically the ratio between pulse width and IPP. The display box below shows: “Duty Ratio is out of Range. Check PRF and PW values” if duty ratio exceeds 15%.
Mean Noise	This parameter specifies the mean noise that will be added when generating the received signal. The user can vary this from 0 to 10 in increments of 0.1.
Variance of noise	This parameter specifies the variance of noise that will be added when generating the received signal. The user can vary this from 0 to 2 in increments of 0.1.
Data points	This parameter gives the number of data points the user wants to plot. It has been presented as a multiple of 1024. The value ranges from 0.25 to 4. Lower values give better resolution while high values give accurate results.
Amplitude	The user can vary amplitude from 0.1 to 100 in increments of 0.1
Doppler Frequency	It is the amount of the change in the observed frequency of a wave due to Doppler Effect. The user can vary Doppler frequency from -10 KHz to 10 KHz in increments of 10 Hz.

The display panel is composed of multiple sub-windows offering plots on the basis of user inputs provided in the control panel (Pulse width, baud length, PRF, mean noise, variance of noise, data points, amplitude, and Doppler frequency). The series of operations performed by the display panel are as follows:

(a) Generates the time series and ACF plots of the individual complementary codes A, B, A', and B', together with the summed ACF as final output in the left sub-windows of the display panel. A' and B' are complements of A and B, respectively (e.g. **Fig. 5.50a-b**).

(b) Generates the modulated carrier wave at 206.5 MHz for 4, 8, 16, 32 bit code pairs in the order A, B, A', and B' (e.g. **Fig. 5.50c**).

(c) Generates Gaussian noise with user-defined mean and variance added to the modulated signal. User defined Doppler is also added, to form a simulated received signal (e.g. **Fig. 5.50d**).

(d) Plots the spectrum of the generated signal (e.g. **Fig. 5.50e**).

(e) Produces the band-limit signal achieved using a bandpass filter of 5MHz bandwidth (e.g. **Fig. 5.50e**).

(f) Samples the filtered signal at a frequency of 9.5 MHz (undersampling) (*Kumar et al*., 2011), and Generate the In-phase (I) and Quadrature-phase (Q) signals of the resulting waveform.

(g) Performs decoding of the filtered signals by performing cross-correlation with original transmit signal for the respective code sequences (e.g. **Fig. 5.50f**).

(h) Generates the final output by summing the cross correlated outputs of the pulses during 4 Radar sweeps. (e.g. **Fig. 5.50g** for coded mode, and **Fig. 5.50h** for uncoded mode of operation)

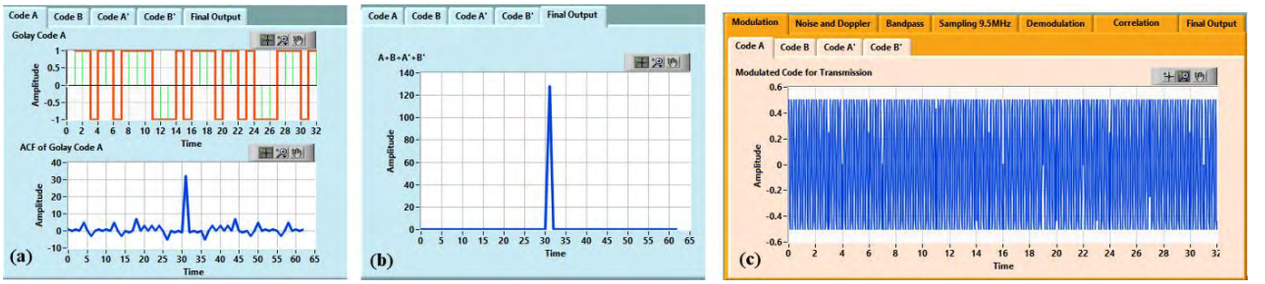

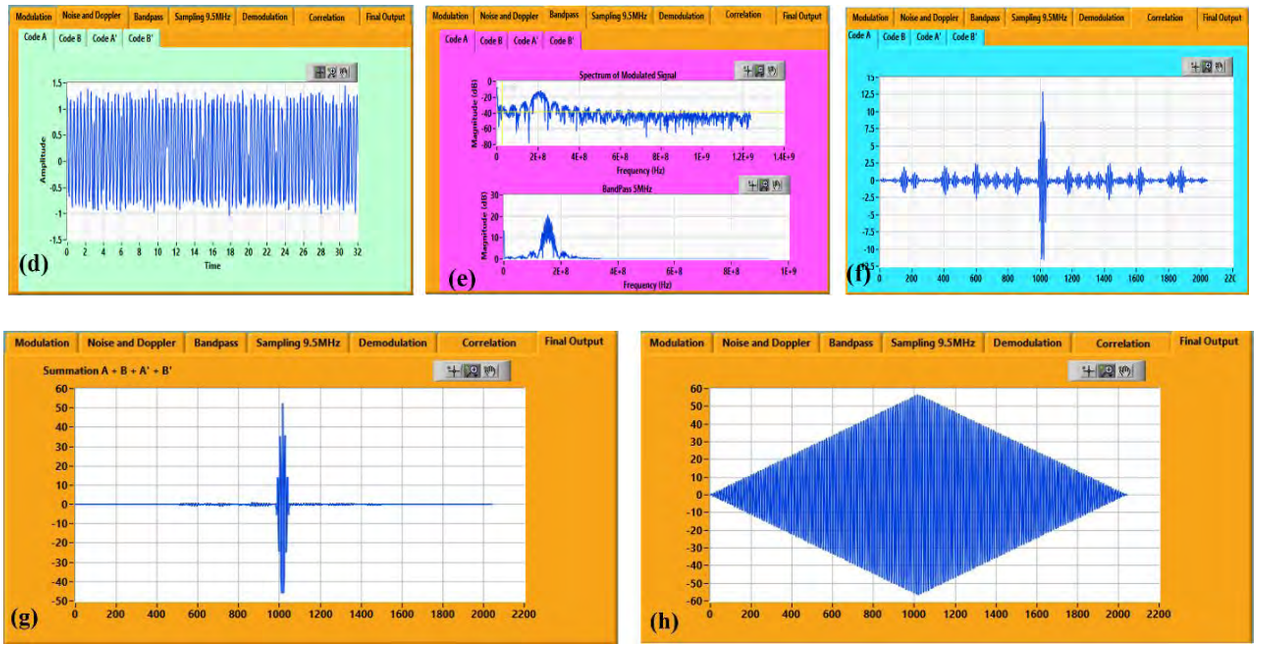

Fig. 5.50. **(a)** Time series and ACF plots of 32 bit code A, **(b)** Sum of the ACFs of codes A, B, A', and B', **(c)** modulated 206.5 MHz RF with code A, (d) modulated signal with noise, variance and Doppler added, **(e)** spectrum (in dB) of the modulated signal and the band-limited signal, **(f)** cross-correlated output of the signal modulated with code A. The sum of the cross correlated outputs of the four consecutive signals modulated **(g)** using the codes A, B, A' and B', and **(h)** uncoded mode.

5.5.2. Pre-processing of Doppler spectra

The spectra obtained from the pulsed Doppler RaDAR are often non-Gaussian in shape and contains unwanted ground clutters and multiple signal peaks of non-atmospheric targets. Hence a pre-processing of the Doppler spectra is needed before extracting the actual wind information. The effect of ZDC, characterized by signal components centred near zero Doppler is mostly visible in the Doppler spectra, as evident in **Fig 5.51(a, c)** and **Fig. 5.52(a1, b1, c1** and **d1)**.

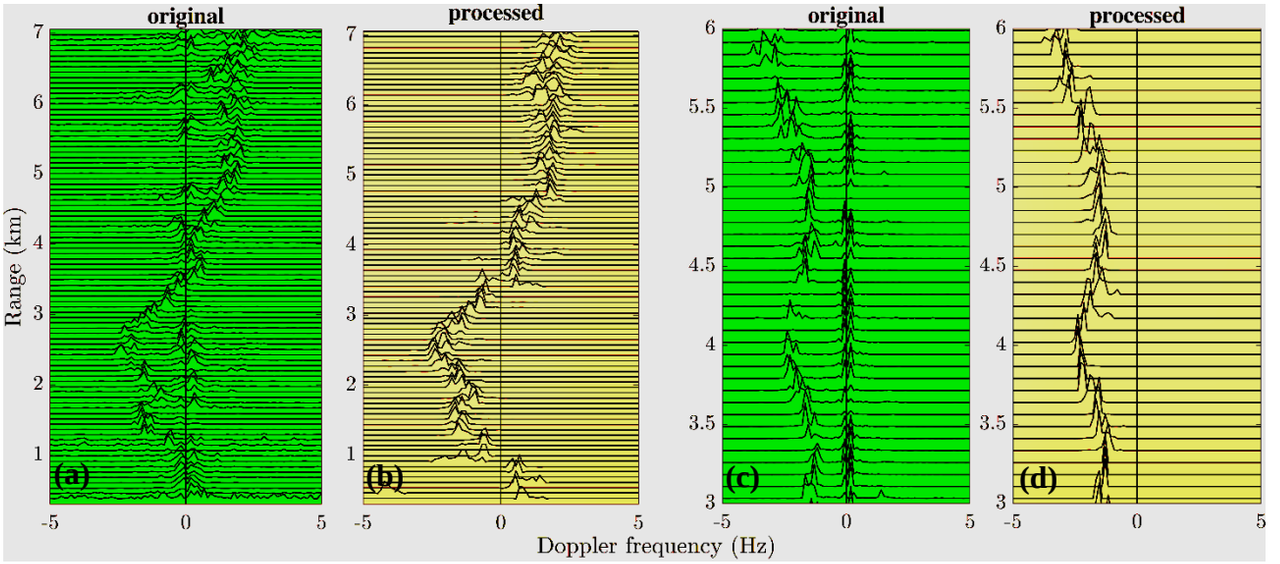

Fig. 5.51. Typical Range-Doppler spectra plots **(a)** and **(c)** in the original form, and plots **(b)** and **(d)** after near zero Doppler clutter removal (processed).

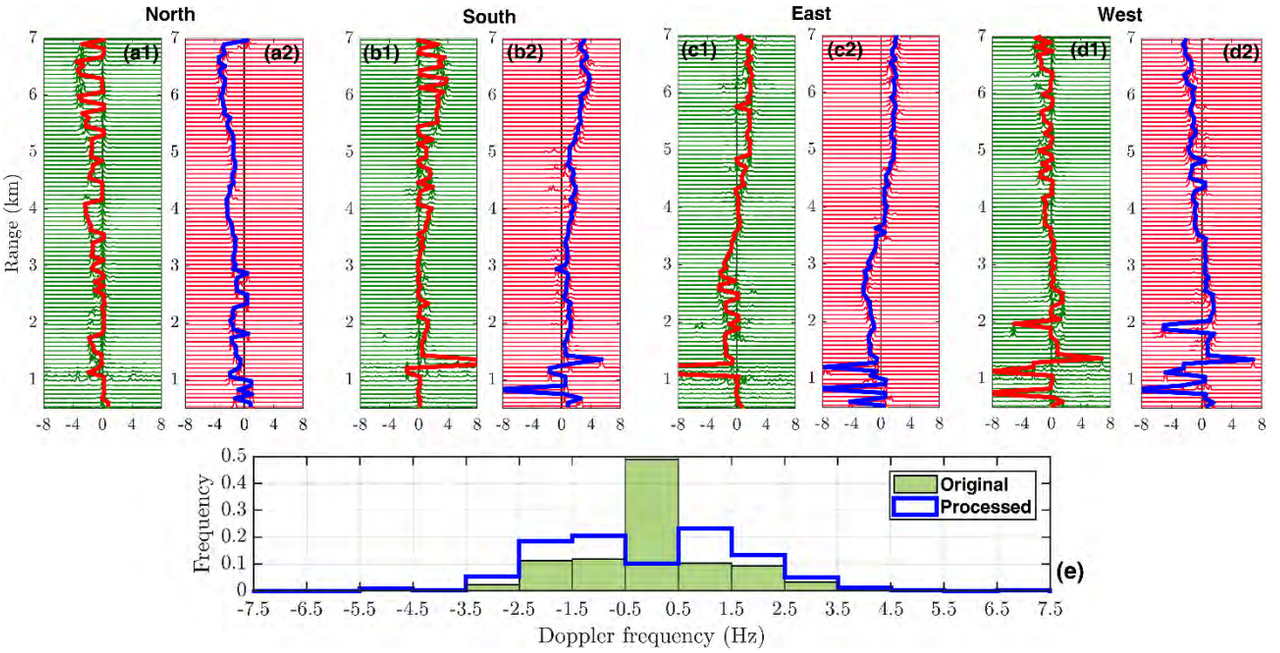

Fig. 5.52. Typical Range-Doppler profiles of North, South, East, and West beams obtained from ASTRAD, where **(a1)**, **(b1)**, **(c1)** and **(d1)** are the original profiles, and the corresponding profiles **(a2)**, **(b2)**, **(c2)** and **(d2)** obtained after zero Doppler clutter removal (processed). **(e)** The composite occurrence frequencies of the identified peaks i.e. Doppler frequency in the Doppler spectra of North, South, East, and West beams.

The ZDC's in the Doppler spectra are removed by interpolation from the adjacent few Doppler points on either side of the zero Doppler point, and by applying the 3 or 5 points running average to create a smoothed spectra. After applying these processing steps, marked improvements in the Doppler spectra is obtained as shown in **Fig 5.51(b, d)** and **Fig. 5.52(a2, b2, c2** and **d2)**. As evident from the **Fig.5.52e**, the occurrence frequency of zero Doppler's have been reduced from the original 48.9 % to 10.1 % after processing, together with the enhancements in peaks at non-zero Doppler points.

The spectra obtained from the pulsed Doppler RaDAR are often gets contaminated from the RFI. One source is the harmonics of power line frequency (50 Hz), marked as strong peaks throughout the range at constant Doppler frequency i.e. at ±25 Hz, ±12.5 Hz, ±6.25 Hz and so on, hence forming multiple bands of undesired peaks. This may arises due to insufficient filtering and poor isolation in the power supply of the subsystems, or due to pick up's by the RF cables from the nearby electric utilities or wirings. The removal of these unwanted peaks is necessary before performing moment estimation and wind extraction, because sometime they get misidentified as the atmospheric signal. A simple approach to remove them is by applying a suitable notch filter throughout the range where the bands are appearing, which allows the rejection of the undesired bands, without affecting other response frequencies. In case if the original Doppler trace is not getting affected in the majority of the range bins due to the constant bands of RFI, then those bands are removed by subtracting the values at a range bin, which does not have Doppler echoes but have interferences, from all other range bins as shown in **Fig. 5.53**.

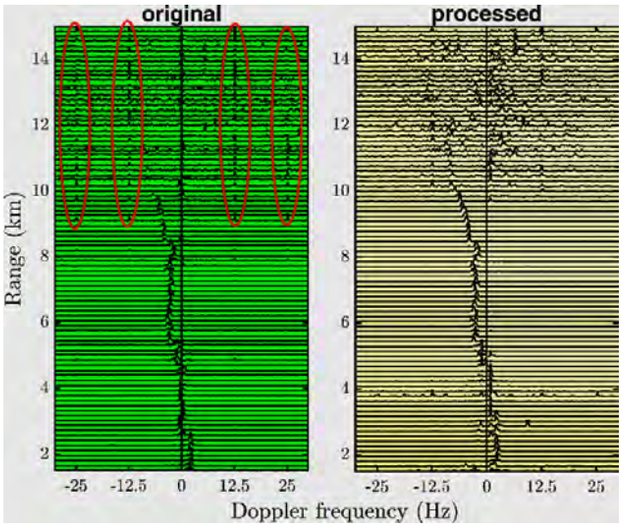

Fig. 5.53. A typical range-Doppler spectra **(a)** with, and **(b)** without power line RFI.

5.5.3. Preliminary results on ASTRAD wind validation

The most seminal job of atmospheric RaDARs like ASTRAD are to provide the vertical profiles of wind (zonal, meridional, and vertical) in the sphere of its reach. The provided information is critical for weather and climate studies, because winds are involved in multiple processes and phenomenon that occurs in the atmosphere. Investigation on the reliability and accuracy in the winds estimates from RaDAR is somewhat challenging, as there is no direct method to derive the wind velocities on a continuous basis. There are wind measurements available with satellites, rockets, aeroplanes etc., however they are mostly used for synoptic scale applications, and rarely used for assessment of ground based RaDAR systems. The in-situ radiosonde observations are primarily used for evaluation of the RaDAR derived wind information. Although the RaDAR provides Eulerian estimates of the wind continuously over the entire range of altitudes at a given time, while the radiosonde provides the Lagrangian values of wind and other meteorological parameters from each altitude levels at different time stamps, however, there have been numerous statistical comparison between the atmospheric RaDARs and radiosonde wind estimates showing very good agreements between them (e.g. *Fukao et al.,* 1982*; Weber and Wuertz,* 1990; *Kottayil et al*., 2016) with root mean square differences of even < 4 m/s, and the Pearson's correlation $R > 0.8$. Hence, it becomes essential that before the ASTRAD is commissioned, the quality of its three-dimensional winds is checked with the concurrent winds measured by radiosondes. To make a preliminary assessment, the wind data from ASTRAD are subjected for comparison with the collocated and simultaneous iMet-1-RSB radiosonde measurements, held on 02 February, 12 April, and 04 May of 2017 as shown in **Fig. 5.54(a-c)**, where the radiosonde profiles are shown by red, and the ASTRAD derived winds are shown by black. The expected accuracy of the wind speed and wind direction provided in the manufacturer's datasheet of iMet-1-RSB is ±1 m/s and ≤ 5°, respectively. To match with the height resolution (150 m) of ASTRAD, the radiosonde winds are averaged over 150 m height intervals. The ASTRAD wind estimates are obtained with the DBS technique using 7 clusters (343 transceivers).

The Pearson's correlation coefficient between ASTRAD and radiosonde wind measurements up to ~10 km height on these three days are observed as 0.89, 0.82, and 0.86 for zonal wind, meridional wind, and wind speed, respectively (**Fig. 5.54d**). The RMSE between the ASTRAD and

radiosonde measurement are found ~ 6.5 m/s (zonal wind), ~ 4.8 m/s (meridional wind), and ~ 7.3 m/s (wind speed). Similarly, the zonal wind estimates from ASTRAD overestimates the radiosonde measurement, with MBE of ~ 3.5 m/s, while the meridional wind and wind speed underestimates the radiosonde observations and shows the MBE of about -1.4 m/s and ~ -2.9 m/s, respectively. As evident in **Fig. 5.54(a-c)**, the biases in wind speed and direction between the ASTRAD and radiosonde measurements are higher in the lower heights (< 3 to 4 km above ground level), which may be attributed to the inhomogeneous terrains in the proximity and influences from local mountain waves. Although the agreements between radiosonde and ASTRAD winds are reasonably good till 8 - 9 km (with $R > 0.93$), however, beyond this the disagreements between them tends to grow. Few possibilities of showing such discrepancies are errors in wind estimation using ASTRAD at higher height due to low SNR, sudden or unpredictable changes in the upper atmosphere, or large separation between the RaDAR volume and radiosonde at higher heights, that generally occurs due to large drifting of the balloon with wind as the height increases.

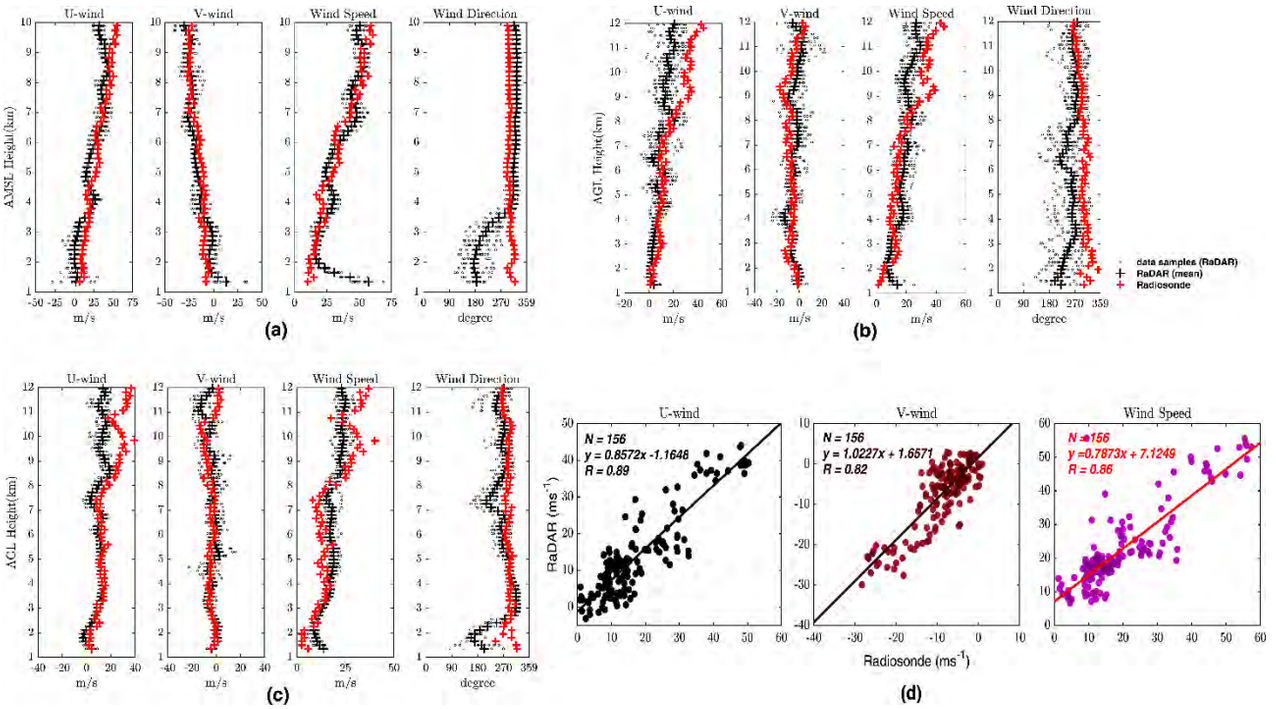

Fig. 5.54. Comparison between the ASTRAD (black) and radiosonde (red) obtained average zonal (U) wind, meridional (V) wind, wind speed, and wind direction for the three balloon flights, labeled as (a), (b), and (c) conducted, respectively, on 02 February, 12 April, and 04 May of 2017. The tiny dots (grey) represents the data samples obtained from the individual ASTRAD profiles used for averaging.

Chapter 6

SUMMARY AND CONCLUSIONS

CHAPTER 6
SUMMARY AND CONCLUSIONS

In this research work, satellite remote sensing measurements have been combined with a range of ground based and in-situ measurements and ancillary data sets to investigate the key atmospheric parameters – aerosols, clouds, and precipitation over the Himalaya on regional and local scales. The study on these parameters are very important from climate change perspective.

The seasonal variations in the aerosol volume-size distribution, total, fine and coarse mode AODs, and FMF from ten AERONET stations (Nainital, Pantnagar, Kanpur, New Delhi, Lahore, Gual Pahari, Gandhi College, Jaipur, Lumbini, and Pokhara) located in the Himalaya and adjacent Gangetic plains are examined to understand the spatial and temporal characteristics of aerosols. **Dominance of coarse mode particles (mainly from long-range transport of dust) during pre-monsoon and monsoon seasons are observed highest ($\geq$ 0.2 $\mu m^3/\mu m^2$) for Kanpur, New Delhi, Lahore, Gual Pahari, Gandhi College, and Jaipur stations**, and about two times lowest over Nainital, Lumbini, and Pokhara stations. **The prevailing fine mode aerosols are observed for almost all the stations during post-monsoon and winter, which are mainly attributed to biomass burning and of continental origine. Lower AOD values are observed at the high altitude station i.e. Nainital than densely populated, low-altitude urban and industrialized stations.**

For the first time over a complex terrain in the southern part of central Himalayan region, the most recent and updated aerosol data products (mainly AOD), retrieved from satellite measurements (MODIS and CALIPSO) were evaluated, compared and utilized in conjunction with the ground based measurements. Essentially the latest and updated information will be utilized by the frontline researchers working on the climate change and modeling studies over the Himalayan region or at the regional scale, and in understanding the dynamics and transport of pollutants. By means of thorough investigation and statistical approaches it has been shown that the **MODIS Terra collection C6.0 DB and CALIPSO ver. 4.10 performed best in comparison to other collections/versions over a complex terrain in Himalayan region.** Over 20 coincident

data sets from AERONET, and MODIS 10 km DB and DT retrievals were examined for various spatio-temporal combinations. Comparison of MODIS (30 km × 30 km) Terra and Aqua AOD values with that from AERONET (averaged within ±30 minutes of the satellite transacts) extricated that **Terra retrievals are much reliable (R~0.90, % EE ~ 62) than the Aqua (R~0.75, % EE ~54), and among various Terra collections, C6.0 DB has the closest agreement (R~0.9 and % EE ~77) with the ground truth.** Positive MBE and AER values **discovered an overestimation of MODIS AOD as compared to the ground truth**, and the reason for the same is explained.

Latest release of CALIPSO aerosol product ver. 4.10, with its improved merits, for the first time is assessed over the Himalayan region and utilized to resolve the aerosol properties at the regional scales and **found to be in better agreement (R ~ 0.92, %EE ~ 86.95 %) as compared to the earlier version (R~0.76, %EE ~56.52).** The surface elevation data obtained from CALIPSO ver.4.10 and ver.3.xx for the 206 night (6510 LASER footprints) and 153 day-time (4644 LASER footprints) overpasses within ± 1° latitude and longitude from the site is analyzed and inveterate the change in the surface elevation in the latest CALIPSO ver. 4.10 release. **The MRD between ver. 4.10 and ver. 3.xx are found to be more positive during nighttime (~3.47 %) as compared to the daytime (~3.33 %).** A typical case of 10 May 2008 is presented to demonstrate eight major changes in CALIPSO ver. 4.10 release. **The degree of closeness between the two CALIPSO versions in terms of vertical feature and aerosol sub-types detections were estimated and found as 94.62 % and 68.62 %, respectively** over the selected study region for the period of August 2006- April 2017. The evaluated MODIS and CALIPSO products also displayed reasonable agreement when inter-compared, especially, **CALIPSO ver. 4.10, demonstrated better correlation (R ~0.79, MRD ~ 31.3%) with MODIS, as compared to ver. 3 (R ~0.66, MRD ~ 38.4%).** The latest satellite products evaluated in this study will help in understanding the dynamics and transport of pollutants and to explore the environmental aspects on a larger scale, over this very sensitive and fragile mountain systems.

The LR for three different LiDAR systems operated during 2008 to 2012, at the site are computed iteratively using the synergetic LiDAR-AERONET, LiDAR-MODIS Terra C5.1 DT, LiDAR-MODIS Terra C6.0 DT and LiDAR-MODIS Terra C6.0 DB measurement pairs. **The LR values in all the combinations showed the minimum values during December and January (< 16) and maximum values during March and May (> 43).** The BL height is estimated using the evaluated CALIPSO ver. 4.10 data and found in a good agreement with the in-situ radiosonde

measurements. **Results showed the effectiveness of WCT method used in the estimation of BL height from CALIPSO ver. 4.10 data.**

Case studies on continental (fine mode particles i.e. smoke), long-range transport (coarse mode particle i.e. dust in the form of elevated aerosol layer), and no-transport of aerosols (formation of local cloud), are carried out and discussed in details by utilizing HYSPLIT trajectory model, satellite and in-situ AERONET and LiDAR measurements. To understand the influence of pollutants over the Himalayan region, long-term data on active fire, carbon monoxide emission, dust column mass density, snow depth, albedo and snowfall over the glaciated surfaces are studied. These studies may expand the horizon of knowledge on the contributions from the major pollutants pertaining to the climate change in the Himalayan context.

Essentially, the ecosystem and socio-economic conditions in majority of the regions across the globe, including the mighty Himalaya are greatly affected due to transport and accumulation of the absorbing aerosols, mainly dust, as they negatively contribute to cloud formation, snowfall, and retreat of glaciers. Therefore, seasonal climatology on the absorbing aerosols with main emphasis on dust has been attempted on a global scale as well as over the Himalayan region, using 38 years of data records from MERRA-2 and multi-sensor observations retrieved from TEMIS. **Study revealed that the dust loading is highest during summer/spring season (March-May) across the globe and over the Himalayan region, however, the contribution from the dust over the Himalayan region to the total global dust volume is highest (8.5 %) during monsoon, and lowest during winter (4.7 %).** Monthly analysis on dust column mass density over the period 1980-2017 showed that May and December are the maxima and minima dust depositing months over the Himalayan region. **The absorbing aerosol index was observed highest (~ 0.4) during JJA and MAM over the globe and Himalayan region (~0.75), respectively.** Further analysis using past 38 years of data showed **the rising trend in the absorbing aerosols over the Himalayan region**, however, the positive anomaly slope of AAI is found negative since October 2004. The quantitative investigation on the absorbing aerosols, mainly dust over the Himalayan region attempted here in this thesis, can be extended further to understand the driving mechanisms behind snow surface darkening, undue melting of snowpack's, increase in the extreme events etc. and overall radiative impacts on the high altitude Himalayan region.

For the first time, a detailed study on the three-dimensional distribution of seven different cloud types is carried out, using ten years (2007-2016) synergic space-borne RaDAR

and LiDAR observations over northern Indian states. Their normalized vertical distribution showed year-to-year variations, and the years showing the maximum occurrences of individual cloud types are identified. Cloud dominant regions are detected over annual and seasonal scales, by accumulating the vertical granules of all the cloud types up to 18 km, in the grid boxes of 1° × 1° resolution. The mean relative frequency distribution of the individual cloud types are also established at annual and seasonal time scales. Further statistics, revealed that **the distribution of altostratus, deep convective, and nimbostratus cloud types are higher than other cloud types during the last decade, and during the seasons – DJFM (western disturbance) and JJAS (southwest monsoon), respectively**. The concurrent occurrences of different cloud types were also noted and quantified.

Making use of the coincident observations available from TRMM and DARDAR retrievals over the NSI region for the period 2007-2016, the frequency of occurrences of liquid precipitation, solid precipitation, and drizzle are deduced for the two contrasting seasons (JJAS and DJFM). **The study revealed that Uttarakhand, Himachal Pradesh and Jammu & Kashmir have experienced maximum liquid and solid precipitation during the last decade**, especially during the monsoon and active months of western disturbances, respectively. The associations between the cloud and precipitation types during DJFM and JJAS, and on annual scales are also investigated, and the relevant statistics are shown. This quantitative study on the association between clouds and precipitation may contribute to a profound understanding and a workable reference for regional numerical models dealing with clouds and/or precipitation. The study on different forms of precipitation over NSI region exhibits opposite circulation of its solid (increase) and liquid (decrease) forms in westward or north-westward. The association of deep convective and nimbostratus cloud types with solid precipitation on an annual scale are observed as 1.6 % and 76 % of their total co-occurrences, respectively. On the other hand, their association with liquid precipitation are found as 98.4 % and 23.7 %, respectively, thereby implying that **nimbostratus and deep convective clouds are the main contributor of solid and liquid precipitations, respectively over the NSI region during the last decade.**

The study on surface meteorological variables – temperature, RH, pressure, winds, and total rainfall at ARIES, Nainital site is carried out using the ground-based AWS measurements for the period 2013-2018. **The minimum and maximum temperature at the site are observed during winter (monthly average: 10.4°C ± 1.5°C) and spring/summer (monthly average: 20.1°C ±**

1.7°C), respectively. The RH varied from 34.3 % to 98.8 %, while the variation in the atmospheric pressure are observed in the range 812.6 – 822.9 hPa. The rainfall measurement records for 6 years duration identified July (567 mm ± 226.7 mm) and August (520.5 mm ± 87 mm) as the most favorable months for rain, and collectively they accounts for more than 55 % of the annual rainfall. **Wind speed at the site is observed highest during March-June (> 6 m/s), and lowest during winter (~2-3 m/s). Wind direction at the site is found to be mainly westerly**, except during winter when northwesterly wind becomes dominant. Further, the uncertainty associated with the wind direction measurement using AWS over the site is explained, and the necessity of meteorological towers and/or atmospheric RaDAR for wind measurement is suggested.

Study on the surface temperature at local (Nainital) and regional (Himalaya) scales over the period 1980-2017 is done using the evaluated MERRA-2 re-analysis data. **Study identified January as the coldest month, while June and July are observed as the hottest months at local and regional levels, respectively. The climatologies and long-term study on meteorology over the Himalayan region revealed the significant departures of the meteorological variables from their usual ranges, especially the surface temperature. Overall surface temperature trend is found positive with slopes +0.019 and +0.0062 at regional and local scales respectively, and hence indicating warming in the Himalayan region.**

Vertical distribution of atmospheric pressure, temperature, RH, wind speed, and wind direction, obtained through the radiosonde measurements from Nainital and Delhi stations are compared for the period June 2011-March 2012, and the seasonal differences in these parameters over the height window from 2 km to 20 km amsl are explained. **The vertical profiles of air pressure and air temperature for both the stations are found nearly similar, however, the temperature profile showed increase (tropopause) at ~ 16 km and ~ 18 km for Delhi and Nainital, respectively**. **Seasonal differences are observed in the vertical profiles of RH, and overall it is on the higher side for Nainital as compared to Delhi station. Wind speed is on the higher side between 2-10 km and 10-20 km over Delhi and Nainital station, respectively. Both the stations showed maximum wind speed during winter, and minimum during post-monsoon. Wind direction are found mostly westerly and northwesterly over both the stations.**

The functionality of the developed front-end GUI demonstrating the pulse compression technique, required to achieve maximum height coverage without sacrificing the range resolution, in the context of atmospheric RaDAR is explained. **The developed GUI introduces the features of**

displaying coded and uncoded transmission and reception based on various user-defined parameters. The pre-processing algorithms, mainly the zero Doppler clutter and radio frequency interference removal, from the Doppler spectra obtained using the ASTRAD observations are implemented and their performance are evaluated. Further, the three-dimensional wind measurements from ASTRAD are inter-compared using the coincident radiosonde observations. This preliminary inter-comparison showed reasonably good agreements. However, there is further scope of improvements in the RaDAR data processing aspect, that essentially to work out during the commissioning phase.

RECOMMENDATIONS

The present research on aerosols, clouds, and precipitation over Himalayan region is nowhere near finished. There are still large uncertainties regarding these key atmospheric parameters, and on their associations/interactions with each other. The uncertainties range from the microscale to the mesoscale to the synoptic scale, and hence extensive research is needed on all the scales. **The mesoscale research presented in this thesis is almost exclusively based on freely available datasets, therefore, it is essential that such datasets continue to be free of charge and easily accessible to carry out further research on the topic in the future.** The present study also utilizes assimilated data products (e.g. MERRA-2, GLDAS etc.) in the trend analysis of aerosols over the Himalayan region, however, this is quite possible that if the observational network will get improved, then there may be an impact on the assimilated data. Therefore, **it is necessary to explore and investigate series of available data sources on aerosols time to time in a systematic manner, to determine the correction factors for different aerosol types, that could be used to re-estimate the long term trends on aerosols**. Further, a reliable database provides higher confidence in explaining or understanding the atmospheric processes over Himalaya, hence, **there is a great need of time to time assessment on the temporal and spatial accuracy and representativeness of the latest releases of satellite remote sensing data products. It is also very much essential to orient the emphasis of the Himalayan research more towards the information-rich approach, instead of principle-based approach, by installing more ground based remote sensing tools, and by establishing large number of in-situ observing facilities.**

REFERENCES

REFERENCES

Adams, A. M., Prospero, J. M., Zhang, C., 2012. CALIPSO-derived three-dimensional structure of aerosol over the Atlantic basin and adjacent continents. J. Climate. 25:6862–6879. http://dx.doi.org/10.1175/JCLI-D-11-00672.1.

Adler, R.F., Huffman, G.J., Bolvin, D.T., Curtis, S., Nelkin, E.J., 2000. Tropical Rainfall Distributions Determined Using TRMM Combined with Other Satellite and Rain Gauge Information. Journal of Applied Meteorology 39(12): 2007–2023. http://dx.doi.org/10.1175/1520-0450(2001)040<2007:TRDDUT>2.0.CO;2.

Alam, K., Trautmann, T., Blaschke, T., Hussain, M., 2012. Aerosol optical and radiative properties during summer and winter seasons over Lahore and Karachi. Atmos. Environ. 50: 234-245.

Alam, K., Khan, R., Sorooshian, A., Blaschke, T., Bibi, S., Bibi, H., 2018. Analysis of aerosol optical properties due to a Haze episode in the Himalayan foothills: Implications for climate forcing. Aerosol and Air Quality Research. 18(5): 1331-1350. https://doi.org/10.4209/aaqr.2017.06.0222.

Albrecht, B. A., 1989. Aerosols, cloud microphysics, and fractional cloudiness. Science. 245: 1227–1230.

Ali, M., Salman, T., Khalid, M., Asim, D., Adila, B., Zia, U.H., 2014. A study of aerosol properties over Lahore (Pakistan) by using AERONET data. Asia Pacific Journal of Atmospheric Science 50: 153-162.

Allen, M. R., Ingram, W. J., 2002. Constraints on future changes in climate and the hydrologic cycle. Nature. 419: 224-232.

Alley, R. B., et al., 2007. Summary for policymakers, in Climate Change 2007: The Physical Science Basis: Contribution of Working Group I to the Fourth Assessment Report of the Intergovernmental Panel on Climate Change, edited by S. Solomon et al. Cambridge Univ. Press, New York. 1–18.

Amiridis, V., Balis, D., Giannakaki, E., Kazadzis, S., Arola, A., Gerasopoulos, E., 2011. Characterization of the aerosol type using simultaneous measurements of the lidar ratio and estimations of the single scattering albedo. Atmos. Res. 101(1-2): 46–53. http://dx.doi.org/10.1016/j.atmosres.2011.01.010.

Anandan, V. K., Jagannatham, D.B.V., 2013. An Autonomous Interference Detection and Filtering Approach Applied to Wind Profilers. IEEE Trans. Geosci. Remote Sens. 51(1): 520-526.

Andreae, M. O., Crutzen, P. J., 1997. Atmospheric aerosols: Bio-geochemical sources and role in atmospheric chemistry. Science. 276: 1052–1056.

Andreae, M. O., Merlet, P., 2001. Emission of trace gases and aerosols from biomass burning. Global Biogeochem. Cy. 15: 955–966. http://dx.doi.org/10.1029/2000GB001382.

Aoki, T., Aoki, T., Fukabori, M., Hachikubo, A., Tachibana, Y., Nishio, F., 2000. Effects of snow physical parameters on spectral albedo and bidirectional reflectance of snow surface. J. Geophys. Res. 105(D8): 10219–10236. http://dx.doi.org/10.1029/1999JD901122.

Archer, D. R., Forsythe, N., Fowler, H. J., Shah, S. M., 2010. Sustainability of water resources management in the Indus Basin under changing climatic conditions. Hydrol. Earth Syst. Sci. 14: 1669–1680.

Arora, M., Goel, N. K., Singh, P., 2005. Evaluation of temperature trends over India. Hydrol. Sci. J. 50(1): 81–93.

Aryal, D., Rosoff, Y. N., Devkota, L. P., 2015. A Severe Hailstorm at Pokhara: CAPE Stability Index Calculations. Journal of Geosciences and Geomatics. 3: 142–153.

Ashouri, H., et al., 2015. PERSIANN-CDR: Daily precipitation climate data record from multi-satellite observations for hydrological and climate studies. Bull. Amer. Meteor. Soc. 96(1): 69–83.

Asthana, A.K.L., Asthana, H., 2014. Geomorphic control of cloud bursts and flash floods in Himalaya with special reference to Kedarnath area of Uttarakhand, India. Int. J. Adv. Earth Environ. Sci. 2(1): 16–24.

Baars, H., Ansmann, A., Engelmann, R., Althausen, D. 2008. Continuous monitoring of the boundary-layer top with lidar. Atmos. Chem. Phys. 8: 7281–7296. https://doi.org/10.5194/acp-8-7281-2008.

Badarinath, K. V. S., Kiran Chand, T. R., Prasad, V. K., 2006. Agriculture crop residue burning in the Indo-Gangetic plains – A study using IRS P6 AWiFS satellite. Current Sci. 91: 1085– 1089.

Bajracharya, S. R., Palash, W., Shrestha, M. S., Khadgi, V. R., Duo, C., Das, P. J., Dorji, C., 2015. Systematic evaluation of satellite-based rainfall products over the Brahmaputra basin for hydrological applications. Adv. Meteor., 398687. http://dx.doi.org/10.1155/2015/398687.

Baklanov, A., Molina, L.T., Gauss, M.M., 2016. Megacities, air quality and climate. Atmos. Environ. 126, 235–249. http://dx.doi.org/10.1016/j.atmosenv.2015.11.059.

Balsley, B. B., Gage, K. S., 1980. The MST radar technique: Potential for middle atmospheric studies, Pure Appl. Geophys., 118, 452–493.

Bandyopadhyay, J., 2013. Securing the Himalayas as the Water Towers of Asia: An Environmental Perspective. Asia Policy. 16(1):45–50.

Banerjee, T., Kumar, M., Singh, N., 2018. Aerosol, Climate, and Sustainability, In Encyclopedia of the Anthropocene. DellaSala, D. A., Goldstein, M. I. (Eds.), Oxford. Elsevier. 2: 419-428. ISBN 9780128135761. https://doi.org/10.1016/B978-0-12-809665-9.09914-6.

Bangia, T., Omar, A., Sagar, R., Kumar, A., Bhattacharjee, S., Reddy, A., Agarwal, P. K., Phanikumar, 2011. Study of atmospheric aerosols over the central himalayan region using a newly developed Mie light detection and ranging system: preliminary results. J. Appl. Remote Sens. 5(1): 053521-053521-12.

Barker, R. H., 1953. Group synchronizing of binary digital systems. Communication theory. Butterworth, London. 273-287.

Basistha, A., Goel, N.K., Arya, D.S., Gangwar, S.K., 2007. Spatial pattern of trends in Indian sub-divisional rainfall. Jalvigyan Sameeksha. 22: 47–57.

Basistha, A. , Arya, D. S. Goel, N. K., 2009. Analysis of historical changes in rainfall in the Indian Himalayas. Int. J. Climatol., 29: 555-572. https://doi.org/10.1002/joc.1706.

Beaudoing, H., Rodell, M., NASA/GSFC/HSL, 2016. GLDAS Noah Land Surface Model L4 monthly 0.25 x 0.25 degree V2.1, Greenbelt, Maryland, USA, Goddard Earth Sciences Data and Information Services Center (GES DISC). https://doi.org/10.5067/SXAVCZFAQLNO.

Bell, T. E., 1995. Remote sensing. IEEE Spectrum. 32(3): 24-31.

Bender, F.A M., Frey, L., McCoy, D.T., et al., 2018. Assessment of aerosol–cloud–radiation correlations in satellite observations, climate models and reanalysis. Clim. Dyn. 1 – 22. https://doi.org/10.1007/s00382-018-4384-z.

Bharti, V., Singh, C., Ettema, J., Turkington, T.A., 2016. Spatiotemporal characteristics of extreme rainfall events over the Northwest Himalaya using satellite data. Int. J. Climatol. 36: 3949-3962. https://doi.org/10.1002/joc.4605.

Bhutiyani, M. R., Kale, V. S., Pawar, N. J., 2007. Long-term trends in maximum, minimum and mean annual air temperatures across the Northwestern Himalaya during the twentieth century. Clim. Change 85: 159–177. https://doi.org/10.1007/s10584-006-9196-1.

Bhutiyani, M. R., Kale, V. S., Pawar, N. J., 2010. Climate change and the precipitation variations in the northwestern Himalaya: 1866–2006. Int. J. Climatol. 30: 535–548. https://doi.org/10.1002/joc.1920.

Bibi, H., Alam, K., Chishtie, F., Bibi, S., Shahid, I., Blaschke, T., 2015. Intercomparison of MODIS, MISR, OMI, and CALIPSO aerosol optical depth retrievals for four locations on the Indo-Gangetic plain and validation against AERONET data. Atmos. Environ. 111: 113-126.

Bilal, M., Nichol, J. E., Nazeer, M., 2016. Validation of Aqua-MODIS C051 and C006 Operational Aerosol Products Using AERONET Measurements over Pakistan. IEEE Journal of Selected Topics in Applied Earth Observations and Remote Sensing. 9(5): 2074-2080.

Blunden, J., Arndt, D. S., 2017. State of the Climate in 2016. Bulletin of the American Meteorological Society. 98(8).

Bodeker, G. E., Bojinski, S., Cimini, D., Dirksen, R. J., Haeffelin, M., Hannigan, J. W., et al., 2016. Reference upper-air observations for climate: From concept to reality. Bulletin of the American Meteorological Society. 97(1): 123–135. https://doi.org/10.1175/BAMS-D-14-00072.1.

Bodhaine, B. A., 1983. Aerosol measurements at four background sites. J. Geophys. Res. 88: 10753–10768. http://dx.doi.org/10.1029/JC088iC15p10753.

Bojinski, S., Verstraete, M., Peterson, T. C., Richter, C., Simmons, A., Zemp, M., 2014. The concept of Essential Climate Variables in support of climate research, applications, and policy. Bull. Am. Meteorol. Soc. 95(9): 1431–1443. http://dx.doi.org/10.1175/BAMS-D-13- 00047.1.

Bolch, T., Kulkarni, A., Kääb, A., Huggel, C., Paul, F., Cogley, J. G., et al., 2012. The state and fate of Himalayan Glaciers. Science 336: 310–314. http://dx.doi.org/10.1126/science.1215828.

Bond, T.C., Doherty, S. J., Fahey, D.W., et al., 2013. Bounding the role of black carbon in the climate system: a scientific assessment, J. Geophys. Res.: Atmosphere 118 (11): 5380-5552. https://doi.org/10.1002/jgrd.50171.

Bonnet, S., Crave, A., 2003. Landscape response to climate change: insights from experimental modeling and implications for tectonics versus climatic uplift of topography. Geology 31(2): 123–126. https://doi.org/10.1130/0091-7613(2003)031<0123:LRTCCI>2.0.CO;2.

Bösenberg, J., et al., 2001. EARLINET: A European Aerosol Research Lidar Network. In: Dabas, A., Loth, C., Pelon, J. (Eds.), Advances in Laser Remote Sensing, Selected papers presented at the 20th International Laser Radar Conference (ILRC), Vichy, France, 155–158.

Bosilovich, M. G., Lucchesi, R., Suarez, M., 2016. MERRA-2: File Specification. GMAO Office Note No. 9 (Version 1.1). 1-73. Online: http://gmao.gsfc.nasa.gov/pubs/office_notes.

Boucher, O., et al., 2013. Clouds and Aerosols. In: Climate Change 2013: The Physical Science Basis. Contribution of Working Group I to the Fifth Assessment Report of the Intergovernmental Panel on Climate Change, Cambridge University Press, Cambridge, United Kingdom and New York, NY, USA.

Boucher, O., 2015. Atmospheric aerosols: Properties and climate impacts, first ed. Springer, Netherlands. http://dx.doi.org/10.1007/978-94-017-9649-1_3.

Brandon, P.C., 1973. Design of a nonlinear pulse compression system to give a low loss high resolution radar performance. Marconi.

Brenguier, J.-L., et al., 2013. In Situ Measurements of Cloud and Precipitation Particles, in Airborne Measurements for Environmental Research, in: Methods and Instruments, edited by: Wendisch, M., Brenguier, J.-L., WileyVCH Verlag GmbH & Co. KGaA, Weinheim, Germany. 225– 301. http://dx.doi.org/10.1002/9783527653218.ch5, 2013.

Bréon, F.-M., Vermeulen, A., Descloitres, J., 2011. An evaluation of satellite aerosol products against sunphotometer measurements. Remote Sens. Environ. 115(12): 3102–3111.

Brooks, I. M., 2003. Finding boundary layer top: Application of a wavelet covariance transform to lidar backscatter profiles. J. Atmos. Oceanic Technol. 20: 1092–1105. https://doi.org/10.1175/1520-0426(2003)020<1092:FBLTAO>2.0.CO;2.

Buchwitz, M., Lavender, S., Chuvieco, E., 2017. Special issue on earth observation of essential climate variables. Remote Sens. Environ. 203, 1 pp. https://doi.org/10.1016/j.rse.2017.09.001.

Butler, T. M., Lawrence, M. G., 2009. The influence of megacities on global atmospheric chemistry: a modelling study. Environ. Chem. 6: 219–225. https://doi.org/10.1071/en08110.

Carboni E., 2006. GOME aerosol optical depth retrieval over ocean: correcting for the effects of residual cloud contamination. Atmos Environ. 40: 6975–87.

Ceccaldi, M., et al., 2013. From CloudSat-CALIPSO to EarthCare: Evolution of the DARDAR cloud classification and its comparison to airborne radar-lidar observations. J. Geophys. Res. Atmos. 118(14): 7962–7981. http://dx.doi.org/10.1002/jgrd.50579.

Census, 2011. Census of India. Office of the Registrar General & Census Commissioner. Ministry of Home Affairs. Government of India.

Cess, R.D., et al., 1989. Interpretation of cloud-climate feedback as produced by 14 atmospheric general circulation models. Science. 245: 513–516.

Cess, R.D., et al., 1990. Intercomparison and interpretation of climate feedback processes in 19 atmospheric general circulation models. J. Geophys. Res. 95:16601–16615. http://dx.doi.org/10.1029/JD095iD10p16601.

Cess, R. D., et al., 1996. Cloud feedback in atmospheric general circulation models: An update. J. Geophys. Res. 101(D8): 12791-12794. http://dx.doi.org/10.1029/96JD00822.

Chettri, N., Sharma, E., Shakya, B., Thapa, R., Bajracharya, B., Uddin, K., Oli, K.P., Choudhury, D., 2010. Biodiversity in the Eastern Himalayas: Status, trends and vulnerability to climate changes; Climate change impact and vulnerability in the eastern Himalayas- Technical Report 2. ICIMOD, Kathmandu, Nepal.

Choudhry, P., Misra, A., Tripathi, S.N., 2012. Study of MODIS Derived AOD at Three Different Locations in the Indo Gangetic Plain: Kanpur, Gandhi College and Nainital. Ann. Geophys. 30: 1479–1493. http://dx.doi.org/10.5194/angeo-30-1479-2012.

Chylek, P., Henderson, B., Mishchenko, M., 2003. Satellite based retrieval of aerosol optical thickness: the effect of sun and satellite geometry. Geophys Res Lett. 30:1533.

Cifelli, R., Boccippio, D. J., Matejka, T., 1996. Horizontal divergence and vertical velocity retrievals from Doppler radar and wind profiler observations. J. Atmos. Oceanic Technol. 13: 948–966.

Clements, C. B., Potter, B. E., Zhong, S., 2006. In-situ measurements of water vapor, heat, and C02 fluxes within a prescribed grass fire. Int. J. Wildland Fire. 15(3): 299-306.

Compton, J.C., Delgado, R., Berkoff, T.A., Hoff, R.M., 2013. Determination of Planetary Boundary Layer Height on Short Spatial and Temporal Scales: A Demonstration of the Covariance Wavelet Transform in Ground-Based Wind Profiler and Lidar Measurements. J. Atmos. Oceanic Technol. 30: 1566–1575. https://doi.org/10.1175/JTECH-D-12-00116.1.

Csiszár, I., et al., 1999. M. Precipitation estimation with satellites and radar. Adv. Space Res. 3: 461-467. http://dx.doi.org/10.1016/ S0273-1177(97)00055-0.

Damtie, B., Lehtinen, M., Orispaa, M., Vierinen, J., 2007. Optimal long binary phase code-mismatched filter pairs with applications to ionospheric radars. Bull. Astr. Soc. India. 35: 619-623.

Dash, S. K., Jenamani, R. K., Kalsi, S. R., Panda, S. K., 2007. Some evidence of climate change in twentieth-century India. Climatic Change. 85: 299–321.

Decker, M., Brunke, M. A., Wang, Z., Sakaguchi, K., Zeng, X., Bosilovich, M. G., 2012. Evaluation of the Reanalysis Products from GSFC, NCEP, and ECMWF Using Flux Tower Observations. J. Climate. 25(6): 1916–1944. http://dx.doi.org/10.1175/JCLI-D-11-00004.1.

Dee, D. P., et al., 2011. The ERA-Interim reanalysis: Configuration and performance of the data assimilation system. Q. J. R. Meteorol. Soc., 137(656): 553–597. http://dx.doi.org/10.1002/qj.828.

Dee, D. P., et al., 2014. Toward a consistent reanalysis of the climate system. Bull. Amer. Meteor. Soc. 95: 1235–1248. http://dx.doi.org/10.1175/BAMS-D-13-00043.1.

Delanoë, J., Hogan, R. J., 2008. A variational scheme for retrieving ice cloud properties from combined radar, lidar, and infrared radiometer. J. Geophys. Res. Atmos. 113: 1-21. http://dx.doi.org/10.1029/2007JD009000.

Delanoë, J., Hogan, R. J., 2010. Combined CloudSat-CALIPSO-MODIS retrievals of the properties of ice clouds. J. Geophys. Res. Atmos. 115: 1–17. http://dx.doi.org/10.1029/2009JD012346.

Deschamps P-Y, et al. 1994. The POLDER mission: instrument characteristics and scientific objectives. IEEE Trans Geosci Remote Sens. 32:598–615.

Dey, S., Girolamo, L., 2011. A decade of change in aerosol properties over the Indian subcontinent. Geophys. Res. Lett. 38. L14811. http://dx.doi.org/10.1029/2011GL048153.

Dickinson, R. E., 1975. Meteorology of the upper atmosphere. Rev. Geophys. 13(3): 771–790.

Dimri, A. P, Niyogi, D., Barros, A. P, Ridley, J., Mohanty, U. C, Yasunari, T., Sikka, D. R., 2015. Western disturbance: a review. Rev Geophys. 53: 225–246. http://dx.doi.org/10.1002/2014 RG000460.

Dimri, A.P., Chevuturi, A., Niyogi, D., Thayyen, R.J., Ray, K., Tripathi, S.N., Pandey, A.K., Mohanty, U.C., 2017. Cloudbursts in indian himalayas: a review. EarthScience Rev. 168: 1-23.

Dimri, A. P., Kumar, D., Choudhary, A., Maharana, P., 2018. Future changes over the Himalayas: mean temperature. Glob Planet Chang. 162: 235–251.

Diner, D.J, et al. 1998. Multi-angle imaging spectroradiometer (MISR) instrument description and experiment overview. IEEE Trans Geosci Remote Sens. 36:1072–87.

Ding, K., Liu, J., Ding, A., Liu, Q., Zhao, T. L., Shi, J., Han, Y., Wang, H., Jiang, F., 2015. Uplifting of carbon monoxide from biomass burning and anthropogenic sources to the free troposphere in East Asia. Atmos. Chem. Phys. 15: 2843-2866. http://dx.doi.org/10.5194/acp-15-2843-2015.

Dobhal, D. P., Gupta, A. K., Mehta, M., Khandelwal, D. D., 2013. Kedarnath disaster: Facts and plausible causes. Current Science. 105(2): 171-174.

Doviak, R. J., Zrnic, D., 1984. Radar observation of the atmosphere, Academic Press, New York.

Draxler, R.R., Hess, G., 1997. Description of the HYSPLIT4 Modeling System.

Draxler, R.R., Hess, G., 1998. An overview of the HYSPLIT_4 modelling system for trajectories. Aust. Meteorol. Mag. 47: 295-308.

Duan, K., Yao, T., Thompson, L. G., 2006. Response of monsoon precipitation in the Himalayas to global warming. Journal of Geophysical Research. 111(D19110): 1 – 8. https://doi.org/10.1029/2006JD007084.

Dubois, N., Oppo, D. W., Galy, V. V., Mohtadi, M., et al. 2014. Indonesian vegetation response to changes in rainfall seasonality over the past 25,000 years. Nature Geoscience. 7: 513–517. https://doi.org/10.1038/NGEO2182.

Dubovik, O., Holben, B., Eck, T.F., Smirnov, A., Kaufman, Y.J., King, M.D., Tanré, D., Slutsker, I., 2002. Variability of Absorption and Optical Properties of Key Aerosol Types Observed in Worldwide Locations. J. Atmos. Sci. 59: 590–608. https://doi.org/10.1175/1520-0469(2002)059<0590:VOAAOP>2.0.CO;2.

Duchi, R., Cristofanelli, P., Marinoni, A., Bourcier, L., Laj, P., Calzolari, F., Adhikary, B., Verza, G.P, Vuillermoz, E., Bonasoni, P., 2014. Synoptic-scale dust transport events in the southern Himalaya. Aeolian Research. 13: 51-57. https://doi.org/10.1016/j.aeolia.2014.03.008.

Duhan, D., Pandey, A., 2013. Statistical analysis of long term spatial and temporal trends of precipitation during 1901–2002 at Madhya Pradesh, India. Atmospheric Research. 122: 136–149.

Dumka, U. C., Tripathi, S. N., Misra, A., Giles, D. M., Eck, T. F., Sagar, R., Holben, B. N., 2014. Latitudinal variation of aerosol properties from Indo-Gangetic Plain to central Himalayan foothills during TIGERZ campaign. J. Geophys. Res. Atmos. 119. http://dx.doi.org/10.1002/2013JD021040.

Easterling, D. R., Meehl, G. A., Parmesan, C., Changnon, S. A., Karl, T. R., Mearns, L. O., 2000. Climate extremes: Observations, modeling and impacts. Science. 289: 2068-2074.

Eck, T. F., Holben, B. N., Reid, J. S., Dubovik, O., Smirnov, A., O'Neill, N. T., Slutsker, I., Kinne, S., 1999. Wavelength dependence of the optical depth of biomass burning, urban, and desert dust aerosols. J. Geophys. Res. 104(D24): 31333–31349. http://dx.doi.org/10.1029/1999JD900923.

Elachi, 1987. Introduction to the Physics and Techniques of Remote Sensing. New York: John Wiley & Sons.

Emeis, S., 2010. Measurement Methods in Atmospheric Sciences, In situ and remote, Borntraeger science publishers, Stuttgart, Germany, 1-257.

Emori, S., Brown, S. J., 2005. Dynamic and thermodynamic changes in mean and extreme precipitation under changed climate. Geophys. Res. Lett. 32. L17706. http://dx.doi.org/10.1029/2005GL023272.

Estrellan, C. R., Iino, F., 2010. Toxic emissions from open burning. Chemosphere. 80(3): 193-207. http://dx.doi.org/10.1016/j.chemosphere.2010.03.057.

Evans, K. F., O'Connor, D., Zmarzly, P., Lawson, R.P., 2006. In Situ Cloud Sensing with Multiple Scattering Lidar: Design and Validation of an Airborne Sensor. J. Atmos. Oceanic Technol., 23: 1068–1081. http://dx.doi.org/10.1175/JTECH1901.1.

Fan, J., Wang, Y., Rosenfeld, D., Liu, X., 2016. Review of aerosol-cloud interactions: Mechanisms, significance and challenges. Journal of the Atmospheric Sciences. 73(11): 4221–4252. https://doi.org/10.1175/JAS-D-16-0037.1.

Farley, D.T., 1985. On-line data processing techniques for MST radars. MAP. 20(6): 1177-1184.

Fernald, F. G., 1984. Analysis of atmospheric lidar observations: Some comments. App. Opt. 23. 652–653.

Fiocco, G., Smullin, L. D., 1963. Detection of scattering layers in the upper atmosphere (60–140 km) by optical radar. Nature. 199: 1275-1276. https://doi.org/10.1038/1991275a0.

Foga, S., Scaramuzza, P.L., Guo, S., Zhu, Z., Dilley, R.D., Beckmann, T., Schmidt, G.L., Dwyer, J.L., Hughes, M.J., Laue, B., 2017. Cloud detection algorithm comparison and validation for operational Landsat data products. Remote Sens. Environ. 194, 379–390.

Foley, A. M., 2010. Uncertainty in regional climate modelling: A review. Prog. Physi. Geogr. 34: 647–670. http://dx.doi.org/10.1177/0309133310375654.

Freestone, D., 2016. The United Nations Framework Convention on Climate Change – The Basis for the Climate Change Regime. in Gray, K. R., Tarasofsky, R.G., Carlarne, C. P., (eds.). The Oxford Handbook of International Climate Change Law. Oxford University Press. Oxford.

Fritsch, J.M., et al., 1998. Quantitative precipitation forecasting: Report of the eight prospectus development team, U.S. weather research program. Bull. Amer. Meteor. Soc. 79(2): 285–299.

Fukao, S., Sato, T., Yamasaki, N., Harper, R.N., Rato, S., 1982. Wind measurement by a UHF Doppler radar and rawinsondes: Comparison made on 26 days (August-September 1977) at Arecibo, Puerto Rico, J. Appl. Meteorol., 21: 1357-1363.

Gadgil, S., 2003. The Indian monsoon and its variability. Annu. Rev. Earth Planet. Sci. 31: 429–467. https://doi.org/10.1146/annurev.earth.31.100901.141251.

Gage, K. S., Balsley, B. B., 1978. Doppler radar probing of the clear atmosphere, Bull. Amer. Meteor. Soc., 59, 1074-1093.

Gamage, N., Hagelberg, C., 1993. Detection and analysis of microfronts and associated coherent events using localized transforms. J. Atmos. Sci. 50:750–756. https://doi.org/10.1175/1520-0469(1993)050<0750:DAAOMA>2.0.CO;2.

Gibbs, W.J., Fournier d'Albe, E.M, Rao, G., Malone, T.F., Baier, W., Flohn, H., Mitchell, J. M., Bolin, B., 1977. Technical Report by the WMO Executive Council Panel of Experts on Climate Change. WMO Bulletin. XXVI(1): 50-55.

Giglio, L., Descloitres, J., Justice, C. O., Kaufman, Y., 2003. An enhanced contextual fire detection algorithm for MODIS. Rem. Sens. Environ. 87(2-3): 273-282. http://dx.doi.org/10.1016/S0034-4257(03)00184-6.

Giglio, L., 2005. MODIS Collection 6 Active Fire Product User's Guide Revision A. NASA. Online: http://modis-fire.umd.edu/pages/manuals.php.

Ginoux, P., Prospero, J. M., Gill, T. E., Hsu, N. C., Zhao, M., 2012. Global-scale attribution of anthropogenic and natural dust sources and their emission rates based on MODIS Deep Blue aerosol products. Rev. Geophys. 50. RG3005. http://dx.doi.org/10.1029/2012RG000388.

Giorgi, F., Raffaele, F., Coppola, E., 2019. The response of precipitation characteristics to global warming from climate projections. Earth System Dynamics. 10: 73-89. http://dx.doi.org/10.5194/esd-10-73-2019.

Gleckler, P. J., Taylor, K. E., Doutriaux, C., 2008. Performance metrics for climate models. J. Geophys. Res. 113. D06104. https://doi.org/10.1029/2007JD008972.

Golay, M. J. E., 1961. Complementary series. IRE Trans. Inform. Theory. 7(2): 82–87.

Goswami, B. N., 1987. A mechanism for the west-north-west movement of monsoon depressions. Nature. 326: 376–378.

Goswami, B. N., Venugopal, V., Sengupta, D., Madhusoodanam, M. S., Xavier, P. K., 2006. Increasing trends of extreme rain events over India in a warming environment. Science. 314: 1442–1445.

Griggs, M., 1975. Measurements of atmospheric aerosol optical thickness over water using ERTS-1 data. J. Air Pollut. Control Assoc. 25: 622–626.

Groisman, P. Y., Knight, R. W., Easterling, D. R., Karl, T. R., Hegerl, G. C., Razuvaev, V. N., 2005. Trends in intense precipitation in the climate record. J. Clim. 18. 1326–1350.

Guhathakurta, P., Rajeevan, M., 2007. Trends in the rainfall pattern over India. Int. J. Climatol. 28: 1453 – 1469. https://doi.org/10.1002/joc.1640.

Gurung, J., Bajracharya, R. M., 2012. Climate change and glacial retreat in the Himalaya: implications for soil and plant development. Kathmandu Univ. J. Sci. Eng. Technol. 8:153–163.

Guzman, J. A., Chu, M. L., Steiner, J. L., Starks, P. J., 2018. Assessing and quantifying changes in precipitation patterns using event-driven analysis. Journal of Hydrology: Regional Studies. 15: 1-15. https://doi.org/10.1016/j.ejrh.2017.11.006.

Hansen, J., Nazarenko, L., 2004. Soot climate forcing via snow and ice albedos. Proc. Natl. Acad. Sci. 101: 423-428. https://doi.org/10.1073/pnas.2237157100.

Hansen, J., Sato, M., Ruedy, R., 1997. Radiative forcing and climate response. J. Geophys. Res., 102: 6831-6864. http://dx.doi.org/10.1029/96JD03436.

Hansen, J., Sato, M., 2016. Regional climate change and national responsibilities. Environ Res Lett. 11(3), 034009. http://dx.doi.org/10.1088/1748-9326/11/3/034009.

Hardy, K. R., Gage, K. S., 1990. The history of radar studies of the clear atmosphere. Radar in Meteorology, D. Atlas, Ed., Amer. Meteor. Soc. 130–142. http://dx.doi.org/10.1007/978-1-935704-15-7_17.

Hart, M. H., 1978. The Evolution of the Atmosphere of the Earth. Icarus. 33: 23-39.

Hartmann, D. L., Ockert-Bell, M., Michelsen, M. L., 1992. The effect of cloud type on Earth's energy balance: Global analysis. J. Climate, 5: 1281–1304. http://dx.doi.org/10.1175/1520-0442(1992)005,1281: TEOCTO.2.0.CO;2.

Hartmann D.L., 1994. Global physical climatology. International Geophysics series, Academic Press, 56, 412 pp.

Hartmann, D.L., et al., 2013. Observations: Atmosphere and Surface. In: Climate Change 2013: The Physical Science Basis. Contribution of Working Group I to the Fifth Assessment Report of the Intergovernmental Panel on Climate Change. Cambridge University Press, Cambridge, United Kingdom and New York, NY, USA.

Haywood, J., Boucher, O., 2000. Estimates of the direct and indirect radiative forcing due to tropospheric aerosols: A review. Reviews of Geophysics, 38(4):513–543.

He, Q. S., Li, C. C., Mao, J. T., Lau, A. K. H., Li, P. R., 2006. A study on the aerosol extinction-to-backscatter ratio with combination of micro-pulse LIDAR and MODIS over Hong Kong. Atmos. Chem. Phys. 6: 3243–3256. http://dx.doi.org/10.5194/acp-6-3243-2006.

He, Q., Zhang, M., Huang, B., Tong, X., 2017. MODIS 3 km and 10 km aerosol optical depth for China: Evaluation and comparison. Atmos. Environ. 153: 150-162. http://dx.doi.org/10.1016/j.atmosenv.2017.01.023.

Hegarty, J.D., Lewis, J., et al., 2018. Analysis of the Planetary Boundary Layer Height during DISCOVER-AQ Baltimore–Washington, D.C., with Lidar and High-Resolution WRF Modeling. J. Appl. Meteor. Climatol. 57: 2679–2696. https://doi.org/10.1175/JAMC-D-18-0014.1.

Hegde, P., Pant, P., Bhavani Kumar, Y., 2009. An integrated analysis of lidar observations in association with optical properties of aerosols from a high altitude location in central Himalayas. Atmosph. Sci. Lett., 10: 48–57.

Hersey, S. P., Garland, R. M., Crosbie, E., Shingler, T., Sorooshian, A., Piketh, S., Burger, R., 2015. An overview of regional and local characteristics of aerosols in South Africa using satellite, ground, and modeling data. Atmos. Chem. Phys. 15: 4259-4278. http://dx.doi.org/10.5194/acp-15-4259-2015.

Hewitt, C. N., Jackson, A. V., 2008. Handbook of atmospheric science: Principles and applications. John Wiley & Sons.

Hildebrand, P.H., Sekhon, R.S., 1974. Objective determination of the noise level in Doppler spectra. J.Appl.Meterol. 13: 808-811.

Hirose, M., Nakamura, K., 2004. Spatiotemporal Variation of the Vertical Gradient of Rainfall Rate Observed by the TRMM Precipitation Radar. J. Climate. 17: 3378–3397. https://doi.org/10.1175/1520-0442(2004)017<3378:SVOTVG>2.0.CO;2.

Hocking, W. K., 2011. A review of Mesosphere-Stratosphere-Troposphere (MST) radar developments and studies, circa 1997–2008. J. Atmos. Sol. Terr. Phys. 73: 848–882. https://doi.org/10.1016/j.jastp.2010.12.009.

Hoff, R. M., Christopher, S. A., 2009. Remote sensing of particulate pollution from space: Have we reached the promised land?, J. Air Waste Manag. Assoc., 59 (10): 645–675.

Holben, B. N., et al., 1998. AERONET—A federated instrument network and data archive for aerosol characterization. Rem. Sens. Environ. 66(1):1–16. http://dx.doi.org/10.1016/S0034-4257(98)00031-5.

Holben, B. N., et al., 2001. An emerging ground-based aerosol climatology: Aerosol optical depth from AERONET. J. Geophys. Res., 106(D11): 12067–12097. http://dx.doi.org/10.1029/2001JD900014.

Hollmann, R., et al., 2013. The ESA climate change initiative: Satellite data records for essential climate variables. Bull. Amer. Meteor. Soc. 94: 1541–1552. http://dx.doi.org/10.1175/BAMS-D-11-00254.1.

Hong, Y., Adler, R. F., 2007. Towards an early-warning system for global landslides triggered by rainfall and earthquake. International Journal of Remote Sensing. 28(16): 3713-3719. http://dx.doi.org/10.1080/01431160701311242.

Hou, A.Y., Kakar, R.K., Neeck, S., Azarbarzin, A.A., Kummerow, C.D., Kojima, M., Oki, R., Nakamura, K., Iguchi, T. 2014. The global precipitation measurement mission. Bull. Am. Meteorol. Soc. 95: 701–722.

Houghton, J.T., Jenkins, G.J., Ephraums. J.J., 1990. Climate Change: The IPCC Scientific Assessment: Report Prepared for IPCC by Working Group 1. Cambridge: Cambridge University Press.

Houghton, J. T., Ding, Y., Griggs, D. J., Noguer, M., van der Linden, P. J., Xiaosu, D., Eds., 2001. Climate Change 2001: The Scientific Basis. Cambridge University Press. 944 pp.

Huffman, G.J., Adler, R.F., Bolvin, D.T., Gu, G., Nelkin, E.J., Bowman, K.P., Hong, Y., Stocker, E.F., Wolff, D.B., 2007. The TRMM Multi-satellite Precipitation Analysis: Quasi-Global, Multi-Year, Combined-Sensor Precipitation Estimates at Fine Scale. J. Hydrometeor., 8: 38-55.

Hulme, M., Barrow, E.M., Arnell, N.W., Harrison, P.A., Johns, T.C., Downing, T.E., 1999. Relative impacts of human-induced climate change and natural climate variability. Nature. 397: 688-691.

Hunt, W. H., Winker, D. M., Vaughan, M. A., Powell, K. A., Lucker, P. L., Weimer, C., 2009. CALIPSO Lidar Description and Performance Assessment. J. Atmos. Oceanic Technol. 26(7): 1214–1228. http://dx.doi.org/10.1175/2009JTECHA1223.1.

Hussain, A., Rais, M., Malik, M. B., 2008. Golay Codes in Ranging Applications. 8th IASTED WOC-2008. Canada. 159-162.

Hyvarinen, A.-P., et al., 2010. Aerosol measurements at the Gual Pahari EUCAARI station: preliminary results from in-situ measurements. Atmos. Chem. Phys. 10: 7241–7252.

Ichoku, C., Chu, D.A., Mattoo, S., Kaufman, Y.J., Remer, L.A., Tanre´, D., Slutsker, I., Holben, B.N., 2002. A spatio-temporal approach for global validation and analysis of MODIS aerosol products. Geophys. Res. Lett. 29(12): 1616, 1–4. http://dx.doi.org/10.1029/2001GL013206.

IMD, 2018. Annual climate summary – 2017. (retrieved from the website : http://www.imdpune.gov.in/Links/annual%20summary%202017.pdf).

Immerzeel, W. W., Pellicciotti, F., Bierkens, M. F. P., 2013. Rising river flows throughout the twenty first century in two Himalayan glacierized watersheds. Nat. Geosci. 6: 742–745. http://dx.doi.org/10.1038/ngeo1896.

Immerzeel, W.W., Kraaijenbrink, P. D. A., et al. 2014. High-resolution monitoring of Himalayan glacier dynamics using unmanned aerial vehicles. Remote Sensing of Environment. 150: 93-103. http://dx.doi.org/10.1016/j.rse.2014.04.025.

IPCC, 2007. Climate change 2007: The physical science basis: Contribution of Working Group I to the Fourth Assessment Report of the Intergovernmental Panel on Climate Change. Chapter 2. Cambridge Univ. Press. New York. 129 p.

IPCC, 2013. Summary for Policymakers. In: Climate Change 2013: The Physical Science Basis. Contribution of Working Group I to the Fifth Assessment Report of the Intergovernmental Panel on Climate Change [Stocker, T.F., Qin, D., Plattner, G.-K., Tignor, M., Allen, S.K.,

Boschung, J., Nauels, A., Xia, Y., Bex, V., Midgley, P.M., (Eds.)]. Cambridge University Press, Cambridge, United Kingdom and New York, NY, USA.

IPCC, 2014. Climate Change 2014: Synthesis Report. Contribution of Working Group I, II and III to the Fifth Assessment Report of the Intergovernmental Panel on Climate Change. In: Core Writing Team, Pachauri, R.K., Meyer, L. A. (Eds.), IPCC, Geneva, Switzerland, 151 pp. http://dx.doi.org/10013/epic.45156.d001.

Islam, T., et al. (edn.), 2018. Remote Sensing of Aerosols, Clouds, and Precipitation. Elsevier. 364 pp. https://doi.org/10.1016/C2015-0-06872-1.

Istanbulluoglu, E., Bras, R. L., 2006. On the dynamics of soil moisture, vegetation, and erosion: Implications of climate variability and change. Water Resour. Res. 42. W06418. https://doi.org/10.1029/2005WR004113.

Jacobson, M.Z., 2001. Strong radiative heating due to the mixing state of black carbon in atmospheric aerosols, Nature 409 (1): 695-697. https://doi.org/10.1038/35055518.

Jain, N., Bhatia, A., Pathak, H., 2014. Emission of air pollutants from crop residue burning in India. Aerosol Air Qual. Res. 14(1): 422–430. http://dx.doi.org/10.4209/aaqr.2013.01.0031.

Janssen, M. A., 1993. Atmospheric Remote Sensing by Microwave Radiometry, John Wiley, New York.

Jayaraman, A., Acharya,Y. B., Subbaraya, B. H., Chandra, H., 1995. Nd:YAG backscatter lidar at Ahmedabad (23° N, 72.5° E) for tropical middle atmospheric studies. Appl. Optics, 34: 6937–6940.

Jordan, N. S., Hoff, R. M., Bacmeister, J. T., 2010. Validation of Goddard Earth Observing System-version 5 MERRA planetary boundary layer heights using CALIPSO. J. Geophys. Res.. 115(D24). D24218. http://dx.doi.org/10.1029/2009JD013777.

Kalnay, E., et al., 1996. The NCEP/NCAR 40-Year Reanalysis Project. Bull. Amer. Meteor. Soc., 77: 437–472. https://doi.org/10.1175/1520-0477(1996)077<0437:TNYRP>2.0.CO;2.

Kaufman, Y.J., Tanr´e, D., Boucher, O., 2002. A satellite view of aerosols in the climate system. Nature, 419(6903): 215–223.

Kazuo, T., 2014. Industrialization and the Development of Regional Economies in the State of Uttarakhand. J. Urban and Regional Studies on Contemporary India. 1(2): 9-20. http://dx.doi.org/10.15027/41499.

Kent, G. S., Wright, R. W., 1970. A review of laser radar measurements of atmospheric properties. J. Atmos. Terr. Phys. 32(5): 917–943. https://doi.org/10.1016/0021-9169(70)90036-X.

Kharol, S. K., Kaskaoutis, D. G., Sharma, A. R., Singh, R. P., 2013. Long-Term (1951–2007) Rainfall Trends around Six Indian Cities: Current State, Meteorological, and Urban Dynamics. Advances in Meteorology. 2013(572954): 1- 15. https://doi.org/10.1155/2013/572954.

Kidd, C., Huffman, G., 2011. Global precipitation measurement. Met. Apps. 18: 334-353. https://doi.org/10.1002/met.284.

King, M.D, et al., 2003. Cloud and aerosol properties, precipitable water, and profiles of temperature and water vapor from MODIS. IEEE Trans. Geosci. Remote Sens. 41: 442–58.

King, O., Quincey, D.J., Carrivick, J.L., et al., 2017. Spatial variability in mass loss of glaciers in the Everest region, central Himalayas, between 2000 and 2015. The Cryosphere. 11(1): 407-426. ISSN 1994-0416.

Kittaka, C., Winker, D. M., Vaughan, M. A., Omar, A., Remer, M. A., 2011. Intercomparison of column aerosol optical depths from CALIPSO and MODIS-Aqua. Atmos. Meas. Tech. 4: 131–141. http://dx.doi.org/10.5194/amt-4-131-2011.

Klett, J. D., 1981. Stable analytical inversion solution for processing lidar returns. App. Opt. 20: 211-220. http://dx.doi.org/10.1364/AO.20.000211.

Kokhanovsky, A. A., et al., 2007. Aerosol remote sensing over land: A comparison of satellite retrievals using different algorithms and instruments. Atmos. Res. 85(3–4): 372-394. http://dx.doi.org/10.1016/j.atmosres.2007.02.008.

Koren, I., Martins, J. V., Remer, L. A., Afargan, H., 2008. Smoke Invigoration Versus Inhibition of Clouds over the Amazon. Science. 321: 946–949. http://dx.doi.org/10.1126/science.1159185.

Kotamarthi, V. R., 2010. Ganges Valley Aerosol Experiment: Science and Operations Plan. DOE/SC-ARM-10-019. 2010.

Kotamarthi, V. R., 2013. Ganges Valley Aerosol Experiment (GVAX) Final Campaign Report. DOE/SC-ARM-14-011. 2013.

Kothawale, D. R., Revadekar, J. V., Kumar, R. K., 2010. Recent trends in pre-monsoon daily temperature extremes over India. J. Earth Syst. Sci. 119(1): 51-65.

Kothawale, D. R., Rajeevan, M., 2017. Monthly, Seasonal and Annual Rainfall Time Series for All-India, Homogeneous Regions and Meteorological Sub-divisions: 1871-2016. Indian Institute of

Tropical Meteorology (IITM). Earth System Science Organization (ESSO). RR-138. ISSN 0252-1075.

Kottayil, A. et al., 2016. Validation of 205 MHz wind profiler radar located at Cochin, India, using radiosonde wind measurements. Radio Sci. 51: 1–12. http://dx.doi.org/10.1002/2015RS005836.

Krishnan, R., et al., 2019. Unravelling Climate Change in the Hindu Kush Himalaya: Rapid Warming in the Mountains and Increasing Extremes. In: Wester, P., Mishra, A., Mukherji, A., Shrestha, A. (eds) The Hindu Kush Himalaya Assessment. Springer, Cham. https://doi.org/10.1007/978-3-319-92288-1_3.

Krishnamurthy, V., Shukla, J., 2000. Intraseasonal and interannual variability of rainfall over India. J. Climate. 13: 4366–4377.

Krishnamurti, T. N., Mishra, A. K., Simon, A., Yatagai, A., 2009. Use of a dense rain-gauge network over India for improving blended TRMM products and downscaled weather models. Journal of the Meteorological Society of Japan. Ser. II 87A: 393–412. https://doi.org/10.2151/jmsj.87A.393.

Kucharik, C. J., Foley, J. A., Delire, C., Fisher, V. A., Coe, M. T., Lenters, J. D., Young-Molling, C., Ramankutty, N., Norman, J. M., Gower, S. T., 2000. Testing the performance of a dynamic global ecosystem model: Water balance, carbon balance, and vegetation structure. Global Biogeochem. Cycles. 14(3): 795–825. http://dx.doi.org/10.1029/1999GB001138.

Kudeki, E., Rastogi, P. K., 1992. A Multibeam Vorticity Measurement Technique for Modular MST Radars. Radio Science. 27(6): 769-774. http://dx.doi.org/10.1029/92RS01784.

Kumar, A., Bhattacharjee, S., Naja, M., Kumar, P., 2011. Front-end Digital Signal Processing Scheme for 206.5 MHz Atmospheric Radar Application, International Journal of Advancements in Technology (IJoAT), 2(1): 71-81.

Kumar, A., Singh, N., Anshumali, Solanki, R., 2018. Evaluation and utilization of MODIS and CALIPSO aerosol retrievals over a complex terrain in Himalaya. Remote Sens. Environ. 206: 139-155. http://dx.doi.org/10.1016/j.rse.2017.12.019.

Kumar, A., Singh, N., Singh, A., 2019. Observations on the distribution of clouds over northern India using joint CloudSat and CALIPSO measurements. Remote Sensing Letters 10(6): 590-597. http://dx.doi.org/10.1080/2150704X.2019.1587198.

Kumar, N., Yadav, B.P., Gahlot, S., Singh, M., 2015. Winter frequency of western disturbances and precipitation indices over Himachal Pradesh, India: 1977-2007. Atmósfera. 28(1): 63-70. https://doi.org/10.1016/S0187-6236(15)72160-0.

Kumar, N., Jaswal, A.K. 2016. Historical temporal variation in precipitation over Western Himalayan Region: 1857-2006. Journal of Mountain Science. 13(4): 672-681. https://doi.org/10.1007/s11629-014-3194-y.

Kumar, M., Tiwari, S., Murari, V., Singh, A.K., Banerjee, T., 2015. Wintertime characteristics of aerosols at middle Indo-Gangetic Plain: impacts of regional meteorology and long range transport. Atmos. Environ. 104: 162–175.

Kumar, V., Jain, S. K., 2010. Trends in seasonal and annual rainfall and rainy days in Kashmir Valley in the last century. Quaternary International. 212(1): 64-69. https://doi.org/10.1016/j.quaint.2009.08.006.

Kumar, V., Jain, S. K., Singh, Y., 2010. Analysis of long-term rainfall trends in India. Hydrological Sciences Journal – Journal des Sciences Hydrologiques. 55(4): 484-496. http://dx.doi.org/10.1080/02626667.2010.481373.

Kumari, P. B., Goswami, B. N., 2010. Seminal role of clouds on solar dimming over the Indian monsoon region. Geophys. Res. Lett. 37(L06703). http://dx.doi.org/10.1029/2009GL042133.

Kummerow, C., et al., 2000. The status of the Tropical Rainfall Measuring Mission (TRMM) after two years in orbit. Journal of Applied Meteorology. 39(12): 1965–1982. https://doi.org/10.1175/1520- 0450(2001)040%3C1965:TSOTTR%3E2.0.CO;2.

Kummerow, C., Barnes, W., Kozu, T., Shiue, J., Simpson, J., 1998. The Tropical Rainfall Measuring Mission (TRMM) sensor package. Journal of Atmospheric and Oceanic Technology 15 (3): 809–817. http://dx.doi.org/10.1175/1520-0426(1998) 0152.0.CO;2.

L'Ecuyer, T. S., Jiang, J. H., 2010. Touring the atmosphere aboard the A-Train. Phys. Today. 63(7): 36–41. http://dx.doi.org/10.1063/1.3463626.

Lal, S., 2007. Trace gases over the Indian region. Indian Journal of Radio & Space Physics 36: 556–570.

Lau, W.K.-M., Kim, M.-K., Kim, K.-M., Lee, W.-S., 2010. Enhanced surface warming and accelerated snow melt in the Himalayas and Tibetan Plateau induced by absorbing aerosols. Environ. Res. Lett. 5, 025204. http://dx.doi.org/10.1088/1748-9326/5/2/025204.

Lee, S., Wang, C., 2015. The Response of the South Asian Summer Monsoon to Temporal and Spatial Variations in Absorbing Aerosol Radiative Forcing. J. Climate, 28**:** 6626–6646. http://dx.doi.org/10.1175/JCLI-D-14-00609.1.

Lehmann, V., Teschke, G., 2001. Wavelet based methods for improved wind profiler signal processing. Annales Geophysicae. 19: 825-836.

Leon, J.-F., Derimian, Y., Chiapello, I., Tanre, D., Podvin, T., Chatenet, B., Diallo, A., Deroo, C., 2009. Aerosol vertical distribution and optical properties over M'Bour (16.96^0W; 14.39^0 N), Senegal from 2006 to 2008. *Atmos. Chem. Phys.,* 9: 9249–9261.

Letcher, T. M., 2015. Climate Change: Observed impacts on Planet Earth, second ed., Elsevier, London.

Levermann, A., Schewe, J., Petoukhov, V., Held, H., 2009. Basic mechanism for abrupt monsoon transitions. Proceedings of the National Academy of Sciences (PNAS) of the United States of America 106(49): 20572–20577. http://dx.doi.org/10.1073/pnas.0901414106.

Levy, R. C., Mattoo, S., Munchak, L. A., Remer, L. A., Sayer, A. M., Patadia, F., Hsu, N. C., 2013. The Collection 6 MODIS aerosol products over land and ocean. Atmos. Meas. Tech. 6(11): 2989–3034. http://dx.doi.org/10.5194/amt-6-2989-2013.

Lillesand, T. M., Kiefer, R. W., Chipman, J. W., 2008. Remote sensing and image interpretation. Wiley. 6th ed. ISBN 978-0-470-05245-7.

Lintner, B. R., Biasutti, M., Diffenbaugh, N. S., Lee, J.-E., Niznik, M. J., Findell, K. L., 2012. Amplification of wet and dry month occurrence over tropical land regions in response to global warming. J. Geophys. Res. 117. D11106. http://dx.doi.org/10.1029/2012JD017499.

Lippmann, M., Ito, K., Nadas, A., Burnett, R.T., 2000. Association of particulate matter components with daily mortality and morbidity in urban populations. Research Report/ Health Effects Institute, 95:5–72.

Liu, J., Li, Z., Zheng, Y., Chiu, J. C., Zhao, F., Cadeddu, M., Weng, F., Cribb, M., 2013. Cloud optical and microphysical properties derived from ground-based and satellite sensors over a site in the Yangtze Delta region. J. Geophys. Res. Atmos., 118: 9141–9152. http://dx.doi.org/10.1002/jgrd.50648.

Lodhi, N. K., Begum, S. N., Singh, S., Kumar, K., 2013. Aerosol Climatology at Delhi in the Western Indo-Gangetic Plain: Microphysics, Long-Term Trends, and Source Strengths. J. Geophys. Res. 118: 1–15. http://dx.doi.org/10.1002/jgrd.50165.

Lohmann, U., Feichter, J., 2005. Global indirect aerosol effects: a review. Atmos. Chem. Phys. 5(5):715–737.

Long, X., Tie, X., Cao, J., Huang, R., Feng, T., Li, N., Zhao, S., Tian, J., Li, G., Zhang, Q., 2016. Impact of crop field burning and mountains on heavy haze in the North China Plain: a case study, Atmos. Chem. Phys. 16: 9675-9691. http://dx.doi.org/10.5194/acp-16-9675-2016.

Mace, G. G., Zhang, Q., Vaughan, M., Marchand, R., Stephens, G., Trepte, C., Winker, D., 2009. A description of hydrometeor layer occurrence statistics derived from the first year of merged Cloudsat and CALIPSO data. J. Geophys. Res. 114. D00A26. http://dx.doi.org/10.1029/2007JD009755.

Madhura, R. K., Krishnan, R., Revadekar, J. V., Mujumdar, M., Goswami, B. N., 2015. Changes in western disturbances over the Western Himalayas in a warming environment. Climate Dyn., 44: 1157–1168, doi:10.1007/s00382-014-2166-9.

Mahesh, A., Walden, V. P., Warren, S. G., 2001. Ground-based infrared remote sensing of cloud properties over the Antarctic Plateau. J. Appl. Meteor., 40: 1279–1294.

Mahmood, R., Pielke Sr., R., Hubbard, K. G., 2007. Effect of Human Activities on the Atmosphere. Detecting the Atmospheric Response to the Changing Face of the Earth: A Focus on Human-Caused Regional Climate Forcings, Land-Cover/Land-Use Change, and Data Monitoring, Eos Trans. Am. Geophys. Union, 88(52): 580-580.

Mal, S., Singh, R.B., Schickhoff, U., 2016. Estimating recent glacier changes in Central Himalaya, India, using remote sensing data. In: Climate change, glacier response, and vegetation dynamics in the Himalaya. Springer, Cham. part II. 205-218. http://dx.doi.org/10.1007/978-3-319-28977-9_11.

Mall, R.K., Gupta, A., Singh, R., Singh, R.S., Rathore, L. S., 2006. Water resources and climate change: An Indian perspective. Curr. Sci. 90(12):1610-1626.

Maranan, M., Fink, A. H., Knippertz, P., 2018. Rainfall types over southern West Africa: Objective identification, climatology and synoptic environment. QJR Meteorol. Soc. 144:1628-1648. http://dx.doi.org/10.1002/qj.3345.

May, P. T., Strauch, R. G., 1998. Reducing the effect of ground clutter on wind profiler velocity measurements. J. Atmos. Oceanic Technol. 15: 579–586.

McGill, M. J., Yorks, J. E., Scott, V. S., Kupchock, A. W., Selmer, P. A., 2015. The Cloud-Aerosol Transport System (CATS): A technology demonstration on the International Space Station.

Proc. SPIE 9612. Lidar Remote Sensing for Environmental Monitoring XV. 96120A. http://dx.doi.org/10.1117/12.2190841.

McGrath-Spangler, E. L., Denning, A. S., 2012. Estimates of North American summertime planetary boundary layer depths derived from space-borne lidar. J. Geophys. Res. 117(D15101). http://dx.doi.org/10.1029/ 2012JD017615.

Mehta, M., Singh, R., Singh, A., Singh, N., 2016. Remote Sensing of Environment Recent global aerosol optical depth variations and trends - a comparative study using MODIS and MISR level 3 datasets. Remote Sens. Environ. 181: 137-150. http://dx.doi.org/10.1016/j.rse.2016.04.004.

Melfi, S. H., Sphinhirne, J. D., Chou, S. H., Palm, S. P., 1985. Lidar observations of the vertically organized convection in the planetary boundary layer over the ocean. J. Climate Appl. Meteor. 24: 806–821. https://doi.org/10.1175/1520-0450(1985)024<0806:LOOVOC>2.0.CO;2.

Mendoza, M. M., Ghosh, A., Rai, S. S., 2016. Dynamic triggering of small local earthquakes in the central Himalaya. Geophys. Res. Lett. 43: 9581–9587. http://dx.doi.org/10.1002/2016GL069969.

Messerli, B., Viviroli, D., Weingartner, R., 2004. Mountains of the world: vulnerable water towers for the 21st century. Contribution to the Royal Colloquium on Mountain Areas: A Global Resource. AMBIO Special Report. 13: 29–34.

Michaelides, S., Levizzani, V., Anagnostou, E., Bauer, P., Kasparis, T., Lane, J. E., 2009. Precipitation: measurement remote sensing, climatology and modelling. Atmos. Res. 94: 512–533.

Middleton, N. J., Goudie, A. S., 2001. Saharan dust: Sources and trajectories. Trans. Inst. Br. Geogr. 26: 165 – 181.

Ming, Y., Ramaswamy, V., Persad, G., 2010. Two opposing effects of absorbing aerosols on global-mean precipitation. Geophys. Res. Lett. 37, L13701. http://dx.doi.org/10.1029/2010GL042895.

Minnis, P., et al., 1995. Cloud properties derived from GOES-7 for the spring 1994 ARM Intensive Observing Period using Version 1.0.0 of the ARM Satellite Data Analysis Program. NASA RP 1366, August, 59 pp.

Mironova, I. A., Desorgher, L., Usoskin, I. G., Flückiger, E. O., Bütikofer, R., 2008. Variations of aerosol optical properties during the extreme solar event in January 2005. Geophys. Res. Lett. 35. L18610. http://dx.doi.org/10.1029/2008GL035120.

Mishra, A., 2014. Changing Climate of Uttarakhand, India. J. Geol. Geosci. 3(163). http://dx.doi.org/10.4172/2329-6755.1000163.

Mishra, A. K., Coulibaly, P., 2009. Developments in hydrometric network design: A review. Reviews of Geophysics. 47(RG2001): 1-24. http://dx.doi.org/10.1029/2007RG000243.

Mishra, A. K., Klingmueller, K., Fredj, E., Lelieveld, J., Rudich, Y., Koren, I., 2014. Radiative signature of absorbing aerosol over the eastern Mediterranean basin. Atmos. Chem. Phys. 14: 7213-7231. https://doi.org/10.5194/acp-14-7213-2014.

MoEFCC, 2018. India: Second Biennial Update Report to the United Nations Framework Convention on Climate Change. Ministry of Environment, Forest and Climate Change, Government of India.

Mohan, K., Narayama Rao, D., Narayama Rao, T., Raghavan, S., 2001. Estimation of temperature and humidity from MST radar observation. Ann. Geophys. 19: 855–861.

Monks, P., et al., 2009. Atmospheric composition change global and regional air quality. Atmos. Environ. 43 (33): 5268–5350. http://dx.doi.org/10.1016/j.atmosenv.2009.08.021.

Moorthy, K. K., Sathessh, S. K., Kotamarthi, V. R., 2016. Evolution of aerosol research in India and the RAWEX-GVAX: An overview.CurrentScience. 11(1): 53–75.

Naidu, C. V., Durgalakshmi, K., Muni Krishna, K., Ramalingeswara Rao, S., Satyanarayana, G. C., Lakshminarayana, P., Rao, L. M., 2009. Is summer monsoon rainfall decreasing over India in the global warming era?, J. Geophys. Res. 114, D24108. http://dx.doi.org/10.1029/2008JD011288.

Naja, M., Bhardwaj, P., Singh, N., Kumar, P., Kumar, R., Ojha, N., Sagar, R., Satheesh, S.K., Krishna Moorthy, K., Kotamarthi, V.R., 2016. High-frequency vertical profiling of meteorological parameters using AMF1 facility during RAWEX-GVAX at ARIES, Nainital. Curr. Sci. 111 (1), 132-140.

Natl. Res. Counc., 2008. Earth Observations from Space: The First 50 Years of Scientific Achievements. Washington, DC: Natl. Acad. Press. 142 pp.

New, M., Hume, M., Jones, P., Todd, M., 2001. Precipitation measurements and trends in the twentieth century. Journal of Climatology. 21: 1899-1922. http://dx.doi.org/10.1002/joc.680.

Nichol, J. E., Bilal, M., 2016. Validation of MODIS 3 km Resolution Aerosol Optical Depth Retrievals over Asia. Remote Sens. 8(4): 328. http://dx.doi.org/10.3390/rs8040328.

Noël, S., Bovensmann, H., Burrows, J. P., Frerick, J., Chance, K. V., Goede, A. P. H., 1999. Global atmospheric modeling with SCIAMACHY. Phys. Chem. Earth. 24:427–434.

OECD: The Cost of Air Pollution, 2014. http://dx.doi.org/10.1787/9789264210448-en.

Ojha, N., Naja, M., Singh, K.P., Sarangi, T., Kumar, R., Lal, S., Lawrence, M.G., Butler, T.M., Chandola, H.C., 2012. Variabilities in ozone at a semi-urban site in the Indo-Gangetic Plain region: association with the meteorology and regional processes. J. Geophys. Res. 117, D20301. http://dx.doi.org/10.1029/2012JD017716.

Ojha, N., Naja, M., Sarangi, T., Kumar, R., Bhardwaj, P., Lal, S., Venkataramani, S., Sagar, R., Kumar, A., Chandola, H.C., 2014. On the processes influencing the vertical distribution of ozone over the central Himalayas: Analysis of yearlong ozonesonde observations. Atmos. Environ. 88: 201-211. http://dx.doi.org/10.1016/j.atmosenv.2014.01.031.

Okamoto, H., Sato, K., 2018. Cloud Remote Sensing by Active Sensors: New Perspectives from CloudSat, CALIPSO and EarthCARE. In: Andronache C. (eds) Remote Sensing of Clouds and Precipitation. Springer Remote Sensing/Photogrammetry. Springer, Cham. http://dx.doi.org/ 10.1007/978-3-319-72583-3_8.

Olsen, T. E., Fetzer, E., Hulley, G., Manning, E., Blaisdell, J., Iredell, L., Susskind, J., Warner, J., Wei, Z., Blackwell, W., Maddy, E., 2013. AIRS/AMSU/HSB Version 6 Level 2 Product User Guide. pp. 134.

Omar, A. H., Winker, D. M., Kittaka, C., Vaughan, M. A., Liu, Z. Y., Hu, Y. X., Trepte, C. R., Rogers, R. R., Ferrare, R. A., Lee, K. P., Kuehn, R. E., Hostetler, C. A, 2009. The CALIPSO automated aerosol classification and lidar ratio selection algorithm. J. Atmos. Ocean. Tech. 26: 1994–2014. http://dx.doi.org/10.1175/2009jtecha1231.1, 2009.

O'Neill, N. T., Eck, T. F., Smirnov, A., Holben, B. N., Thulasiraman, S., 2003. Spectral discrimination of coarse and fine mode optical depth. J. Geophys. Res. 108(D17): 4559-4573. http://dx.doi.org/10.1029/2002JD002975.

Ottersten, H., 1969. Atmospheric structure and radar backscattering in clear air. Radio Sci. 4: 1179-1193.

Palm, S. P., Benedetti, A., Spinhirne, J., 2005. Validation of ECMWF global forecast model parameters using GLAS atmospheric channel measurements. Geophys. Res. Lett. 32, L22S09. https://doi.org/10.1029/2005GL023535.

Pant, G.B., Kumar, P.P., Revadekar, J.V., Singh, N., 2018. Climate Change in the Himalayas. Springer. Cham. doi: 10.1007/978-3-319-61654-4.

Pant, P., Hegde, P., Dumka, U.C., Sagar, R., Satheesh, S.K., Moorthy, K.K., Saha, A., Srivastava, M.K., 2006. Aerosol characteristics at a high altitude location in Central Himalayas: optical properties and radiative forcing. J. Geophys. Res. 111. D17206. http://dx.doi.org/10.1029/2005JD006768.

Parkinson, C. L., 2003. Aqua: An Earth-Observing Satellite Mission to Examine Water and other Climate Variables. IEEE Trans. Geosci. Remote Sensing. 41: 173-183.

Parmar, R. S., Welling, M., Andreae, M. O., Helas, G., 2008. Water vapor release from biomass combustion. Atmos. Chem. Phys. 8: 6147-6153. https://doi.org/10.5194/acp-8-6147-2008.

Parrish, D. D., Singh, H. B., Molina, L., Madronich, S., 2011. Air quality progress in North American megacities: A review. Atmos. Environ. 45: 7015–7025. http://dx.doi.org/10.1016/j.atmosenv.2011.09.039.

Penner, J. E., Zhang, S. Y., Chuang, C. C., 2003. Soot and smoke aerosol may not warm climate. J. Geophys. Res. 108. 4657. http://dx.doi.org/10.1029/2003JD003409.

Pope III, C. A., Dockery, D. W., 2006. Health Effects of Fine Particulate Air Pollution: Lines that Connect. J. Air Waste Manage. 56: 709–742. http://dx.doi.org/10.1080/10473289.2006.10464485.

Powell, K.A., Hostetler, C.A., Liu, Z., et al., 2009. CALIPSO lidar calibration algorithms. Part I: nighttime 532-nm parallel channel and 532-nm perpendicular channel. J. Atmos. Oceanic Technol. 26 (10): 2015-2033. http://dx.doi.org/10.1175/2009JTECHA1242.1.

Prakash, S., 2019. Performance assessment of CHIRPS, MSWEP, SM2RAIN-CCI, and TMPA precipitation products across India. Journal of Hydrology. 571: 50-59. http://dx.doi.org/10.1016/j.jhydrol.2019.01.036.

Prasad, A. K., Singh, R. P., 2009. Validation of MODIS Terra, AIRS, NCEP/DOE AMIP-II Reanalysis-2, and AERONET Sun photometer derived integrated precipitable water vapor using ground-based GPS receivers over India. J. Geophys. Res. 114. D05107. http://dx.doi.org/10.1029/ 2008JD011230.

Prigent, C., 2010. Precipitation retrieval from space: An overview. Comptes Rendus Geoscience. 342(4–5): 380–389.

Qian, Y., Long, C.N., Wang, H., Comstock, J.M., McFarlane, S.A., Xie, S., 2012. Evaluation of cloud fraction and its radiative effect simulated by IPCC AR4 global models against ARM surface observations. Atmos. Chem. Phys. 12(4):1785–1810. http://dx.doi.org/10.5194/Acp-12-1785-2012.

Quante, M. 2004. The role of clouds in the climate system. J. Phys. IV France, 121: 61–86. http://dx.doi.org/10.1051/jp4:2004121003.

Rainbird, A.F., 1967. Precipitation—Basic principles of network design. Symposium on Design of Hydrological Networks. WMO IASH Pub. 67, 19–30.

Rajeevan, M., Bhate, J., Kale, J. D., Lal, B., 2006. High resolution daily gridded rainfall data for the Indian region: Analysis of break and active monsoon spells. Current Science. 91(3): 296-306. http://www.jstor.org/stable/24094135.

Rajeevan, M., Rohini, P., Kumar, K. N., Srinivasan, J., Unnikrishnan, C. K., 2013. A study of vertical cloud structure of the Indian summer monsoon using CloudSat data. Clim. Dyn, 40: 637-650. http://dx.doi.org/10.1007/s00382-012-1374-4.

Ram, K., Singh, S., Sarin, M. M., Srivastava, A. K., Tripathi, S. N., 2016. Variability in aerosol optical properties over an urban site, kanpur, in the indo-gangetic plain: a case study of haze and dust events. Atmos. Res. 174–175: 52–61.

Ramachandran, S., Kedia, S., Srivastava, R., 2012. Aerosol optical depth trends over different regions of India. Atmos. Environ. 49: 338–347.

Ramachandran, S., Kedia, S., 2013. Aerosol Optical Properties over South Asia from Ground-Based Observations and Remote Sensing: A Review. Climate. 1: 84-119. http://dx.doi.org/10.3390/cli1030084.

Ramachandran, S., Kedia, S., 2013a. Aerosol, clouds and rainfall: interannual and regional variations over India. Clim. Dynam. 40: 1591–1610.

Ramanathan, V. et al., 1989. Cloud-radiative forcing and climate: Results from the earth radiation budget experiment. Science, 243(4887): 57–63, http://dx.doi.org/10.1126/science.243.4887.57.

Ramanathan, V., Ramana, M.V., 2005. Persistent, widespread, and strongly absorbing haze over the Himalayan foothills and the Indo-Gangetic Plains. Pure Appl. Geophys. 162: 1609–1626.

Rao, D. N., Kishore, P., Reddy, K. K., 1996. Refractivity turbulence structure constant (C_n^2) measurements using Indian MST radar. Indian Journal of Radio & Space Physics. 25: 237-244.

Rao, D. N., Ratnam, M. V., Rao, T. N., Rao, S. V., 2001. Seasonal variation of vertical eddy diffusivity in the troposphere, lower stratosphere and mesosphere over a tropical station. Ann. Geophys. 19: 975–984.

Redemann, J., et al., 2012. The comparison of MODIS-Aqua (C5) and CALIOP (V2 & V3) aerosol optical depth. Atmos. Chem. Phys. 12: 3025–3043. http://dx.doi.org/10.5194/acp-12-3025-2012.

Rees, D., Bernett, J. J., Labitzke, K., 1990. CIRA 1986, COSPAR International Reference Atmosphere, Part II: Middle Atmosphere models. Adv. Space Res. 10(12).

Remer, L. A., et al., 2002. Validation of MODIS aerosol retrieval over ocean. Geophys. Res. Lett. 29(12): 2-5. http://dx.doi.org/10.1029/2001GL013204.

Remer, L.A., et al., 2005. The MODIS aerosol algorithm, products, and validation. Journal of the Atmospheric Sciences 62: 947-973. http://dx.doi.org/10.1175/JAS3385.1.

Remer, L. A., Mattoo, S., Levy, R. C., Munchak, L. A., 2013. MODIS 3 km aerosol product: Algorithm and global perspective. Atmos. Meas. Tech. 6(7): 1829–1844. http://dx.doi.org/10.5194/amt-6-1829-2013.

Ren, J., Jing, Z., Pu, J., Qin, X, 2006. Glaciers variations and climate change in the central Himalaya over the past few decades. Ann. Glaciol. 43: 218–222. https://doi.org/10.3189/172756406781812230.

Revathy, K., Nair, S. R. P., Murthy, B. V. K., 1996. Deduction of Temperature profile from MST radar observations of vertical wind. Geophy Res. Lett. 23: 285–288.

Richardson, S. D., Reynolds, J. M., 2000. An overview of glacial hazards in the Himalayas. Quat. Int. 65: 31–47.

Robinson, J. W., 1974. Remote sensing devices for air pollution control. Sci. Total Environ. 3(2): 169-77.

Rodell, M., Houser, P.R., Jambor, U., Gottschalck, J., Mitchell, K., Meng, C., Arsenault, K., Cosgrove, B., Radakovich, J., Bosilovich, M., Entin, J.K., Walker, J.P., Lohmann, D., Toll, D., 2004. The Global Land Data Assimilation System. Bull. Amer. Meteor. Soc. 85: 381–394. https://doi.org/10.1175/BAMS-85-3-381.

Rodríguez-Iturbe, I., Mejía, J. M., 1974. The design of rainfall networks in time and space. Water Resources Research. 10(4): 713– 728. https://doi.org/10.1029/WR010i004p00713.

Roguin, A., 2002. Christian Johann Doppler: the man behind the effect. British Journal of Radiology. 75(895): 615–619.

Rolt, L. T. C., 1966. The Aeronauts: A History of Ballooning - 1783-1903. Walker & Co. New York.

Rosenfeld, D., Rudich, Y., Lahav, R., 2001. Desert dust suppressing precipitation: A possible desertification feedback loop. Proc. Natl. Acad. Sci. USA. 98: 5975–5980. https://doi.org/10.1073/pnas.101122798.

Ross, R. S., Krishnamurti, T. N., Pattnaik, S., Pai, D. S., 2018. Decadal surface temperature trends in India based on a new high-resolution data set. Sci. Rep. 8(7452): 1-10.

Rossow, W. B., Schiffer R. A., 1991. ISCCP cloud data products, Bull. Am. Meteorol. Soc. 71: 2–20.

Röttger, J., 1986. Determination of Brunt-Väisäla frequency from vertical velocity spectra. MAP Handbook. 20: 168–172.

Röttger, J., Larsen, M. F., 1990. UHF/VHF radar techniques for atmospheric research and wind profile applications, Radar in Meteorology, D. Atlas, Ed., Amer. Meteor. Soc., 235-281.

Roy, S. S., and Roy, S. S., 2011. Regional variability of convection over northern India during the pre-monsoon season. Theoretical and Applied Climatology, 103(1): 145-158. https://doi.org/10.1007/s00704-010-0289-4.

Rudari, R., D. Entekhabi, and G. Roth, 2004. Terrain and Multiple-Scale Interactions as Factors in Generating Extreme Precipitation Events. *J. Hydrometeor.*, 5: 390–404. https://doi.org/10.1175/1525-7541(2004)005<0390:TAMIAF>2.0.CO;2.

Rupakheti, D., Adhikary, B., Praveen, P.S., Rupakheti, M., Kang, S., Mahata, K.S., Naja, M., Zhang, Q., Panday, A.K., Lawrence, M.G., 2017. Pre-monsoon air quality over Lumbini, a world heritage site along the Himalayan foothills. Atmospheric Chemistry and Physics. 17: 11041- 11063.

Rupakheti, D., Kang, S., Rupakheti, M., Cong, Z., Tripathee, L., Panday, A., Holben, B. N., 2018. Observation of optical properties and sources of aerosols at Buddha's birthplace, Lumbini, Nepal. Environmental Science and Pollution Research. http://dx.doi.org/10.1007/s11356-018-1713-z.

Ruzer, L. S., Harley, N. H. (Eds.), 2004. Aerosols Handbook: Measurement, Dosimetry, and Health Effects. CRC Press, Boca Raton. FL 33487-2742. 728 pp.

Sabins, F. F., 2007. Remote sensing. Principles and interpretation, 3rd ed., xii, 494, Waveland Press, Long Grove, III.

Sagar, R., Kumar, B., Dumka, U.C., Moorthy, K.K., Pant, P., 2004. Characteristics of aerosol spectral optical depths over Manora Peak: a high-altitude station in the central Himalayas. J. Geophys. Res. 109, D06207. http://dx.doi.org/10.1029/2003JD003954.

Sagar, R., Dumka, U. C., Naja, M., Singh, N., Phanikumar, D. V., 2015. ARIES, Nainital: a strategically important location for climate change studies in the Central Gangetic Himalayan region. Current Science. 109(4): 703-715.

Saha, K., 2008. The Earth's Atmosphere: Its Physics and Dynamics. Springer-Verlag, Berlin, Germany.

Sarangi, T., Naja, M., Ojha, N., Kumar, R., Lal, S., Venkataramani, S., Kumar, A., Sagar, R., Chandola, H.C., 2014. First simultaneous measurements of ozone, CO, and NOy at a high-altitude regional representative site in the central Himalayas. J. Geophys. Res. Atmos. 119: 1592–1611. http://dx.doi.org/10.1002/2013JD020631.

Sasano, Y., Nakane, H., 1984. Significance of the Extinction/Backscatter Ratio and the Boundary Value Term in the Solution for the Two-Component Lidar Equation. App. Opt. 23: 11-13. http://dx.doi.org/10.1364/AO.23.0011_1.

Sassen, K., Wang, Z, 2008. Classifying clouds around the globe with the CloudSat radar: 1-year of results. Geophysical Research Letters 35(L04805): 1-5. http://dx.doi.org/10.1029/2007GL032591.

Satheesh, S.K., Suresh Babu, S., Padmakumari, B., Pandithurai, G., Soni, V.K., 2017. Variability of Atmospheric Aerosols Over India. in: Rajeevan M., Nayak S. (eds) Observed Climate Variability and Change over the Indian Region. Springer Geology. Springer. Singapore.

Satheesan, K., Murthy, B. V. K., 2002. Turbulence parameters in the tropical troposphere and lower stratosphere. J. Gephys. Res. 107(D1): 1–13.

Satheesan, K., Murthy, B. V. K, 2005. A study of tropical tropopause using MST radar. Ann. Geophys. 23: 2441 – 2448.

Sato, T., Woodman, R. F., 1982. Spectral parameter estimation of CAT radar echoes in the presence of fading clutter. Radio Sci. 17: 817–826.

Sauvageot, H., 1992. Basic concepts of radar. Radar meteorology, Artech House, Norwood, MA, USA. 1-68.

Savtchenko, A., Ouzounov, D., Ahmad, S., Acker, J., Leptoukh, G., Koziana, J., Nickless, D., 2004. Terra and Aqua MODIS products available from NASA GES DAAC. Advances in Space Research. 34(4): 710-714. http://dx.doi.org/10.1016/j.asr.2004.03.012.

Sayer, A. M., Hsu, N. C., Bettenhausen, C., Jeong, M.-J., 2013. Validation and uncertainty estimates for MODIS Collection 6 "Deep Blue" aerosol data. J. Geophys. Res. Atmos. 118(14): 7864–7872. http://dx.doi.org/10.1002/jgrd.50600.

Schepanski, K., 2018. Transport of Mineral Dust and Its Impact on Climate. Geosciences. 8: 1-19.

Schiffer, R. A., Rossow, W. B., 1983. The International Satellite Cloud Climatology Project (ISCCP): The first project of the World Climate Research Programme. B. Am. Meteorol. Soc. 64: 779–784.

Schmid, J., 2000. The SEVIRI Instrument. Proceedings of the 2000 EUMETSAT Meteorological Satellite, 13–32.

Schulz, M., et al., 2006. Radiative forcing by aerosols as derived from the AeroCom present-day and pre-industrial simulations. Atmos. Chem. Phys. 6(12):5225–5246.

Schumacher, C., Houze, R.A., 2003. Stratiform Rain in the Tropics as Seen by the TRMM Precipitation Radar. J. Climate. 16: 1739–1756. https://doi.org/10.1175/1520-0442(2003)016<1739:SRITTA>2.0.CO;2.

Schuster, G., Dubovik, O., Holben, B. N., 2006. Angstrom exponent and bimodal aerosol size distributions. J. Geophys. Res. 111(D07207). http://dx.doi.org/10.1029/2005JD006328.

Seibert, P., Beyrich, F., Gryning, S.-E., Joffre, S., Rasmussen, A., Tercier, P., 2000. Review and intercomparison of operational methods for the determination of the mixing height. Atmos. Environ. 34(7): 1001–1027. http://dx.doi.org/10.1016/S1352-2310(99)00349-0.

Seidel, D. J., Ao, C. O., Li. K., 2010. Estimating climatological planetary boundary layer heights from radiosonde observations: Comparison of methods and uncertainty analysis. J. Geophys. Res. 115(D16). D16113. http://dx.doi.org/10.1029/2009JD013680.

Seinfeld, J.H., Pandis, S.N., 2012. Atmospheric Chemistry and Physics from Air Pollution to Climate Change. Wiley, New York.

Shao, Y., Ishizuka, M., Mikami, M., Leys, J. F., 2011. Parameterization of size-resolved dust emission and validation with measurements. J. Geophys. Res. 116(D08203). http://dx.doi.org/10.1029/2010JD014527.

Shaw, N., 1926. Meteorology in History. Manual of Meteorology. Cambridge (Univ. Pres). London.

Shrestha, D., Singh, P., Nakamura, K., 2012. Spatiotemporal variation of rainfall over the central Himalayan region revealed by TRMM Precipitation Radar. J. Geophys. Res. 117. D22106. http://dx.doi.org/10.1029/2012JD018140.

Simmons, A. J., Poli, P., Dee, D. P., Berrisford, P., Hersbach, H., Kobayashi, S., Peubey, C., 2014. Estimating low-frequency variability and trends in atmospheric temperature using ERA-Interim. Q.J.R. Meteorol. Soc. 140: 329-353. http://dx.doi.org/10.1002/qj.2317.

Singh, C. P., Panigrahy, S., 2011. Characterisation of residue burning from agricultural system in India using space based observations. J. Indian Soc. Remote Sens. 39(3): 423–429.

Singh, N., Joshi, R. R., Chun, H.-Y., Pant, G. B., Damle, S. H., Vashishtha, R. D., 2008. Seasonal, annual and inter-annual features of turbulence parameters over the tropical station Pune (18°32' N, 73°51'E) observed with UHF wind profiler. Ann. Geophys. 26: 3677–3692. http://dx.doi.org/10.5194/angeo-26-3677-2008.

Singh, N., Solanki, R., Ojha, N., Janssen, R. H. H., Pozzer, A., Dhaka, S. K., 2016. Boundary layer evolution over the central Himalayas from radio wind profiler and model simulations. Atmos. Chem. Phys. 16: 10559-10572. http://dx.doi.org/10.5194/acp-16-10559-2016.

Singh, R. B. and Mal, S., 2014. Trends and variability of monsoon and other rainfall seasons in Western Himalaya, India. Atmos. Sci. Lett., 15: 218-226. doi:10.1002/asl2.494.

Singh, V. P., Singh, P., Haritashya, U. K., 2011. Encyclopedia of snow, ice and glaciers. Springer. Dordrecht. The Netherlands. 1240 pp.

Sivakumar, B., 2001. Rainfall dynamics at different temporal scales: A chaotic perspective. Hydrol. Earth Syst. Sci. 5(4):645–651.

Skolnik, M., 2008. Radar Handbook, third ed., McGraw-Hill, New York.

Smith, W. L., Platt, C. M. R., 1978. Comparison of satellite-deduced cloud heights with indications from radiosonde and ground-based laser measurements. J. Appl. Meteor., 17: 1796–1802.

Smirnov, A., Holben, B., Eck, T., Dubovik, O., Slutsker, I., 2000. Cloud-screening and quality control algorithms for the AERONET database. Remote Sens. Environ. 73: 337-349.

Solanki, R., Singh, N., Pant, P., Dumka, U.C., Bhavani Kumar, Y., Srivastava, A.K., Bist, S., Chandola, H.C., 2013. Detection of long range transport of aerosols with elevated layers over high altitude station in the central Himalayas: a case study on 22 and 24 March 2012 at ARIES, Nainital. Indian J. Radio Space Phys. 42(5): 332-339.

Solanki, R., Singh, N., 2014. LiDAR observations of the vertical distribution of aerosols in free troposphere: Comparison with CALIPSO level-2 data over the central Himalayas. Atmos. Environ. 99: 227–238.

Solanki, R., Singh, N., Kiran Kumar, N.V.P., Rajeev, K., Dhaka, S. K., 2016. Time Variability of Surface-Layer Characteristics over a Mountain Ridge in the Central Himalayas during the Spring Season. Boundary-Layer Meteorol. 158(3): 453–471. http://dx.doi.org/10.1007/s10546-015-0098-5.

Sreekanth, V., 2016. Discussion on linear long-term trends in aerosol and cloud properties over India and its surrounding waters. Advances Space Res. 57: 2104–2114.

Srivastava, A.K., Singh, S., Tiwari, S., Bisht, D.S., 2012. Contribution of anthropogenic aerosols in direct radiative forcing and atmospheric heating rate over Delhi in the IndoGangatic basin. Environ. Sci. Pollut. Res. 19: 1144–1158.

Srivastava, A.K., Bisht, D.S., Ram, K., Tiwari, S., Srivastava, M., 2014. Characterization of carbonaceous aerosols over Delhi in Ganga basin: seasonal variability and possible sources. Environ. Sci. Pollut. Res. 21: 8610–8619. http://dx.doi.org/10.1007/s11356- 014-2660-y.

Standford, M. C. W., 1967. Optical radar performance in the atmospheric scattering. J. Atmos. Terr. Phys. 29: 1651-1656.

Steen, R. A., 1992. Ionospheric Research by Radar. RadCom. Radio Society of Great Britain. 68(8): 42-44. ISSN 1367-1499.

Stein, A.F., Draxler, R.R., Rolph, G.D., Stunder, B.J.B., Cohen, M.D., Ngan, 2015. NOAA's HYSPLIT atmospheric transport and dispersion modeling system. Bull. Amer. Meteor. Soc. 96: 2059-2077. http://dx.doi.org/10.1175/BAMS-D-14-00110.1.

Stephens, G. L., et al., 2002. The CloudSat mission and the A-Train: A new dimension of space-based observations of clouds and precipitation. Bull. Amer. Meteor. Soc. 83: 1771–1790.

Stephens, G. L., 2005. Cloud Feedbacks in the Climate System: A Critical Review. J. Climate. 18(2): 237–273. http://dx.doi.org/10.1175/JCLI-3243.1.

Stephens, G. L., Kummerow, C.D., 2007. The Remote Sensing of Clouds and Precipitation from Space: A Review. J. Atmos. Sci., 64(11): 3742–3765. http://dx.doi.org/10.1175/2006JAS2375.1.

Stewart, I. T., 2009. Changes in snowpack and snowmelt runoff for key mountain regions. Hydrol. Process., 23: 78-94. doi:10.1002/hyp.7128.

Stowe, L. L., Carey, R. M., Pellegrino, P. P., 1992. Monitoring the Mt. Pinatubo aerosol layer with NOAA/11 AVHRR data. Geophys. Res. Lett. 19: 159–162.

Strauch, R. G., Merritt, D. A., Moran, K. P., Earnshaw, K. B., van de Kamp, J. D., 1984. The Colorado wind-profiling network. J. Atmos. Oceanic Technol. 1: 37–49.

Streets, D.G., Yarber, K.F., Woo, J.H., Carmichael, G.R., 2003. Biomass Burning in Asia: Annual and Seasonal Estimates and Atmospheric Emissions. Global Biogeochem. Cycles 17: 1099. http://dx.doi.org/10.1029/2003GB002040.

Su, T., Li, J., Li, C., Xiang, P., Lau, A. K.-H., Guo, J., Yang, D., Miao, Y., 2017. An intercomparison of long-term planetary boundary layer heights retrieved from CALIPSO, ground-based lidar, and radiosonde measurements over Hong Kong. J. Geophys. Res. Atmos. 122: 3929–3943. http://dx.doi.org/10.1002/2016JD025937.

Sudhira, H. S., Gururaja, K. V., 2012. Population crunch in India: is it urban or still rural? Curr Sci. 103:37–40.

Sun, Q., Miao, C., Duan, Q., Ashouri, H., Sorooshian, S., Hsu, K-L., 2018. A review of global precipitation datasets: data sources, estimation, and intercomparisons. Rev Geophys. 56: 79-107. http://dx.doi.org/10.1002/ 2017RG000574.

Swanson, P.N., Harris, W.M., Johnston, E.J., Soltis, F.S., 1980. The TIROS-N Microwave Sounder Unit. MTT-S International Microwave Symposium Digest. 80: 123-125.

Tan, M.L., Ibrahim, A., Duan, Z., Cracknell, A.P., Chaplot, V., 2015. Evaluation of six high resolution satellite and ground-based precipitation products over Malaysia. Remote Sens. 7: 1504–1528.

Tanelli, S., Durden, S. L., Im, E., Pak, K. S., et al.. 2008. CloudSat's cloud profiling radar after two years in orbit: Performance, calibration, and processing. IEEE Transactions on Geoscience and Remote Sensing 46(11): 3560–3573. http://dx.doi.org/10.1109/TGRS.2008.2002030.

Tapiador, F. J., Navarro, A., Levizzani, V., García-Ortega, E., Huffman, G. J., Kidd, C., et al. 2017. Global Precipitation Measurements for Validating Climate Models. Atmospheric Research 197: 1–20. http://dx.doi.org/10.1016/j.atmosres.2017.06.021.

Tegen, I., Fung, I., 1994. Modeling of mineral dust in the atmosphere: Sources, transport, and optical thickness. J. Geophys. Res. 99(D11): 22897–22914. http://dx.doi.org/10.1029/94JD01928.

Thayyen, R.J., Dimri, A.P., Kumar, P., Agnihotri, G., 2013. Study of cloudburst and flash floods around Leh, India during August 4–6, 2010. Nat. Hazards. 65 (3): 2175–2204. http://dx.doi.org/10.1007/s11069–012-0464-2.

Tilstra, L.G., de Graaf, M., Tuinder, O.N.E., van der A, R.J., Stammes, P., 2011. Studying trends in aerosol presence using the Absorbing Aerosol Index derived from GOME-1, SCIAMACHY, and GOME-2. EUMETSAT Meteorological Satellite Conference. Oslo. Norway. P.59.

Tilstra, L. G., de Graaf, M., Tuinder, O.N.E., van der A, R. J., Stammes, P., 2013. Monitoring Aerosol Presence Over A 15- Year Period Using The Absorbing Aerosol Index Measured By GOME-1 Sciamachy, and GOME-2. ESA Living Planet Symposium. ESA SP-722. 2-13. p.364.

Tiwari, P. C., Joshi, B., 2016. Rapid urban growth in mountainous regions: The case of Nainital, India. Urbanization and Global Environment Change (UGEC) Viewpoints. Global Institute of Sustainability. Arizona. USA.

Torres, O., et al., 2002a. A long-term record of aerosol optical depth from TOMS observations and comparison to AERONET measurements. J. Atmos. Sci. 59:398–413.

Torres, O., Decae, R., Veefkind, P., de Leeuw, G., 2002b. OMI aerosol retrieval algorithm. In: Stammes, P., editor. OMI algorithm theoretical basis document, clouds, aerosols and surface UV irradiance. Utrecht: Royal Netherlands Meteorological Institute. 3:47–71.

Torres, O., Ahn, C., Chen, Z., 2013. Improvements to the OMI near UV Aerosol Algorithm using A-train CALIOP and AIRS observations. Atmos. Meas. Tech. 6: 5621–5652. http://dx.doi. org/10.5194/amtd-6-5621-2013.

Trenberth, K.E., et al., 2007: Observations: Surface and Atmospheric Climate Change. In: Climate Change 2007: The Physical Science Basis. Contribution of Working Group I to the Fourth Assessment Report of the Intergovernmental Panel on Climate Change. Cambridge University Press, Cambridge, United Kingdom and New York, NY, USA.

Tripathi, S.N., Dey, S., Tare, V., Satheesh, S.K., 2005. Aerosol black carbon radiative forcing at an industrial city in northern India. Geophys. Res. Lett. 32. L08802. http://dx.doi. org/10.1029/2005GL022515.

Tsang, L., Kong, J.A., Shin, R.T., 1985. Theory of Microwave Remote Sensing, Wiley Interscience, New York.

UCOST and USERC. Uttarakhand State Council for Science and Technology & Uttarakhand Science Education and Research Centre, 2012. Uttarakhand: state of environment report

(SOER). Dobhal, R. (Eds.). M/s Bishen Singh Mahendra Pal Singh. Dehradun. India. Online: http://www.ucost.in/document/publication/books/env-books.pdf.

Valdiya, K. S., 2008. Facing the Hazards: Earthquakes & Landslides. Gyanodaya Prakashan. Nainital. 1-87.

VanZandt, T. E., Green, J. L, Gage K. S., Clark, W. L., 1978. Vertical profiles of refractivity turbulence structure constant. Comparison of observations by the Sunset radar with a new theoretical model. Radio Sci. 13: 819-829.

Vaughan, M., et al., 2016. Cloud – Aerosol LIDAR Infrared Pathfinder Satellite Observations (CALIPSO), Data Management System, Data Products Catalog, Document No: PC-SCI-503, Release 4.10. NASA Langley Research Center, Hampton, Virginia, USA. Online: https://www-calipso.larc.nasa.gov/products/CALIPSO_DPC_Rev4x10.pdf.

Veefkind, J.P., de Leeuw, G., Stammes, P., Koelemeijer, R. B. A., 2000. Regional distribution of aerosol over land, derived from ATSR-2 and GOME. Remote Sens Environ. 74:377–86.

Verma, S., Prakash, D., Ricaud, P., Payra, S., Attié, J., Soni, M., 2015. A New Classification of Aerosol Sources and Types as Measured over Jaipur, India. Aerosol Air Qual. Res. 15: 985-993.

Verma, S., Prakash, D., Srivastava, A.K., Payra, S., 2017. Radiative forcing estimation of aerosols at an urban site near the thar desert using ground-based remote sensing measurements. Aerosol Air Qual. Res. 17: 1294–1304.

Vijayakumar, K., Safai, P.D., Devara, P.C.S., Rao, S. V. B., Jayasankar, C. K., 2016. Effects of agriculture crop residue burning on aerosol properties and long-range transport over northern India: A study using satellite data and model simulations. Atmos. Res. 178–179. pp. 155-163. http://dx.doi.org/10.1016/j.atmosres.2016.04.003.

Vincent, R. A., Reid, I. M., 1983. HF Doppler measurements of mesospheric gravity wave momentum fluxes. J. Atmos. Sci. 40: 1321–1333.

Vinnikov, K., Graisman, P. Y., Lugina, K. M., 1990. Empirical data on contemporary global climatic changes (Temperature and precipitation). J Climate 3: 662–677.

Viviroli, D., Durr, H. H., Messerli, B., Meybeck, M., Weingartner, R., 2007. Mountains of the world – water towers for humanity: typology, mapping and global significance. Water Resour. Res. 43. W07447. http://dx.doi.org/10.1029/2006WR005653.

Viviroli, D., Archer, D. R., Buytaert, W., Fowler, H. J., Greenwood, G. B., Hamlet, A. F., Huang, Y., Koboltschnig, G., Litaor, M. I., López-Moreno, J. I., Lorentz, S., Schädler, B., Schreier, H.,

Schwaiger, K., Vuille, M., Woods, R, 2011. Climate change and mountain water resources: overview and recommendations for research, management and policy. Hydrol. Earth Syst. Sci. 15: 471-504. https://doi.org/10.5194/hess-15-471-2011.

Wallace, J. M., Hobbs, P. V., 2006. Atmospheric Science: An Introductory Survey. Academic Press, San Diego, second ed. http://dx.doi.org/10.1016/B978-0-12-732951-2.50001-6.

Wang, C., 2013. Impact of anthropogenic absorbing aerosols on clouds and precipitation: a review of recent progresses. Atmos. Res. 122, 237–249.

Wang, M., Bailey, S., McClain, C.R., 2000. SeaWiFS provides unique global aerosol optical property data. EOS Trans. Am. Geophys Union. 81:197.

Wang, S., Fang, L., Gu, X., Yu, T., Gao, J., 2011. Comparison of aerosol optical properties from Beijing and Kanpur. Atmos. Environ., 45(39): 7406–7414. http://dx.doi.org/10.1016/j.atmosenv.2011.06.055.

Wang, Y., et al., 2004. Regional climate modeling: progress, challenges, and prospects. J. Meteorol. Soc., Japan. 82: 1599–1628. http://dx.doi.org/10.2151/jmsj.82.1599.

Wang, Z., Sassen, K., 2001. Cloud Type and Macrophysical Property Retrieval Using Multiple Remote Sensors. J. Appl. Meteor. 40: 1665–1682. http://dx.doi.org/10.1175/1520-0450(2001)040<1665:CTAMPR>2.0.CO;2.

Wang, Z., et al., 2018. Cloud-Base Height Derived from a Ground-Based Infrared Sensor and a Comparison with a Collocated Cloud Radar. J. Atmos. Oceanic Technol., 35(4): 689–704. http://dx.doi.org/10.1175/JTECH-D-17-0107.1.

Washington, R., Todd, M., Middleton, N. J., Goudie, A. S., 2003. Duststorm source areas determined by the Total Ozone Monitoring Spectrometer and surface observations. Ann. Assoc. Am. Geogr. 93(2): 297 – 313.

Weber, B.L., Wuertz, D.B., 1990. Comparison of Rawinsonde and Wind Profiler Radar Measurements, J. Atm.Oceanic Technol., **7:** 157-174.

Welton, E.J., et al., 2000. Ground-based Lidar Measurements of Aerosols During ACE-2: Instrument Description, Results, and Comparisons with other Groundbased and Airborne Measurements. Tellus B. 52: 635-650.

Whitby, K., 1978. The physical characteristics of sulfur aerosols. Atmos. Environ. 12: 135–159.

White, R.M., 1979. The World Climate Conference: Report by the Conference Chairman. WMO Bull. 28(3): 177-178.

Wielicki, B.A., Coakley, J.A., 1981. Cloud Retrieval Using Infrared Sounder Data: Error Analysis. J. Appl. Meteor., 20: 157–169. https://doi.org/10.1175/1520-0450(1981)020<0157:CRUISD>2.0.CO;2.

Wierenga, R.D., Parini, J., 2005. InterMet 403 MHz Radiosonde System.

Wiscombe, W.J., Warren, S.G., 1980. A Model for the Spectral Albedo of Snow. I: Pure Snow. J. Atmos. Sci. 37: 2712–2733.

Winker, D. M., McCormick, M. P., Couch, R., 1996. An overview of LITE: NASA's Lidar In-space Technology Experiment, Proc. IEEE, 84:164– 180.

Winker, D. M., Pelon, J., McCormick, M. P., 2002. The CALIPSO mission: Spaceborne lidar for observation of aerosols and clouds, Proc. SPIE Int. Soc. Opt. Eng., 4893:1–11.

Winker, D.M., Vaughan, M.A., Omar, A., Hu, Y., Powell, K.A., Liu, Z., Hunt, W.H., Young, S.A., 2009. Overview of the CALIPSO mission and CALIOP data processing algorithms. J. Oceanogr. Atmos. Meas. 26(11): 2310–2323. http://dx.doi.org/10.1175/2009JTECHA1281.1.

Winker, D.M., et al., 2010. The CALIPSO mission: a global 3D view of aerosols and clouds. Bull. Amer. Meteor. Soc. 91(9): 1211–1229. http://dx.doi.org/10.1175/2010BAMS3009.1.

WMO, 1956. International Cloud Atlas: abridged atlas. WMO. Geneva.

WMO, 1979. Proceedings of the World Climate Conference. Geneva. February 1979. WMO-No. 537.

WMO, 1987. Tenth World Meteorological Congress: Abridged Final Report with Resolutions. Geneva.

Woodman, R. F., Guillen, A., 1974. Radar Observations of Winds and Turbulence in the Stratosphere and Mesosphere, J. Atmos. Sci., 31, 493-505.

Woodman, R. F., 1983. Spectral Moment Estimation in MST Radars. Handbook for Middle Atmosphere Program. 9: 548-562.

Wu, G., Liu, Y., He, B., Bao, Q., Duan, A., Jin, F. F., 2012. Thermal controls on the Asian summer monsoon. Scientific reports 2: 404. http://dx.doi.org/10.1038/srep00404.

Xu, C., Ma, Y. M., Panday, A., Cong, Z. Y., Yang, K., Zhu, Z. K., Wang, J. M., Amatya, P. M., Zhao, L., 2014. Similarities and differences of aerosol optical properties between southern and northern sides of the Himalayas, Atmos. Chem. Phys. 14: 3133–3149. http://dx.doi.org/10.5194/acp-14-3133-2014.

Xu, J., Grumbine, R., Shrestha, A., Eriksson, M., Yang, X., Wang, Y., Wilkes, A., 2009. The melting Himalayas: cascading effects of climate change on water, biodiversity, and livelihoods. Conservation Biology. 23(3): 520–530.

Xu, J. et al., 2010. A 108.83-m ice-core record of atmospheric dust deposition at Mt. Qomolangma (Everest), Central Himalaya. Quatern. Res. 73 (1): 33–38. http://dx.doi.org/10.1016/j.yqres.2009.09.005.

Yilmaz, K. K., Hogue, T. S., Hsu, K., Sorooshian, S., Gupta, H. V., Wagener, T., 2005. Intercomparison of Rain Gauge, Radar, and Satellite-Based Precipitation Estimates with Emphasis on Hydrologic Forecasting. Journal of Hydrometeorology. 6: 497–517. http://dx.doi.org/10.1175/JHM431.1.

Young, S. A., Vaughan, M. A., 2009. The retrieval of profiles of particulate extinction from Cloud-Aerosol Lidar Infrared Pathfinder Satellite Observations (CALIPSO) data: Algorithm description. J. Atmos. Oceanic Technol. 26: 1105–1119. http://dx.doi.org/10.1175/2008JTECHA1221.1.

Yu, H., Kaufman, Y.J., Chin, M., Feingold, G., Remer, L.A., et al., 2006. A review of measurement-based assessments of the aerosol direct radiative effect and forcing. Atmos. Chem. Phys. 6(3):613–666.

Zhang, T., Wu, D., 2016. Differences between attenuated backscatters obtained from CALIOP version 3 and latest version 4 products for clouds and aerosols. Laser & Optoelectronics Progress. 53.

Zhao, Z.-C., Luo, Y., Huang, J.-B., 2013. A review on evaluation methods of climate modeling. Adv. Clim. Change Res. 4(3): 137-144. http://dx.doi.org/10.3724/SP.J.1248.2013.137.

Zhu, Z., Wang, S., Woodcock, C.E., 2015. Improvement and expansion of the Fmask algorithm: cloud, cloud shadow, and snow detection for Landsats 4-7, 8, and Sentinel 2 images. Remote Sens. Environ. 159: 269–277.

Zillman, J. W., 2009. A history of climate activities. WMO Bulletin. 58(3): 141-150.

Zwally, H. J., et al., 2002. ICESat's laser measurements of polar ice, atmosphere, ocean, and land. J. Geodyn. 34:405– 445.

ANNEXURES

ANNEXURE-1

STATEMENT OF CO-AUTHORS' PERMISSIONS

I, *Ashish Kumar*, committed that all co-authors have granted their permissions for the usage of the following publications in this thesis:

1. **Ashish Kumar**, Narendra Singh, Anshumali, and Raman Solanki, 'Evaluation and utilization of MODIS and CALIPSO aerosol retrievals over a complex terrain in Himalaya', *Remote Sensing of Environment*, vol. 206, pp. 139-155, 2018. doi: 10.1016/j.rse.2017.12.019.
2. **Ashish Kumar**, Narendra Singh, and Anshumali Singh, 'Observations on the distribution of clouds over northern India using joint CloudSat and CALIPSO measurements', *Remote Sensing Letters*, vol. 10(6), pp. 590-597, 2019. doi: 10.1080/2150704X.2019.1587198.
3. **Ashish Kumar**, Narendra Singh, and Anshumali Singh, 'Signal analysis for ground based LiDAR', *Research Journal of Engineering Sciences*, vol. 8(2), pp. 17-22, 2019.
4. Narendra Singh, **Ashish Kumar,** Anshumali, C. Prakash, and C. P. Pandey, 'Study on the satellite and ground based aerosol measurements over Himalayan region', *URSI Asia Pacific Radio Science Conference* 2019, New Delhi, India, 09 - 15 March 2019. doi: 10.23919/URSIAP-RASC.2019.8738690.
5. **Ashish Kumar,** Narendra Singh, and Anshumali, 'Study on cloud types distribution over northern India using raDAR-liDAR (DARDAR)', *URSI Asia Pacific Radio Science Conference* 2019, New Delhi, India, 09 - 15 March 2019. doi: 10.23919/URSIAP-RASC.2019.8738218.

LIST OF PUBLICATIONS

List of Publications

Remote Sensing of Environment 206 (2018) 139–155

Contents lists available at ScienceDirect

Remote Sensing of Environment

journal homepage: www.elsevier.com/locate/rse

Evaluation and utilization of MODIS and CALIPSO aerosol retrievals over a complex terrain in Himalaya

Ashish Kumar[a,b,*], Narendra Singh[a], Anshumali[b], Raman Solanki[c]

[a] Aryabhatta Research Institute of Observational Sciences (ARIES), Manora peak, Nainital, India
[b] Indian Institute of Technology (Indian School of Mines), Dhanbad, India
[c] National Astronomical Research Institute of Thailand (NARIT), Chiang Mai, Thailand

ARTICLE INFO

Keywords:
Aerosols
CALIPSO
AOD
AERONET
MODIS
LiDAR
LR
Radiosonde
Dust
Smoke

ABSTRACT

The study elucidate upon the evaluation of satellite retrievals with ground based aerosol optical depth (AOD) measurements, their utilization in LiDAR ratio (LR) estimation, boundary layer (BL) height determination and the case studies on aerosol transport over Himalayan region. The AOD retrievals from the latest level-2 data collections (C5.1 and C6.0) of MODerate resolution Imaging Spectroradiometer (MODIS) onboard Aqua and Terra satellites and Cloud-Aerosol LiDAR and Infrared Pathfinder Satellite Observations (CALIPSO) versions (4.10 and 3) are subjected for quantitative analysis to assess the level of agreement with the quality assured level-2 ground based AErosol RObotic NETwork (AERONET) measurements over Manora peak (29.36° N, 79.46°E), a high altitude site in the Himalayas. Analysis revealed that the AOD from the latest MODIS Terra C6.0 deep blue (DB) 30 km × 30 km and CALIPSO ver. 4.10 (overpass within ~100 km distance) are in a very good agreement ($R \geq 0.9$) with that from coincident AERONET measurements averaged over the span of ± 30 min. About 77% of the AOD retrieved using MODIS and ~87% from CALIPSO were found to be within the expected error (EE) limits. The AOD comparison between MODIS Terra C6.0 DB and CALIPSO ver. 4.10, suggested their synergic use for aerosol characterization over Himalayas. In comparison to the ver. 3, CALIPSO ver. 4.10 is found to have undergone substantial changes, and their long term inter-comparison in the grid 28.86°-29.86° N and 78.96°–79.96° E revealed that their vertical feature and aerosol sub-types are in agreement of ~94.6% and ~68.6%, respectively. Utilizing the AOD retrievals from AERONET and MODIS collections, the iteratively computed LR for three LiDAR systems was found to be lower (< 16) during winter and higher (> 43) during summer. Study on the BL height estimations suggested that the wavelet covariance transform (WCT) method for CALIPSO could be the best choice as compared to the threshold method, and complements well with the specific humidity gradient method used with the radiosonde observation. Case studies on the continental transport of smoke plumes emanating from crop-residue burning in post-monsoon, and long range transport of aerosols and dust over the region in summer are also discussed using the collocated measurements from ground-based AERONET and LiDAR, in conjunction with MODIS, CALIPSO, reanalysis data and trajectory modeling.

1. Introduction

The phenomena such as fossil fuel combustion and biomass burning are directly linked to the anthropogenic activities across the globe, affecting the weather and climate at various spatial and temporal scales. These anthropogenic sources as well as the natural sources like airborne dust, storms etc. can alter the concentration, chemical composition, size distribution and shapes of the atmospheric aerosols (Boucher, 2015). Any such alterations in aerosol distribution can affect the climate on regional as well as on global scales (IPCC, 2014; Hansen and Sato, 2016). The understanding of the atmospheric aerosol sources and their variations over a region in conjunction with the prevailing meteorological conditions may improve the knowledge of atmospheric processes such as the radiation balance, cloud formation, precipitation and chemical processes aloft. Rising concerns on climate change demand better insight of the physical and optical properties of the aerosols by means of ground and satellite based measurements such as AERONET, LiDAR, CALIPSO and MODIS. The correlations and improved understanding on the relationship between ground based and space borne observations are also essential in formulating the reliable current and future predictions (Ramachandran and Kedia, 2013). Moreover, it is important that any artefacts or inconsistencies

* Corresponding author at: Aryabhatta Research Institute of Observational Sciences (ARIES), Manora peak, Nainital, India.
E-mail address: ashish@aries.res.in (A. Kumar).

https://doi.org/10.1016/j.rse.2017.12.019
Received 12 May 2017; Received in revised form 3 December 2017; Accepted 15 December 2017
Available online 27 December 2017
0034-4257/

REMOTE SENSING LETTERS
2019, VOL. 10, NO. 6, 590–597
https://doi.org/10.1080/2150704X.2019.1587198

Observations on the distribution of clouds over northern India using joint CloudSat and CALIPSO measurements

Ashish Kumar[a,b], Narendra Singh[a] and Anshumali Singh[b]

[a]Atmospheric Science Division, Aryabhatta Research Institute of observational sciencES (ARIES), Nainital, India; [b]Environmental Science and Engineering Department, Indian Institute of Technology (Indian School of Mines), Dhanbad, India

ABSTRACT

A detailed study on the distribution of basic cloud types over the northern states of India (NSI) is performed using the decadal (2007–2016) raDAR-liDAR (DARDAR) data, which facilitates merged CloudSat and Cloud aerosol liDAR infrared pathfinder satellite observations (CALIPSO) observations onto the high resolution matched geographical grid points. The study demonstrates the seasonal variations, with south-west monsoon (June–September) exhibiting the maximum (>50%) cloud appearances while during the active period of western disturbances (December–March), ~25% of the total annual clouds, over the NSI region. Altostratus is found to be the most frequent cloud type (~20%) among others in the last decade over this region, while during south-west monsoon and western disturbances, the most dominant cloud types are deep convective (~25%) and nimbostratus (~33%), respectively.

ARTICLE HISTORY
Received 7 January 2019
Accepted 20 February 2019

1. Introduction

Clouds are critical and multi-scale atmospheric features least understood as they occur over wide spatio-temporal scales, and play a crucial role in the Earth's radiation budget by modulating the flow of incoming solar and outgoing thermal radiation, climate, weather, hydrological cycle, circulations and chemical reaction processes occurring in the atmosphere (Ramanathan et al. 1989; Quante 2004; Stephens 2005; Kumari and Goswami 2010). The quantitative investigation on the vertical structures, spatial variability, distribution, and properties of clouds is a necessary step (Wang and Sassen 2001; Rajeevan et al. 2013). Their accurate representation, especially on regional scales, is needed to understand their association with underlying forcing and feedback mechanisms in which they are involved. The study on a regional scale may help in unravelling the subtle influences, e.g., due to orography or due to aerosols from the highly polluted urban-industrial cities, like Delhi (Lodhi et al. 2013) and Kanpur (Chakraborty and Gupta 2010). Additionally, the study may further be supportive in forming the base-lines for the development and validation of the regional climate models and simulations (Cess et al. 1996; Wang et al. 2004; Foley 2010), for better predicting the weather and climate changes.

CONTACT Ashish Kumar ashish@aries.res.in Aryabhatta Research Institute of observational sciencES (ARIES), Manora peak, Nainital, India

Research Journal of Engineering Sciences ISSN 2278 – 9472
Vol. **8(2),** 17-22, May **(2019)** *Res. J. Engineering Sci.*

Signal analysis for ground based LiDAR

Ashish Kumar[1,2*], Narendra Singh[1] and Anshumali Singh[2]
[1]Aryabhatta Research Institute of Observational Sciences (ARIES), Manora peak, Nainital, Uttarakhand, India
[2]Indian Institute of Technology (Indian School of Mines), Dhanbad, Jharkhand, India
ashish@aries.res.in

Available online at: www.isca.in, www.isca.me
Received 23rd February 2019, revised 6th April 2019, accepted 24th May 2019

Abstract

Light Detection and Ranging (LiDAR) is an indispensable active remote sensing tool used to study vertical structure and dynamics. The variations in the atmospheric constituents such as aerosols, dust, clouds, water vapor and temperature can be studied using LiDARs depending upon the operating wavelengths. It is the optical counterpart of the well known Radio Detection and Ranging (RaDAR). This article presents the fundamental approaches involved in analyzing the LiDAR signals. The language used for the signal analysis is MATLAB and the data acquisition board is of ORTEC make.

Keywords: LiDAR, RaDAR, Data Acquisition, atmosphere, MATLAB.

Introduction

Remote sensing is the technique through which a volume or area of the atmosphere is observed to study certain parameters. Atmospheric RaDARs, LiDARs, and satellites are some of the instruments to carry out such observations. Remote sensing is needed to observe our environment and to understand how the atmosphere and the climate are getting affected by human activities. Remote sensing tools have advantage of being able to make multiple measurements from a range of heights simultaneously with high resolution at both space and time, compared to the in-situ measurements[1,2]. They emerge as the best tool to study the dynamically changing environments due to their repetitive capability and synoptic coverage.

The optical probing of the atmosphere is primarily achieved using LiDAR, which probes the atmosphere by two means i.e. ground based as well as airborne or space-borne[3,4]. The LiDAR is an active remote sensing instrument that relies on the propagation of light waves, and its principle of operation is very similar to RaDARs, thus many time refer as 'Optical RaDARs'[5]. The principle of a LiDAR system can be described in simplest way as: a pulse of 'light' emitted towards the sky where the target under investigation is located and its 'echo' is measured some time later. By measuring this time delay and knowing the speed of propagation of the emitted light we get the distance of the target. The 'light' source referred here is always a monochromatic, coherent and directional Light Amplification by Stimulated Emission of Radiation (LASER). The LASER beam travels upward in the atmosphere, interacts with various objects and a part of it is reflected back, which is collected by the telescopes[5]. A generalized schematic of the LiDAR system is illustrated in Figure-1.

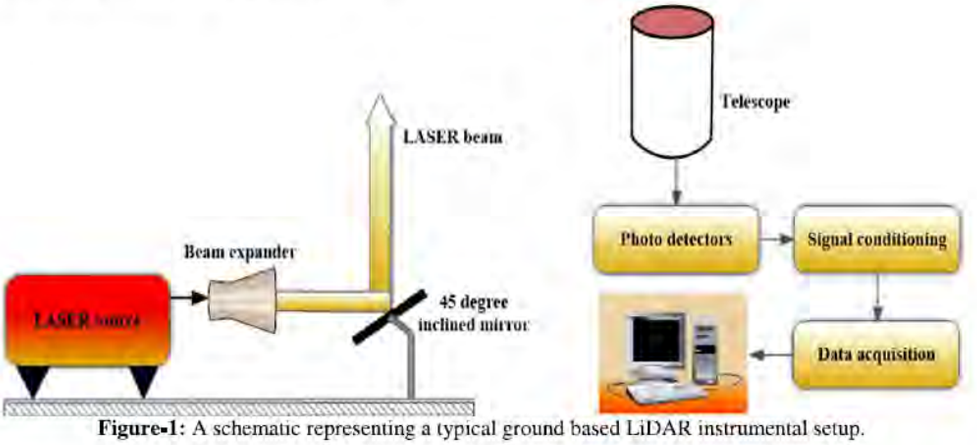

Figure-1: A schematic representing a typical ground based LiDAR instrumental setup.

Study on the satellite and ground based aerosol measurements over Himalayan region

Narendra Singh[1], Ashish Kumar[1, 2], Anshumali[2], Chandra Prakash[1], Chhavi P. Pandey[3]
(1) Aryabhatta Research Institute of Observational Sciences (ARIES), Nainital, India, https://www.aries.res.in/
(2) Indian Institute of Technology (Indian School of Mines), Dhanbad, India
(3) Wadia Institute of Himalayan Geology, Dehradun, India

Abstract

In this study, the evaluation of satellite retrievals with ground based aerosol measurements and a case study on hygroscopic aerosol transport is discussed. Latest aerosol product levels 1B and 2 (version 4.10) of Cloud-Aerosol LiDAR and Infrared Pathfinder Satellite Observations (CALIPSO) are evaluated with its earlier versions at a regional scale. A marked improvement is observed in the surface detection and tropospheric aerosol classification over the complex mountainous terrain in the latest version. A typical case on the measurements from ground-based sensors, in conjunction with CALIPSO, and reanalysis products is also discussed.

1. Introduction

The anthropogenic sources can alter the climate on regional as well as on global scales [1, 2]. The understanding on their variability over a region may improve the in-situ knowledge of the processes such as the radiation balance, cloud formation, precipitation etc. Rising concerns on climate change demand better insight of the physical and optical properties of aerosols by means of ground and satellite based measurements such as LiDAR, AErosol RObotic NETwork (AERONET), and CALIPSO. The improved understanding on the relationships between ground based and space borne observations is also essential in formulating the reliable current and future predictions [3, 4]. Moreover, the space borne measurements and retrieval algorithms are to be improved from time to time.

Past studies have proven that satellites are the best tool for broader understanding of aerosol parameters on a global scale, however, satellite measurements possess some uncertainties, especially, on the local scale which can be quantified through their assessment with the ground based measurements [5]. Further, the regional climate, particularly, in the mountain regions is being greatly affected due to deleterious anthropogenic interventions. The preliminary assessment of climate change with impact studies have also been reported [6, 7]. Considering the aforementioned facts, an attempt is made to evaluate the latest version of satellite aerosol retrievals from CALIPSO with its earlier version and compared with the ground truth to be useful at the regional scale studies and better understanding the nature of the aerosols.

2. Study region

The observational site [8], Manora Peak (29.36° N, 79.46°E, 1939 amsl) in the Nainital region of Uttarakhand is surrounded by the southern slopes of central Himalayas. This pristine site often influenced by the transport of the pollutants from Indo-Gangetic plains which are towards south as well as from the long range [9-11]. Thus provides a natural laboratory for transport of pollutants and the background measurements of the aerosol parameters.

3. Data and methodology

The CALIPSO satellite is operational since April 2006 and is equipped with a dual wavelength (532 and 1064 nm) polarization LiDAR system referred as Cloud and Aerosol LiDAR with Orthogonal Polarization (CALIOP) for providing the long term database of global aerosol vertical profiles [12]. The researchers worldwide are utilizing the CALIPSO products to a great extent in order to understand the impact of aerosols and clouds on the Earth's radiation budget. To evaluate the CALIPSO/CALIOP product versions (ver. 4.10 and ver. 3.xx) and for further studies, we identified three closest satellite overpasses (within ~80 km distance from the observation site) coinciding with the ground observations: 30 March 2012 (08:06 UTC), 9 December 2010 (20:43 UTC) and 10 November 2011 (20:42 UTC).

The 6-hourly ERA-Interim reanalysis product, are produced from the available atmospheric observations and dynamic models [13], and we utilize it to understand the prevailing meteorological conditions over the site during the period of study.

4. Assessment of CALIOP product versions

CALIPSO mission announced the release of its level 1B ver. 4.00 data product in November 2014 and, level 1B and 2 ver. 4.10 during November 2016, however, the two differ only in the ancillary data sets used for

Study on cloud types distribution over northern India using raDAR-liDAR (DARDAR)

Ashish Kumar[1, 2], Narendra Singh[1], and Anshumali[2]
(1) Aryabhatta Research Institute of Observational Sciences (ARIES), Nainital, India, https://www.aries.res.in/
(2) Indian Institute of Technology (Indian School of Mines), Dhanbad, India

Abstract

A detailed study on the distribution of basic cloud types over the northern states of India (NSI) is performed using the decadal (2007-2016) DARDAR data, which facilitates merged raDAR and liDAR observations onto the high resolution matched geographical grid points. Study demonstrates the seasonal variations, with southwest monsoon (June-September) exhibiting the maximum (> 50%) cloud appearances while during the active period of western disturbances (December-March), ~25% of the total annual clouds, over the NSI region. Altostratus is found to be the most frequent cloud type (~ 20%) among others in the last decade over this region, while during southwest monsoon and western disturbances, the most dominant cloud types are deep convective (~25%) and nimbostratus (~33%), respectively.

1. Introduction

Clouds are critical and multi-scale atmospheric features least understood as they occurs over wide spatio-temporal scales, and play a crucial role in the Earth's radiation budget by modulating the flow of incoming solar and outgoing thermal radiation, climate, weather, hydrological cycle, circulations and chemical reaction processes occurring in the atmosphere [1-4]. The quantitative investigation on the vertical structures, spatial variability, distribution, and properties of clouds is a necessary step [5-6]. Their accurate representation, especially on regional scales, is needed to understand their association with underlying forcing and feedback mechanisms in which they are involved. The study on regional scale may help in unravelling the subtle influences e.g. due to orography. Additionally, the study may further be supportive in forming the base-lines for the development and validation of the regional climate models and simulations [7-9], for better predicting the weather and climate changes.

Observing clouds with in-situ [10], ground-based [11] sensors and the satellite systems [12], contribute in understanding the composition and distribution of clouds in the atmosphere. However, satellites are the only observing platform that offers the characterization of clouds over large areas with better spatio-temporal resolution and the proliferation of satellite platforms carrying modern and advanced sensors nurtured wealth of cloud related information with accuracy [12-14].

2. Study region

The NSI region considered for study is confined within 23° - 38°N and 72° - 85°E, which encompasses Jammu & Kashmir, Himachal Pradesh, Punjab, Haryana and Chandigarh, Uttarakhand, Delhi & non-capital region (NCR), and Uttar Pradesh states as shown in Figure 1.

Figure 1. Study region i.e. Northern states of India

The understanding on cloud vertical structures, their spatio-temporal distributions, and the impact on changing climate is still poor. Therefore, the quantitative study focussed on the clouds over NSI region may be an important step in the direction of mitigating the natural catastrophes like -cloudbursts, flash floods, and landslides causing the loss of life and ecosystem. The analysis on cloud related parameters over this region will help reducing the uncertainties associated with regional climate models, and in quantifying the feedback by the clouds in radiation and latent heat calculations [4, 7].

The varied and complex topography of NSI region, covering the major part of Indo-Gangetic plains (IGP) as well as the Himalayas, possesses the large variability in meteorological parameters which are mainly controlled by two major atmospheric circulations– southwest monsoon and the western disturbances. These two contrasting periods: (i) June to September (JJAS), and (ii) December

CURRICULUM VITAE

Curriculum Vitae

Ashish Kumar
Research Scholar
Department of Environmental Science and Engineering,
Indian Institute of Technology (Indian School of Mines),
Dhanbad, 826004, Jharkhand, India

Engineer-D, Aryabhatta Research Institute of
Observational Sciences (ARIES),
Manora Peak, Nainital 263 002, Uttarakhand, India

Tel: +91- 5942- 270815/270790
Cell: +91-9759891466, +91-6398180086
E-mail: ashish@aries.res.in, ashish452@yahoo.com

Personal Details:
Date & Place of Birth : 1st March 1984, Ranchi (Jharkhand)
Nationality : Indian
Marital Status : Married

Area of Interests:
Remote sensing, atmospheric studies – aerosols, clouds, and precipitation, digital signal processing, digital image processing, radio frequency (RF) and microwave engineering, electronics engineering.

***Educational qualifications*:**

Qualification	*Institute/Board*	*Year of passing*
Ph.D. (ESE)	IIT(ISM), Dhanbad	ongoing
M.Tech (ECE)	NIET, NIMS University, Jaipur	2012
BE (Electronics)	B.V.P C.O.E, Bharati Vidyapeeth, Pune	2006
Diploma in Engg.	SLIET, Sangrur	2003
Certificate in Engg. (10+2)	SLIET, Sangrur	2001
Matriculation	CBSE	1999

Journal Publications:

1. **Ashish Kumar**, Narendra Singh, and Anshumali Singh, 'Observations on the distribution of clouds over northern India using joint CloudSat and CALIPSO measurements', *Remote Sensing Letters*, vol. 10(6), pp. 590-597, 2019. doi: 10.1080/2150704X.2019.1587198.
2. **Ashish Kumar**, Narendra Singh, and Anshumali Singh, 'Signal analysis for ground based LiDAR', *Research Journal of Engineering Sciences*, vol. 8(2), pp. 17-22, 2019.

3. **Ashish Kumar**, Narendra Singh, Anshumali, Raman Solanki, 'Evaluation and utilization of MODIS and CALIPSO aerosol retrievals over a complex terrain in Himalaya', *Remote Sensing of Environment*, vol. 206, pp. 139-155, ISSN 0034-4257, 2018. https://doi.org/10.1016/j.rse.2017.12.019.
4. **Ashish Kumar**, 'A Simple Approach for Designing a Filter on Microstrip Lines', *Applied Engineering Letters*, vol. 4(1), pp. 19-23, 2019. ISSN 2466-4677. https://doi.org/10.18485/aeletters.2019.4.1.3.
5. **Ashish Kumar**, 'A Simple Approach for Design and Fabrication of Wilkinson Power Divider on Microstrip Line.' *J. Engr. Desg. Anal.*, 2(1):1-4, 2019.
6. S. Bhattacharjee, **Ashish Kumar**, and M. Naja, "Array factor optimization of an active planar phased array using evolutionary algorithm", *International Journal of Antennas* (JANT) Vol.2, No.3, July 2016.
7. N. Ojha, M. Naja, T. Sarangi, R. Kumar, P. Bhardwaj, S. Lal, S. Venkataramani, R. Sagar, **Ashish Kumar**, H. C. Chandola, "On the processes influencing the vertical distribution of ozone over the central Himalayas: Analysis of yearlong ozonesonde observations", *Atmospheric Environment*, vol. 88, pp. 201-211, ISSN 1352-2310, Jan. 2014. http://dx.doi.org/10.1016/ j. atmosenv. 2014. 01.031.
8. T. Sarangi, M. Naja, N. Ojha, R. Kumar, S. Lal, S. Venkataramani, **Ashish Kumar**, R. Sagar, and H. C. Chandola, "First simultaneous measurements of ozone, CO, and NO_y at a high-altitude regional representative site in the central Himalayas", *J. Geophys. Res. Atmos.*, 119, 1592–1611, Feb. 2014. doi:10.1002 /2013JD020 631.
9. **Ashish Kumar**, A. Shrivastava, S. Bhattacharjee, P. Kumar, M. Naja, "Generation, analysis and evaluation of bi-phase complementary pairs", *International Journal of Advancements in Technology* (IJoAT), ISSN 0976-4860, 3(4), Dec. 2012.
10. T. Bangia, P. K. Agarwal, **Ashish Kumar**, S. K. Singh and R. Sagar, "Opto-mechanical design, analysis and economical manufacture of a large aperture LIDAR receiver telescope", *Journal of Engineering and Technology Research*, vol. 3(6), pp.180-196, June 2011.
11. T. Bangia, A. Omar, R. Sagar, **Ashish Kumar**, S. Bhattacharjee, A. Reddy, P. K. Agarwal, and P. Kumar, "Study of atmospheric aerosols over the Central Himalayan region using a newly developed Mie light detection and ranging system: Preliminary results", *Journal of Applied Remote Sensing*, 5(1):053521, May 02, 2011. doi:10.1117/1.3579158.
12. T. Bangia, **Ashish Kumar**, R. Sagar, P. K. Agarwal and S. K. Singh**,** "Development of Mie LIDAR system and initial cloud observations over Central Himalayan region", *Scientific Research and Essays*, **6**(4), pp. 896-907, 18 Feb., 2011.
13. **Ashish Kumar**, S. Bhattacharjee, M. Naja, P. Kumar, "Front-end Digital Signal Processing Scheme for 206.5 MHz Atmospheric Radar Application", *International Journal of Advancements in Technology* (IJoAT), ISSN 0976-4860, **2**(1), Jan, 2011.

***Conferences/Symposiums/Workshops**:*

1. **Ashish Kumar,** Narendra Singh, and Anshumali, 'Study on cloud types distribution over northern India using raDAR-liDAR (DARDAR)', *URSI Asia Pacific Radio Science Conference* 2019, New Delhi, India, 09 - 15 March 2019. doi: 10.23919/URSIAP-RASC.2019.8738690.
2. Narendra Singh, **Ashish Kumar,** Anshumali, C. Prakash, and C. P. Pandey, 'Study on the satellite and ground based aerosol measurements over Himalayan region', *URSI Asia Pacific Radio Science Conference* 2019, New Delhi, India, 09 - 15 March 2019. doi: 10.23919/URSIAP-RASC.2019.8738218.
3. M. Naja, S. Bhattacharjee, **Ashish Kumar**, N. Singh, P. Kumar, "ARIES ST Radar (ASTRAD) at a mountain site (Nainital) in the central Himalayas", *URSI Asia Pacific Radio Science Conference 2019*, New Delhi, India, 09 - 15 March 2019. doi: 10.23919/URSIAP-RASC.2019.8738224.
4. N. Singh, **Ashish Kumar**, V. K. Soni, 'Transport of dust and their influence over the glaciated surfaces in the Himalayan region', *The 29th International Laser Radar Conference* (ILRC29), Hefei, Anhui, China, June 24-28, 2019.
5. Narendra Singh, **Ashish Kumar**, and Anshumali, 'Transport and influence of pollutants over Himalayan region', *National conference on Biogeochemical Cycles and Climate Change*, IIT(ISM), Dhanbad, India, 11 August 2018.
6. K. K. Shukla, D.V. Phani Kumar, **Ashish Kumar**, K. N. Kumar, M. Naja, M.V. Ratnam, and S. Bhattacharjee, "Signatures of Elevated aerosol layers over Central Himalayan region", *National Space Science Symposium (NSSS)*, 2012, S. V. University, Tirupati.
7. T. Sarangi, M. Naja, N. Ojha, R. Kumar, **Ashish Kumar**, S. Lal, H. C. Chandola and R. Sagar, "Variations in ozone and precursors over a high altitude site in the Central Himalayas", *National Space Science Symposium (NSSS)*, 2012, S. V. University, Tirupati.
8. N. Ojha, M. Naja, T. Sarangi, R. Kumar, S. Lal, S. Venkataramani, **Ashish Kumar**, and H. C. Chandola, "First Yearlong Ozonesonde observations over the central Himalayas: Influences of Biomass Burning and Downward Transport", *AGU Fall Meeting*, 3-7 Dec, 2012, San Francisco, USA.
9. N. Ojha, N., M. Naja, T. Sarangi, R. Kumar, K. P. Singh, Y. Kant, S. Lal, S. Venkataramani, **Ashish Kumar**, and H. C. Chandola, "Tropospheric Ozone variations over the Northern India: Balloon-borne and surface based measurements", *IGAC-2012*, 17-21 Sept, 2012, Beijing, China.
10. N. Ojha, M. Naja, R. Kumar, T. Sarangi, **Ashish Kumar**, S. Lal, S. Venkataramani, K. P. Singh and H. C. Chandola, "Tropospheric ozone distribution over the Northern India: Balloonborne and surface based measurements", *Indo-German workshop on air quality and climate change (CHOP-C)*, 16-18 Jan, 2012, IITM, Pune.
11. T. Sarangi, M. Naja, N. Ojha, R. Kumar, **Ashish Kumar**, S. Lal, H. C. Chandola and R. Sagar, "Variations in ozone and precursors over a high altitude site in the central

Himalayas", *Indo-German workshop on air quality and climate change (CHOP-C)*, 16-18 Jan, 2012, IITM, Pune.

12. M. Naja, N. Ojha, T. Sarangi, P. Bhardwaj, R. Kumar, N. Singh, **Ashish Kumar**, S. Lal, and R. Sagar, "Influences of regional pollution over the Northern India: Ozone soundings from the central Himalayas", *39th COSPAR Scientific Assembly*, 14-22 July, 2012, Mysore.
13. T. Sarangi, M. Naja, N. Ojha, R. Kumar, S. Lal, S. Venkataramani, **Ashish Kumar**, H. C. Chandola, and R. Sagar, "Variabilities and inter-relation among ozone, CO, NO_y and SO_2 over the Central Himalayas", *COSPAR-2012*, Mysore.
14. N. Ojha, M. Naja, T. Sarangi, R. Kumar, **Ashish Kumar**, S. Lal, S.Venkataramani, K. P. Singh, "Balloon borne and surface measurement of Tropospheric ozone over the Northern India". *In-house Meeting* held at ARIES, Manora Peak during April 19-20, 2012.
15. M. Naja, S. Bhattacharjee, N. Singh, C. Prakash, **Ashish Kumar**, D. Phani Kumar, G. Viswanathan and R. Sagar, "Upcoming ST Radar at Nainital over Central Himalayas", *Asia Oceanic Geosciences Society (AOGS) International Conference 2010*, Hyderabad, India, 5-9 July, 2010.
16. **Ashish Kumar**, V.K. Anandan, S. Bhattacharjee, C. Prakash, M. Naja, P. Rao, C. Sudhir, S. Damle, G. Viswanathan and R. Sagar, "FPGA Based Implementation Of DSP Scheme for Upcoming 206.5 MHz ST Radar at ARIES Nainital, India", *MST-12 Radar International Conference* at University of Western Ontario, Canada during 22 – 24 May, 2009.
17. S. Bhattacharjee, M. Naja, C. Prakash, **Ashish Kumar**, P. Rao, Balakrishnan, C. Sudhir, S. Damle, G. Viswanathan, P. Srinivasulu and R Sagar, "Design aspects of the antenna array for ST Radar in central Himalayan region at Nainital, India", *MST-12 Radar International Conference* at University of Western Ontario, Canada during 22 – 24 May, 2009.
18. C Prakash, S. Bhattacharjee, M Naja, **Ashish Kumar**, and N. Singh, "Peak Power Aperture calculation for ARIES ST Radar by measuring Cn^2 in Shivalik Range of Himalaya at Nainital, India", *MST-12 Radar International Conference* at University of Western Ontario, Canada during 22 – 24 May, 2009.